UNIVERSITÀ DEGLI STUDI DI PISA

FACOLTÀ DI SCIENZE MATEMATICHE, FISICHE E NATURALI

Tesi per il Conseguimento del
Dottorato di Ricerca in Fisica

XII Ciclo – Anni Accademici 1996-1999

Scalar Quark searches with the ALEPH Experiment at LEP2

Giacomo Sguazzoni

Supervisore:
Prof. Ettore Focardi

Coordinatore:
Prof. Ennio Arimondo

Contents

Introduction

The description of the strong, weak and electromagnetic interactions within matter, the Standard Model theory, has been shown to be very consistent with experimental data up to explored energy scale even if the Higgs boson, the visible remnant of mechanism responsible of the gauge symmetry breaking and of the fermion mass hierarchy, is not yet discovered.

Despite this success it is common opinion that Standard Model is a lower energy effective theory of a larger and more fundamental framework not suffering the several problems that occur as soon as one tries to extend the Standard Model to higher energies (typically the Planck scale). *Supersymmetry* (*SUSY*) is one of the most elegant theory that provides such a solid framework.

Supersymmetry enlarges the elementary particle spectra predicting the existence of new particles. The supersymmetric particles have the same couplings as the Standard Model particles. Therefore the LEP e^+e^- collider is almost ideal to confirm or exclude their presence. In particular the supersymmetric scalar partners of top and bottom quarks could be enough light; thus they are a natural target of an experimental search of SUSY existence.

In this report the extensive scalar quark (*squarks*) search performed at LEP2 with the ALEPH experiment will be described. The obtainable results are complementary to the ones from similar searches performed at the TEVATRON collider since the LEP experiments have the possibility of testing for squarks domains left unexplored by the TEVATRON experiments.

The results presented here are based on ALEPH data sample collected at energies up to 202 GeV.

The report is organised as follows: the chapter 1 is a short introduction to Supersymmetry and its motivations compared with weak aspects of the Standard Model. In chapter 2 some detail about the squark sector phenomenology is given. In chapter 3 the ALEPH experiment and the LEP collider are described. Chapter 4 gives details about the Monte Carlo generation of signal samples that is critical in several aspects; the Monte Carlo simulation of backgrounds processes is described as well. Chapter 5 is dedicated to the detailed description of the selections used to search for squark signal, while in the chapter 7 the results and their interpretation are discussed after the description of systematic uncertainties of chapter 6.

1 Standard Model and SuperSymmetry

1.1 The Standard Model

Elementary constituents of ordinary matter behave as spin-1/2 particles (*fermions*). The Standard Model describes two out of three types of their interactions observed in nature: the electroweak and the strong interactions. A consistent quantum theory of gravity is not yet available. The fermions are divided into two fundamental types: *leptons*, interacting via electroweak interactions, and *quarks*, feeling also the strong interactions. A short description of the Standard Model will be given, with particular care to the electroweak sector where the arguments suggesting a supersymmetric extension originate. The Standard Model electroweak interaction kernel is the Glashow-Weinberg-Salam model [1], a quantum field theory based on the $SU(2)_L \otimes U(1)_Y$ group. Electroweak gauge bosons and fermions acquire mass via the Higgs mechanism, responsible for the spontaneous $SU(2)_L \otimes U(1)_Y$ breaking of the $SU(2)_L \otimes U(1)_Y$ symmetry. The theory is renormalizable [2].

So far three charged and massive leptons (e, μ, τ) and two neutral and massless leptons known as *neutrinos* (ν_e, ν_μ) have been directly observed. Moreover there is indirect evidence of the third neutrino (ν_τ). The observed kind of quarks are six, all massive, three with electric charge 2/3 (u, c and t) and three with charge $-1/3$ (d, s and b), the charge being measured in units of the massive leptons charge. These fermions are described in terms of families as tables 1.1 and 1.3 show.

According to the Standard Model, the phenomenology confirms the existence of four bosons that mediate the electroweak interactions: two charged bosons (W^+ and W^-) with mass of $\sim 80\,\mathrm{GeV}/c^2$, one neutral boson (Z) with mass of $\sim 91\,\mathrm{GeV}/c^2$ and one neutral and massless boson (the *photon* γ). The strong interaction behaves as it was mediated by eight massless bosons (*gluons*), also in this case as the Standard Model predicts.

1.1.1 The lepton sector

The fields describing the leptons within each family include two left-handed spinorial fields, that make a $SU(2)_L$ doublet, and a right-handed spinorial field that is a $SU(2)_L$ singlet. The $SU(2)_L$ doublets can be written as L_L^α and the $SU(2)_L$ singlets as ℓ_R^α where $\alpha = 1, 2, 3$ is the family index.

The bare lagrangian $\mathcal{L}_{EW}$ of the model contains the kinetic terms for massless fermions

Family $\rightarrow$	I	II	III
$SU(2)_L$ doublet	$\begin{pmatrix} \nu_{e_L} \\ e_L \end{pmatrix}$	$\begin{pmatrix} \nu_{\mu_L} \\ \mu_L \end{pmatrix}$	$\begin{pmatrix} \nu_{\tau_L} \\ \tau_L \end{pmatrix}$
$SU(2)_L$ singlet	e_R	μ_R	τ_R

Table 1.1: Leptons and their families.

and massless gauge bosons:

$$\begin{aligned} & & \mathcal{L}_{\rm EW}^{\rm leptons} = & \qquad (1.1) \\ \text{Boson kinetic terms} \rightarrow & & -\frac{1}{4}F^a_{\mu\nu}F^{a\mu\nu} - \frac{1}{4}B_{\mu\nu}B^{\mu\nu} & \\ \text{Lepton kinetic terms} \rightarrow & & +i\sum_\alpha \left(L_{\rm L}^{\dagger\alpha}\overline{\sigma}^\mu \partial_\mu L_{\rm L}^\alpha + \ell_{\rm R}^{\dagger\alpha}\sigma^\mu\partial_\mu \ell_{\rm R}^\alpha \right), & \end{aligned}$$

where

$$\sigma^\mu = \left(1, \sigma^i\right), \quad \overline{\sigma}^\mu = \left(1, -\sigma^i\right) \qquad (1.2)$$

with σ^i, $i = 1, 2, 3$ that represents the standard Pauli matrices

$$\sigma^1 = \begin{pmatrix} 0 & 1 \\ 1 & 0 \end{pmatrix}, \quad \sigma^2 = \begin{pmatrix} 0 & -i \\ i & 0 \end{pmatrix}, \quad \sigma^3 = \begin{pmatrix} 1 & 0 \\ 0 & -1 \end{pmatrix}. \qquad (1.3)$$

Local gauge invariance under $\mathrm{SU(2)_L} \otimes \mathrm{U(1)_Y}$ is obtained by introducing the covariant derivatives acting on the lepton fields, that means:

$$\partial_\mu L_{\rm L}^\alpha \rightarrow D_\mu L_{\rm L}^\alpha = \left(\partial_\mu + \frac{i}{2}gW_\mu^a\sigma^a - \frac{i}{2}g'B_\mu\right) L_{\rm L}^\alpha, \qquad (1.4)$$

$$\partial_\mu \ell_{\rm R}^\alpha \rightarrow D_\mu \ell_{\rm R}^\alpha = \left(\partial_\mu - ig'B_\mu\right) \ell_{\rm R}^\alpha, \qquad (1.5)$$

where W_μ^a and B_μ are the bosonic gauge fields of $\mathrm{SU(2)_L} \otimes \mathrm{U(1)_Y}$, g and g' their couplings. The gauge fields tensors are:

$$F^a_{\mu\nu} = \partial_\mu W^a_\nu - \partial_\nu W^a_\mu - g\epsilon^{abc}W^b_\mu W^c_\nu, \qquad (1.6)$$

$$B_{\mu\nu} = \partial_\mu B_\nu - \partial_\nu B_\mu, \qquad (1.7)$$

where ϵ^{abc} is the Ricci antisymmetric tensor.

The quantum numbers for leptons are given in table 1.2. The *weak hypercharge* Y is responsible for the $\mathrm{U(1)_Y}$ transformations; the *weak isospin* T^3, third component of $\overrightarrow{T} = \frac{1}{2}(\sigma^1, \sigma^2, \sigma^3)$, controls the behaviour under $\mathrm{SU(2)_L}$. The *electric charge* Q is a special combination chosen is such a way to guarantee the correct behaviour under $\mathrm{U(1)_{em}}$ after the electroweak symmetry breaking.

By the lagrangian (1.1) the neutral and charged weak interactions and the electromagnetic interactions can be reproduced, but it would fail taking into account the observed fermion and bosons masses. In fact the mass terms are not gauge invariant and cannot be added to the electroweak lagrangian without destroying the gauge structure. Nevertheless, this apparently impossible result can be reached enlarging the Standard Model field content. These new fields, known as Higgs fields, are organized in doublet $\mathcal{H}$ (see table 1.2) that feels a potential which minima are not $\mathrm{SU(2)_L} \otimes \mathrm{U(1)_Y}$ invariant. The gauge interactions of the Higgs doublet is able to give mass to gauge bosons after an appropriate choice of the vacuum expectation value (VEV). The Higgs doublet is made interacting with the fermions by suitable terms, known as *Yukawa couplings*, and also the fermions acquire mass. All this procedure is usually referred as *Higgs mechanism*.

	$\mathrm{SU(2)_L},\ 2\cdot T^3$	Y	$Q = Y/2 + T^3$
$L_{\mathrm{L}}^{\alpha} = \begin{pmatrix} \nu_{\mathrm{L}}^{\alpha} \\ \ell_{\mathrm{L}}^{\alpha} \end{pmatrix}$	$\mathbf{2},\ \begin{pmatrix} 1 \\ -1 \end{pmatrix}$	-1	$\begin{pmatrix} 0 \\ -1 \end{pmatrix}$
$\ell_{\mathrm{R}}^{\alpha}$	$\mathbf{1},\ 0$	-2	-1
$\mathcal{H} = \begin{pmatrix} \mathcal{H}_1 \\ \mathcal{H}_2 \end{pmatrix}$	$\mathbf{2},\ \begin{pmatrix} 1 \\ -1 \end{pmatrix}$	1	$\begin{pmatrix} 1 \\ 0 \end{pmatrix}$

Table 1.2: Lepton and Higgs quantum numbers.

The Higgs sector terms to be added to the lagrangian (1.1) are therefore the Higgs kinetic term, the Higgs potential and the Yukawa couplings:

$$\begin{aligned} & \mathcal{L}_{\mathrm{EW}}^{\mathrm{Higgs}} = \\ \text{Higgs part} \rightarrow \quad & \partial_\mu \mathcal{H}^\dagger \partial^\mu \mathcal{H} - V\left(\mathcal{H}^\dagger \mathcal{H}\right) \\ \text{Yukawa couplings} \rightarrow \quad & -\sum_\alpha y_\alpha \left(L_{\mathrm{L}}^{\dagger\alpha} \mathcal{H} \ell_{\mathrm{R}}^{\alpha} + \ell_{\mathrm{R}}^{\dagger\alpha} \mathcal{H}^\dagger L_{\mathrm{L}}^{\alpha}, \right) \end{aligned} \tag{1.8}$$

where y_α are the Yukawa coupling constants. Also for the Higgs fields, the gauge invariance means replace the standard derivatives by the covariant derivatives:

$$\partial_\mu \mathcal{H} \rightarrow D_\mu \mathcal{H} = \left(\partial_\mu + \frac{i}{2} g W_\mu^a \sigma^a + \frac{i}{2} g' B_\mu \right) \mathcal{H}, \tag{1.9}$$

according to the Higgs fields quantum numbers given in table 1.2.

The Higgs potential, $\mathrm{SU(2)_L} \otimes \mathrm{U(1)_Y}$ invariant, is

$$V\left(\mathcal{H}\mathcal{H}^\dagger\right) = \frac{k^2}{4}\left(\mathcal{H}^\dagger \mathcal{H} - v^2\right)^2, \tag{1.10}$$

where k^2 is an adimensional and positive coupling constant and the parameter v is the vacuum expectation value. The minima $\mathcal{H}_{min}$ of V are only $\mathrm{U(1)_{em}}$ invariant and satisfy $\mathcal{H}_{min}^\dagger \mathcal{H}_{min} = v^2$.

The new effective particle content of the model becomes evident writing the Higgs potential around a minimum. This corresponds to the *symmetry breaking* $\mathrm{SU(2)_L} \rightarrow \mathrm{U(1)_{em}}$. The minimum expectation value on the vacuum is chosen to be neutral:

$$\langle 0 | \mathcal{H}_{min} | 0 \rangle = \begin{pmatrix} 0 \\ v \end{pmatrix}. \tag{1.11}$$

The Higgs complex doublet can be expressed in terms of deviations from the chosen minimum with the following change of variables:

$$\mathcal{H} = \exp\left(-\frac{i}{2}\theta^a \sigma^a\right) \begin{pmatrix} 0 \\ v + \frac{H}{\sqrt{2}} \end{pmatrix} \tag{1.12}$$

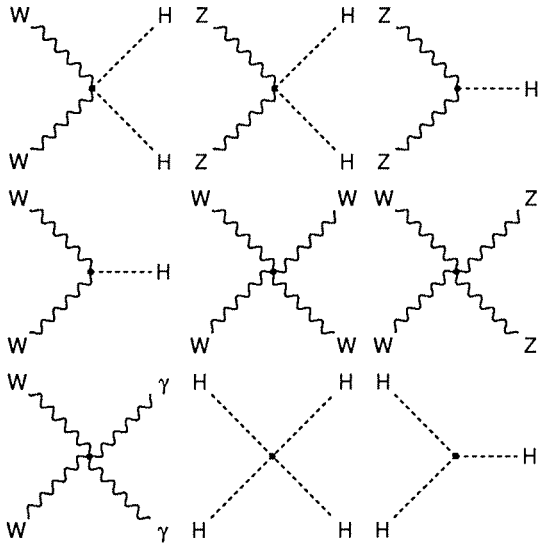

Figure 1.1: Cubic and quartic boson vertices.

where θ^a, $a = 1, 2, 3$ and H are the new scalar and real variables called *Goldstone bosons*. The exponential in (1.12) is absorbed by the gauge invariance[1] and the boson part of the lagrangian (1.1) can be rewritten as:

$$\begin{aligned} & \mathcal{L}_{\text{BOSONS}} = \\ \text{Higgs} \rightarrow \quad & \frac{1}{2}\partial_\mu H \partial^\mu H - \frac{k^2 v^2}{2} H^2 \\ \text{W bosons} \rightarrow \quad & -\frac{1}{2}\left(\partial_\mu W_\nu^+ - \partial_\nu W_\mu^+\right)\left(\partial^\mu W^{-\nu} - \partial^\nu W^{-\mu}\right) \\ & -\frac{g^2 v^2}{4}\left(W_\mu^+ W^{+\mu} + W_\mu^- W^{-\mu}\right) \\ \text{Z boson} \rightarrow \quad & -\frac{1}{4}\left(\partial_\mu Z_\nu - \partial_\nu Z_\mu\right)^2 + \frac{1}{4} v^2 \left(g^2 + g'^2\right) Z_\mu Z^\mu \\ \text{Photon} \rightarrow \quad & -\frac{1}{4}\left(\partial_\mu A_\nu - \partial_\nu A_\mu\right)^2 \\ \text{Bosons couplings} \rightarrow \quad & + \ldots, \end{aligned} \tag{1.14}$$

where the last omitted part contains the cubic and quartic boson couplings shown in fig. 1.1. W_μ^3 and B_μ are combined to obtain the two neutral mass eigenstate fields needed to reproduce observations. The photon field,

$$A_\mu = W_\mu^3 \sin\theta_W + B_\mu \cos\theta_W, \tag{1.15}$$

[1] Algebraically the symmetry breaking in the lagrangian corresponds to the simple substitution

$$\mathcal{H} \rightarrow \begin{pmatrix} 0 \\ v + \frac{H}{\sqrt{2}} \end{pmatrix}. \tag{1.13}$$

remain massless since $U(1)_{em}$ is not broken. The massive field responsible of weak neutral current interaction,

$$Z_\mu = W_\mu^3 \cos\theta_W - B_\mu \sin\theta_W, \tag{1.16}$$

acquires the mass

$$m_Z = \frac{v}{\sqrt{2}}\sqrt{g^2 + g'^2}. \tag{1.17}$$

The *Weinberg angle* θ_W is such that:

$$\cos\theta_W = \frac{g}{\sqrt{g^2 + g'^2}}, \qquad \sin\theta_W = \frac{g'}{\sqrt{g^2 + g'^2}}. \tag{1.18}$$

The other two bosonic fields W_μ^1 and W_μ^2 acquire a common mass

$$m_W = \frac{gv}{\sqrt{2}}, \tag{1.19}$$

and they can be conveniently written as two charged fields mediating the weak charged current interaction:

$$W_\mu^+ = \frac{1}{\sqrt{2}}\left(W_\mu^1 - iW_\mu^2\right), \qquad W_\mu^- = \frac{1}{\sqrt{2}}\left(W_\mu^1 + iW_\mu^2\right). \tag{1.20}$$

The real field H, called physical Higgs field, describes a scalar particle with mass $m_H = kv$. It is the observable remnant of the mechanism causing the symmetry breaking.

After the symmetry breaking the leptonic part of the lagrangian reads:

$$\begin{aligned}
&\mathcal{L}_{\text{LEPTONS}} = \\
\text{Propagation} \rightarrow \quad & i\sum_\alpha \left(\nu_L^{\dagger\alpha}\overline{\sigma}^\mu\partial_\mu\nu_L^\alpha + \overline{\ell}^\alpha\gamma^\mu\partial_\mu\ell^\alpha - vy_\alpha\overline{\ell}^\alpha\ell^\alpha\right) \\
\text{Charged weak int.} \rightarrow \quad & -\frac{g}{2\sqrt{2}}\sum_\alpha\left[W_\mu^-\overline{\ell}^\alpha\gamma^\mu\left(1-\gamma^5\right)\nu^\alpha + W_\mu^+\overline{\nu}^\alpha\gamma^\mu\left(1-\gamma^5\right)\ell^\alpha\right] \\
\text{Neutral weak int.} \rightarrow \quad & +\frac{g}{4\cos\theta_W}Z_\mu\sum_\alpha\left[\overline{\ell}^\alpha\gamma^\mu\left(1-4\sin^2\theta_W-\gamma^5\right)\ell^\alpha\right. \\
& \left.-\overline{\nu}^\alpha\gamma^\mu\left(1-\gamma^5\right)\nu^\alpha\right] \\
\text{E.M. int.} \rightarrow \quad & +g\sin\theta_W A_\mu\sum_\alpha\overline{\ell}^\alpha\gamma^\mu\ell^\alpha \\
\text{Fermion} - \text{Higgs int.} \rightarrow \quad & -\frac{y_\alpha}{\sqrt{2}}\sum_\alpha H\overline{\ell}^\alpha\ell^\alpha.
\end{aligned} \tag{1.21}$$

In writing these terms the following properties of a fermionic field Ψ have been used:

$$\overline{\Psi} = \Psi^\dagger\gamma^0, \tag{1.22}$$

$$\Psi_{R,L} = \frac{1}{2}\left(1 \pm \gamma^5\right)\Psi, \quad \Psi = \Psi_L + \Psi_R, \tag{1.23}$$

$$\overline{\Psi}\Psi = \Psi_{\mathrm{L}}^{\dagger}\Psi_{\mathrm{R}} + \Psi_{\mathrm{R}}^{\dagger}\Psi_{\mathrm{L}}, \tag{1.24}$$

coming from the gamma matrices definitions:

$$\gamma^i = \begin{bmatrix} 0 & \sigma^i \\ -\sigma^i & 0 \end{bmatrix}, \quad \gamma^0 = \begin{bmatrix} 1 & 0 \\ 0 & -1 \end{bmatrix}, \quad \gamma_5 = i\gamma^0\gamma^1\gamma^2\gamma^3. \tag{1.25}$$

The neutrinos remains massless while the leptons acquire mass $m_\alpha = v y_\alpha$.

The coupling constant to the photon field A_μ is identified with the electric charge e:

$$e = g\sin\theta_W = g'\cos\theta_W = \frac{gg'}{\sqrt{g^2+g'^2}}. \tag{1.26}$$

The vacuum expectation value v can be extracted from measured values of m_{Z}, m_{W} and e,

$$v \sim 174\,\mathrm{GeV}/c^2, \tag{1.27}$$

and the Yukawa couplings y_α from the measured lepton masses. The interactions of leptons are therefore consequently specified. From the structure of the lagrangian it turns out that the lepton interactions are family number conserving.

1.1.2 The quark sector

All the observed hadrons are described as bounded states of the six types of quarks of table 1.3. As for the leptons, the hadron weak decays are described dividing the quarks into three $\mathrm{SU(2)_L} \otimes \mathrm{U(1)_Y}$ families. Nevertheless the experimental observation shows that the quark family number is not conserved as the lepton family number. This suggests that quark mass eigenstates and quark interaction eigenstates are different. Therefore each quark family is a suitable combination of the mass eigenstates of table 1.3:

$$U^{\alpha}_{\mathrm{L,R}} = \mathcal{U}^{\alpha\beta}_{\mathrm{L,R}} u^{\beta}_{\mathrm{L,R}}, \quad D^{\alpha}_{\mathrm{L,R}} = \mathcal{D}^{\alpha\beta}_{\mathrm{L,R}} d^{\beta}_{\mathrm{L,R}}, \tag{1.28}$$

where α is the family index and β runs over the mass eigenstates index: $u^1 = \mathrm{u}$, $u^2 = \mathrm{c}$, $u^3 = \mathrm{t}$, $d^1 = \mathrm{d}$, $d^2 = \mathrm{s}$, $d^3 = \mathrm{b}$. Thus $\mathcal{U}_{\mathrm{R}}$, $\mathcal{U}_{\mathrm{L}}$, $\mathcal{D}_{\mathrm{R}}$ and $\mathcal{D}_{\mathrm{L}}$ are 3×3 unitary matrices. The quarks field terms to be added to the leptonic lagrangian are:

$$\begin{aligned} & \mathcal{L}^{\mathrm{quarks}}_{\mathrm{EW}} = \\ \text{Quark part} \rightarrow \quad & +i\sum_{\alpha}\left(Q^{\dagger\alpha}_{\mathrm{L}}\overline{\sigma}^{\mu}\partial_\mu Q^{\alpha}_{\mathrm{L}} + U^{\dagger\alpha}_{\mathrm{R}}\sigma^{\mu}\partial_\mu U^{\alpha}_{\mathrm{R}} + D^{\dagger\alpha}_{\mathrm{R}}\sigma^{\mu}\partial_\mu D^{\alpha}_{\mathrm{R}}\right) \\ \text{Yukawa couplings} \rightarrow \quad & -\sum_{\alpha\alpha'}\left(\Upsilon_{\alpha\alpha'} Q^{\dagger\alpha}_{\mathrm{L}}\mathcal{H} D^{\alpha'}_{\mathrm{R}} + \Upsilon'_{\alpha\alpha'} Q^{\dagger\alpha}_{\mathrm{L}}\widehat{\mathcal{H}} U^{\alpha'}_{\mathrm{R}} + \mathrm{h.c.}\right) \end{aligned} \tag{1.29}$$

Charge	Quark labels
$\frac{2}{3}$	u, c, t
$-\frac{1}{3}$	d, s, b

Table 1.3: The six types of quarks.

	$\mathrm{SU(2)_L}$, $2\cdot T^3$	Y	$Q=Y/2+T^3$
$Q^\alpha_{\mathrm{L}}=\begin{pmatrix} U^\alpha_{\mathrm{L}} \\ D^\alpha_{\mathrm{L}}\end{pmatrix}$	$\mathbf{2}, \begin{pmatrix} 1 \\ -1\end{pmatrix}$	$1/3$	$\begin{pmatrix} 2/3 \\ -1/3\end{pmatrix}$
U^α_{R}	$\mathbf{1}, 0$	$4/3$	$2/3$
D^α_{R}	$\mathbf{1}, 0$	$-2/3$	$-1/3$

Table 1.4: Quark multiplets quantum numbers.

where the covariant derivatives are

$$\partial_\mu Q^\alpha_{\mathrm{L}} \rightarrow D_\mu Q^\alpha_{\mathrm{L}} = \left(\partial_\mu + \frac{i}{2}gW^a_\mu\sigma^a + \frac{i}{6}g'B_\mu\right) Q^\alpha_{\mathrm{L}}, \tag{1.30}$$

$$\partial_\mu U^\alpha_{\mathrm{L}} \rightarrow D_\mu U^\alpha_{\mathrm{R}} = \left(\partial_\mu + \frac{2}{3}ig'B_\mu\right) U^\alpha_{\mathrm{R}}, \tag{1.31}$$

$$\partial_\mu D^\alpha_{\mathrm{R}} \rightarrow D_\mu D^\alpha_{\mathrm{R}} = \left(\partial_\mu - \frac{i}{3}g'B_\mu\right) D^\alpha_{\mathrm{R}}, \tag{1.32}$$

according to quantum numbers in table 1.4. The main difference with respect to the lepton case is the term containing $\widehat{\mathcal{H}} = i\sigma^2\mathcal{H}^*$, added to give mass to U^α_{R} field that has no leptonic equivalent. The matrices $\Upsilon_{\alpha\alpha'}, \Upsilon'_{\alpha\alpha'}$, a generalization of the y_α Yukawa couplings of (1.8), are defined after the gauge symmetry breaking:

$$\mathcal{H} \rightarrow \begin{pmatrix} 0 \\ v+\frac{H}{\sqrt{2}}\end{pmatrix}, \quad \widehat{\mathcal{H}} \rightarrow \begin{pmatrix} v+\frac{H}{\sqrt{2}} \\ 0\end{pmatrix}. \tag{1.33}$$

It turns out that to reproduce the observed quark masses m_{u}, m_{d}, m_{c}, m_{s}, m_{t}, m_{b}, the Υ matrices are:

$$\Upsilon = \frac{1}{v}\,\mathcal{D}_{\mathrm{L}}\cdot\begin{pmatrix} m_{\mathrm{d}} & 0 & 0 \\ 0 & m_{\mathrm{s}} & 0 \\ 0 & 0 & m_{\mathrm{b}}\end{pmatrix}\cdot\mathcal{D}^{-1}_{\mathrm{R}}, \quad \Upsilon' = \frac{1}{v}\,\mathcal{U}_{\mathrm{L}}\cdot\begin{pmatrix} m_{\mathrm{u}} & 0 & 0 \\ 0 & m_{\mathrm{c}} & 0 \\ 0 & 0 & m_{\mathrm{t}}\end{pmatrix}\cdot\mathcal{U}^{-1}_{\mathrm{R}}. \tag{1.34}$$

Nevertheless, after symmetry breaking the lagrangian can be written in terms of mass eigenstates fields with masses $m^1_u = m_{\mathrm{u}}$, $m^1_d = m_{\mathrm{d}}$, $m^2_u = m_{\mathrm{c}}$, $m^2_d = m_{\mathrm{s}}$, $m^3_u = m_{\mathrm{t}}$, $m^3_d = m_{\mathrm{b}}$. The quark part of the electroweak lagrangian written in terms of quark eigenstates reads as

follows:

$$\begin{aligned}
&\mathcal{L}_{\text{QUARKS}} = \qquad (1.35)\\
\text{Propagation} \rightarrow \quad &\sum_{\alpha}\left[\overline{u}^{\alpha}\left(i\gamma^{\mu}\partial_{\mu}-m_{\text{u}}^{\alpha}\right)u^{\alpha}+\overline{d}^{\alpha}\left(i\gamma^{\mu}\partial_{\mu}-m_{\text{d}}^{\alpha}\right)d^{\alpha}\right]\\
\text{Charged weak int.} \rightarrow \quad &-\frac{g}{2\sqrt{2}}\sum_{\alpha\alpha'}\left[W_{\mu}^{+}\overline{u}^{\alpha}\gamma^{\mu}\left(1-\gamma^{5}\right)V_{\alpha\alpha'}d^{\alpha'}\right.\\
&\left.-W_{\mu}^{-}\overline{d}^{\alpha}\gamma^{\mu}\left(1-\gamma^{5}\right)V_{\alpha\alpha'}^{\dagger}u^{\alpha'}\right]\\
\text{Neutral weak int.} \rightarrow \quad &+\frac{g}{4\cos\theta_{W}}Z_{\mu}\sum_{\alpha}\left[\overline{u}^{\alpha}\gamma^{\mu}\left(1-\frac{8}{3}\sin^{2}\theta_{W}-\gamma^{5}\right)u^{\alpha}\right.\\
&\left.-\overline{d}^{\alpha}\gamma^{\mu}\left(1-\frac{4}{3}\sin^{2}\theta_{W}-\gamma^{5}\right)d^{\alpha}\right]\\
\text{E.M. int.} \rightarrow \quad &-eA_{\mu}\sum_{\alpha}\left(\frac{2}{3}\overline{u}^{\alpha}\gamma^{\mu}u^{\alpha}-\frac{1}{3}\overline{d}^{\alpha}\gamma^{\mu}d^{\alpha}\right)\\
\text{Fermion}-\text{Higgs int.} \rightarrow \quad &-\frac{g}{2}\sum_{\alpha}\left(\frac{m_{u}^{\alpha}}{m_{\text{W}}}H\overline{u}^{\alpha}u^{\alpha}+\frac{m_{d}^{\alpha}}{m_{\text{W}}}H\overline{d}^{\alpha}d^{\alpha}\right).
\end{aligned}$$

The lagrangian reproduces the experimentally observed absence of flavour changing neutral current (FCNC) since the matrices in (1.28) disappear from the terms relative to weak neutral interactions. On the other hand, the weak charged interaction term contains the matrix $V_{\alpha\alpha'} = (\mathcal{U}_{\text{L}}^{-1}\cdot\mathcal{D}_{\text{L}})_{\alpha\alpha'}$, usually referred to as the *Cabibbo-Kobayashi-Maskawa (CKM) mixing matrix*, that parametrizes the observed flavour changing neutral currents.

In conclusion the full Standard Model lagrangian relative to the electroweak interaction is:

$$\mathcal{L}_{\text{EW}}^{\text{Standard Model}} = \mathcal{L}_{\text{LEPTONS}} + \mathcal{L}_{\text{QUARKS}} + \mathcal{L}_{\text{BOSONS}}. \qquad (1.36)$$

Strong interactions are also described in terms of a locally symmetric gauge field theory. The symmetry group that reproduces strong interactions phenomenology is SU(3)_{C}, and the related "charge" is called *colour*. The 8 spin-1 gauge bosons of SU(3)_{C} are called *gluons*. Each flavour of quarks u, d, s, c, b, t comes in three 'colours' which form a basis for the three dimensional representation of SU(3)_{C}. Gluons also carry colour charge and can therefore interact with themselves. In contrast with $\text{SU(2)}_{\text{L}}\otimes\text{U(1)}_{\text{Y}}$, SU(3)_{C} is not broken and gluons are massless.

The motivations suggesting the introduction of a more general framework as SuperSymmetry can now be discussed.

1.2 Beyond the Standard Model

The Standard Model is in a very good agreement with the experimental measurements. However, very little it is known about one of the its building blocks: the Higgs sector. The negative results of the direct searches of the Higgs boson have been translated into a lower limit on its mass of $95.2\,\text{GeV}/c^2$ (95% C.L.) [3]. Indirect constraints are obtained from the precise measurements of the Z lineshape suggesting $\log(m_H/\,\text{GeV}/c^2) = 1.88^{+0.33}_{-0.41}$ [4]. The

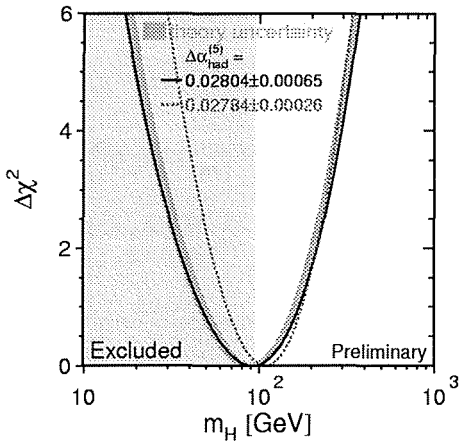

Figure 1.2: Standard Model fit over data with respect to the Higgs mass. The gray region indicates the region excluded by the direct search.

present situation is depicted in fig. 1.2. Thus, if the Standard Model Higgs boson exists, its mass should be quite close to the electroweak scale, let's say $m_H \sim 100\,\mathrm{GeV}/c^2$. Moreover m_H had to be less than about $1\,\mathrm{TeV}/c^2$ to preserve unitarity of $\mathrm{W}^+\mathrm{W}^-$ scattering.

Despite the success of Standard Model in reproducing observations, there are theoretical problems that cannot be solved without the introduction of some new physics. A new framework will be certainly necessary at least at the Planck scale $M_P = (8\pi G_{\mathrm{Newton}})^{-1/2} = 2.4 \times 10^{18}\,\mathrm{GeV}$ where quantum gravitational effects become important. The 16 orders of magnitude dividing the explored weak scale and the Planck scale are considered somewhat unnatural. This argument, called *hierarchy problem*, is based also on more quantitative facts [5][6].

It is very instructive to compute the first order correction to Higgs mass m_H due to a generic fermion loop (see fig. 1.3). It depends on the fermion-antifermion production probability integrated on all possible values of the momentum k carried by the fermion in the loop. Since the Higgs coupling to a fermion f is $(y_f/\sqrt{2})H\overline{f}f$ (see eq. (1.21) and (1.35))

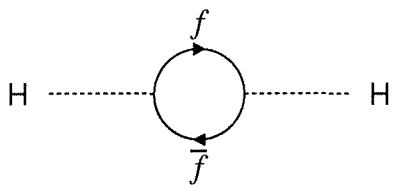

Figure 1.3: 1-loop diagrams contributing to m_H correction.

one finds:

$$\begin{aligned}\Delta m_H^2 &= -\int \frac{d^4k}{(2\pi)^4}\mathrm{Tr}\left[\left(i\frac{y_f}{\sqrt{2}}\right)\frac{i}{\widehat{k}-m_f}\left(i\frac{y_f}{\sqrt{2}}\right)\frac{i}{\widehat{k}-m_f}\right] \\ &= -2y_f^2\int\frac{d^4k}{(2\pi)^4}\left[\frac{1}{k^2-m_f^2}+\frac{2m_f^2}{\left(k^2-m_f^2\right)^2}\right], \end{aligned} \tag{1.37}$$

where $\widehat{k}=\gamma_\mu k^\mu$. A colour factor 3 must be added for quarks. The first term of the second line is quadratically divergent. If no new physics is expected up to the Planck scale, M_P will be the cutoff used to "regulate" the integral. A huge m_H^2 correction results, more than 30 orders of magnitude bigger than the mass expected from Standard Model fit. There is always the possibility to renormalize away the bad quadratic term, as for logarithmic divergences is done. But, even if such a bad ultraviolet behaviour is accepted in the theory, the correction term proportional to $y_f^2 m_f^2$ still remains. For the Standard Model fermions these corrections are quite small. If some new physics appears at a very high scale the new fermions will have masses close to that scale. Then the corrections will be very large. They must cancel themselves to bring the Higgs mass well below 1 TeV and this is possible only if the involved parameters undergo to an extreme fine-tuning. This mechanism is considered very "unnatural".

The 1-loop correction Δm_e to the electron mass due to photon emission can be computed for comparison. As in the previous case, according to the diagram in fig. 1.4, one finds:

$$\begin{aligned}\Delta m_\mathrm{e} &= \int\frac{d^4k}{(2\pi)^4}(-ie\gamma_\mu)\frac{i}{\widehat{k}-m_\mathrm{e}}(-ie\gamma_\nu)\frac{-ig^{\mu\nu}}{k^2} \\ &= -4e^2m_\mathrm{e}\int\frac{d^4k}{(2\pi)^4}\frac{1}{k^2\left(k^2-m_\mathrm{e}^2\right)} \end{aligned} \tag{1.38}$$

where $g^{\mu\nu}$ is the standard Lorentz metric tensor. The integral has a logarithmic divergence in the ultraviolet but the m_e correction is proportional to m_e itself. Even if M_P is used to cut-off the divergence a small correction turns out:

$$\Delta m_e \simeq 4e^2 m_\mathrm{e}\log\frac{M_P}{m_\mathrm{e}} \simeq 0.24 m_\mathrm{e}. \tag{1.39}$$

In the limit $m_\mathrm{e}\to 0$ the model becomes invariant under chiral rotations and the correction vanishes; in other words, the chiral symmetry protects the electron mass against divergences (like any fermion mass as well). Similarly the gauge invariance prevents gauge bosons from having dangerous divergences.

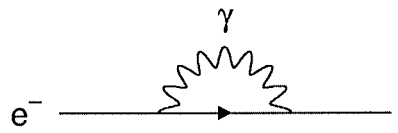

Figure 1.4: 1-loop diagram contributing to m_e correction.

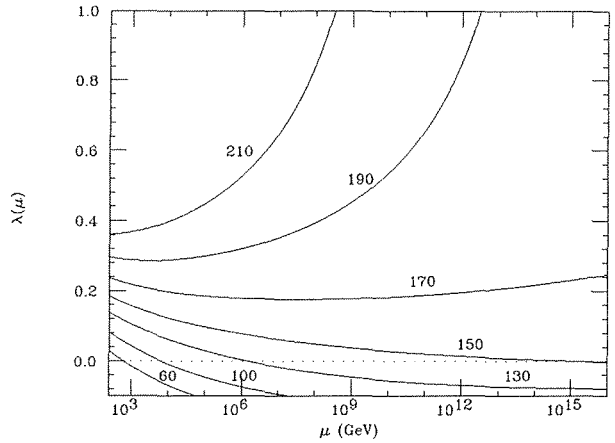

Figure 1.5: Quartic coupling constant running for different values of the Higgs mass in GeV.

In the Standard Model there is no symmetry that protects scalar masses. Hence they are sensitive to physics at higher scale. The hierarchy problem just consists in scalar masses that like to be close to the highest scale in the theory; only with the introduction of some intermediate new physics the hierarchy problem can be solved.

It turns out that the new physics must be quite close to the present explored scale. In fact, the small expected value for Higgs yields to a small quartic coupling constant $\lambda = k^2/4$. Fig. 1.5 shows the evolution of λ starting from several initial conditions that set the Higgs mass at the scale $\mu = \sqrt{2}v = 246\,\mathrm{GeV}/c^2$. The constant λ must be positive to have a stable minimum in the Higgs potential (1.12). If the Higgs mass is as small as Standard model fit suggests, λ becomes negative for μ values quite close to the electroweak scale. There some new physics occurs to alter the λ running.

The message of this short description about the weak points of the Standard Model is: some new physics just "behind the corner" ($\lesssim 1\,\mathrm{TeV}$) is necessary and reasonable.

1.3 SuperSymmetry

One of the most interesting extension of the Standard Model is based on SuperSymmetry [7][8][5][9][6]. In supersymmetric field theories the Higgs mass problem is solved since the loops corrections profit from contributions from new particles.

1.3.1 Introduction

SuperSymmetry can be introduced studying the Higgs mass corrections in case that the Standard Model is extended by adding two complex scalar fields $\tilde{f}_\mathrm{L}$, $\tilde{f}_\mathrm{R}$ that couple with H according to the following lagrangian [6]:

$$\mathcal{L}_{H\tilde{f}} = \frac{y_{\tilde{f}}}{2}H^2\left(\left|\tilde{f}_\mathrm{L}\right|^2 + \left|\tilde{f}_\mathrm{R}\right|^2\right) + \sqrt{2}vH\left(\left|\tilde{f}_\mathrm{L}\right|^2 + \left|\tilde{f}_\mathrm{R}\right|^2\right) + \left(\frac{y_f}{\sqrt{2}}A_f H\tilde{f}_\mathrm{L}\tilde{f}_\mathrm{R}^* + \mathrm{h.c.}\right). \quad (1.40)$$

The second term comes from the $SU(2)_L \otimes U(1)_Y$ symmetry breaking and therefore it is proportional to v. The third term contains an arbitrary factor (A_f) because its coupling may assume any value.

The 1-loop mass correction due to the above lagrangian consists in the diagrams shown in fig. 1.6. Their contributions are:

$$\begin{aligned}
\Delta m_H^2 &= -y_{\tilde{f}} \int \frac{d^4k}{(2\pi)^4} \left[\frac{1}{k^2 - m^2_{\tilde{f}_L}} + \frac{1}{k^2 - m^2_{\tilde{f}_R}} \right] \\
&+ 2y_{\tilde{f}}^2 v^2 \int \frac{d^4k}{(2\pi)^4} \left[\frac{1}{\left(k^2 - m^2_{\tilde{f}_L}\right)^2} + \frac{1}{\left(k^2 - m^2_{\tilde{f}_R}\right)^2} \right] \\
&+ |y_f A_f|^2 v^2 \int \frac{d^4k}{(2\pi)^4} \left[\frac{1}{\left(k^2 - m^2_{\tilde{f}_L}\right)\left(k^2 - m^2_{\tilde{f}_R}\right)} \right]. \qquad (1.41)
\end{aligned}$$

Only the first integral, coming from the quartic coupling, contains a quadratic divergence. In case that $y_{\tilde{f}} = -y_f^2$, this cancels exactly the fermion contribution (1.37) whatever the values of $m_{\tilde{f}_R}$, $m_{\tilde{f}_L}$ and A_f are.

A standard regularization procedure means

$$\int \frac{d^4k}{(i\pi^2)} \frac{1}{k^2 - m^2} \to m^2 \left(1 - \log \frac{m^2}{\mu^2}\right), \qquad (1.42)$$

$$\int \frac{d^4k}{(i\pi^2)} \frac{1}{(k^2 - m^2)^2} \to -\log \frac{m^2}{\mu^2}, \qquad (1.43)$$

where μ is the renormalization scale. Thus, assuming $m_{\tilde{f}_R} = m_{\tilde{f}_L} = m_{\tilde{f}}$ without lost of generality, the total contribution to m_H from (1.37) and (1.41) is:

$$\begin{aligned}
\Delta m_H^2 = i\frac{y_f^2}{16\pi^2} \Bigg[& -2m_f^2 \left(1 - \log \frac{m_f^2}{\mu^2}\right) + 4m_f^2 \log \frac{m_f^2}{\mu^2} \\
& +2m_{\tilde{f}}^2 \left(1 - \log \frac{m_{\tilde{f}}^2}{\mu^2}\right) - 4m_f^2 \log \frac{m_{\tilde{f}}^2}{\mu^2} \\
& - |A_f|^2 \log \frac{m_{\tilde{f}}^2}{\mu^2} \Bigg]. \qquad (1.44)
\end{aligned}$$

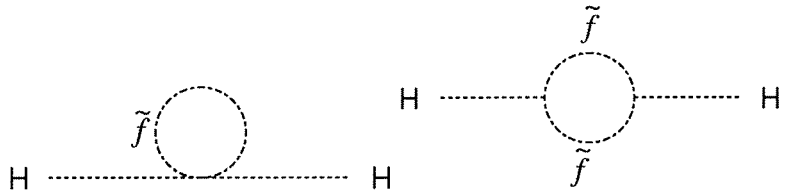

Figure 1.6: 1-loop diagram coming from a scalar $\tilde{f}$ and contributing to m_H correction .

The remarkable result is that a null total correction turns out if $m_{\tilde{f}} = m_f$ and $A_f = 0$. If the above conditions are less stringent ($m^2_{\tilde{f}} = m^2_f + \delta^2$ with $\delta \ll m_f$, $A_f \ll m_f$) one finds:

$$\Delta m_H^2 \simeq -i\frac{y_f^2}{16\pi^2}\left[2\delta^2 + \left(\delta^2 + |A_f|^2\right)\log\frac{m_f^2}{\mu^2}\right]. \tag{1.45}$$

The correction to Higgs mass remains small even if m_f becomes huge.

The introductions of the scalar fields $\tilde{f}_{\rm L}$, $\tilde{f}_{\rm R}$ has two benefits: the quadratic divergences of Higgs mass disappear as well the Higgs mass trend to be close to the heaviest fermions. A mass splitting between fermions and new bosons being of the order of the weak scale is the only requirement.

The message from the electron mass correction is: a nice high energy behaviour is the result of an underlying symmetry. In fact the described benefits come directly once the existence of a symmetry relating fermions and bosons is assumed. This symmetry, known as **SuperSymmetry**, transforms a boson into a fermion and vice versa through an operator $\mathcal{Q}$:

$$\mathcal{Q}|\text{Boson}\rangle = |\text{Fermion}\rangle, \qquad \mathcal{Q}|\text{Fermion}\rangle = |\text{Boson}\rangle. \tag{1.46}$$

Naively speaking, the Higgs mass is now protected by the chiral symmetry via the supersymmetric link between scalars and fermions.

Since $\mathcal{Q}$ operator swaps half-integer spin with integer spin, $\mathcal{Q}$ itself is an anticommuting spinor carrying spin-1/2. Therefore SuperSymmetry is a spacetime symmetry and the hermitian conjugate of $\mathcal{Q}$, $\mathcal{Q}^\dagger$ is also a symmetry generator.

Adding SuperSymmetry to the Standard Model in order to get a realistic theory implies quite stringent conditions on the $\mathcal{Q}$, $\mathcal{Q}^\dagger$ algebra. Using α, β and $\dot{\alpha}, \dot{\beta}$ for $\mathcal{Q}$ and $\mathcal{Q}^\dagger$ spinorial indices, it turns out that

$$\left\{\mathcal{Q}_\alpha, \mathcal{Q}^\dagger_{\dot{\alpha}}\right\} = 2\sigma^\mu_{\alpha\dot{\alpha}}p^\mu, \qquad \left\{\mathcal{Q}_\alpha, \mathcal{Q}_\beta\right\} = \left\{\mathcal{Q}^\dagger_{\dot{\alpha}}, \mathcal{Q}^\dagger_{\dot{\beta}}\right\} = 0, \qquad \left[p^\mu, \mathcal{Q}_\alpha\right] = \left[p^\mu, \mathcal{Q}^\dagger_{\dot{\alpha}}\right] = 0, \tag{1.47}$$

where p^μ is the momentum, that is the generator of spacetime translations.

The irreducible representations of the supersymmetry algebra, known as *supermultiplets* or *superfields*, contain the same number of bosonic or fermionic states in such a way that in each superfield the number of fermionic degrees of freedom is exactly equal to the number of bosonic degrees of freedom. This condition is unavoidable to get the divergence cancellation described before. The particles of the same superfield have the same mass since the mass operator $p_\mu p^\mu$ commutes with $\mathcal{Q}$, $\mathcal{Q}^\dagger$ and with the spacetime rotation and translations. $\mathcal{Q}$ and $\mathcal{Q}^\dagger$ commute with gauge transformation too, therefore the particles of the same superfield have also the same gauge quantum numbers, i.e. electric charge, weak isospin and colour.

The superfield representations interesting for building a supersymmetric extension of the Standard Model are of three types:

Chiral superfields, containing a complex scalar field and a single Weyl fermion with two helicity states (in total 2 bosonic degrees of freedom and 2 fermionic degrees of freedom).

Gauge superfields, containing a massless vector field (2 bosonic degrees of freedom) and a massless spin-1/2 Weyl fermion (2 fermionic degrees of freedom).

Gravity superfields, containing a massless spin-2 vector field (2 bosonic degrees of freedom) and a massless spin-3/2 Weyl fermion (2 fermionic degrees of freedom).

The gravity superfields come from the possibility to introduce in the SuperSymmetry also the gravity.

1.3.2 The Minimal SuperSymmetric Model

The supersymmetric extension of the Standard Model with the minimal content of new particles is known as *Minimal Supersymmetric Standard Model* (MSSM). In a supersymmetric extension of the Standard Model all known particle must be organized in either chiral or gauge superfields together with their superpartners differing by 1/2 in spin. All superpartners of standard particles are the new particles predicted by the model.

Each Standard Model fermion fits in two chiral superfield, one per each chirality projection. The spin-0 superpartners needed to fill completely the superfields are called generally *scalar fermions* or *sfermions* and, in particular, *scalar quarks* or *squarks* and *scalar leptons* or *sleptons*[2].

The Higgs boson is also described with the field of a chiral superfield. But supersymmetric Higgs sector is bigger than the Standard Model one. There are two Higgs doublets, one with weak hypercharge $Y = +1/2$ the other with $Y = -1/2$. The supersymmetric model would suffer a triangle gauge anomaly in the $\mathrm{SU(2)_L} \otimes \mathrm{U(1)_Y}$ symmetry if there was only an Higgs doublet like in the Standard Model. Adding another doublet the anomalies cancel and the model is consistent. Moreover, because of the structure of SuperSymmetry, two Higgs doublets are anyhow necessary to give masses either to up and to down quarks. The notation will be $(\mathcal{H}_U^+, \mathcal{H}_U^0)$ for the $Y = +1/2$ doublet giving mass to up quarks and $(\mathcal{H}_D^0, \mathcal{H}_D^-)$ for the $Y = -1/2$ doublet giving mass to down quarks.

The two chiral superfields containing Higgs doublets contain also their fermion superpartners arranged in $\mathrm{SU(2)_L}$ Weyl spinor fields: $\widetilde{\mathcal{H}}_U = \left(\widetilde{\mathcal{H}}_U^+, \widetilde{\mathcal{H}}_U^0\right)$ and $\widetilde{\mathcal{H}}_D = \left(\widetilde{\mathcal{H}}_D^0, \widetilde{\mathcal{H}}_D^-\right)$. They are called *higgsinos*[3]. It is worth to notice that two Higgs doublet are also necessary to give masses to the higgsinos, since the scalar Higgs of a given superfield cannot be made coupling to the higgsinos of the same superfield.

The chiral superfields just described are collected in the table 1.5. The Weyl notation is used. For a generic fermion ψ it means

$$\begin{pmatrix} \psi \\ \overline{\psi}^\dagger \end{pmatrix}_{\text{Weyl}} \equiv \begin{pmatrix} \psi_\mathrm{L} \\ \psi_\mathrm{R} \end{pmatrix}_{\text{Dirac}}. \tag{1.48}$$

[2] A standard model fermion superpartner in the symbolic notation is indicated with the standard model symbol overwritten by a "$\sim$". For example, the sleptons are $\tilde{\mathrm{e}}_\mathrm{L}$, $\tilde{\mathrm{e}}_\mathrm{R}$, $\tilde{\mu}_\mathrm{L}$, $\tilde{\mu}_\mathrm{R}$, $\tilde{\tau}_\mathrm{L}$, $\tilde{\tau}_\mathrm{R}$ and $\tilde{\nu}_\mathrm{e}$, $\tilde{\nu}_\mu$, $\tilde{\nu}_\tau$; the squarks are $\tilde{\mathrm{q}}_\mathrm{R}$ and $\tilde{\mathrm{q}}_\mathrm{L}$, with $\mathrm{q} = \mathrm{u, d, c, s, b, t}$. The label L or R refers to the helicity of the standard fermion superpartner. The sfermion is scalar and does not carry helicity.

[3] Generally, the fermionic superpartners of bosons are named adding to the Standard Model name the suffix "-ino".

Chiral Superfield Ψ_i	spin-0 ϕ_i	spin-1/2 ψ_i
($\times$ 3 families)	Squarks	Quarks
$\mathbf{Q}$	$\widetilde{Q}_{\rm L} = (\widetilde{U}_{\rm L}, \widetilde{D}_{\rm L})$	$Q_{\rm L} = (U_{\rm L}, D_{\rm L})$
$\overline{\mathbf{U}}$	$\widetilde{U}^*_{\rm R}$	$U^\dagger_{\rm R}$
$\overline{\mathbf{D}}$	$\widetilde{D}^*_{\rm R}$	$D^\dagger_{\rm R}$
($\times$ 3 families)	Sleptons	Leptons
$\mathbf{L}$	$\widetilde{L}_{\rm L} = (\widetilde{\nu}, \widetilde{\ell}_{\rm L})$	$L_{\rm L} = (\nu, \ell_{\rm L})$
$\overline{\boldsymbol{\ell}}$	$\widetilde{\ell}^*_{\rm R}$	$\ell^\dagger_{\rm R}$
	Higgs	Higgsinos
$\boldsymbol{\mathcal{H}}_U$	$\mathcal{H}_U = (\mathcal{H}^+_U, \mathcal{H}^0_U)$	$\widetilde{\mathcal{H}}_U = (\widetilde{\mathcal{H}}^+_U, \widetilde{\mathcal{H}}^0_U)$
$\boldsymbol{\mathcal{H}}_D$	$\mathcal{H}_D = (\mathcal{H}^0_D, \mathcal{H}^-_D)$	$\widetilde{\mathcal{H}}_D = (\widetilde{\mathcal{H}}^0_D, \widetilde{\mathcal{H}}^-_D)$

Table 1.5: Chiral superfields.

In a similar way the Standard Model gauge boson can be arranged in a supersymmetric framework. Their natural locations are the gauge superfields together with their fermionic superpartners, called *gauginos*. There are several new particles: the *gluinos* $\widetilde{g}$, the *winos* $\widetilde{W}^1$, $\widetilde{W}^2$, and $\widetilde{W}^3$ and the *bino* $\widetilde{B}$. Since the Z boson and the photon are combinations of W^3 and B, the corresponding combinations of $\widetilde{W}^3$ and $\widetilde{B}$ can be call *zino* $\widetilde{Z}$ and *photino* $\widetilde{\gamma}$.

The table 1.6 summarizes the content of gauge superfields.

1.3.3 SuperSymmetric Lagrangian

After the definition of the fields of our minimal SuperSymmetric theory the lagrangian to define the interactions between these fields can be written. As below described, the general supersymmetric lagrangian is defined by the symmetry properties to be satisfied: the gauge interactions terms are set by the gauge structure; the mass terms and the other non-gauge couplings are strictly fixed requiring the invariance under supersymmetric transformations.

Up to now no experimental evidence has been shown of any existence of bosons with the same masses of standard particles, thus, to built a realistic theory, SuperSymmetry must be broken at some level to have superpartners heavier than Standard Model fermions. Therefore the lagrangian must contain SuperSymmetry breaking terms to match the actual non evidence of supersymmetric particles. Hence, the supersymmetric lagrangian $\mathcal{L}_{\rm SUSY}$ is

Gauge Superfield $\Phi^a_{\mathcal{G}}$	spin-$\frac{1}{2}$ $\Omega^a_{\mathcal{G}}$	spin-1 $A^a_{\mathcal{G}}$
	Gluinos	Gluons
$\Phi^1_{\rm SU(3)_C}, \ldots, \Phi^8_{\rm SU(3)_C}$	$\widetilde{g}^1, \ldots, \widetilde{g}^8$	$g^1, \ldots, g^8$
	Winos	W bosons
$\Phi^1_{\rm SU(2)_L}, \Phi^2_{\rm SU(2)_L}, \Phi^3_{\rm SU(2)_L}$	$\widetilde{W}^1, \widetilde{W}^2, \widetilde{W}^3$	W^1, W^2, W^3
	Bino	B boson
$\Phi^1_{\rm U(1)_Y}$	$\widetilde{B}$	B

Table 1.6: Gauge superfields.

the sum of three contributions:

$$\mathcal{L}_{\text{SUSY}} = \mathcal{L}_{\text{chiral}} + \mathcal{L}_{\text{gauge}} + \mathcal{L}_{\text{soft}} \tag{1.49}$$

$\mathcal{L}_{\text{chiral}}$ is relative to chiral superfields. $\mathcal{L}_{\text{gauge}}$ contains gauge superfields terms and gauge invariant interaction terms. $\mathcal{L}_{\text{soft}}$ contains all supersymmetry breaking terms.

Chiral superfield lagrangian

For a given superfield Ψ_i, where i runs for all families over the first column of table 1.5, ψ_i and ϕ_i represent the fermionic and the bosonic component respectively. The lagrangian density is:

$$\mathcal{L}_{\text{chiral}} = -\partial^\mu \phi_i^* \partial_\mu \phi_i - i\psi_i^\dagger \overline{\sigma}^\mu \partial_\mu \psi_i - \frac{1}{2}\left(\mathbf{W}^{ij}\psi_i\psi_j + \mathbf{W}^{*ij}\psi_i^\dagger\psi_j^\dagger\right) - \mathbf{W}^{*i}\mathbf{W}^i. \tag{1.50}$$

The sum over the indices i and j is assumed here and in the following.

The $\mathbf{W}$ terms contain all the non-gauge interactions that are compatible with supersymmetric transformations. They can be simply expressed by a very useful object known as **Superpotential** $\mathcal{W}$, an analytic function of complex fields ϕ

$$\mathcal{W} = \frac{1}{2}M^{ij}\phi_i\phi_j + \frac{1}{6}y^{ijk}\phi_i\phi_j\phi_k, \tag{1.51}$$

such that

$$\mathbf{W}^{ij} = \frac{\delta^2\mathcal{W}}{\delta\phi_i\delta\phi_j}, \tag{1.52}$$

$$\mathbf{W}^{i} = \frac{\delta\mathcal{W}}{\delta\phi_i}. \tag{1.53}$$

It turns out that the superpotential can be expressed also in terms of chiral superfields:

$$\mathcal{W} = \frac{1}{2}M^{ij}\Psi_i\Psi_j + \frac{1}{6}y^{ijk}\Psi_i\Psi_j\Psi_k. \tag{1.54}$$

M^{ij} is a mass matrix for fermion fields and y^{ijk} is a set of Yukawa couplings between the scalar ϕ_k and two fermion $\psi_i\psi_j$. The gauge invariance allows only a subset of M^{ij} and y^{ijk} to be non zero. At this level fermions and scalars have the same masses since the SuperSymmetry breaking is still missing.

Gauge lagrangian and gauge interactions

The gauge bosons are hold in the gauge superfield. For a given gauge superfield $\Phi^a_{\mathcal{G}}$, where $\mathcal{G}$ indicates the gauge group ($\mathcal{G} = \text{SU(3)}_\text{C}$, SU(2)_L, U(1)_Y) and a runs over the generators in $\mathcal{G}$, $\Omega^a_{\mathcal{G}}$ and $A^a_{\mathcal{G}\mu}$ represent the $\Phi^a_{\mathcal{G}}$ fermionic (gaugino) component and the $\Phi^a_{\mathcal{G}}$ bosonic component respectively, according to table 1.6.

To introduce the gauge interactions in the chiral lagrangian the ordinary derivatives must be replaced by covariant derivatives:

$$\partial_\mu\phi_i \;\rightarrow\; D_\mu\phi_i = \partial_\mu\phi_i + ig_{\mathcal{G}}A^a_{\mathcal{G}\mu}\left(T^a_{\mathcal{G}}\phi\right)_i, \tag{1.55}$$

$$\partial_\mu\psi_i \;\rightarrow\; D_\mu\psi_i = \partial_\mu\psi_i + ig_{\mathcal{G}}A^a_{\mathcal{G}\mu}\left(T^a_{\mathcal{G}}\psi\right)_i. \tag{1.56}$$

The sum over a and $\mathcal{G}$ is assumed here and in the following. For a given gauge group $\mathcal{G}$, $g_{\mathcal{G}}$ is the coupling constant and $T^a_{\mathcal{G}}$ represents the set of generators satisfying $[T^a, T^b] = i f^{abc}_{\mathcal{G}} T^c$. The antisymmetric $f^{abc}_{\mathcal{G}}$ stands for the group structure constants (i.e. $f^{abc}_{\mathrm{SU(2)_L}} = \epsilon^{abc}$).

There are other terms compatible with gauge transformation that can be added to the lagrangian. Their couplings are fixed from the total invariance under SuperSymmetry transformations. These terms are grouped in $\mathcal{L}_{\text{gauge}}$, the gauge part of the lagrangian, together with the appropriate kinetic terms:

$$\begin{aligned} \mathcal{L}_{\text{gauge}} \;=\; & -\frac{1}{4} F^a_{\mathcal{G}\mu\nu} F^{a\mu\nu}_{\mathcal{G}} - i\Omega^{a\dagger}_{\mathcal{G}} \overline{\sigma}^{\mu} D_{\mu} \Omega^a_{\mathcal{G}} \\ & -\sqrt{2}(\phi_i^* T^a_{\mathcal{G}} \psi_i)\Omega^a_{\mathcal{G}} - \sqrt{2}\Omega^{\dagger a}_{\mathcal{G}} (\psi_i^{\dagger} T^a_{\mathcal{G}} \phi_i) \\ & -\frac{1}{2} g^2_{\mathcal{G}} \left(\phi_i^* T^a_{\mathcal{G}} \phi_i\right)^2 . \end{aligned} \tag{1.57}$$

The kinetic terms contain

$$F^a_{\mathcal{G}\mu\nu} = \partial_\mu A^a_{\mathcal{G}\nu} - \partial_\nu A^a_{\mathcal{G}\mu} - g_{\mathcal{G}} f^{abc} A^b_{\mathcal{G}\mu} A^c_{\mathcal{G}\nu}, \tag{1.58}$$

and the covariant derivative of the gaugino fields is

$$D_\mu \Omega^a_{\mathcal{G}} = \partial_\mu \Omega^a_{\mathcal{G}} - g_{\mathcal{G}} f^{abc}_{\mathcal{G}} A^b_{\mathcal{G}\mu} \Omega^c_{\mathcal{G}}. \tag{1.59}$$

Scalar Potential

From the lagrangian it is possible to pick up the terms making the scalar potential:

$$\begin{aligned} & & V(\phi, \phi^*) = & \\ & F-\text{terms} \;\rightarrow & \mathbf{W}^{*i}\mathbf{W}^i & \\ & D-\text{terms} \;\rightarrow & +\frac{1}{2} g^2_{\mathcal{G}} \left(\phi_i^* T^a_{\mathcal{G}} \phi_i\right)^2 . & \end{aligned} \tag{1.60}$$

The two different parts are known as "F-terms" and "D-terms". Being V a sum of squares, it is always non negative. It turns out that the scalar potential is uniquely defined by the other interactions in the theory: the F-terms are fixed by the superpotential (Yukawa couplings and fermion mass term) while the D-terms are fixed by the gauge interactions. This is a feature of supersymmetric theories.

1.3.4 MSSM Superpotential and R parity

The most general gauge invariant and renormalizable MSSM superpotential is made up of two parts, differing in the properties of the generated interaction. The first part, labelled RPC for reasons that will become clear soon, is:

$$\mathcal{W}^{\text{RPC}}_{\text{MSSM}} = \Upsilon_{\alpha\alpha'} \overline{\mathrm{U}}_\alpha \mathbf{Q}_{\alpha'} \boldsymbol{\mathcal{H}}_U - \Upsilon'_{\alpha\alpha'} \overline{\mathrm{D}}_\alpha \mathbf{Q}_{\alpha'} \boldsymbol{\mathcal{H}}_D - y_\alpha \bar{\ell}_\alpha \mathrm{L}_\alpha \boldsymbol{\mathcal{H}}_D + \mu \boldsymbol{\mathcal{H}}_U \boldsymbol{\mathcal{H}}_D, \tag{1.61}$$

where the sum over the restored family indices α and α' is assumed. It is important to stress that the products between superfields must be done in a gauge invariant way with respect to $\mathrm{SU(2)_L}$ and $\mathrm{SU(3)_C}$ indices. That means, for example:

$$\overline{\mathrm{U}}_\alpha \mathbf{Q}_{\alpha'} \boldsymbol{\mathcal{H}}_U = (\overline{\mathrm{U}}_\alpha)^c (\mathbf{Q}_{\alpha'})^c_t (\boldsymbol{\mathcal{H}}_U)_{t'} \epsilon^{tt'}, \qquad \boldsymbol{\mathcal{H}}_U \boldsymbol{\mathcal{H}}_D = (\boldsymbol{\mathcal{H}}_U)_t (\boldsymbol{\mathcal{H}}_D)_{t'} \epsilon^{tt'}, \tag{1.62}$$

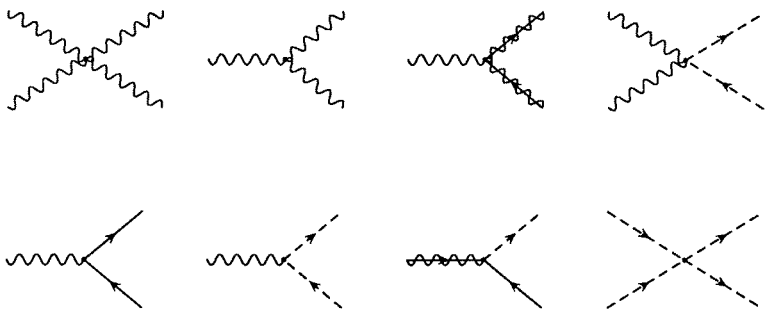

Figure 1.7: Supersymmetric gauge interaction vertices. The gaugino fields are indicated with the solid line superimposed on the waved line.

where the sum over the $SU(2)_L$ indices t and t' is understood as well over the $SU(3)_C$ colour index c.

The quantities y_α, $\Upsilon_{\alpha\alpha'}$ and $\Upsilon'_{\alpha\alpha'}$ are the Yukawa coefficients and matrices already used in (1.8) and in (1.29). They are exactly the same since the superpotential generates also the lagrangian terms for standard particles. As soon as the neutral Higgs fields acquire the vacuum expectation values (see section 1.3.6), sfermions will have the same masses of their standard partners (still unbroken SuperSymmetry) and also the same CKM flavour mixing.

When used in (1.54) the superpotential (1.61) yields to vertices between Higgs bosons and fermions similar to Standard Model ones. The difference is that only H_U couples with u-type quarks and H_D couples with d-type quarks and charged leptons. Moreover all the scalar-scalar-fermion terms involving higgsinos or sfermions are generated. Generally speaking all these new vertices can be obtained from the standard ones replacing two of the three standard particles with their superpartners. These cubic vertices are proportional to the Yukawa coupling coefficient. The superpotential generates also quartic scalar interactions of the type $(sfermion)^4$, $(squark)^2(slepton)^2$ and $(sfermion)^2(Higgs)^2$. The strength of these quartic vertices is proportional to the squared Yukawa coupling coefficient.

The above interactions, known as dimensionless interactions, are very weak because the Yukawa couplings are small at least for the first two families. The gauge interactions, which strength is fully fixed from the gauge coupling constants, are more important for the phenomenology. Also in case of gauge interactions, the vertices involving supersymmetric particles can be derived from the standard gauge vertices replacing two standard fields with their superpartners, having care to get a renormalizable vertex[4]. All the supersymmetric gauge interaction vertices are shown in fig. 1.7.

The last term of the superpotential is proportional to the μ parameter and thus known as μ-term. It provides Higgs and higgsinos mass terms and cubic scalar vertices of the type sfermion-sfermion-Higgs that are combinations of the μ-term and the Yukawa terms. They are important for the determination of mass spectra and mixing of sparticles.

Although the MSSM superpotential is properly the one in expression (1.61), there are other allowed terms having interesting and peculiar phenomenological consequences. Their

[4]For example, replacing two bosons fields with two gauginos fields in the quartic boson vertex a dimension $3/2 + 3/2 + 1 + 1 = 5$ results. A vertex is renormalizable if its dimension is ≤ 4.

major drawback consists in the lepton number L and barion number B violations they introduce in the lagrangian. This extra part, labelled RPV for reasons that will be clear soon, completes the most general gauge invariant and renormalizable superpotential within the MSSM framework. To write this is useful to introduce the scalar partner of the mass eigenstates quark fields. This can be done applying the transformations (1.28) also to the sfermion gauge fields $\widetilde{U}$ and $\widetilde{D}$, that is

$$\widetilde{U}^{\alpha}_{\mathrm{L,R}} = \mathcal{U}^{\alpha\beta}_{\mathrm{L,R}} \widetilde{u}^{\beta}_{\mathrm{L,R}}, \quad \widetilde{D}^{\alpha}_{\mathrm{L,R}} = \mathcal{D}^{\alpha\beta}_{\mathrm{L,R}} \widetilde{d}^{\beta}_{\mathrm{L,R}}. \tag{1.63}$$

Thus, the $\widetilde{Q}_{\mathrm{L}}$ $\mathrm{SU(2)_L}$ doublet transforms in $\widetilde{q}_{\mathrm{L}} = (\widetilde{u}_{\mathrm{L}}, \widetilde{d}_{\mathrm{L}})$. The chiral superfields containing the quark mass eigenstates and their partner will be indicated with bold lower case letters: $\mathbf{q}$, $\overline{\mathbf{u}}$ and $\overline{\mathbf{d}}$.

The RPV superpotential is:

$$\begin{aligned} & & \mathcal{W}^{\mathrm{RPV}}_{\mathrm{MSSM}} = & \\ \Delta L = 1 \rightarrow & & \frac{1}{2}\lambda_{\alpha\alpha'\alpha''}\mathbf{L}_{\alpha}\mathbf{L}_{\alpha'}\overline{\boldsymbol{\ell}}_{\alpha''} + \lambda'_{\alpha\alpha'\alpha''}\mathbf{L}_{\alpha}\mathbf{q}_{\alpha'}\overline{\mathbf{d}}_{\alpha''} + \mu'_{\alpha}\mathbf{L}_{\alpha}\boldsymbol{\mathcal{H}}_{U} + & \\ \Delta B = 1 \rightarrow & & \frac{1}{2}\lambda''_{\alpha\alpha'\alpha''}\overline{\mathbf{u}}_{\alpha}\overline{\mathbf{d}}_{\alpha'}\overline{\mathbf{d}}_{\alpha''}. & \end{aligned} \tag{1.64}$$

As usual α, α' and α'' are family indices and $\lambda_{\alpha\alpha'\alpha''}$, $\lambda'_{\alpha\alpha'\alpha''}$, $\lambda''_{\alpha\alpha'\alpha''}$ and μ'_{α} represent a set of arbitrary couplings. These terms yield to three particle vertices with one sfermion and two fermions and are very disturbing for the presence of lepton and barion numbers violations. For instance, since a low-energy process can be effected by the exchange of virtual sparticles, the simultaneous presence of λ' and λ'' would lead the proton to undergo a fast decay. Hence the only realistic scenario consists to assume that only one of the lambda couplings is dominant with respect to the others. Under this hypothesis upper limits on each couplings are derived from low-energy processes thanks to the good agreement with the Standard Model predictions [10].

R-parity

The experimental observation forces the λ couplings to be almost negligible. Nevertheless, the only theoretical argument useful to completely discard the RPV terms from the superpotential consists in the introduction of a new symmetry, known as **R-parity**, that avoids the introduction of such not elegant terms. After the R-parity definition also the labels are finally clear: RPC stands for *R-parity conservation* while RPV means *R-parity violation*.

R-parity parameter R can be defined as a multiplicative quantum number such that all Standard Model particles have $R = 1$ while their SUSY partners have $R = -1$ or

$$R = (-1)^{3(B-L)+s} \tag{1.65}$$

for a particle of spin s.

R-parity conservation means lepton and barion number conservation and thus the superpotential (1.64) is automatically forbidden. Said differently, R-parity conservation implies that vertices involving supersymmetric particles must contain an odd number of these particles.

1.3.5 SuperSymmetry Breaking

Without the SUSY breaking the superpartners are degenerate in mass to the standard particles. Thus MSSM must contain SUSY breaking to be a realistic theory. The SUSY breaking terms are the last part of MSSM to be defined in order to predict the sparticle spectrum.

SuperSymmetry breaking interactions

SuperSymmetry breaking mechanism is an ultimate model which lagrangian is invariant under SuperSymmetry, but a vacuum state which is not. Thus SuperSymmetry is hidden at the lower energies corresponding to the present explored scale. The spontaneous breaking can be obtained in several ways, all involving new particles and interactions at very high mass scale (likely including gravity) but there is not a model really preferred. The breaking part is usually introduced in the lagrangian "by hand" without any further hypothesis on the bare breaking mechanism [11]. The only requirement regards the couplings mass dimensions that must be positive to naturally maintain the hierarchy between the electroweak scale and the Planck scale as discussed in section 1.3.1. These new terms must be renormalizable.

Without loosing generality, all these possible "soft" SuperSymmetry breaking interactions are:

$$\begin{aligned}\mathcal{L}_{\text{soft}} &= -\frac{1}{2}(M_{\mathcal{G}}\Omega^a_{\mathcal{G}}\Omega^a_{\mathcal{G}} + \text{h.c.}) - (\widetilde{m}^2)^{ij}\phi^*_j\phi_i \\ &\quad - \left(\frac{1}{2}\mathrm{b}^{ij}\phi_i\phi_j + \frac{1}{6}\mathrm{a}^{ijk}\phi_i\phi_j\phi_k + \text{h.c.}\right).\end{aligned} \tag{1.66}$$

There are several parameters involved: $M_{\mathcal{G}}$ for each group $\mathcal{G}$ for the gaugino mass terms, $(\widetilde{m}^2)^{ij}$ and b^{ij} for the quadratic scalar couplings and a^{ijk} for the cubic scalar couplings. $\mathcal{L}_{\text{soft}}$ clearly breaks the SuperSymmetry since it involves only scalars and gauginos and not the standard particles. On the other hand, $\mathcal{L}_{\text{soft}}$ is able to give mass to the gauginos and to the scalars even if the standard particles were massless.

Taking into account the MSSM particle content and the gauge invariance, the above general form can be specialized for the case of MSSM:

$$\begin{aligned}\mathcal{L}^{\text{MSSM}}_{\text{soft}} &= -\frac{1}{2}(M_1\widetilde{B}\widetilde{B} + M_2\widetilde{W}\widetilde{W} + M_3\widetilde{g}\widetilde{g}) + \text{h.c.} \\ &\quad - \left(\widetilde{U}^*_{\text{R}}\mathbf{a}_U\widetilde{Q}_{\text{L}}\mathcal{H}_U - \widetilde{D}^*_{\text{R}}\mathbf{a}_D\widetilde{Q}_{\text{L}}\mathcal{H}_D - \widetilde{\ell}^*_{\text{R}}\mathbf{a}_\ell\widetilde{L}_{\text{L}}\mathcal{H}_D\right) + \text{h.c.} \\ &\quad - \widetilde{q}^\dagger_{\text{L}}\widetilde{\mathbf{m}}^{\mathbf{2}}_q\widetilde{q}_{\text{L}} - \widetilde{L}^\dagger_{\text{L}}\widetilde{\mathbf{m}}^{\mathbf{2}}_L\widetilde{L}_{\text{L}} - \widetilde{u}^*_{\text{R}}\widetilde{\mathbf{m}}^{\mathbf{2}}_u\widetilde{u}_{\text{R}} - \widetilde{d}^*_{\text{R}}\widetilde{\mathbf{m}}^{\mathbf{2}}_d\widetilde{d}_{\text{R}} - \widetilde{\ell}^*_{\text{R}}\widetilde{\mathbf{m}}^{\mathbf{2}}_\ell\widetilde{\ell}_{\text{R}} \\ &\quad - m^2_{\mathcal{H}_U}\mathcal{H}^\dagger_U\mathcal{H}_U - m^2_{\mathcal{H}_D}\mathcal{H}^\dagger_D\mathcal{H}_D \\ &\quad - \left[\mathrm{b}(\mathcal{H}_U)_t(\mathcal{H}_D)_{t'}\epsilon^{tt'} + \text{h.c.}\right]\end{aligned} \tag{1.67}$$

where the family indices are omitted and in the last term the gauge invariant product procedure has been used like in (1.62). In the $\widetilde{\mathbf{m}}^{\mathbf{2}}$ terms is convenient to use the scalar partner of the mass eigenstates quark fields.

There are many new parameters in the MSSM model: M_1, M_2 and M_3 the bino, wino and gluino masses; three matrices 3×3 in the family space ($\mathbf{a}_U$, $\mathbf{a}_D$ and $\mathbf{a}_\ell$) which elements have the mass dimension. The other matrices 3×3 in the family space are the sfermion

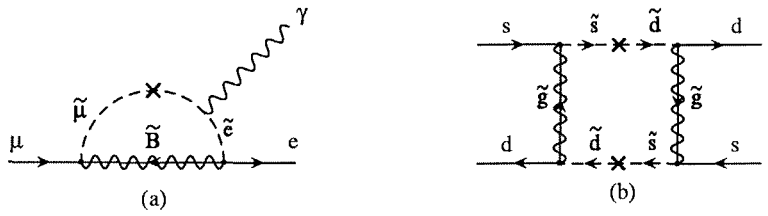

Figure 1.8: Flavour violating diagrams involving virtual sfermions.

squared mass matrices ($\widetilde{\mathbf{m}}_q^2$, $\widetilde{\mathbf{m}}_L^2$, $\widetilde{\mathbf{m}}_u^2$, $\widetilde{\mathbf{m}}_d^2$, $\widetilde{\mathbf{m}}_\ell^2$). They must be hermitian to have a real lagrangian. Then there are the two squared masses for the Higgs fields $m_{\mathcal{H}_U}^2$ and $m_{\mathcal{H}_D}^2$ and the coupling b of the only b^{ij} term (see (1.66)) allowed in the MSSM.

All these new parameters will be of the order of a mass m_{soft} or m_{soft}^2 (depending on their dimension) giving the magnitude of the mass splitting between fermion and sfermions. Following the argument discussed in section 1.3.1, m_{soft} cannot be too much larger than 1 TeV.

Origin of SUSY breaking

The number of new parameters is 105, thus a large number. Using experimental observations and SUSY breaking models this number can be drastically reduced obtaining a workable model.

If the $\widetilde{\mathbf{m}}^2$ matrices would not be diagonal in the Standard Model mass eigenstates, the slepton and squark mixing would occur contributing to flavour changing processes where virtual sfermions enter. For example, if $\widetilde{\mathbf{m}}_\ell^2$ is not diagonal, the one-loop diagrams of the type plotted in fig. 1.8(a) would contribute significantly to the process $\mu \to e\gamma$. On the contrary it is strictly forbidden from the experiments ($BR(\mu \to e\gamma) < 5 \times 10^{-11}$). In the squark case, a not diagonal squared mass matrix would allow diagrams altering the Standard Model prediction on the meson system oscillation and CP-violation parameters. For example the $K^0 - \overline{K}^0$ system behaviour would depend on diagrams like the one in fig 1.8(b). Also in this case there is no evidence of deviations from the Standard Model. Similarly the **a** matrices are constrained from the absence of flavour changing neutral current (FCNC) that **a** off-diagonal terms would generate.

To avoid all these very unlikely effects, further assumptions can be done on the soft breaking parameters. In particular, to avoid extra contributions to FCNC with respect to the Standard Model the $\widetilde{\mathbf{m}}^2$ matrices could be just diagonal [12] (*flavour alignment hypothesis*), or even proportional to the identity matrix **1** [13]:

$$\widetilde{\mathbf{m}}_q^2 = \widetilde{m}_q^2\mathbf{1}, \quad \widetilde{\mathbf{m}}_L^2 = \widetilde{m}_L^2\mathbf{1}, \quad \widetilde{\mathbf{m}}_u^2 = \widetilde{m}_u^2\mathbf{1}, \quad \widetilde{\mathbf{m}}_d^2 = \widetilde{m}_d^2\mathbf{1}, \quad \widetilde{\mathbf{m}}_\ell^2 = \widetilde{m}_\ell^2\mathbf{1}. \tag{1.68}$$

The **a** matrices must be proportional to the Standard Model Yukawa matrices:

$$\mathbf{a}_{U\alpha\alpha'} = A_U\Upsilon_{\alpha\alpha'}, \quad \mathbf{a}_{D\alpha\alpha'} = A_D\Upsilon'_{\alpha\alpha'}, \quad \mathbf{a}_{\ell\alpha\alpha'} = A_\ell\delta_{\alpha\alpha'}y_\alpha, \tag{1.69}$$

where the family indices α and α' are explicitally typed. The quantities Υ and Υ' and y are

the Yukawa couplings already used in (1.8), (1.29) and (1.61). The further assumptions

$$M_1 = M_1^*, \;\; M_2 = M_2^*, \;\; M_3 = M_3^*, \;\; A_U = A_U^*, \;\; A_D = A_D^*, \;\; A_\ell = A_\ell^*, \tag{1.70}$$

together with (1.68) and (1.69), avoid that extra complex phases are introduced in the model. In other words, there are no extra CP-violating effects with respect to the Standard Model ones that comes from the CKM matrix complex phase.

The conditions (1.68), (1.69) and (1.70), known as *soft breaking universality assumptions*, will follow from the SuperSymmetry breaking mechanism. They have to be valid at least at some very high scale Q_0, known as input scale, where one expects an underlying simplicity or symmetry of the lagrangian. Observable quantities at the present scale (m_Z) can be then computed applying the Renormalization Group (RG) equations to sum the contributions of logarithms like $\ln(Q_0/m_Z)$. It turns out that the running does change the relations (1.68), (1.69) and (1.70) but not dramatically. As long as the relations are valid at the input scale, the supersymmetric contribution to FCNC and CP violation at the weak scale is still small and thus acceptable with respect to the present limits.

The apparent unification of gauge couplings within the MSSM is a very strong hint that this scenario is correct. The gauge group $\mathrm{SU(2)_L} \otimes \mathrm{U(1)_Y} \otimes \mathrm{SU(3)_C}$ is supposed to unify in SU(5) or SO(10) according to grand unification theories (GUT), that are not in contrast with a SuperSymmetry scenario. Rescaling the Standard Model gauge couplings by the standard normalization of the groups SU(5) or SU(10), ($g_1 = \sqrt{5/3}g' = \sqrt{5/3}g_{\mathrm{U(1)_Y}}$, $g_2 = g = g_{\mathrm{SU(2)_L}}$ and $g_3 = g_{\mathrm{SU(3)_C}}$) the 1-loop RG equations for the couplings are easy to write:

$$\frac{d}{d\ln(Q/Q_0)} g_a = \frac{1}{16\pi^2} b_a g_a^3 \quad \rightarrow \quad \frac{d}{d\ln(Q/Q_0)} \alpha_a^{-1} = -\frac{b_a}{2\pi} \qquad a = (1,2,3). \tag{1.71}$$

Q is the RG scale. In the standard model $b_a^{\mathrm{SM}} = (41/10, -19/16, -7)$, while in the MSSM the contribution of the new particles gives $b_a^{\mathrm{MSSM}} = (33/5, 1, -3)$.

Comparing the 2-loop RG running of the gauge couplings in case of Standard Model and MSSM (see fig. 1.9), MSSM seems to have just the right particle content to get the coupling unifying at a scale $M_U \sim 2 \times 10^{16}$ GeV.

After the general considerations about the SUSY breaking sector within the MSSM and about the SUSY breaking properties at the input scale, a brief outlook on the nature of SUSY breaking is given.

Spontaneously broken SuperSymmetry means the vacuum state $|0\rangle$ being not invariant under SuperSymmetry transformations, i.e. $\mathcal{Q}_\alpha|0\rangle \neq 0$ and $\mathcal{Q}_{\dot{\alpha}}^\dagger|0\rangle \neq 0$. Following the $\mathcal{Q}$ operator properties (1.47), the Hamiltonian operator H, i.e. the energy component of the momentum p^0, can be written:

$$\mathrm{H} = p^0 = \frac{1}{4}(\mathcal{Q}_1\mathcal{Q}_1^\dagger + \mathcal{Q}_1^\dagger\mathcal{Q}_1 + \mathcal{Q}_2\mathcal{Q}_2^\dagger + \mathcal{Q}_2^\dagger\mathcal{Q}_2). \tag{1.72}$$

If the vacuum state is invariant under SuperSymmetry $\mathrm{H}|0\rangle = 0$. On the contrary, if the SuperSymmetry is broken the vacuum has a positive energy:

$$\langle 0|\mathrm{H}|0\rangle = \frac{1}{4}(|\mathcal{Q}_1|0\rangle|^2 + |\mathcal{Q}_1^\dagger|0\rangle|^2 + |\mathcal{Q}_2|0\rangle|^2 + |\mathcal{Q}_2^\dagger|0\rangle|^2) > 0. \tag{1.73}$$

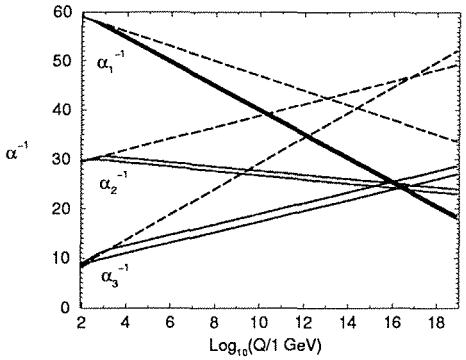

Figure 1.9: Evolution of the gauge couplings according to the RG equations: dashed lines for the Standard Model case and solid lines for the MSSM case ($\alpha_3(m_Z) = 0.113 \div 0.123$ and the sparticle thresholds between 250 GeV and 1 TeV) [5].

Neglecting spacetime-dependent effects or fermion condensate, since $\langle 0|\mathrm{H}|0\rangle = \langle 0|V|0\rangle$ the SuperSymmetry breaking can only occur if the F-terms or D-terms in the scalar potential V do not annihilate the vacuum.

It turns out that only the F-terms can have non zero vacuum energy without generating unsolvable problems that, on the other hand, appear using the D-terms. Moreover, this F-term cannot be generated by the superfields of the MSSM but only by some new chiral superfield coming from a very high scale frame not accessible at the present scale [14]. In other words, SuperSymmetry breaking occurs in a very high scale "hidden sector" that couples very weakly with the "visible" MSSM sector by some type of mediating interactions. If these interactions are flavour blind the conditions (1.68), (1.69) and (1.70) will be automatically satisfied.

Since the SuperSymmetry generators commute with the momentum, the space-time translation generators, it is thought to be natural to include also the gravity in the model. This can be done adding to the MSSM particle spectrum a gravity superfield holding the graviton G and its superpartner $\widetilde{\mathrm{G}}$, the *gravitino*. Even if a consistent theory of the gravity is not yet available, a model based on the gravity can be used to mediate the SuperSymmetry breaking. This *gravity-mediated* model is one of the most popular proposal for the SuperSymmetry breaking mechanism [15]. Hence, if SuperSymmetry is broken in a hidden sector by a not zero vacuum expectation value $\langle F\rangle$, the soft terms in the visible sector can be estimated of the order

$$m_{\mathrm{soft}} \sim \frac{\langle F\rangle}{M_P}. \tag{1.74}$$

In fact, m_{soft} must vanish in case that the SuperSymmetry remains unbroken ($\langle F\rangle = 0$) or in case that the breaking is not transmitted to the visible sector. This occurs if the gravity disappears ($M_P = (8\pi G_{\mathrm{Newton}})^{-1/2}$; $G_{\mathrm{Newton}} \to 0 \Rightarrow M_P \to \infty$).

If a particularly constrained version of the gravity mediated model is assumed, one finds

that the lagrangian $\mathcal{L}_{\text{soft}}$ can be written in terms of only four parameters:

$$m_{1/2} \propto \frac{\langle F \rangle}{M_P}\,; \quad m_0^2 \propto \frac{\langle F \rangle^2}{M_P^2}\,; \quad A \propto \frac{\langle F \rangle}{M_P}\,; \quad B \propto \frac{\langle F \rangle}{M_P}\,. \tag{1.75}$$

They allow to write:

$$M_1 = M_2 = M_3 = m_{1/2}; \tag{1.76}$$

$$\widetilde{m}_q^2 = \widetilde{m}_u^2 = \widetilde{m}_d^2 = \widetilde{m}_L^2 = \widetilde{m}_\ell^2 = m_{\mathcal{H}_U}^2 = m_{\mathcal{H}_D}^2 = m_0^2; \tag{1.77}$$

$$A_U = A_D = A_\ell = A; \tag{1.78}$$

$$\mathrm{b} = B\mu. \tag{1.79}$$

These conditions are very attractive and also more stringent that the generic soft breaking universality conditions. At least at the input scale, there is a common mass for scalars, m_0, and a common mass for fermions $m_{1/2}$ and the Standard model flavour mixing is preserved. This somehow explains the success and the popularity of the gravity-mediated models.

Independently from the model assumed to describe the SuperSymmetry breaking, the RG equations similar to (1.71) have to be applied to extrapolate the parameters values from the input scale, where they are fixed from the model, to the present scale.

For example, starting from the gravity mediation, the gaugino mass term prediction (1.76) at the present scale becomes:

$$\frac{M_1}{g_1^2} = \frac{M_2}{g_2^2} = \frac{M_3}{g_3^2}. \tag{1.80}$$

Although they are not longer equal to $m_{1/2}$, the gaugino mass parameters are still linked through the known gauge couplings. Surprisingly the above conclusion is common to several breaking models, being essentially related to the GUT hypothesis. Thanks to this solid theoretical motivation, the gaugino sector is normally set by only one parameter.

1.3.6 The electroweak symmetry breaking in MSSM

In the MSSM the breaking of the group $\mathrm{SU(2)_L \otimes U(1)_Y \rightarrow U(1)_{em}}$ occurs in the Higgs sector as in the Standard Model is. The full scalar potential V_{Higgs} relative to the Higgs sector contains terms coming from (1.60), which parameters are the gauge couplings and μ, and terms coming from the soft breaking lagrangian (1.66) that depend on $m_{\mathcal{H}_U}^2$, $m_{\mathcal{H}_D}^2$ and b:

$$\begin{aligned} V_{\text{Higgs}} \;=\; & (|\mu|^2 + m_{\mathcal{H}_U}^2)(|\mathcal{H}_U^0|^2 + |\mathcal{H}_U^+|^2) + (|\mu|^2 + m_{\mathcal{H}_D}^2)(|\mathcal{H}_D^0|^2 + |\mathcal{H}_D^-|^2) + \qquad (1.81) \\ & + (\mathrm{b}\mathcal{H}_U^+\mathcal{H}_D^- - \mathrm{b}\mathcal{H}_U^0\mathcal{H}_D^0 + \mathrm{h.c.}) \\ & + \frac{1}{8}(g^2 + g'^2)(|\mathcal{H}_U^0|^2 + |\mathcal{H}_U^+|^2 - |\mathcal{H}_D^0|^2 - |\mathcal{H}_D^-|^2)^2 \\ & + \frac{1}{2}g^2|\mathcal{H}_U^+\mathcal{H}_D^{0*} + \mathcal{H}_U^0\mathcal{H}_D^{-*}|^2. \qquad (1.82) \end{aligned}$$

Requiring $SU(2)_L \otimes U(1)_Y$ to break in $U(1)_{em}$ and using the gauge properties it turns out that $\mathcal{H}_U^+ = \mathcal{H}_D^- = 0$ and that the vacuum expectation values ($v_U = \langle 0|\mathcal{H}_U^0|0\rangle$, $v_D = \langle 0|\mathcal{H}_D^0|0\rangle$) and b can be chosen real and positive without loosing generality.

The breaking algebraically consists in a suitable rewriting of the Higgs sector degrees of freedom. Three scalar neutral fields (θ^0, h^0, H^0), one pseudo-scalar neutral field (A^0) and two charged complex fields ($\theta^\pm$, $H^\pm$) can be used in place of the four complex fields $\mathcal{H}_U^0$, $\mathcal{H}_U^+$, $\mathcal{H}_D^0$ and $\mathcal{H}_D^-$. The θ fields are the Goldstone bosons reabsorbed by the gauge invariance to make massive the Z and W. The remaining fields acquire masses, building the physical Higgs content of the MSSM: there are two neutral CP-even scalar bosons, h^0 and H^0, a neutral CP-odd scalar boson, A^0 and two charged scalar bosons, H^+ and H^-.

Nevertheless a couple of conditions have to be satisfied in order to have the mechanism properly working. In particular,

$$\mathrm{b}^2 > (|\mu|^2 + m_{\mathcal{H}_U}^2)(|\mu|^2 + m_{\mathcal{H}_D}^2), \tag{1.83}$$

to prevent the point $\mathcal{H}_U^0 = \mathcal{H}_D^0 = 0$ to be a minimum and

$$2\mathrm{b} < 2|\mu|^2 + m_{\mathcal{H}_U}^2 + m_{\mathcal{H}_D}^2, \tag{1.84}$$

to have the potential bounded from below. The vacuum expectation values can be constrained asking the observation to be reproduced, that is

$$v_U^2 + v_D^2 = v^2 = 2\frac{m_Z^2}{g^2 + g'^2} \sim (174\,\mathrm{GeV}/c^2)^2. \tag{1.85}$$

Thus the ratio of the two vacuum values

$$\tan\beta \equiv \frac{v_U}{v_D}, \quad 0 < \beta < \frac{\pi}{2}, \tag{1.86}$$

is undefined. Using the above definitions the conditions to have V minimized in $\mathcal{H}_U = (0, v_U)$ and $\mathcal{H}_D = (v_D, 0)$ are:

$$\left.\frac{\partial V}{\partial \mathcal{H}_U^0}\right|_{\mathcal{H}_U=(0,v_U)} = |\mu|^2 + m_{\mathcal{H}_D}^2 = \mathrm{b}\tan\beta - \frac{m_Z^2}{2}\cos 2\beta, \tag{1.87}$$

$$\left.\frac{\partial V}{\partial \mathcal{H}_D^0}\right|_{\mathcal{H}_D=(v_D,0)} = |\mu|^2 + m_{\mathcal{H}_U}^2 = \mathrm{b}\cot\beta + \frac{m_Z^2}{2}\cos 2\beta. \tag{1.88}$$

It is easy to check that the above conditions indeed satisfy the requirements (1.83) and (1.84). Moreover b and μ turn out to be functions of $\tan\beta$. Thus, fixing $\tan\beta$ and the phase of μ the whole SUSY-conserving sector, i.e. $\tan\beta$ and μ, is set together with the SUSY-breaking parameter b as well.

The mass-eigenstate fields can be written explicitly:

$$\begin{pmatrix} \theta^0 \\ A^0 \end{pmatrix} = \sqrt{2}\begin{pmatrix} \sin\beta & -\cos\beta \\ \cos\beta & \sin\beta \end{pmatrix}\begin{pmatrix} \mathcal{H}_U^0 + \mathcal{H}_U^{0*} \\ \mathcal{H}_D^0 + \mathcal{H}_D^{0*} \end{pmatrix}, \tag{1.89}$$

$$\begin{pmatrix} h^0 \\ H^0 \end{pmatrix} = \sqrt{2} \begin{pmatrix} \sin\alpha & -\cos\alpha \\ \cos\alpha & \sin\alpha \end{pmatrix} \begin{pmatrix} \mathcal{H}_U^0 - \mathcal{H}_U^{0*} - v_U \\ \mathcal{H}_D^0 - \mathcal{H}_D^{0*} - v_D \end{pmatrix}, \tag{1.90}$$

$$\begin{pmatrix} \theta^+ \\ H^\pm \end{pmatrix} = \sqrt{2} \begin{pmatrix} \sin\beta & -\cos\beta \\ \cos\beta & \sin\beta \end{pmatrix} \begin{pmatrix} \mathcal{H}_U^+ \\ \mathcal{H}_D^{-*} \end{pmatrix}, \tag{1.91}$$

where the angles β, above defined, and α play the role of mixing angles.

As soon as the Higgs mechanism is applied in the lagrangian also fermions acquire masses according to the Yukawa couplings magnitude.

1.3.7 The mass spectrum of MSSM

An overview of the expected particle spectrum can be given after the above definitions of the MSSM relevant parameters.

Higgs bosons

The Higgs bosons masses are:

$$m_{A^0}^2 = \frac{2\mathrm{b}}{\sin 2\beta}, \tag{1.92}$$

$$m_{H^\pm}^2 = m_{A^0}^2 + m_{\mathrm{W}}^2, \tag{1.93}$$

$$m_{h^0}^2 = \frac{1}{2}\left(m_{A^0}^2 + m_{\mathrm{Z}}^2 - \sqrt{(m_{A^0}^2 + m_{\mathrm{Z}}^2)^2 - 4m_{\mathrm{Z}}^2 m_{A^0}^2 \cos^2 2\beta}\right), \tag{1.94}$$

$$m_{H^0}^2 = \frac{1}{2}\left(m_{A^0}^2 + m_{\mathrm{Z}}^2 + \sqrt{(m_{A^0}^2 + m_{\mathrm{Z}}^2)^2 - 4m_{\mathrm{Z}}^2 m_{A^0}^2 \cos^2 2\beta}\right). \tag{1.95}$$

Since at tree level α depends exactly on the above masses without any new parameter,

$$\frac{\sin 2\alpha}{\sin 2\beta} = -\frac{m_{A^0}^2 + m_{\mathrm{Z}}^2}{m_{H^0}^2 - m_{h^0}^2}, \qquad \frac{\cos 2\alpha}{\cos 2\beta} = -\frac{m_{A^0}^2 - m_{\mathrm{Z}}^2}{m_{H^0}^2 - m_{h^0}^2}, \tag{1.96}$$

also α is fixed once β and the phase of μ are fixed.

If the masses of A^0, H^0 and $H^\pm$ can be arbitrarily large depending on $\mathrm{b}/\sin 2\beta$, the mass of h^0 is bounded from above. In particular at tree level it turns out that

$$m_{h^0} < |\cos 2\beta| m_{\mathrm{Z}}. \tag{1.97}$$

Thus h^0 seems to be well within the LEP2 discovery range. However this optimistic prediction is strongly modified by taking into account several corrections. For example, including corrections due to stop and top loops, that are significant because the large Yukawa coupling, it follows that [16]:

$$m_{h^0}^2 < \cos^2 2\beta m_{\mathrm{Z}}^2 + \frac{3g^2}{8\pi^2}\frac{m_{\mathrm{t}}^4}{m_{\mathrm{W}}} \log \frac{m_{\tilde{\mathrm{t}}_1} m_{\tilde{\mathrm{t}}_2}}{m_{\mathrm{t}}^2}, \tag{1.98}$$

where $m_{\tilde{\mathrm{t}}_1}$ and $m_{\tilde{\mathrm{t}}_2}$ are the stop masses below defined. Anyhow the h^0 mass prediction remains below 130÷150 GeV depending on the assumptions on the other relevant parameters.

Charginos, neutralinos and gluinos

As a consequence of electroweak symmetry breaking, the higgsinos and the electroweak charginos mix to form the mass eigenstates. The neutral gauginos $\widetilde{\mathrm{B}}$ and $\widetilde{\mathrm{W}}^0$ together with the neutral higgsinos $\widetilde{\mathcal{H}}_U^0$ and $\widetilde{\mathcal{H}}_D^0$ yield to four mass eigenstates known as *neutralinos* usually indicated with the symbols χ_1, χ_2, χ_3 and χ_4 sorted by increasing mass. The lightest one is χ_1, often simply indicated with χ.

In the gauge eigenstates basis $\psi^0 = (\widetilde{\mathrm{B}}, \widetilde{\mathrm{W}}^0, \widetilde{\mathcal{H}}_D^0, \widetilde{\mathcal{H}}_U^0)$, the neutralinos mass term in the lagrangian is

$$-\frac{1}{2}\psi^{0T}\mathbf{M}_\chi\psi^0. \tag{1.99}$$

The mass matrix $\mathbf{M}_\chi$ is

$$\mathbf{M}_\chi = \begin{pmatrix} M_1 & 0 & -m_\mathrm{Z}\cos\beta\sin\theta_W & m_\mathrm{Z}\sin\beta\sin\theta_W \\ 0 & M_2 & m_\mathrm{Z}\cos\beta\cos\theta_W & -m_\mathrm{Z}\sin\beta\cos\theta_W \\ -m_\mathrm{Z}\cos\beta\sin\theta_W & m_\mathrm{Z}\cos\beta\cos\theta_W & 0 & -\mu \\ m_\mathrm{Z}\sin\beta\sin\theta_W & -m_\mathrm{Z}\sin\beta\cos\theta_W & -\mu & 0 \end{pmatrix}. \tag{1.100}$$

Similarly the charged winos $\widetilde{\mathrm{W}}^\pm$ and the higgsinos $\widetilde{\mathcal{H}}_U^+$ and $\widetilde{\mathcal{H}}_D^-$ mix to form two charged mass eigenstates known as *charginos* usually indicated with the symbols $\chi^\pm{}_1$ and $\chi^\pm{}_2$. The lightest one is $\chi^\pm{}_1$, often simply indicated with $\chi^\pm$. In the gauge eigenstate basis $\psi^\pm = (\widetilde{\mathrm{W}}^+, \widetilde{\mathcal{H}}_U^+, \widetilde{\mathrm{W}}^-, \widetilde{\mathcal{H}}_D^-)$, the charginos mass term in the lagrangian is

$$-\frac{1}{2}\psi^{\pm T}\mathbf{M}_{\chi^\pm}\psi^\pm, \tag{1.101}$$

where the mass matrix $\mathbf{M}_{\chi^\pm}$ is

$$\mathbf{M}_{\chi^\pm} = \begin{pmatrix} 0 & 0 & M_2 & \sqrt{2}m_\mathrm{W}\cos\beta \\ 0 & 0 & \sqrt{2}m_\mathrm{W}\sin\beta & \mu \\ M_2 & \sqrt{2}m_\mathrm{W}\sin\beta & 0 & 0 \\ \sqrt{2}m_\mathrm{W}\cos\beta & \mu & 0 & 0 \end{pmatrix}. \tag{1.102}$$

The gluino is a colour octet thus it cannot mix with other MSSM particle. From the relation (1.80) between gaugino masses that is usually assumed, one realizes that $M_3/M_2/M_1 \sim 7/2/1$ at the electroweak scale. Therefore the gluino is typically much heavier than lighter charginos and neutralinos.

Sfermions

The sfermions are not degenerate in mass with their fermionic partners, thanks to the the soft breaking terms. The soft breaking universality assumptions makes the mixing between sfermions restricted to the charged f_L, f_R fields of each flavour. Otherwise, for example, all up-type squark could mix to form the mass eigenstates. The sfermion mass matrices depend on the trilinear couplings and on the fermion masses through the Yukawa couplings. This can be explicitly stated rewriting the second line of the soft breaking lagrangian (1.67) in

terms of the partner fields of the mass eigenstates fermions. Hence, the squark soft breaking lagrangian terms turn out as follows:

$$\widetilde{U}^*_{\rm R}\mathbf{a}_U\widetilde{Q}_{\rm L}\mathcal{H}_U \to \widetilde{u}^*_{\rm R}\begin{pmatrix} \mathrm{a_u} = A_U m_{\rm u}/v_U & & \\ & \mathrm{a_c} = A_U m_{\rm c}/v_U & \\ & & \mathrm{a_t} = A_U m_{\rm t}/v_U \end{pmatrix}\widetilde{q}_{\rm L}\mathcal{H}_U, \quad (1.103)$$

$$\widetilde{D}^*_{\rm R}\mathbf{a}_D\widetilde{Q}_{\rm L}\mathcal{H}_D \to \widetilde{d}^*_{\rm R}\begin{pmatrix} \mathrm{a_d} = A_D m_{\rm d}/v_D & & \\ & \mathrm{a_s} = A_D m_{\rm s}/v_D & \\ & & \mathrm{a_b} = A_D m_{\rm b}/v_D \end{pmatrix}\widetilde{q}_{\rm L}\mathcal{H}_D. \quad (1.104)$$

The slepton case is more straightforward since the Yukawa couplings are already diagonal:

$$\widetilde{\ell}^*_{\rm R}\mathbf{a}_\ell\widetilde{L}_{\rm L}\mathcal{H}_D \to \widetilde{\ell}^*_{\rm R}\begin{pmatrix} \mathrm{a_e} = A_\ell m_{\rm e}/v_D & & \\ & \mathrm{a}_\mu = A_\ell m_\mu/v_D & \\ & & \mathrm{a}_\tau = A_\ell m_\tau/v_D \end{pmatrix}\widetilde{L}_{\rm L}\mathcal{H}_D. \quad (1.105)$$

Taking into account all terms that can contribute, one finds that the mass term of a given sfermion $\tilde{f}$, partner of the standard model fermion f, is

$$-(\,\tilde{f}^*_{\rm L}\;\;\tilde{f}^*_{\rm R}\,)\;\mathbf{m}^2_{\tilde{f}}\;\begin{pmatrix}\tilde{f}_{\rm L}\\ \tilde{f}_{\rm R}\end{pmatrix}, \quad (1.106)$$

the mass matrix $\mathbf{m}^2_{\tilde{f}}$ being:

$$\mathbf{m}^2_{\tilde{f}} = \begin{pmatrix} m^2_{\tilde{f}_{\rm L}} & \Delta_{\tilde{f}}\, m_f \\ \Delta_{\tilde{f}}\, m_f & m^2_{\tilde{f}_{\rm R}}\end{pmatrix}. \quad (1.107)$$

The off-diagonal elements contain the quantity $\Delta_{\tilde{f}}$ defined as

$$\Delta_{\tilde{f}} = \begin{cases} A_U - \mu\cot\beta, & \tilde{f} = (\tilde{\rm u}, \tilde{\rm c}, \tilde{\rm t}) \\ A_D - \mu\tan\beta, & \tilde{f} = (\tilde{\rm d}, \tilde{\rm s}, \tilde{\rm b}) \\ A_\ell - \mu\tan\beta, & \tilde{f} = (\tilde{\rm e}, \tilde{\mu}, \tilde{\tau}) \end{cases} \quad (1.108)$$

The diagonal elements are:

$$m^2_{\tilde{f}_{\rm L}} = m^2_f + \begin{cases} \widetilde{m}^2_q + m^2_{\rm Z}\left(\frac{1}{2} - \frac{2}{3}\sin^2\theta_W\right)\cos 2\beta, & \tilde{f} = (\tilde{\rm u}_{\rm L}, \tilde{\rm c}_{\rm L}, \tilde{\rm t}_{\rm L}) \\ \widetilde{m}^2_q - m^2_{\rm Z}\left(\frac{1}{2} - \frac{1}{3}\sin^2\theta_W\right)\cos 2\beta, & \tilde{f} = (\tilde{\rm d}_{\rm L}, \tilde{\rm s}_{\rm L}, \tilde{\rm b}_{\rm L}) \\ \widetilde{m}^2_L + m^2_{\rm Z}\left(\frac{1}{2} - \sin^2\theta_W\right)\cos 2\beta, & \tilde{f} = (\tilde{\rm e}_{\rm L}, \tilde{\mu}_{\rm L}, \tilde{\tau}_{\rm L}) \end{cases}, \quad (1.109)$$

$$m^2_{\tilde{f}_{\rm R}} = m^2_f + \begin{cases} \widetilde{m}^2_u - \frac{2}{3}m^2_{\rm Z}\sin^2\theta_W\cos 2\beta, & \tilde{f} = (\tilde{\rm u}_{\rm R}, \tilde{\rm c}_{\rm R}, \tilde{\rm t}_{\rm R}) \\ \widetilde{m}^2_d + \frac{1}{3}m^2_{\rm Z}\sin^2\theta_W\cos 2\beta, & \tilde{f} = (\tilde{\rm d}_{\rm R}, \tilde{\rm s}_{\rm R}, \tilde{\rm b}_{\rm R}) \\ \widetilde{m}^2_\ell - m^2_{\rm Z}\sin^2\theta_W\cos 2\beta, & \tilde{f} = (\tilde{\rm e}_{\rm R}, \tilde{\mu}_{\rm R}, \tilde{\tau}_{\rm R}) \end{cases}. \quad (1.110)$$

The splitting factors proportional to $m^2_{\rm Z}$ come from the electroweak symmetry breaking. They depend on the weak isospin T^3 and on the electric charge Q being of the form:

$$m^2_{\rm Z}\left(T^{3\tilde{f}} - Q_{\tilde{f}}\sin^2\theta_W\right)\cos 2\beta. \quad (1.111)$$

The off-diagonal elements of the mass matrix are proportional to the fermion masses, thus one realizes that the mixing between the left-type and the right-type sfermions is important only for the third family. For that case the two mass eigenstates $\tilde{f}_1$ and $\tilde{f}_2$ are defined through a mixing matrix parametrized with the mixing angle $\theta_{\tilde{f}}$:

$$\begin{pmatrix} \tilde{f}_1 \\ \tilde{f}_2 \end{pmatrix} = \begin{pmatrix} \cos\theta_{\tilde{f}} & \sin\theta_{\tilde{f}} \\ -\sin\theta_{\tilde{f}} & \cos\theta_{\tilde{f}} \end{pmatrix} \begin{pmatrix} \tilde{f}_{\mathrm{L}} \\ \tilde{f}_{\mathrm{R}} \end{pmatrix} \tag{1.112}$$

Since the mass eigenstates are

$$m^2_{\tilde{f}_1\tilde{f}_2} = \frac{1}{2}\left(m^2_{\tilde{f}_{\mathrm{L}}} + m^2_{\tilde{f}_{\mathrm{R}}} \mp \sqrt{(m^2_{\tilde{f}_{\mathrm{L}}} m^2_{\tilde{f}_{\mathrm{R}}})^2 + 4\Delta^2_{\tilde{f}} m^2_{\tilde{f}}}\right), \tag{1.113}$$

the $\tilde{f}_1$ is lighter than $\tilde{f}_2$.

The mass of a sneutrino $\tilde{\nu}$, partner of the standard model particle ν is:

$$m^2_{\tilde{\nu}} = \widetilde{m}^2_{\nu} + \frac{1}{2} m^2_{\mathrm{Z}} \cos 2\beta, \quad \tilde{\nu} = (\tilde{\nu}_{\mathrm{e}}, \tilde{\nu}_{\mu}, \tilde{\nu}_{\tau}). \tag{1.114}$$

It is very important to notice that the $\widetilde{m}^2$ above used are the ones appearing in (1.68) after the appropriate running to the present scale. Hence, for example, it is not always true that the three sneutrinos are degenerate in mass, as apparently one concludes from the above sneutrino mass formula.

1.4 Outlook

The table 1.7 summarizes the new mass eigenstates predicted by the MSSM and not yet discovered. The mass spectrum is defined once the relevant parameters are fixed. As already mentioned, in case of highly predictive models, i.e. minimal supergravity model, only few parameters are independent.

Anyhow, from the point of view of the search of a SUSY signal, one tries to limit the starting hypothesis in order to get a result as much as possible independent from the model.

Nevertheless there are some hypothesis generally assumed since somehow unavoidable for several reasons:

- as already mentioned MSSM needs some assumption to be a workable and predictive model;
- historically the searches of SUSY signal started assuming a lot of simplifications; the need of more general results has come later and generally the transition is painful and not straightforward;
- some hypothesis is theoretically strong favoured.

As a general conclusive comment, one could also observe that the main target of a SUSY searches is to test the occurrence of topologies that are not predicted by the Standard Model. The interpretation of the results within a given model to exactly quantify these results and to make them comparable between the various experiments comes afterwards.

	Spin	R parity	Mass Eigenstates	Components
Higgs bosons	0	+1	h^0 H^0 A^0 $H^\pm$	$\mathcal{H}_U^0$ $\mathcal{H}_D^0$ $\mathcal{H}_U^+$ $\mathcal{H}_D^-$
squarks	0	−1	$\tilde{u}_L$ $\tilde{u}_R$ $\tilde{d}_L$ $\tilde{d}_R$ $\tilde{c}_L$ $\tilde{c}_R$ $\tilde{s}_L$ $\tilde{s}_R$ $\tilde{t}_1$ $\tilde{t}_2$ $\tilde{b}_1$ $\tilde{b}_2$	" " " " $\tilde{t}_L$ $\tilde{t}_R$ $\tilde{b}_L$ $\tilde{b}_R$
sleptons	0	−1	$\tilde{e}_L$ $\tilde{e}_R$ $\tilde{\nu}_e$ $\tilde{\mu}_L$ $\tilde{\mu}_R$ $\tilde{\nu}_\mu$ $\tilde{\tau}_1$ $\tilde{\tau}_2$ $\tilde{\nu}_\tau$	" " " " $\tilde{\tau}_L$ $\tilde{\tau}_R$ $\tilde{\nu}_\tau$
neutralinos charginos gluino	1/2 1/2 1/2	−1 −1 −1	χ_1 χ_2 χ_3 χ_4 $\chi^\pm{}_1$ $\chi^\pm{}_2$ $\widetilde{g}$	$\widetilde{B}$ $\widetilde{W}^3$ $\widetilde{\mathcal{H}}_U^0$ $\widetilde{\mathcal{H}}_D^0$ $\widetilde{W}^\pm$ $\widetilde{\mathcal{H}}_U^+$ $\widetilde{\mathcal{H}}_D^-$ " "
gravitino	3/2	−1	$\widetilde{G}$	" "

Table 1.7: New particles predicted by the MSSM.

2 Scalar top and scalar bottom

In this chapter an overview of the squark sector is given. The squark searches strategies are reviewed with a particular care to the e^+e^- collider phenomenology.

2.1 Mixing and masses

The lightest stop $\tilde{t}_1$ could be the lightest supersymmetric charged particle and even the next to lightest supersymmetric particle (NLSP). In fact, according to (1.107), the off-diagonal terms of its mixing matrix are proportional to the large m_t. Especially for small $\tan\beta$ values but not necessarily, the consequence could be a consistent mixing resulting in a huge mass difference between $\tilde{t}_1$ and $\tilde{t}_2$. Hence $\tilde{t}_1$ could be detected at LEP2 even if the diagonal masses are not close to the accessible scale.

In the case of sbottom, the bottom mass is too small to contribute significantly to the mixing. Nevertheless for large $\tan\beta$ values the sbottom mixing could be such that $\tilde{b}_1$ is the NLSP making the sbottom a SUSY particle to look for. Therefore, from the point of view of $\tan\beta$, the stop and sbottom searches are complementary.

In the following the symbols $\tilde{t}$ and $\tilde{b}$ will be used to indicate $\tilde{t}_1$ and $\tilde{b}_1$, respectively.

2.2 Phenomenology of R-parity conservation

From the phenomenological point of view the consequences of R-parity conservation are the following:

- SUSY particles can only be produced in pair;
- the lightest SUSY particle (LSP) is stable;
- the final state resulting from the decay chain of any other supersymmetric particle must contain an odd number of LSPs.

Therefore the LSP is probably the most important supersymmetric particle for its huge phenomenological impact in the RPC scenario. The LSP must be weakly interacting, thus neither charged or coloured, otherwise it would be easy to detect. Moreover the LSP is a good dark matter candidate and also for cosmological reasons it is favoured to be neither charged or coloured. Only the lightest neutralino χ or the sneutrinos are the only LSP reasonable candidate.

The general preferences are for a χ LSP, since this occurs in a great part of the MSSM parameter space. On the contrary, the sneutrinos are less popular as LSPs since they tend to be close in mass to the sleptons. The existing limits on the slepton masses [17] disfavour the $\tilde{\nu}$ LSP scenario.

The lightest χ is therefore generally assumed to be the LSP, but also the $\tilde{\nu}$ case is also sometimes considered for completeness.

2.3 e^+e^- collider searches

In a e^+e^- machine the squarks can be directly discovered or their existence can be pointed indirectly. In the second case the presence of effects due to virtual squarks would alter an observable quantity with respect to the value predicted from the Standard Model.

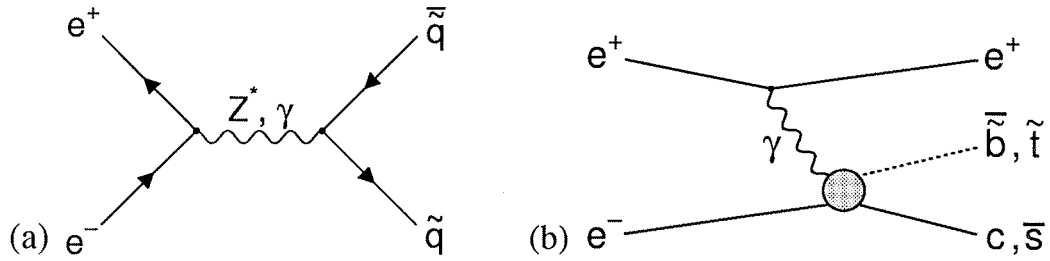

Figure 2.1: Squark production diagrams at LEP2: (a) RPC case double production; (b) RPV case single photo-production.

During the LEP1 phase limits on stop masses have been obtained from the Z width measurement that have an accuracy of $\sim 10\,\mathrm{MeV}/c^2$. As below explained, the stop production cross section depends on the mixing angle. For a particular value of the mixing angle the squarks decouple from the Z being the production only possible by photon exchange. Z width measurement is thus not useful in this case. Nevertheless dedicated analysis for the s-channel photon exchange have been used too. The final result of the LEP1 stop searches consists in the exclusion up to masses close to the kinematic limit (see fig. 2.10).

At LEP2 the direct search strategy is used. In the following sections the squark phenomenology with respect to the squark searches is discussed.

2.3.1 Production at e^+e^- collider

The squark production at an e^+e^- collider normally is possible only in couple according to R-parity conservation. But if RPC is not assumed, also the single production by an RPV vertex is possible. Both possibilities will be discussed below.

RPC case

In case that the production vertex does conserve R-parity, the production processes for $\tilde{t}$ and $\tilde{b}$ are $e^+e^- \rightarrow \tilde{t}\bar{\tilde{t}}$ and $e^+e^- \rightarrow \tilde{b}\bar{\tilde{b}}$. Fig. 2.1(a) shows the diagram of the process that occurs through the s-channel exchange of a photon or a Z.

The tree-level cross section σ^{tree} is [18][19]:

$$\sigma^{tree} = \frac{\pi\alpha^2}{s}\beta_{\tilde{q}}^3 \cdot \tag{2.1}$$

$$\begin{aligned}
\gamma \text{ exchange} &\rightarrow \quad \left[Q_{\tilde{q}}^2 \right. \\
\mathrm{Z} \text{ exchange} &\rightarrow \quad + \frac{(v_e^2 + a_e^2)v_{\tilde{q}}^2}{16\sin^4\theta_W\cos^4\theta_W} \frac{s^2}{(s-m_Z^2)^2 + m_Z^2\Gamma_Z^2} \\
\mathrm{Z}-\gamma \text{ Interference} &\rightarrow \quad \left. - \frac{Q_{\tilde{q}} v_e v_{\tilde{q}}}{\sin^2\theta_W\cos^2\theta_W} \frac{s(s-m_Z^2)}{(s-m_Z^2)^2 + m_Z^2\Gamma_Z^2} \right],
\end{aligned}$$

where the couplings coming from the $e^+e^- \rightarrow$ Z vertex are

$$v_e = 2sin^2\theta_W - 1/2, \quad a_e = -1/2, \tag{2.2}$$

while the coupling from $Z \rightarrow \tilde{q}\bar{\tilde{q}}$ are

$$v_{\tilde{q}} = 2(T^3_{\tilde{q}} - Q_{\tilde{q}} \sin^2 \theta_W). \tag{2.3}$$

The cross section is proportional to the cubic power of the outgoing squark speed $\beta_{\tilde{q}} = \sqrt{1 - 4m^2_{\tilde{q}}/s}$, that is a typical for scalar particles.

The mixing angle enters through $v_{\tilde{q}}$ in the Z exchange term and in the interference term. The cross section assumes a minimum value when the mixing angle is such that:

$$\cos^2 \theta_{\tilde{q}}|_{\sigma^{\text{tree}}\ \text{min}} = \frac{Q_{\tilde{q}}}{T^3_{\tilde{q}}} \sin^2 \theta_W \left[1 + 2\cos^2 \theta_W \left(1 - \frac{m^2_Z}{s}\right) \frac{v_e}{v^2_e + a^2_e}\right]. \tag{2.4}$$

Within few percents, the minimum occurs roughly when the $\tilde{q}$ does not couple anymore with the Z and only the γ contribution survives, that is for $\cos\theta_{\tilde{q}} = Q_{\tilde{q}} \sin^2 \theta_W / T^3_{\tilde{q}}$. The minimum cross section mixing angles are $\theta_{\tilde{t}\ \text{min}} \sim 56°$ for the stop and $\theta_{\tilde{b}\ \text{min}} \sim 68°$ for the sbottom. In both cases, the cross section is maximal for null mixing angle.

The angular distribution has the typical $\sin^2\theta$ behaviour, being θ the azimuthal angle:

$$\frac{d\sigma^{\text{tree}}}{d\cos\theta} = \frac{3}{4} \sin^2 \theta \sigma^{\text{tree}}. \tag{2.5}$$

For a correct evaluation of the final cross section the QCD corrections and the initial state radiation have to be taken into account.

The QCD corrections consist in the rescaling of the cross section by a factor

$$1 + \frac{4\alpha_s(s')}{3\pi} F(\beta), \tag{2.6}$$

where $F(\beta)$ is the so-called β-function for the scalar particles. The scale where the strong coupling constant α_s is considered is the available kinetic energy $s' = (\sqrt{s} - 2m_{\tilde{q}})^2$ [20].

The initial state radiation (ISR) consists in a photon emitted by one of the incoming leptons that reduces the actual interaction energy thus reducing the cross section too. The numerical computation code `REMT` has been used to evaluate ISR impact on the cross section [21].

Fig. 2.2 shows the stop and sbottom RPC production cross sections as a function of their mass with and without the corrections just discussed. One realizes that their effect is not negligible.

RPV case

One of the consequences of R-parity violation from the point of view of squarks is the possibility of single production. The cross section of this process has been evaluated within this work.

Since the LEP initial state is purely leptonic, from the point of view of squark production the interesting potential is the one proportional to the coupling λ' between squarks and leptons. This part of the potential in eq. (1.64) can be written in terms of matter fields:

$$\begin{aligned} \mathcal{L} = \lambda'_{ijk} \Big[& \tilde{u}^j_L d^{\dagger k}_R e^i_L + \tilde{d}^{*k}_R e^i_L u^j_L + \tilde{e}^i_L d^{\dagger k}_R u^j_L \\ & - \tilde{\nu}^i d^{\dagger k}_R d^j_L - \tilde{d}^j_L d^{\dagger k}_R \nu^i - \tilde{d}^{*k}_R \nu^i_L d^j_L + h.c. \Big], \end{aligned} \tag{2.7}$$

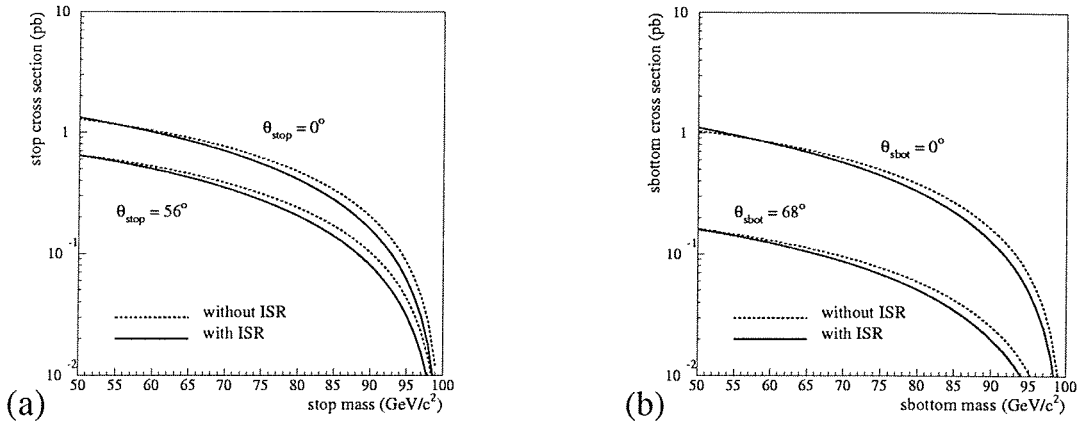

Figure 2.2: RPC production cross sections at $\sqrt{s} = 200\,\text{GeV}$ with and without the ISR: (a) stop; (b) sbottom.

where ijk are the family indices.

With the actual low-energy limits on the various couplings, the direct search of single production at LEP is possible only via the vertices $\tilde{b}ce$ ($\lambda'_{123} < 0.2$) and $\tilde{t}se$ ($\lambda'_{132} < 0.33$) [10]. Taking into account that the initial state is e^+e^-, the terms needed for cross section calculation are:

$$\lambda'_{123}\left[\tilde{b}^*_R e_L c_L + h.c.\right], \tag{2.8}$$

for the sbottom production and

$$\lambda'_{132}\left[\tilde{t}_L s^\dagger_R e_L + h.c.\right], \tag{2.9}$$

for the stop production. The resulting process is the photo-production shown in fig. 2.1. The photon emitted by an incoming electron enters in one of the diagrams shown in fig. 2.3. The mixing will be neglected in the following for sake of simplicity.

In this kind of processes it is very convenient to use the Weizsäcker-Williams approximation consisting in the assumption that the photon is on-shell [22]. Thus the $e^+e^- \to e\tilde{b}c$ ($e\tilde{t}s$) cross-section is the cross-section of the elementary process $\gamma e \to \tilde{b}c$ ($\tilde{t}s$) convoluted with the photon energy distribution [23].

Neglecting the electron mass, the following Mandelstam invariants can be defined for the subprocess:

$$\hat{s} = ys = (p_\gamma + p_e)^2 = 2p_\gamma \cdot p_e, \tag{2.10}$$

$$\hat{t} = (p_\gamma - p_{q'})^2 = m^2 - 2p_\gamma \cdot p_{q'}, \tag{2.11}$$

$$\hat{u} = (p_\gamma - p_{\tilde{q}})^2 = M^2 - 2p_\gamma \cdot p_{\tilde{q}}, \tag{2.12}$$

where M and m are the masses of the outcoming squark and quark respectively. The incoming particles momenta are p_γ and p_e, while the outcoming particles ones are $p_{q'}$ and

$p_{\tilde{q}}$. The quantity $y = \hat{s}/s$ represent the fraction of the squared center-of-mass energy in the e^+e^- collision available for the subprocess $\gamma e \to \tilde{q}q'$.

The spin averaged squared invariant amplitude $|\overline{\mathcal{M}}|^2$ coming from the three diagrams in fig. 2.3 turns out to be:

$$
\begin{aligned}
|\overline{\mathcal{M}}|^2 \;=\; & \frac{e^2\lambda^2}{2}\Bigg\{\frac{\hat{t}-m^2}{\hat{s}} + (1+Q)^2\,\frac{\hat{s}\hat{t}+m^2(-3\hat{s}-2\hat{u}+2m^2)}{(\hat{t}-m^2)^2} - \\
& 2(1+Q)\,\frac{\hat{s}m^2-(\hat{t}+\hat{u}-2m^2)(\hat{s}+\hat{u}-m^2)}{\hat{s}(\hat{t}-m^2)} - \\
& Q^2\,\frac{(\hat{u}-m^2)(\hat{u}+M^2)}{(\hat{u}-M^2)^2} + \\
& Q(1+Q)\frac{1}{(\hat{t}-m^2)(\hat{u}-M^2)}\left[\hat{s}^2-\hat{t}^2+\hat{u}(2\hat{s}+\hat{t}+\hat{u}) - \right. \\
& \left. m^2(3\hat{s}+4\hat{u}-3m^2-2M^2) - M^2(\hat{s}-\hat{t}+3\hat{u})\right] - \\
& Q\,\frac{t^2-\hat{s}^2+\hat{u}(\hat{s}+2\hat{t}+\hat{u}) - m^2(3\hat{t}+\hat{u}-4M^2) + M^2(\hat{s}-\hat{t}-3\hat{u})}{\hat{s}(\hat{u}-M^2)}\Bigg\},
\end{aligned}
\tag{2.13}
$$

being Q the squark charge and neglecting the electron mass. Since for a two-body decay the differential cross section is

$$
\frac{d\sigma}{dt} = \frac{|\overline{\mathcal{M}}|^2}{16\pi s^2}, \tag{2.14}
$$

the total cross-section $\hat{\sigma}_{\gamma e\to\tilde{q}q'}$ for the $\gamma e \to \tilde{q}q'$ subprocess comes out from the integration over $\hat{t}$:

$$
\hat{\sigma}_{\gamma e\to\tilde{q}q'}(\hat{s}) = \int_{\hat{t}_0}^{\hat{t}_1} \frac{1}{16\pi\hat{s}^2}|\overline{\mathcal{M}}|^2 d\hat{t}, \tag{2.15}
$$

where the integration range is given by:

$$
\hat{t}_{0/1} = \left(\frac{M^2-m^2}{2\sqrt{\hat{s}}}\right)^2 - \left(\frac{\sqrt{\hat{s}}}{2} \mp \sqrt{\left(\frac{\hat{s}+m^2-M^2}{2\sqrt{\hat{s}}}\right)^2 - m^2}\right)^2. \tag{2.16}
$$

According to the Weizsäcker-Williams approximation the subprocess total cross section $\hat{\sigma}_{\gamma e\to\tilde{q}q'}$ must be convoluted with the photon spectrum to obtain the total cross section $\sigma_{e^+e^-\to e\tilde{q}q'}(s)$ for the entire process $e^+e^- \to e\tilde{q}q'$, that is:

$$
\sigma_{e^+e^-\to e\tilde{q}q'}(s) = 6\int_{s_{\rm th}/s}^{1} dy f_\gamma(y)\,\hat{\sigma}_{\gamma e\to\tilde{q}q'}(\hat{s}). \tag{2.17}
$$

The factor 6 comes from the charge conjugation factor 2 times the colour factor 3. The lower limit of integration is given by the squared minimum production energy $s_{\rm th} = (m+M)^2$ while the photon spectrum $f_\gamma(y)$ is [23]:

$$
f_\gamma\left(y=\frac{\hat{s}}{s}\right) = \frac{\alpha_{em}}{2\pi}\cdot\left[\frac{1+(1-y)^2}{y}\log\left(\frac{p^2_{\rm max}}{p^2_{\rm min}}\right) - 2m_e^2 y\left(\frac{1}{p^2_{\rm min}} - \frac{1}{p^2_{\rm max}}\right)\right], \tag{2.18}
$$

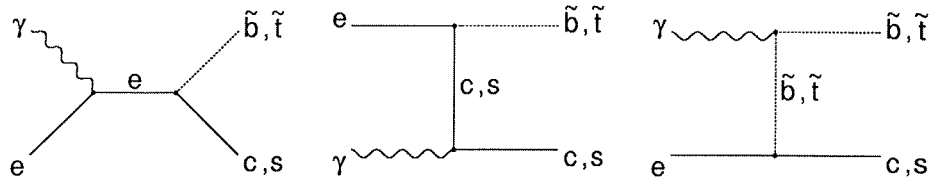

Figure 2.3: Diagrams contributing to the subprocess $\gamma e \to \tilde{b}c(\tilde{t}s)$.

where:

$$p^2_{\min} = \frac{m_e^2 y^2}{1-y}, \quad p^2_{\max} = E^2_{\text{beam}} = \frac{s}{4}. \tag{2.19}$$

The resulting $\sigma_{e^+e^- \to e\tilde{q}q'}(s)$ as a function of the squark mass for the two considered processes is shown in fig. 2.4 (with $\sqrt{s} = 189\,\text{GeV}$ and $\lambda'_{123} = 0.1$, $\lambda'_{132} = 0.1$). The sbottom cross section production is higher than the stop one since the dominant diagram is the one with the outcoming quark in the t-channel that couples with the photon. The electromagnetic coupling is proportional to $(1+Q)^2$, i.e. the charge of the outcoming quark is greater in the sbottom case.

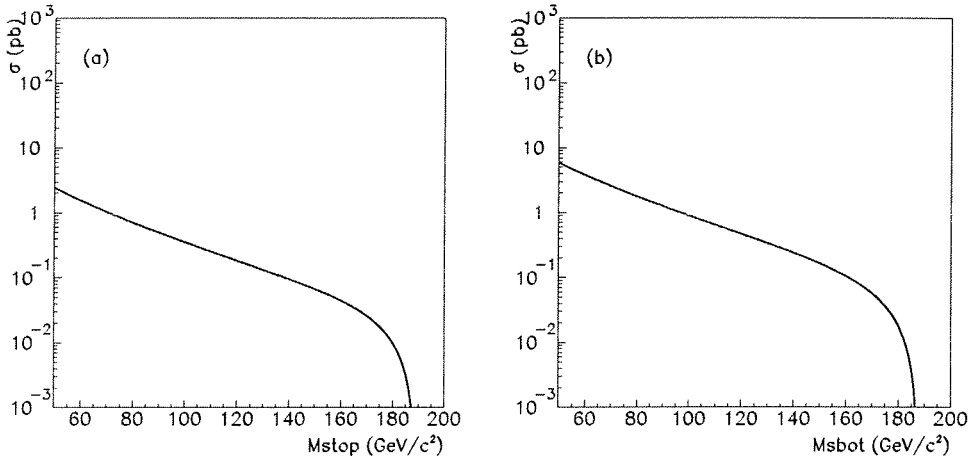

Figure 2.4: Single squark production cross section for $\sqrt{s} = 189$ GeV: (a) stop case with $\lambda'_{132} = 0.1$, (b) sbottom case with $\lambda'_{123} = 0.1$.

2.3.2 Decay

RPC case

Within the R-parity conserving scenario the stop searches here described rely on the assumption that all supersymmetric particle except the LSP were heaviest than the stop itself.

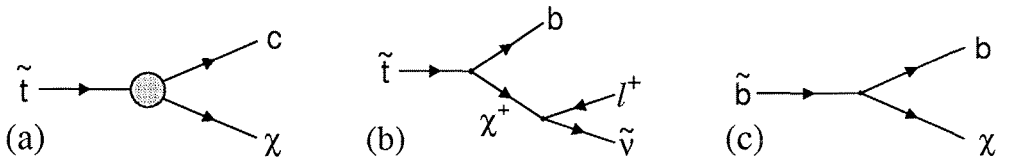

Figure 2.5: $\tilde{t}$ and $\tilde{b}$ RPC decay diagrams: (a) $\tilde{t} \to c\chi$; (b) $\tilde{t} \to b\ell\tilde{\nu}$; (c) $\tilde{b} \to b\chi$.

In these hypothesis the two main stop decay channels are $\tilde{t} \to c\chi$ and $\tilde{t} \to b\ell\tilde{\nu}$ [24][19]. The decays $\tilde{t} \to t\chi$ and $\tilde{t} \to b\chi W$ are kinematically not allowed at LEP2, otherwise they would be dominant.

As fig. 2.5(a) shows, the decay $\tilde{t} \to c\chi$ occurs through the FCNC processes possible only via loops, represented in the figure by the grey blob. Within the accepted hypothesis (1.68) and (1.69), this FCNC process is however strongly suppressed in the MSSM by the GIM mechanism as in the Standard Model. The width for the decay $\tilde{t} \to c\chi$ can be parametrized as

$$\Gamma_{\tilde{t}\to c\chi} = (0.3 \div 3) \times 10^{-10} \times m_{\tilde{t}} \left(1 - \frac{m_\chi^2}{m_{\tilde{t}}^2}\right)^2 \tag{2.20}$$

and it turns out to be quite small ($\sim 0.01 \div 10\,\text{eV}$) [24].

Fig. 2.5(b) shows the decay $\tilde{t} \to b\ell\tilde{\nu}$ that occurs by chargino exchange. Assuming that $\tilde{\nu}_e$, $\tilde{\nu}_\mu$, $\tilde{\nu}_\tau$ are degenerate in mass, the leptonic flavour of the final state depends only on the $\chi^\pm$ composition: if the $\widetilde{W}$ component is dominant $\tilde{t} \to be\tilde{\nu}_e$, $\tilde{t} \to b\mu\tilde{\nu}_\mu$, $\tilde{t} \to b\tau\tilde{\nu}_\tau$ are equal in probability. If the higgsino component is dominant the last one is favoured. The width of $\tilde{t} \to b\ell\tilde{\nu}$, parametrizable as

$$\Gamma_{\tilde{t}\to b\ell\tilde{\nu}} = (0.1 \div 10) \times 10^{-7} \times m_{\tilde{t}} \left(\frac{m_{\tilde{t}} m_W}{100\,\text{GeV} m_{\chi^\pm}}\right)^2, \tag{2.21}$$

is $\sim 0.1 \div 10\,\text{keV}$ [24], thus being dominant with respect to $\tilde{t} \to c\chi$ if kinematically allowed either in case of $\tilde{\nu}$ LSP either not. The experimental topology does not depend on the mass hierarchy between χ and $\tilde{\nu}$. The $\tilde{\nu}$ is not visible in an experimental apparatus but also an heavier $\tilde{\nu}$ decaying in $\chi\nu$ is not visible as well.

In the sbottom mass range within LEP2 reach, the dominant sbottom decay is $\tilde{b} \to b\chi$ since, differently from the stop, it occurs without loops (see fig. 2.5(c)). That results in a huge width, roughly given by

$$\Gamma_{\tilde{b}\to b\chi} = 10^{-3} \times m_{\tilde{b}} \left(1 - \frac{m_\chi^2}{m_{\tilde{b}}^2}\right)^2, \tag{2.22}$$

ranging between ~ 10 and $\sim 100\,\text{MeV}$.

The supersymmetric partner of the other lightest quarks that are supposed to be in the LEP2 reach has $\tilde{q} \to q\chi$ as the dominant decay mode. The width of these decays are similar to the $\tilde{b} \to b\chi$ decay.

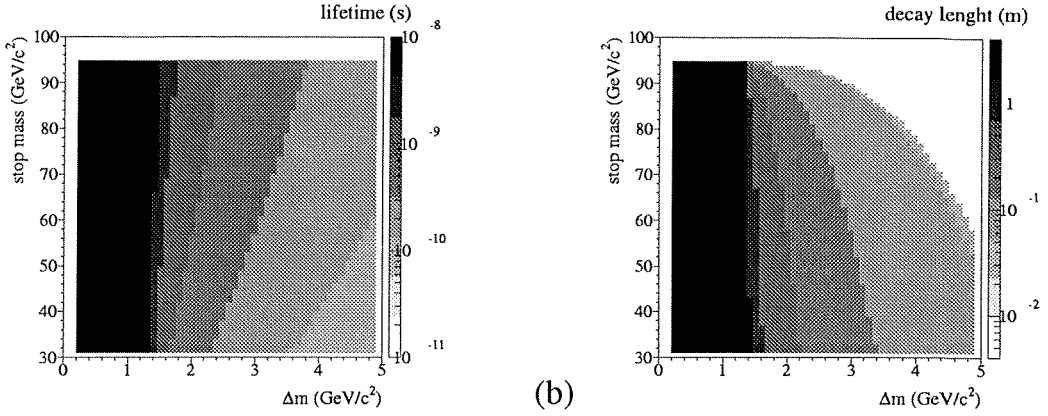

Figure 2.6: (a) The $\tilde{t}$ lifetime as a function of Δm; (b) the $\tilde{t}$ decay length for a couple of $\tilde{t}$ produced at $\sqrt{s} = 189\,\text{GeV}$.

Small Δm phenomenology

Assuming $\tilde{t} \to c\chi$ scenario, if Δm gets small enough the already small stop width reduces more and the stop acquires a sizeable lifetime yielding to decay lengths comparable to the detector dimensions. If the decay channel $\tilde{t} \to c\chi$ is kinematically closed, the dominant decay channel is $\tilde{t} \to u\chi$ and the stop has again a huge lifetime. In fact, also this process proceeds via FCNC loops and has a width much smaller with respect to $\tilde{t} \to c\chi$ since it involves the CKM elements connecting the third family with the first one. Fig. 2.6(a) shows the stop lifetime as a function of the stop mass and Δm. It has been obtained for 56° of stop mixing by using `MSMLIB` package [25] setting $\mu = -100\,\text{GeV}$, $M_2 = 250\,\text{GeV}$ and $\tan\beta = 1.5$. Fig. 2.6(b) shows the corresponding stop decay length λ for a stop energy equal to $\sqrt{s}/2$, being $\sqrt{s} = 189\,\text{GeV}$. From the figures one realizes that the decay lengths ranges between few microns to hundred of meters in the case of the decay $\tilde{t} \to u\chi$ for $\Delta m < m_c \sim 1.3\,\text{GeV}$. However these theoretical calculations are not accurate because of FCNC loops and they can be used only taking into account these big uncertainties.

RPV case

The decay has to occur via the same coupling causing the single production because of the prescription that only one can be dominant. The interesting vertices are again those proportional to λ'_{123} for sbottom decay and λ'_{132} for stop decay. RPV decays can be divided in two classes: *direct* decays and *indirect* or *cascade* decays.

In direct decays the sparticle decays directly in standard particles via the RPV vertex. In our case, the only possible stop direct decay is $\tilde{t} \to se^+$ (fig. 2.7(a)) via λ'_{132}. On the other hand, the Lagrangian term proportional to λ'_{123} allows sbottom to decay in the "charged" channel $\tilde{b} \to ce^-$ (fig. 2.7(b)) but also in the "neutral" channel $\tilde{b} \to s\nu_e$ (fig. 2.7(c)) due to the following vertex, not present in the up squark sector:

$$\lambda'_{123}\left[\tilde{b}^*_R \nu_{eL} s_L + h.c.\right]. \tag{2.23}$$

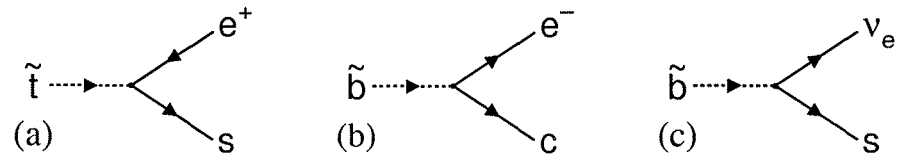

Figure 2.7: RPV direct decay channels: (a) $\tilde{t} \to e^+s$; (b) $\tilde{b} \to e^-c$; (c) $\tilde{b} \to \nu_e s$.

In cascade decays the true RPV decay occurs after that an intermediate state has been reached by an R-parity conserving decay. This is possible because many hypotheses usually assumed in the RPC case can be dropped. In RPV scenario it is no longer necessary to have a neutral LSP and the single production allows the exploration of the mass region above 180 GeV. Present limits on sparticle masses do not exclude that the chargino and/or the neutralino may be lighter than singly produced squark [26]. Considering R-parity conserving decays in charginos and neutralinos, several cascade decays are possible (fig. 2.8). It can be noticed that chargino and neutralino RPV decays occur via the same coupling of the production by means of a virtual $\tilde{t}$ or $\tilde{b}$.

2.3.3 Experimental topologies

The process $e^+e^- \to \tilde{q}\bar{\tilde{q}} \to q\bar{q}\chi\chi$ is characterized by two jets produced in the final state quark hadronization and by missing momentum and energy carried away by the not interacting $\chi\chi$ system (see fig. 2.9(a)). The two jets are not expected back-to-back since the missing momentum makes the event unbalanced. With respect to the $\tilde{t}$ searches, the sbottom searches profit of the b content of the two jets that can be used to greatly reject the backgrounds.

If the stop decays in $b\ell\tilde{\nu}$ is considered, the two jets plus missing momentum are accompanied by leptonic tracks as electron or muon ones or by typical τ systems (see fig. 2.9(b)).

The main characteristic of the RPC processes searches is the topology dependence on the $\Delta m = m_{\tilde{q}} - m_{LSP}$ mass difference. In fact Δm turns out to be roughly the visible energy in the event since the LSP leaves the apparatus undetected.

In the small Δm case the final state consist of stop hadron with consistent lifetimes. If the hadron might be considered stable with respect to the detector dimension, the stringent topology signature will be the ionization tracks of the stop hadron, characterised by a big

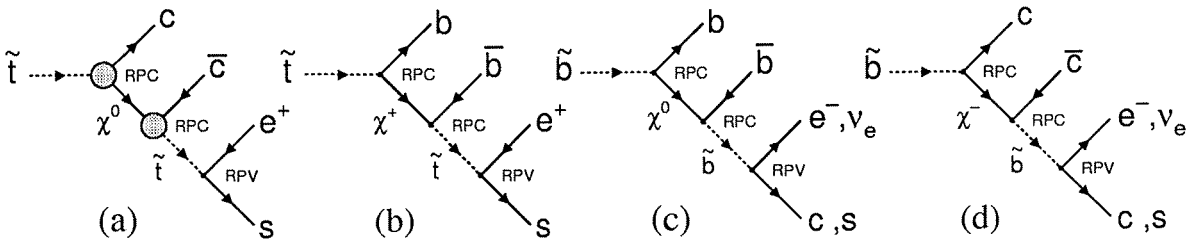

Figure 2.8: (a), (b) RPV cascade decays diagrams for the stop. (c), (d) RPV cascade decays diagrams for the sbottom.

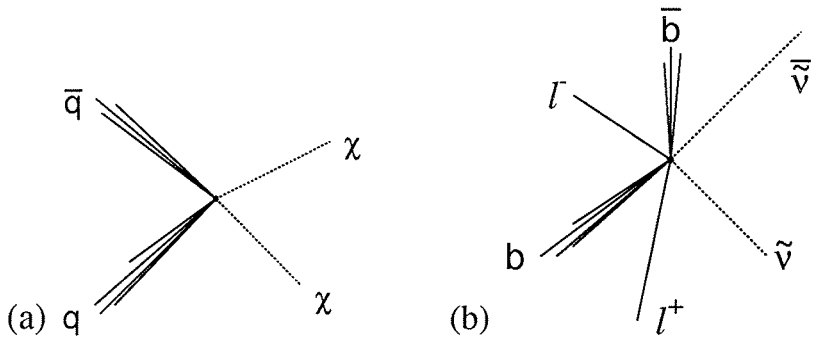

Figure 2.9: Topologies for squark double production: (a) $\tilde{q} \rightarrow q\chi$ decay channel and (b) $\tilde{t} \rightarrow b\ell\tilde{\nu}$ decay channel.

specific ionization loss. If the decay occurs inside the apparatus the signature is given by the decay product tracks not coming from the interaction point, plus kinks or secondary vertices.

The single production topologies depends on the squark decay. In both cascade and direct decays, the topology should allow a very good signal discrimination: if the squark decays directly, the events are characterised by one jet plus lepton ($\tilde{t} \rightarrow es$, $\tilde{b} \rightarrow ec$) or one jet and missing momentum ($\tilde{b} \rightarrow \nu s$). The topology in the cascade decay case yields to high multiplicity and many jets events that are well tagged because they are not typical of any Standard Model process. Energy deposits close to the beam axis are expected because both the scattered electron and the quark produced in the primary RPV vertex are directed at small angles.

2.4 Hadron collider searches

At a $p\bar{p}$ hadron collider the squarks can be produced in couple or individually produced in association with a gluino by the standard strong interaction processes between coloured particles. Two searches are under study at the TEVATRON experiments D0 and CDF: the light stop ($m_{\tilde{t}} < m_t$) search and the search for mass degenerate squarks. Moreover, the leptoquark searches results can be reinterpreted as squark searches in RPV case and will be discussed too.

Light stop

In this case the $\tilde{t}$ is assumed to be the lightest charged supersymmetric particle, the χ is the LSP while the gluino is very heavy. Within this scenario the stops are doubly produced by quark annihilation or gluon fusion. The cross section has strong interaction typical values ($\sim 100\,\text{pb}$ for $m_{\tilde{t}} \sim 65\,\text{GeV}/c^2$, $\sim 10\,\text{pb}$ for $m_{\tilde{t}} \sim 105\,\text{GeV}/c^2$). The $\tilde{t} \rightarrow c\chi$ is the decay channel considered. The overall process $p\bar{p} \rightarrow \tilde{t}\bar{\tilde{t}} + X \rightarrow c\bar{c}\chi\chi + X$ yields to a signature consisting in two acoplanar jets plus missing energy and momentum. The topology depends on the $\Delta m = m_{\tilde{t}} - m_\chi$ that roughly is the energy visible in the detectors. In order to reject the minimum bias events the transverse energy is required greater than $\sim 35\,\text{GeV}$.

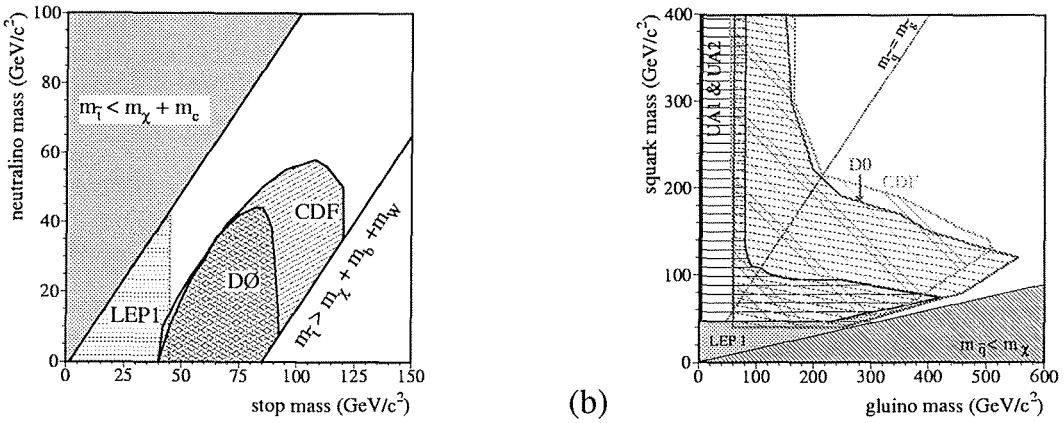

Figure 2.10: (a) Excluded region in the plane $(m_{\mathrm{t}}, m_{\chi})$ from LEP1, D0 and CDF. The regions in the left-top corner and in the right-bottom corner are not kinematically allowed for the $\tilde{\mathrm{t}} \rightarrow \mathrm{c}\chi$ decay. (b) Excluded region in the plane $(m_{\tilde{\mathrm{q}}}, m_{\tilde{\mathrm{g}}})$ from UA1, UA2, LEP1, D0 and CDF. There is an unexcluded corridor at higher gluino masses for the squark mass close to m_{χ}.

This cut makes the sensitivity vanishing for $\Delta m < 35\,\mathrm{GeV}/c^2$. The main backgrounds come from multijets events with poor missing energy measurement and by vector boson production processes. There is no evidence of stop signal within the D0 and CDF analysed data sample [27][28]. Fig. 2.10(a) shows the 95 % C.L. limits on the stop mass versus the neutralino mass. The best limit is the CDF one: the stop mass is 95 % C.L. excluded up to $\sim 120\,\mathrm{GeV}/c^2$ but for $\Delta m > 35\,\mathrm{GeV}/c^2$. The LEP2 searches play a crucial role extending sensitivities for smaller Δm.

Squark and gluino searches

For this search all squarks other than the stop are assumed to be degenerate in mass. The main production mechanism is the strong elementary process between gluons and quarks resulting in final states of two squarks, two gluinos or one squark and one gluino. The sensitivity reaches squark and gluino masses up to $\sim 200\,\mathrm{GeV}/c^2$ and $\sim 300\,\mathrm{GeV}/c^2$ respectively since the cross section is still in the pb range. The decay chains of squarks and gluinos depend on the MSSM particle spectrum. If $m_{\tilde{\mathrm{q}}} > m_{\tilde{\mathrm{g}}}$ the squark decay is $\tilde{\mathrm{q}} \rightarrow \mathrm{q}\tilde{\mathrm{g}}$; then the gluino decays in quarks plus chargino or neutralino. If $m_{\tilde{\mathrm{q}}} < m_{\tilde{\mathrm{g}}}$ the gluino decay is $\tilde{\mathrm{g}} \rightarrow \tilde{\mathrm{q}}\mathrm{q}$, with the squark then decaying in quark plus chargino or neutralino. The end point of the decay chain is always the LSP. The experimental signature for any initial state $(\tilde{\mathrm{q}}\bar{\tilde{\mathrm{q}}}, \tilde{\mathrm{q}}\tilde{\mathrm{g}}, \tilde{\mathrm{g}}\tilde{\mathrm{g}})$ is transverse energy in multijets events plus leptons coming from the decay of charginos if any.

One realizes that the hadron collider are ideal to search for degenerate squarks since the cross section is huge. Nevertheless the experimental topology is not clean enough to cover the parameter region where the gluino mass is large and the squark mass is close to the neutralino mass, as shown by the TEVATRON result in fig. 2.10(b) [29][30].

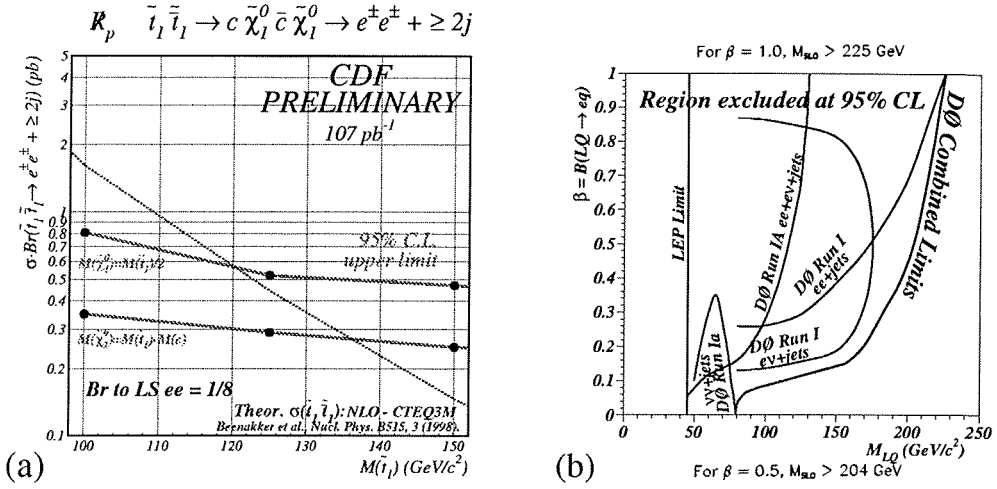

Figure 2.11: (a) CDF results for RPV stop indirect decays; (b) D0 limits on LQs for various topologies and their combination.

RPV squark searches

High-energy experimental limits on squarks in the RPV scenario have been already obtained at TEVATRON: CDF has analyses for squarks indirect decays [31] (see fig. 2.11(a)) and D0 results on scalar leptoquarks (LQs) decaying in electron and quark [32] (see fig. 2.11(b)) could be interpreted in terms of RPV squarks.

The leptoquark are scalar or vector quark-lepton bound states predicted within some unification theories. Their coupling to ordinary leptons and quarks is modeled by contact vertices like the ones coming from the RPV superpotential. Thus the scalar leptoquark is virtually equal to a squark from the production point of view. The main difference is in the decay modes: leptoquarks can only decay in the quark and lepton that bind to form the leptoquark itself, while in general a squark can decay directly in neutral or charged lepton plus quark or even indirectly by RPC processes.

Nevertheless the limits on leptoquarks production cross sections can be reinterpreted in terms of RPV squarks taking into account how the efficiencies and the excluded cross section rescales according to the various branching ratios. To do this the direct decay widths, depending on the RPV couplings, and the cascade decay widths, depending only on the RPC couplings, are considered and the limits rescaled accordingly. The D0 experiment is supposed to be completely unefficient for the cascade decays. The results of this rescaling can be seen in fig. 2.13.

2.5 Single production search feasibility study

The LEP experiments potential with respect to the squark single production has been studied in comparison with the TEVATRON collider experiments results on the same topic discussed in the previous section. In this section an outlook of this investigation is given referring to the single sbottom production as an example. In this study the MSSM model

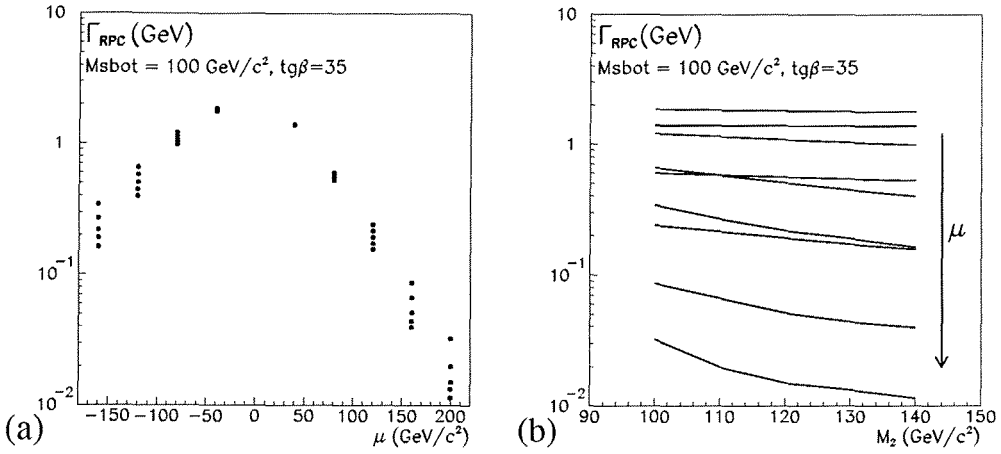

Figure 2.12: Cascade decay (RPC) width for a $\tilde{b}$ of 100 GeV/c^2 as a function of μ (a) and M_2 (b).

with the GUT relations is assumed.

LEP searches are competitive in the regions of the parameter space where cascade decays are dominant. In these channels hadronic collider experiments have a huge background and consequently rather weak limits. For that reasons the RPC squark width must be studied as a function of the MSSM parameter to look for MSSM parameters region where the cascade decay dominates. In fig. 2.12 the sbottom RPC width (i.e. the cascade decays width) is shown for various choices of the parameters. The computation has been done by using `MSMLIB`, the value of $\tan\beta$ being big enough to expect a light sbottom.

A selection to look for single production has necessarily to take into account both cascade decays as well direct decays and, with the large amount of data collected at high energy and assuming that no signal is recorded, it is reasonable to predict an upper limit of ~ 0.1 pb to be easily set on the sbottom single production cross section (see section 5.1 on the limit extraction from a search experiment).

In this hypothesis, the improvement on the upper limit for the λ coupling relative to the given process can be expressed as a function of SUSY parameters and compared with the TEVATRON results. As an example, two extreme scenarios are shown in fig. 2.13 for the sbottom case ($\lambda = \lambda'_{123}$). In the first case (fig. 2.13(a), $\mu = 40$ GeV/c^2) the improvement with respect to the TEVATRON-based limits is clearly visible. In the second case (fig. 2.13(b), $\mu = 200$ GeV/c^2) the cascade decays width where LEP is favoured is too small and obtainable limits are comparable with the TEVATRON ones. The parameter M_2 is chosen equal to 100 GeV/c^2 since the cascade width does not depend too much on M_2 (fig. 2.12(b)).

Even if some favoured regions have been discovered, one could ask if other analysis to search for RPV SUSY signals may have already explored these MSSM regions. In particular, very stringent limits come from the chargino and neutralinos RPV search that assumes their direct three body decays for a dominant λ' coupling [33]. The cross section excluded at 95% C.L. is shown in fig. 2.14.

This limit can be compared with the chargino and/or neutralino cross section predicted

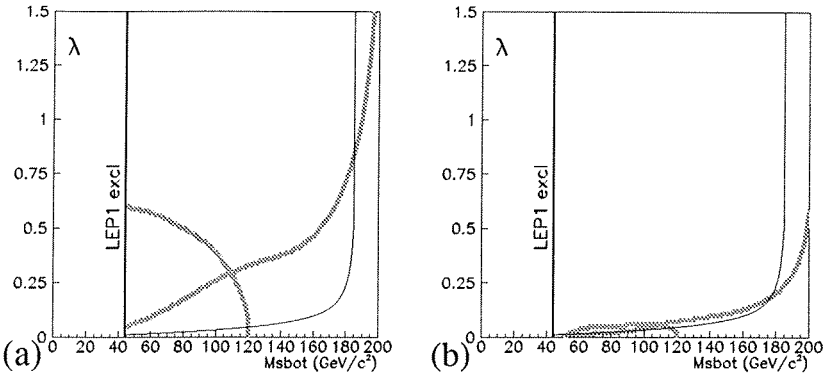

Figure 2.13: $\lambda = \lambda'_{123}$ limits as a function of $M_{\tilde{b}}$ (solid line) assuming an upper limit on the cross section of 0.1pb for singly produced $\tilde{b}$: $\mu = 40$ GeV/c^2 and $M_2 = 100$ GeV/c^2 in (a), $\mu = 200$ GeV/c^2 and $M_2 = 100$ GeV/c^2 in (b). Gray lines represent TEVATRON based limits on direct decays (excluded regions at big λ) and on cascade decays (excluded regions at small λ).

by the MSSM model in the parameter region where squark cascade decays dominate and thus LEP is competitive with TEVATRON. The comparison shows that these MSSM regions are already excluded by the chargino and neutralino direct searches in the RPV scenario. This could be expected since the cascade decays dominate if the chargino or the neutralino are light enough, but the small mass regions are easily excluded from a direct search. Said differently, the MSSM regions not excluded by the direct search of chargino and neutralino are characterized by a dominant squark direct decay.

The conclusion of this study is that LEP is not competitive with TEVATRON in the not excluded MSSM regions with respect to the single squark production search. As a consequence of that it has been decided to not proceed further on this topic.

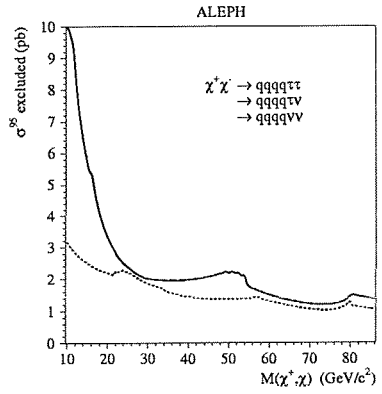

Figure 2.14: The 95 % c.l. limit on the χ or $\chi^{\pm}$ cross section (at $\sqrt{s} = 172\,\mathrm{GeV}/c^2$) for direct decays of χ or $\chi^{\pm}$ and a non-zero coupling λ'. The dashed line corresponds to the most favourable chargino branching ratio, while the solid line corresponds to the worst case branching ratio. The latter is used in the feasibility study.

2.6 Background processes at LEP2

The expected background processes are very similar in all considered RPC topologies since missing momentum is a common feature. Moreover the expected leptons not always are identified as such. Typically the dangerous Standard Model processes produce events with hadronic final states with undetected particles.

Above the Z resonance energy the processes are mainly $\gamma\gamma$ events, double fermion production and four fermion production. Among these the most important are the ones where one or more vector boson are produced as $e^+e^- \to WW$ (fig. 2.15(c)), $e^+e^- \to We\nu$ (fig. 2.15(e)), $e^+e^- \to ZZ(\gamma^*)$ (fig. 2.15(d)) and $e^+e^- \to Zee$ (fig. 2.15(f)). Their cross sections are shown in fig. 2.16. It can be noticed that the $e^+e^- \to f\bar{f}$ process (fig. 2.15(b)) with a Z exchanged in the s-channel is substantially enhanced by the initial state radiation that yields the radiative return of the Z resonance. Anyhow, the total cross section is dominated by the $\gamma\gamma \to f\bar{f}$ process (fig. 2.15(a)) [23].

The process $e^+e^- \to WW$ can appear like the squark signal when one of the two W decays hadronically while the other decays leptonically; the neutrino carries away momentum and the lepton not always is identified. Moreover both W could decay in $\tau\nu$. If one τ then decays hadronically the event topology is very similar to the expected squark one. If both W decay leptonically the topology could be more similar to $\tilde{t} \to b\ell\nu$ topology. Similar behaviour can be found in the process $e^+e^- \to ZZ(\gamma^*)$ if the Z decays in neutrinos and the Z/γ decays hadronically, or if they decay both in τ. The process $e^+e^- \to We\nu_e$ is a background source since the missing momentum is due not only to the neutrino but also to the electron that tends to go at very small polar angle were normally the detectors are not sensitive. The $\gamma\gamma$ events yield naturally to large missing momentum since the produced particles often escape detection since they are produced at very small polar angle. If the event is of the type $\gamma\gamma \to q\bar{q}$, the quarks hadronize into two low energy jets and the event is very similar to a $e^+e^- \to \tilde{q}\bar{\tilde{q}} \to \chi\chi q\bar{q}$. The same could happen for $\gamma\gamma \to \tau^+\tau^-$.

The main background process for the stable stop hadron ($\widetilde{T}$) signal comes from dimuon events. They are quite similar to the signal events especially when the $\widetilde{T}$ has the mass value for which the specific ionization losses is very close to the muon one (see section 5.5).

On the other hand, in case of the stop hadron decaying in the sensitive volume there are no standard model process that could resemble the signal. In general, the possible backgrounds may come from any type of events, not necessarily related to an e^+e^- collision, where tracks not coming from the interaction point are produced. Among these there are events like: cosmic ray tracks recorded together a e^+e^- collision, photon conversion and charged tracks undergoing multiple scattering. Also spurious events due to the machine background (like beam-gas collisions) could yield to tracks not coming from the interaction point.

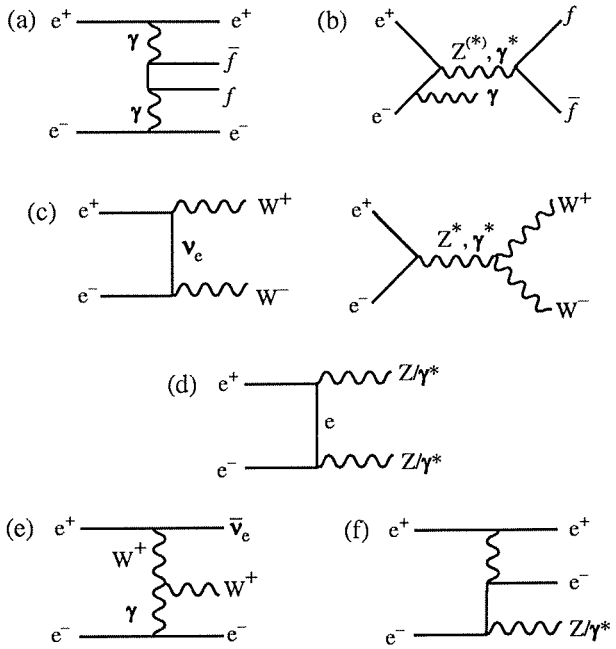

Figure 2.15: Diagrams contributing to Standard Model background processes: (a) two-photon, (b) $q\bar{q}(\gamma)$, (c) W pair production, (d) Z/γ pair production, (e) single W production and (f) single Z production.

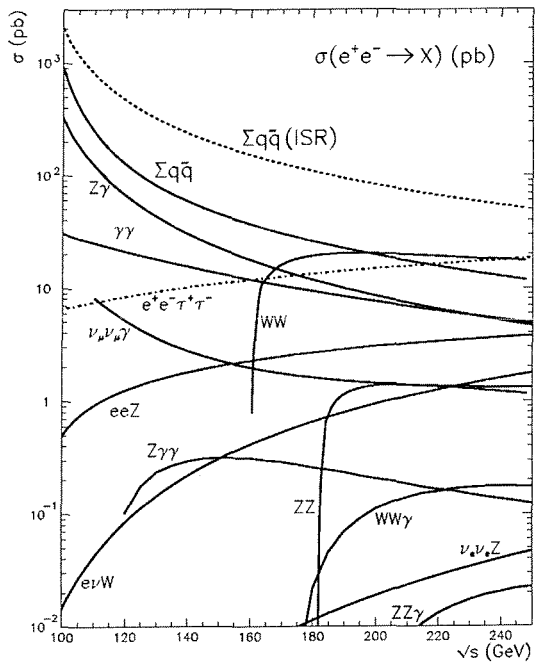

Figure 2.16: Standard Model background processes cross sections versus the LEP center of mass energy.

3 The LEP collider and the ALEPH experiment

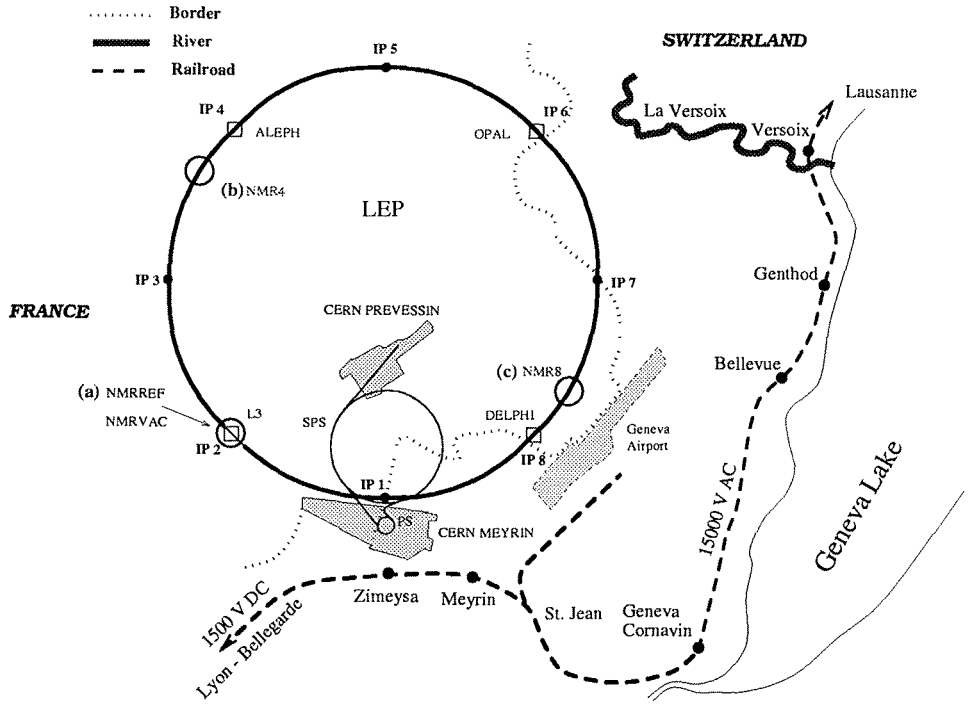

Figure 3.1: LEP ring and Geneva area.

3.1 LEP

The *Large Electron-Positron collider* or *LEP* is the world's largest circular e^+e^- collider. It is part of the accelerator complex of CERN, European laboratory of Particle Physics, located in Geneve (see fig. 3.1). LEP is fully described elsewhere [34][35], only a brief summary is given here.

LEP is located in a $\sim$ 27 km underground circular tunnel. To minimize the depth and the difficult excavation in the stone the ring has a slope of 1.4° with respect to the horizontal plane, being higher nearby the Jura mountains. Nevertheless the depth varies between $\sim$ 50 m and $\sim$ 150 m. The vacuum tube where the beams flow, known as *beam pipe*, has a polygonal shape made up by eight 500 m long linear sections connected by eight circular sectors having a radius of curvature of 3.3 km. The overall length is 26658 m.

The LEP accelerator follows a chain of four smaller accelerators that makes up the LEP injector system. All the complex is sketched in fig. 3.2. The LPI - Lepton Pre-Injector complex is made up by a linear accelerator, LIL and by the electron-positron accumulator, EPA. The LEP Injector Linacs (LIL) produce and accelerate electrons to 600 MeV. Deriving from the first LIL section a high current 200 MeV electron beam that strikes a tungsten target, positrons are produced and then accelerated up to 600 MeV from the second section of LIL. Both electrons and positrons are injected into the electron-positron accumulator, EPA, which serves as a buffer before the following stages. The beams are then transferred to the PS, Proton Synchrotron, operating as a 3.5 GeV e^+e^- synchrotron. The PS then injects into the CERN Super Proton Synchrotron (SPS), which operates as a 23 GeV e^+e^- injector for LEP that finally completes the acceleration up to the requested energy. The entire preparation of the beams inside LEP by using all the auxiliary accelerators is known as *filling*. It usually lasts from 30 minutes to 1 hour. In order to serve LEP, both PS and

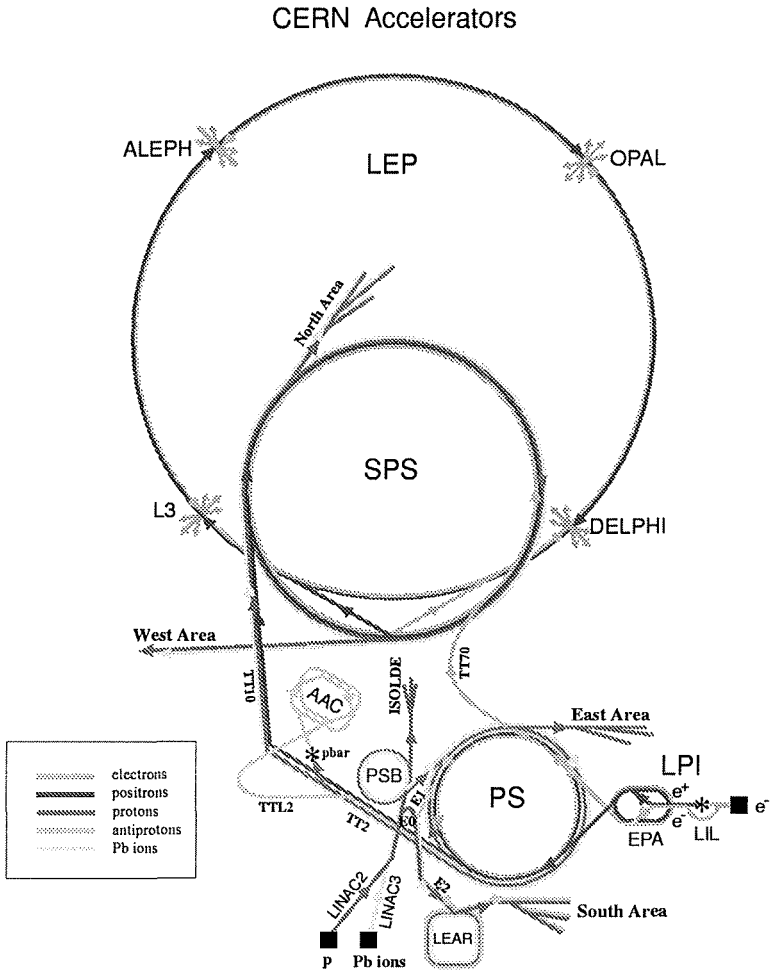

LEP: Large Electron Positron collider
SPS: Super Proton Synchrotron
AAC: Antiproton Accumulator Complex
ISOLDE: Isotope Separator OnLine DEvice
PSB: Proton Synchrotron Booster
PS: Proton Synchrotron
LPI: Lep Pre-Injector
EPA: Electron Positron Accumulator
LIL: Lep Injector Linac
LINAC: LINear ACcelerator
LEAR: Low Energy Antiproton Ring

Figure 3.2: CERN accelerator complex (dimensions are not in scale!).

SPS operate in multicycle mode: every four cycles of lepton acceleration a cycle of proton acceleration follows allowing PS and SPS to provide high energy protons (up to 450 GeV) for fixed target physics [36].

Leptons are injected in LEP grouped in bunches of $\sim 5 \cdot 10^{11}$ particles. The electron bunches and the positron bunches circulate in opposite directions. In the curved section of LEP are installed the dipole magnets to bend the beam and define the orbits of electron and positrons that, anyhow, run in the same vacuum tube. Due to the bending, the particles lose energy by synchrotron radiation. The energy loss, that is the radiated energy, is proportional to E^4/r, being E the particle energy and r the bending radius. This is the reason of the huge LEP radius. Several radio frequency (RF) cavities supply the energy for the acceleration as well as for the compensation of these losses.

While LEP is accelerating, the beams are kept separated by electrostatic separators. A system of quadrupole magnets focuses the beams and prepare the optimal transversal adjustment. As soon as the target energy is reached, electrostatic separators are closed making the bunches colliding in four of the eight straight sections. Four experiments surround the interaction points. These are ALEPH, DELPHI [37], L3 [38] and OPAL [39].

During its first phase (LEP1) from 1989 to 1995, LEP operated successfully at a center of mass energy $\sqrt{s} \sim 91.2$ GeV to allow high statistics studies of the Z resonance. During this phase the relatively small amount of energy loss due to synchrotron radiation (~ 100 MeV per turn, per electron) allowed standard RF cavities to be used. The LEP second phase, LEP2, has been characterized by the gradual increase of the energy up to ~ 100 GeV per beam. This goal needed the introduction of extra accelerating gradients to be reached. In fact the energy loss for a 100 GeV electron is > 2800 MeV per turn. Since 1995, all the 128 standard RF cavities had been gradually replaced by more powerful superconducting (SC) cavities. With the SC cavities a mean field intensity of 7 MV/m can reached to be compared with the $\sim$ 1.5 MV/m mean value of the standard ones. In late 1995, 68 GeV per beam were reached with 56 new SC cavities. Other 84 were installed the year after and 87 GeV per beam were reached. During 1997 91.5 GeV per beam were reached profiting of extra 84 SC cavities. Other 48 were installed in 1998 reaching 94 GeV per beam and finally the installation of the last 16 cavities (no more free space was physically available in the LEP ring) made possible to run at ~ 100 GeV per beam for mostly 1999.

During phase 1, LEP operated in either a *bunch* mode with four equidistant bunches per beam (collision every 22 μs) or following a *pretzel* scheme which allows eight bunches per beam [40] (collision every 11 μs). For the phase 2, also a *bunch train* configuration of the circulating beams was experimented in order to increase the performances. In this configuration, each beam contains four equidistant trains, each consisting of up to four bunches of leptons [41] (collision every 22 μs). Nevertheless LEP is actually operating in four bunches mode.

The *instantaneous luminosity* $L(t)$ is one of the most important LEP parameters and it is defined as:

$$L(t) = \frac{N_{e^+} N_{e^-} n_{\text{bunch}} n_{\text{train}} f}{4\pi s_x s_y}, \tag{3.1}$$

where N_{e^+} and N_{e^-} are the number of e^+ and e^- per bunch, n_{bunch} is the number of bunches per train, n_{train} is the number of trains per beam, f is the revolution frequency and s_x and s_y are the RMS bunches sizes in the x and y directions at the interaction point. The bunch

measures $\sim$ 10 μm in height, $\sim$ 1 cm in length and $\sim$ 150 μm in width but only close to the interaction points where special superconducting magnet, known as *low-β*, are used to squeeze the beam to increase the luminosity.

The instantaneous luminosity has to be high as possible since on it depends the rate of events potentially visible from the experiments. The rate dn/dt of events involving interesting processes, being σ the cross section, is:

$$\frac{dN}{dt} = \sigma L(t). \tag{3.2}$$

Typical values for the phase 2 luminosity sit around $\sim 10^{31}$ cm^{-2}s^{-1}. Once the expression (3.2) is integrated over the time we get

$$N = \sigma \int L(t)dt = \sigma \mathcal{L}, \tag{3.3}$$

where N is the total amount of events produced for that process and $\mathcal{L}$, called *integrated luminosity*, is expressed in units of an inverse cross section, i.e. pb^{-1}.

The instantaneous luminosity becomes worse with time due to normal beams interactions and other effects like spurious interactions with residual gas molecules in the pipe. When the instantaneous luminosity gets too low, the beams are dumped and the filling procedure starts again.

To reduce beam-gas collisions an extreme vacuum ($\sim 8 \times 10^{-12}$torr) is made in the pipe but there is a pressure increase up to $\sim 9 \times 10^{-9}$torr because atoms of the beam pipe walls are extracted by the synchrotron radiation.

The beam pipe is an aluminium tube, with an elliptical cross section, internally coated with lead. In correspondence with the interactions points the pipe is cylindrical and made in beryllium, a low density and small atomic number material, in order to minimize the interaction probability with the particles produced in the collision.

One of the powerful features of LEP is the very high accuracy which can be achieved in the beam energy determination. This is mandatory to perform high precision experiments. During phase 1 the method based on resonant spin depolarization (RD method) has been successfully applied together with traditional magnetic field measurements providing the beam energy value with an accuracy better than 1 MeV [42]. The RD method profits the natural build-up of the beam transverse polarization [43]. The spin precession frequency, measurable applying a magnetic RF radial field, is proportional to the beam energy. Unfortunately, there are many polarization destroying effects whose strength increases with the squared beam energy, and, at LEP2 energy, has been found impossible to apply RD method [44]. Phase 2 LEP operation profits of a new extrapolation method [45][46][47]. Partially polarized beams of $45 \div 60$ GeV are first circulated in LEP to allow a RD method measurement. The beams are then accelerated to the higher LEP2 energies and the energy increment with respect to RD value is computed from the change in magnetic field strength. The accuracy is 30 MeV. During 1999 a dedicated spectrometer has been installed to increase the extrapolation accuracy. The operating principle is to measure the angular deviations from the nominal deflection of a precisely mapped dipole while ramping from RD energy value to the final energy value [47][48]. Results from this new technique are not available yet.

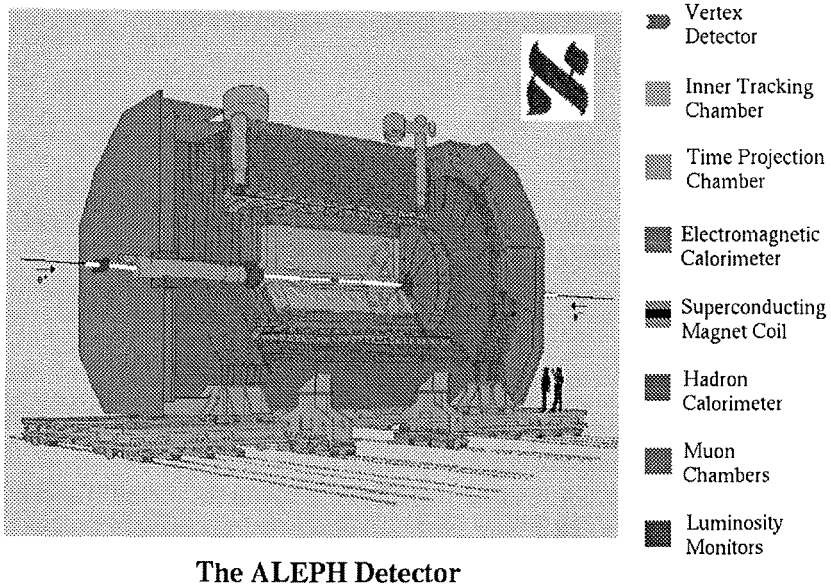

Figure 3.3: Overview of the ALEPH detector.

A variety of environmental phenomena affects the energy in the machine and are taken into account. For example the orbit deformations due to lunar and terrestrial tides [42][49], the amount of rainfall as well the underground water level [50], parasitic currents in the LEP beam pipe caused by the TGV trains passing nearby [51] (see fig. 3.1) and some more obvious effects due to temperature and humidity on dipole magnetic fields [45].

3.2 The ALEPH detector

ALEPH (*Apparatus for LEp PHysics*) is one of the four multi-purpose experiments installed on the LEP ring. It consists of a $\sim$ 1000m^3 volume of instrumented sensitive material surrounding with high hermeticity the LEP collision point nr.4. An overall view of the detector is visible in fig. 3.3.

In this section the ALEPH detector will be briefly described. Full description can be found in [52][53]. A detailed discussion of its performances can be found in [54].

The origin of the ALEPH detector coordinate system coincides with the nominal interaction point where the two beams collide. The actual interaction point depends on LEP orbits and it is determined event by event using the tracks. The z axis is defined to be the nominal direction of e^+; the x axis is the horizontal line pointing the centre of LEP and the y axis points upward, orthogonal to xz plane. Often a standard system of cylindrical coordinates (z, θ, ϕ) is used.

ALEPH is made up of a number of subdetectors generally having cylindrical structure coaxial with the beam axis and symmetrically located with respect to the nominal interaction point. These subdetectors form two subsystems that are complementary with respect to the purpose: the inner one, known as *tracking system*, is mainly devoted to record the trajectories of the charged particles; being immersed in a huge magnetic field the curvature

of the trajectory let us know the charged particles momentum and charge. The outer subsystem is made up of devices known as *calorimeters*, designed to identify the particles and to measure their energy.

The philosophy underlying these two subsystem is substantially different: the tracking devices have to be as much transparent as possible in order to minimize the influence on the particle motion. Hence the sensitive materials are gases or very thin layers of high density materials. On the other hand, the calorimeters perform a destructive measurement on the particle that, being completely stopped in their volume, deposits all its energy which becomes easily measurable. Hence calorimeters are made up of big and compact volumes of high density materials. The sensor instrumentation, however, must have a good geometrical resolution for a reliable reconstruction of the particle direction and also to record the shape of the energy deposit that, depending on the kind of the particle, is very useful for its identification.

The ALEPH apparatus is made up by the following subdetectors, listed from the inner one to the outer one. The tracking subdetectors are:

- **VDET**, *Vertex DETector*;
- **ITC**, *Inner Tracking Chamber*;
- **TPC**, *Time Projection Chamber*;

then we find the calorimeter devices:

- **ECAL**, *Electromagnetic CALorimeter*;
- **HCAL**, *Hadronic CALorimeter*.

The outermost layer of the apparatus is made up by the *Muon Chambers* used to provide extra informations on the trajectory of muons tha are not stopped by the innermost detectors. The coil of the superconducting magnet is located between the two calorimeters.

Very close to the beam pipe, ± 2.5 m far from the interaction point a number of small calorimeters, known as *luminosity monitors*, are used to measure the luminosity trough the rate of *Bhabha scattering* ($e^+e^- \rightarrow \gamma \rightarrow e^+e^-$) processes which cross section is very well known.

3.2.1 The Vertex DETector, VDET

The silicon microstrip Vertex DETector (VDET) is the tracking device closest to the beam pipe. This favourable location together with the very high precision in measuring charged particle trajectory allows a powerful identification of long living hadrons (with typical lifetimes of few ps) containing b and c quarks.

From late 1995 the ALEPH VDET was upgraded to cope with improved performances requested by LEP2 physics, Higgs searches in particular. The new VDET is here described; it is twice as long as the previous one, features new radiation-hard readout chips and have a new arrangement of the electronics in order to minimize the amount of passive materials in the active region. A discussion of the performances of both VDET can be found in [55] and [56] for old version and new version respectively.

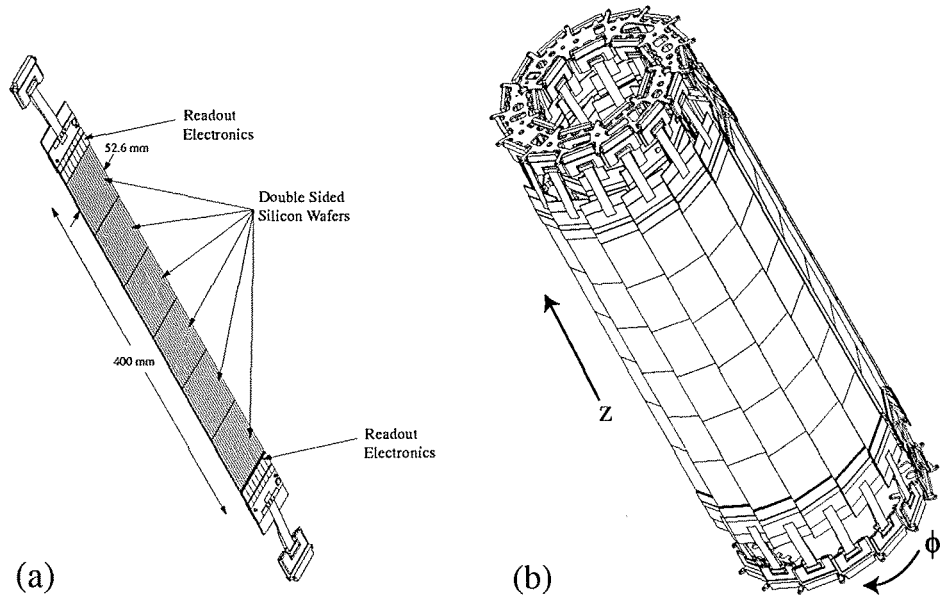

Figure 3.4: (a); view of a VDET face seen from the junction side of wafers. (b); VDET overall view.

The VDET has an active length of $\sim$ 39 cm (at least one hit if the track has $|\cos\theta| < 0.95$) and consists of two concentric cylindrical layers of 144 double-sided micro-strip silicon detectors. Each silicon detector is a 300 μm thick wafer of n-type silicon and measures 52.6 mm $\times$ 65.4 mm. To work as a particle detector the silicon is operated as a reverse biased diode. The p^+ (*junction*) electrode of the diode is divided in 2041 strips (12 μm wide, 25 μm pitch) parallel to the long side of the wafer. The n^+ (*ohmic*) electrode is divided in 1280 (12 μm wide, 50 μm pitch) strips parallel to the short side of the wafer. Between each n^+ strip and the closest one there is p^+ strip, known as blocking strip, needed to remove the charge accumulation at the Si/SiO_2 interface that, having a low resistivity, would make unuseful the segmentation. Since the n-type bulk is chosen to have a fairly high resistivity ($>$ 4KΩ cm), a reverse bias voltage $<$ 80V depletes completely the bulk; a charged particle, traversing the bulk, generates electron-hole pairs, about 2.4×10^4 for a minimum ionizing particle (MIP). In the depleted silicon the concentration of thermal generated carriers is small, thus the drifting under electric fields of the carriers from the ionization builds up a measurable signal on the closest strips.

Six silicon wafers are glued together and instrumented with readout electronics on each end to form the VDET elementary unit, known as *face* (see fig. 3.4(a)). The inner layer ($\sim$ 6.3 cm radius) is formed by 9 faces and it is close as much as possible to the beryllium beam pipe ($\sim$ 5.3 cm radius). The outer layer ($\sim$ 10.5 cm radius) consists of 15 faces and is close as much as possible to the ITC inner radius ($\sim$ 12.8 cm radius) in order to maximize the lever arm. Adjacent faces in each layer are arranged to overlap $\sim$ 0.2 cm in the $r\phi$ view. An overall view of VDET is visible in fig. 3.4(b). The strips on the junction side run parallel to the z axis in the ALEPH reference system, allowing $r\phi$ coordinate measurement; ohmic side strips, running normal to the z axis, allow z coordinate measurement. To reduce the

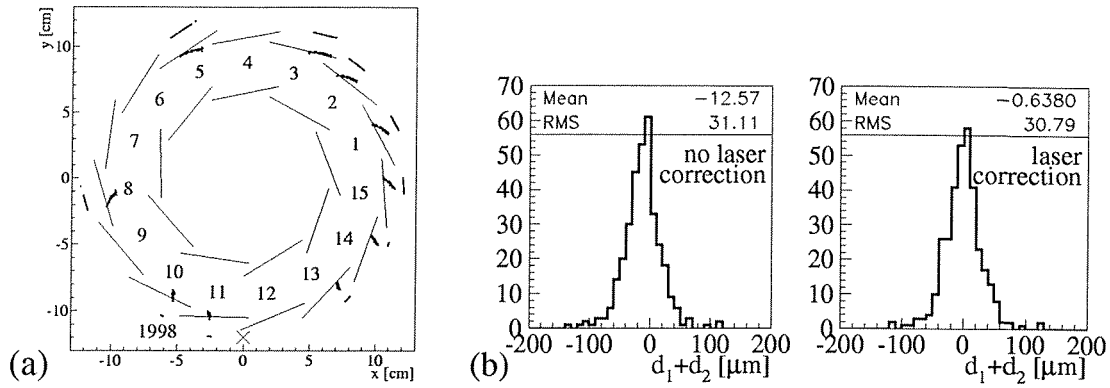

Figure 3.5: 1998 VDET laser system results: (a) reconstructed $z \sim +20$ cm spots: the dots represent the spot position during time. The displacement is amplified by a factor of 1000. The small segments, plotted outside the outer layer, are the actual raw deviations of the corresponding spot (same magnification). The cross is the probable rotation centre. (b) Distribution of sum of impact parameters of the two tracks in dimuon events for final calibration run before and after laser correction to the alignment.

number of readout channels only every second junction p^+ and ohmic n^+ strips is connected to readout electronics. Thus the readout pitch is 50 μm in $r\phi$ view and 100 μm in the z view. Using a center-of-gravity algorithm over the group of close strips collecting the ionization signal (*cluster*), the particle impact position is reconstructed with a resolution of ~ 10 μm in $r\phi$ and ~ 15 μm in z. The independent $r\phi$ and z measurements are combined offline by the event reconstruction in order to remove ambiguity and build track points candidates in the space.

Since the VDET intrinsic spatial resolution is fairly high, the position of each wafer with respect to the outer tracking devices have to be known with an accuracy comparable with the spatial resolution itself. Using a consistent sample of tracks from real physics events, it is possible to extract the 864 parameters (6 degrees of freedom $\times$ 144 wafers) by a complex fit procedure [57], known as *alignment*. During LEP2 physics, the VDET alignment is performed on a initial sample of events collected during a calibration run at the Z resonance because the standard high energy running suffers for the reduced event rate. Hence VDET features a laser system to monitor its mechanical stability with respect to the external tracker as a function of time. An optical system, fired every ~ 100 real physic events, produces several infrared laser spots uniformly distributed on the outer layer [58]. The position of the spot can be reconstructed as a charged particle impact position. The long term analysis of the 1997, 1998 and 1999 laser system data shows an unexpected global displacement of the VDET. This is compatible with a rigid rotation around one of the support brackets of about $\sim 10^{-4}$rad over the 6–7 months of data taking, that is a maximum local displacement of $\sim 20\mu$m (see fig. 3.5(a)). The origin is still unknown. A time-dependent laser-based correction has been applied to data; the effect of such a correction is visible on the impact parameter[1] distributions. In fig. 3.5(b) is clearly visible how the corrected distribution of the sum of impact parameters in dimuon events has a mean value compatible with zero as

[1]See section 3.3.1 for the definition of impact parameter.

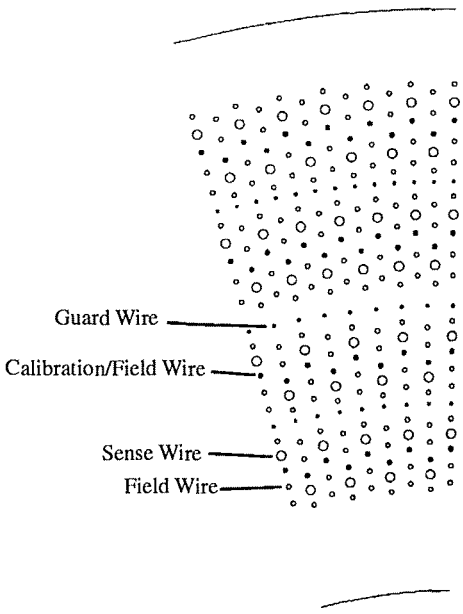

Figure 3.6: Detail of the ITC endplate with the position of the support holes for the wires.

expected, while the not corrected distribution shows a significant shift.

3.2.2 The Inner Tracking Chamber, ITC

The ITC, Inner Tracking Chamber, is a cylindrical multi-wire drift chamber serving a dual purpose in ALEPH. It provides up to 8 accurate $r\phi$ points for tracking in the radial region between 160 mm and 260 mm (i.e. track with $|\cos\theta| < 0.97$) and it provides the only tracking information for the Level-1 trigger (see subsection 3.2.9). The ITC active length is about 2 m and its inner and outer radii are 12.8 cm and 28.8 cm respectively. The chamber operates with a gas mixture of 80% argon and 20% CO_2 at the atmospheric pressure. The charges left in the volume by the ionization of a charged particle are collected by a number of gold-plated tungsten sense wires, 30 μm in diameter, that run parallel to the z axis. These wires are arranged in four concentric inner layers, made up of 96 wires each, and other four outer layers, made up of 144 wires each. Six gold-plated aluminium field wires, 147 μm in diameter, are arranged around each sense wire defining a drift cell hexagonal in the xy cross section. Four of these six wires are shared by neighbouring cells in the same layer. The sense wires are kept at $1.8 \div 2.0$kV with respect to the grounded field wires. In this configuration, the signal gain due to avalanche mechanism close to the sense wire sits around $\sim 1 \div 5 \times 10^4$. One field wire per cell can be used also to inject calibration pulses. Moreover there is a system of guard wires (copper/beryllium wires, 120 μm in diameter) that support 51 hoops of 147 μm aluminium wires. The purpose of this cage is to catch any wires that might break in order to minimize the possible damage. In fig. 3.6 is visible a detail of the ITC end-plate with the the xy plug position of the various wires.

By the drift time inside the single cell the $r\phi$ coordinates are determined with an accuracy of ~ 150 μm. The half-cell offset between the drift cells of two adjacent layers makes possible

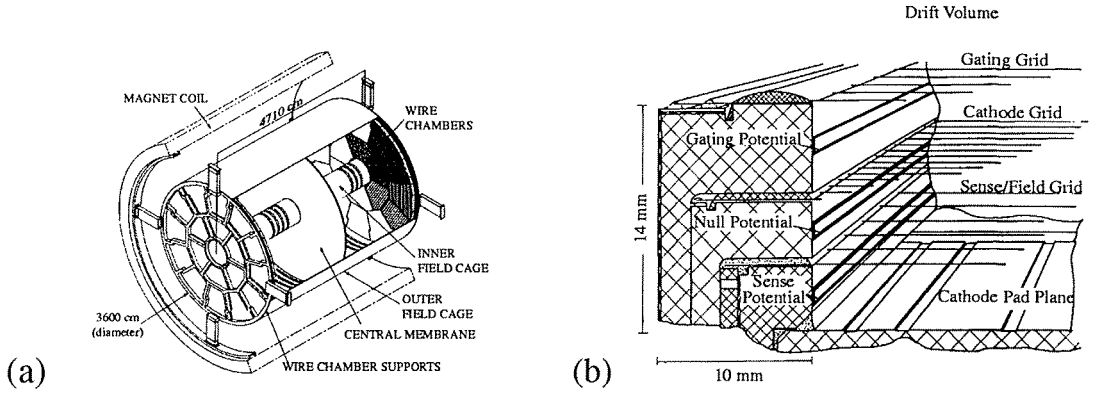

Figure 3.7: The TPC: (a) an overall cut-away view; (b) detail of a sector multi-wire proportional counter.

to resolve the left-right track ambiguities with respect to the single sense wire. The size of the cell, that measures $4.7 \div 6.5$ mm, has been optimized to keep the drift time small enough to quickly provide to the trigger a raw $r\phi$ tracking information, that in fact is available within 1 μs from the beam crossing. The z coordinate is measured with a precision of $\sim$ 5 cm from the difference in arrival times of pulses at the two ends of each sense wire. Also the z coordinate contributes to the trigger since a 3D tracking info is submitted within $2 \div 3$ μs.

3.2.3 The Time Projection Chamber, TPC

The Time Projection Chamber, TPC, is an imaging drift cylindrical chamber coaxial with the beam axis, 4.4 m long, which external and internal diameters are 3.6 m and 0.6 m. It provides 3D points for track reconstruction.

The sensitive volume, filled with argon (91%) and methane (9%) at $8 \div 12$mbar above the atmospheric pressure, is divided into two half-detectors by the disc-shaped membrane (graphite coated, 25 μm thick mylar) located at the mid-point, parallel to the xy plane. The membrane is kept at -27 kV with respect to the grounded endplates to build a 11.5 kV/m electric field parallel to the beam axis. The inner and outer cylinders behave as *field cages* supporting a series of ring-shaped electrodes (made of $\sim$ 10.2 mm wide copper strip) suitable biased to shape the electric field and reduce border effects. The TPC is visible in fig. 3.7(a).

The electrons left in the volume by charged particles ionization move towards the endplates at 5.2 cm/ μm. To record their signal the endplates are equipped with 18 sectors of multi-wire proportional chambers. Each sector is a "sandwich" of 3 planes of wires over a cathode plane. In fig. 3.7(b) a sector detail is shown: the first plane, closest to the drift volume, is the gating grid consisting of 76 μm diameter copper wires, 2 mm spaced. The second plane, 6 mm behind the gating grid, is cathode grid consisting of 76 μm copper wires, 1 mm spaced. The cathode grid is at null potential. The third plane, 4 mm behind the cathode grid, is the sense/field grid. It is made by a plane of 4 mm spaced field wires (127 μm gold-plated copper) biased at null potential, interleaved with a plane of 4 mm spaced sense wires (20 μm gold-plated tungsten) biased at $\sim$ 1.3 kV. The cathode plane, 4 mm behind the

sense/field grid, is divided in pads ($r\Delta\phi = 6.2$ mm, $\Delta\phi = 30$ mm) with a pitch of 6.7 mm in azimuth. A number of long circular *trigger pads* ($\Delta\phi \sim 15°$, $\Delta r = 6.3$ mm) divide each row of standard pads and are used for the Level-2 trigger.

The gating grid, made up by 76 μm copper wires, is necessary to prevent the ions generated in the avalanche from entering the drift volume. When the gating grid is "closed" a grid wire is at $-67 + 100$ V while the next one is at $-67 - 100$ V. Thus there is 200 V potential difference between adjacent wires. The ions move towards the negative biased wires and do not enter the drift volume. The same mechanism would prevent also drift electrons to reach the sense grid. So, from 3 μm before the beam crossing the gate grid is "open", i.e. all grid wires are at -67 V. If the Level-1 trigger is positive the gate is left open for the maximum drift time within the TPC, i.e. ~ 45 μs.

Only the ~ 6000 sense wires and the ~ 40000 cathode pads are readout to record the electron signal amplified by the avalanche mechanism. A charged particle trajectory can produce a signal on a maximum of 21 pad rows and 338 sense wire. The $r\phi$ coordinate is obtained with 180 μm accuracy interpolating the signals from the cathode pads. Thanks to the magnetic field the drift electron trajectory is an helix, thus the diffusion effects that would degrade the $r\phi$ resolution are reduced. The z coordinate is known with a resolution of 800 μm measuring the drift time either from sense wires and from cathode pads too.

Also the TPC features a calibration laser system. Thirty straight ionization tracks are created in the TPC volume firing a couple of Nd-YAG ultraviolet lasers. Drift velocity and distortions can be measured.

Measurement of dE/dx

The TPC is also used to measure the specific ionization energy loss of charged particles to help their identification. The ionization produced in the drift volume is measured by the sense wires and the pads in the end plates giving a total of ~ 350 samples of the particle energy loss. Hits are associated with the fitted TPC tracks using a window in drift time around the projected helix position and discarding individual pulses which match more than a single track. Sensitivity to threshold fluctuations and to Landau tails is reduced by discarding respectively the lowest 8% and the highest 40% of the pulses before making the average. The dE/dx is calibrated directly on data with minimum-ionizing pions with momentum between 0.3 GeV/c^2 and 0.6 GeV/c^2: the normalization is fixed such that they have $\langle \mathrm{dE/dx} \rangle \equiv 1$.

The wire and pad resolution is expressed in the form

$$\sigma_I = \sigma_0 N^{p_1} (l/N)^{p_2} (I/I_0)^{p_3}, \tag{3.4}$$

where N is the number of hits, l/N is the useful track length seen by one pad or wire, I is the measured dE/dx and $I_0 \equiv 1$, being the specific ionization loss at minimum. From data the constants are $\sigma_0 \sim 1.19$, $p_1 \sim -0.5$, $p_2 \sim p_3 \sim -0.4$ for wire measurements [54] and $\sigma_0 \sim 1.0$, $p_1 \sim -0.5$, $p_2 \sim -0.2$ and $p_3 \sim -0.3$ for pads [59].

The specific ionization R_I for a track in the TPC is defined by

$$R_I = \frac{I - \langle I \rangle}{\sigma_I}, \tag{3.5}$$

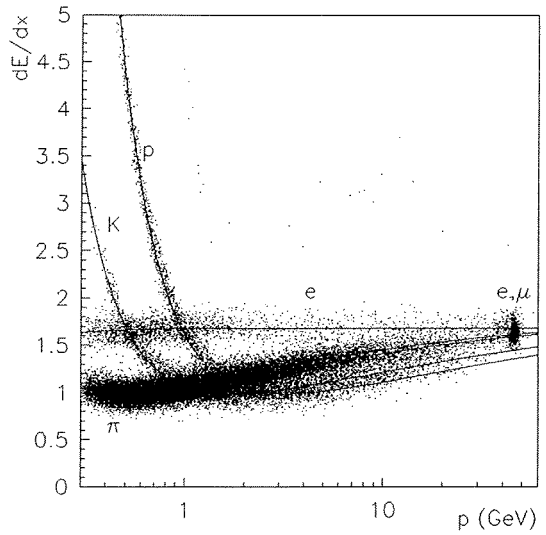

Figure 3.8: The measured dE/dx versus particle momentum for tracks having at least 150 dE/dx measurements. The fitted parametrization for protons, kaons, pions, muons and electrons is shown [54].

where $I = dE/dx$, $\langle I \rangle$ is the expected ionization for a given particle hypothesis, and σ_I is the resolution on I for which the above parametrization are used. A minimum of 50 wire or pad hits is required to ensure a reliable measurement.

The dE/dx measurement is a powerful tool to identify particles: as it is shown in fig. 3.8, electrons have a separation from other particles greater than 3σ up to $p \sim 8\,\mathrm{GeV}/c^2$ [52].

3.2.4 The Electromagnetic CALorimeter, ECAL

The electromagnetic calorimeter is a lead/wire chamber sampling device with a thickness of 22 radiation lengths. Twelve modules surround the TPC cylinder and comprise the central barrel while twelve petal-shaped modules form each of the two endcap modules closing both ends. The barrel has inner and outer radii of 185 cm and 225 cm for an angular coverage of 3.9π. The endcaps are 251 cm on either side of the interaction point and have active inner and outer radii of 57 and 228 cm and a depth of 41 cm. Fig. 3.9(a) shows the ECAL overall geometry.

Each module has 45 lead and proportional wire chamber layers. A single layer, shown in fig. 3.9(b), consists of $2 \div 4$ mm thick lead sheet, an Al sheet with open extrusion on one side, a plane of 25 μm diameter gold-plated tungsten anode wires with 5 mm pitch, a thin highly resistive graphite-coated Mylar window and a plane of cathode pads. The modules are operated with a xenon (80%) and CO_2 (20%) gas mixture at 60 mbar above the atmospheric pressure.

The energy measurement is provided by the cathode pads connected internally to form projective "towers", which are read out in three sections in depth ("storeys") for pattern recognition purposes. The segmentation is 0.94° in azimuth and $0.93° \times \sin\theta$ in polar angle. This high granularity is needed to ensure an efficient identification of photons, electrons and

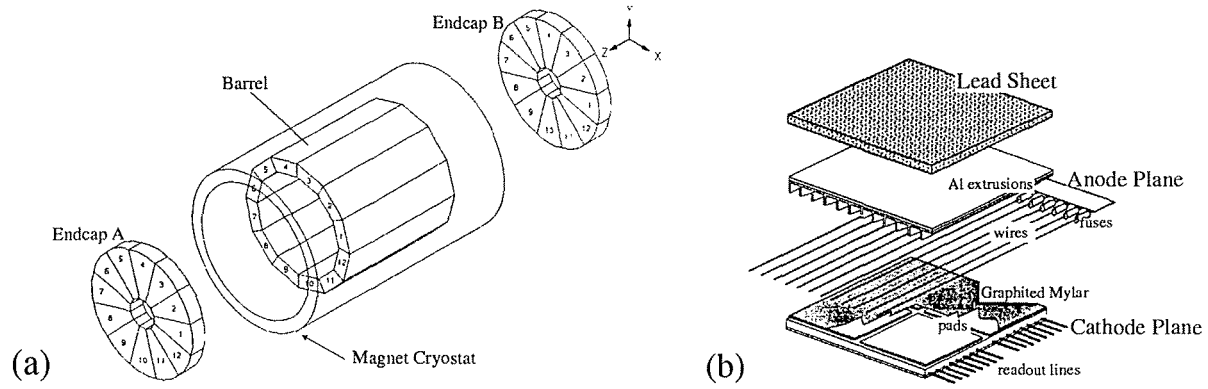

Figure 3.9: (a); an overall view of the ECAL barrel and endcaps surrounded by the magnet cryostat. (b); the lead/wire chamber layer of the ECAL.

neutral pions, especially in a hadronic jet. Signals from the anode wires are also used to improve the energy measurement and for the trigger.

The gas gain is monitored by small proportional chambers associated to Fe^{55} sources, after corrections the stability of the gain is better than 0.3%. The energy calibration is performed with electrons from different sources (Bhabha events, tau decays and two-photon events) to provide a full energy coverage from 1 to 45 GeV. The recorded energy is corrected for the storey threshold, ionization losses before entering the calorimeter, shower leakage at the edges and the non-linearity in the response to electrons. The energy resolution as a function of the electron energy is found to be

$$\frac{\sigma(E)}{E} = \frac{0.18}{\sqrt{E/\mathrm{GeV}}} + 0.009. \tag{3.6}$$

The angular resolution on the shower direction is $\sigma_{\theta,\phi} = (2.5/\sqrt{E/\mathrm{GeV}} + 0.25)$ mrad.

3.2.5 Magnet

The electromagnetic calorimeter is surrounded by a superconducting solenoidal coil which generates a magnetic field of 1.5 T parallel to the beam axis. The coil, 6.35 m in length, is made up of NbTi/Cu conductor operated by a liquid helium cooling at a temperature near 4.4°K. The nominal magnetic field of 1.5 T is reached with a current of 5000 A running in the coil. Near both ends of the main coil there are two 40 cm long compensating coils. When the compensating coils are in operation the field within the tracking volume is homogeneous within 0.2% in the z component, while the radial and azimuthal spurious components are respectively less than 0.4% and 0.04% with respect to the z component. The HCAL serves as the return yoke for the magnetic field.

3.2.6 HCAL, the Hadronic CALorimeter

The hadron calorimeter (see fig. 3.2.6) consists of 23 layers of streamer tubes [60] separated by 22 iron slabs of 5 cm in thickness. There is also a final 10 cm thick iron slab. The amount

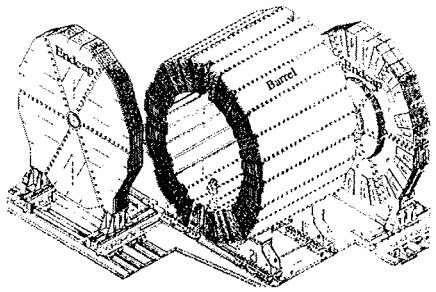

Figure 3.10: Overall geometry of the hadron calorimeter.

of material at normal incidence corresponds to 7.16 interaction lengths. The barrel, 7.24 m in length, has inner and outer radii of 3.0 m and 4.7 m and consists of 12 modules. The endcaps extends from a 0.45 m inner radius to 4.35 m outer radius and are situated 3.15 m away from the interaction point. They consist of six petal-shaped modules each. In the endcaps there is not the first streamer tube layer. Both the barrel and endcap modules are rotated by 32.7 mrad with respect to the ECAL ones to avoid the cracks to overlap.

The streamer tubes are made up of graphite-coated PVC extrusions that form tube cells (9 mm $\times$ 9 mm square cross section). In the middle of each cell, running parallel to their length, there are 100 μm thick beryllium-copper anode wires. The streamer tubes are operated with a argon (22.5%), CO_2 (47.5%) and isobutane (30%) gas mixture with the anode wires at $\sim$ 4.1 kV. The gas discharge generates induced signals on cathode pads which are summed in projective towers of about $\Delta\phi \times \Delta\theta \sim 3.7° \times 3.0°$ in the barrel and $7.5° \times 2.7°$ or $15° \times 2.5°$ in the endcaps. In addition, 0.4 cm wide aluminium strips parallel to the anode wires provide a digital signal used to reconstruct the shape of the energy deposition in the rϕ projection. This digital pattern is essential for the muon identification algorithm. The signal derived from the anode wires is used in the trigger.

A system of streamer tubes and radioactive sources connected to the gas circuit of the detector is used to monitor the gas gain and correct it for variations with time. After taking into account the dependence on the temperature and the pressure, a sensitivity of 0.40% is achieved on the gas gain.

The calibration of the energy measurement is performed with muons from $Z \rightarrow \mu^+\mu^-$ events to set the absolute energy scale, while $Z \rightarrow q\bar{q}$ events are used to equalize the response of the calorimeter modules. When running at energies above the Z peak, muons from two-photon events are also used. The energy resolution for pions at normal incidence is

$$\frac{\sigma(E)}{E} = \frac{0.85}{\sqrt{E/\mathrm{GeV}}}. \tag{3.7}$$

3.2.7 The Muon Chambers

Two double layers of streamer tubes surround the detector, providing a means to identify muons, which behave as minimum ionizing particles and penetrate the whole detector when

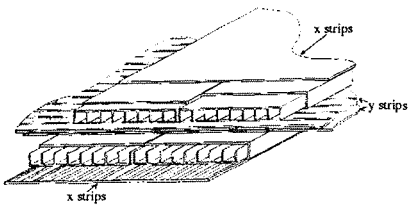

Figure 3.11: Scheme of a double layer of the muon chambers.

their momentum exceeds approximately 2.5 GeV/c. The separation of the two double layers is between 40 and 50 cm.

Each layer has, on one side, 0.4 cm wide aluminium strips, 10 mm pitch, that are parallel to the wires and, on the other side, 1 cm wide aluminium strips, 10 mm pitch, extending orthogonally to the wires. This configuration, shown in fig. 3.2.7, allows a three-dimensional reconstruction of the impact points of the tracks. Such hits are associated to a charged particle when their position is compatible with the extrapolation of the particle trajectory, allowing for multiple scattering in the detector material. Adding the information from the muon chambers greatly improves the muon identification with respect to use of the HCAL digital pattern alone: in fact, misidentified hadrons in HCAL are unlikely to reach the muon chambers. In addition, the hits in the muon chambers allow to solve the ambiguity in the association of HCAL digital hits to tracks which overlap in the rϕ projection.

3.2.8 The Luminosity Monitors

The beam luminosity is determined by comparing the measured rate of low angle Bhabha scattering events with the cross section predicted by the Standard Model. Since the cross section varies as $1/\theta^4$, where θ is the polar angle of the scattered particle, the measurement is performed at low angles with respect to the beam in order to have large statistics. The experimental acceptance must be known with high accuracy. In the ALEPH detector, the luminosity measurement is provided by two subdetectors, a lead/proportional wire chamber sampling device (LCAL) [61], and a silicon-tungsten calorimeter (SICAL) [62].

The LCAL covers a polar angle range between 46 mrad and 122 mrad on both sides of the interaction region, and is 24.6 radiation lengths thick. There are four semi-annular modules per side, very similar to those of the ECAL. The energy measurement is provided by cathode pads which are summed in projective towers; clusters are formed by joining together towers for which two storeys with more than 50 MeV share a side or a corner, but only the central nine towers in a cluster are used. The uncertainty on the radial position of a tower is about 190 μm. Bhabha events are selected requiring one cluster in each side of the LCAL, one inside a fiducial region of the calorimeter, and the other cluster contained in a slightly larger (non-fiducial) region. In addition, each cluster energy must exceed 44% of the beam energy and their sum must exceed 60% of the centre-of-mass energy; furthermore, the difference in azimuthal angle is required to satisfy $170° < \Delta\phi < 190°$. Background contamination from accidental coincidences of off-momentum tracks and from genuine interactions (mainly

$t-$channel production of hard photons) is subtracted. The integrated luminosity for a given period is:

$$\mathcal{L} = \frac{N_{Bhabha}}{\sigma_{ref}}, \tag{3.8}$$

where N_{Bhabha} is the number of selected Bhabha events and σ_{ref} is the theoretical cross section times the experimental efficiency estimated by means of a Monte Carlo simulation. The systematic uncertainty on the luminosity coming from experimental errors is about 0.4%, the main contributions coming from the alignment errors and the definition of the fiducial region. The contribution due to the cross section calculation is 0.28%.

In September 1992 an additional detector (SICAL) was installed. It consists of two cylindrical tungsten/silicon calorimeters covering the 24-58 mrad angular interval. Twelve layers of tungsten alternate with layers of silicon detectors, for a total of 23 radiation lengths. The internal alignment is known with a precision in the radial direction of 18 μm. The Bhabha selection is very similar to the one performed with the LCAL, but the systematic error on the luminosity is only 0.09%, while the theoretical uncertainty is 0.25%. The two luminosity measurements, from the LCAL and the SICAL, are found to be in very good agreement [63]. At LEP2, LCAL is used for the luminosity measurement since it resulted necessary to add a set of tungsten masks very close to the beam pipe to cope with the larger machine background of the LEP2 phase. These masks cover a great part of the SICAL acceptance drastically reducing its performances.

3.2.9 Trigger and Readout

The ALEPH trigger is designed to identify all events coming from e^+e^- annihilation and Bhabha scattering and to initiate their readout. In order to keep the trigger rate low, which is necessary to reduce the dead time of the TPC and the acquisition system and the amount of unwanted data written on disk, the trigger is organized in three levels.

The Level 1 trigger is hardware based and has a response time of 5 μs, less than the time between two beam crossings (11 μs or more, depending on the number of bunches). It looks for good charged tracks in the ITC or energy deposits in the calorimeters. The Level 1 trigger requirements are defined in order to select events with particular topologies. Up to 32 trigger definitions ("physics triggers") may be used at the same time, and the information on which physics triggers were satisfied is written in the event record. The following physics triggers apply to the events used in this work:

1. *single muon trigger*: a ionizing particle must penetrate at least 4 double planes of HCAL and must have been detected in the ITC;

2. *single charged electromagnetic energy trigger*: an energy deposit in ECAL of at least 1 GeV (1.2 GeV) in the barrel (endcaps) and a track in the ITC in the same angular region must be found;

3. *total energy trigger*: requires energy in the ECAL, with a higher threshold than in the single charge electromagnetic trigger;

4. *random trigger*: the event is randomly selected independently of its nature; this is usually done to study the noise level in the detector.

If an event is accepted by the Level 1 trigger, the Level 2 trigger, hardware based too, performs a similar selection, but with the TPC information replacing the ITC information.

The Level 3 trigger is a software based algorithm that checks the decision made at Level 2 with all the detector data and rejects events that clearly should have not been accepted.

The trigger thresholds can be set in such a way to have a Level 1 rate of a few Hz, while Level 2 and 3 rejecting only a small fraction of events. The trigger efficiency is almost 100% on events with two or more charged tracks.

The data acquisition system has a tree structure. The subdetector signals are managed by Readout Controllers (ROC's), which reset the subdetector electronics and read them out whenever an event is accepted by the Level 2 trigger. The information of the ROC's is then collected by one Event Builder (EB) for each subdetector, and the EB's communicate their data to the Main Event Builder, which performs the synchronization and transfers the data to the computer room. After being examined by the Level 3 trigger, the event data are passed to the Main Readout Computer and made available for mass storage and online analysis. The so-called "raw" data are processed offline by the ALEPH reconstruction program, JULIA [64]: it essentially performs the pattern recognition, reconstructs the charged particles and the calorimeter deposits and applies all the calibrations.

3.3 Event Reconstruction

3.3.1 Track Reconstruction

A e^+e^- collision event may produce many charged particles leaving their signals in the tracking devices. An appropriate algorithm, known as *pattern recognition*, translate the resulting huge number of hits in physical trajectories (tracks) candidates. The pattern recognition uses Kalman filtering techniques to perform the final global track fit.

The trajectory of a charged track within an uniform magnetic field is an helix, being the helix inversely proportional to particle transverse momentum p_T (the component orthogonal to the field). Fig. 3.12 shows the five parameters used by ALEPH to define an helix in the space:

1. the inverse radius of curvature ω, positive if the helix bends counter-clockwise, left-handed with respect to the z axis;
2. the tangent of the angle λ made by the helix with respect to the xy plane;
3. the track azimuthal angle ϕ_0 at the point of closest approach to the z axis;
4. z_0, the z impact parameter, that is the z position z_0 of the point of closest approach to the nominal ALEPH origin.
5. d_0, the signed xy impact parameter, i.e. the distance of closest approach to the nominal ALEPH origin in the xy plane multiplied by the factor

$$\left|\frac{z_0}{\cos\theta_0}\right|\frac{\cos\theta_0}{z_0}, \tag{3.9}$$

where θ_0 is the track polar angle in the point of closest approach to the nominal ALEPH origin in the xy plane.

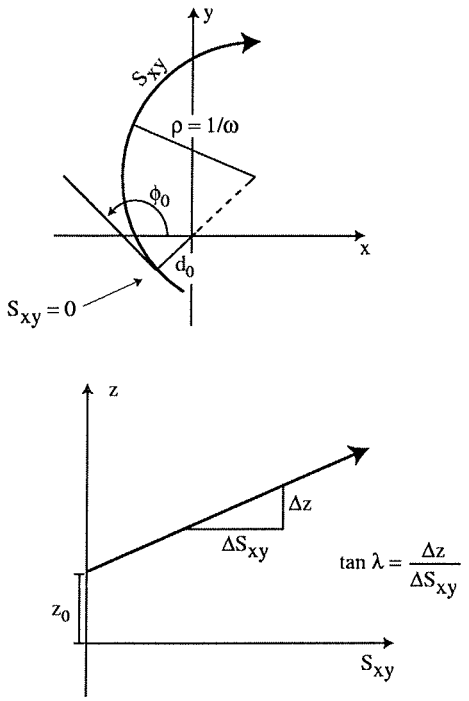

Figure 3.12: The five helix parameters.

A $1/p_T$ tracking resolution of $10^{-4}(\text{GeV}/c)^{-1} \oplus 5 \times 10^{-3}/p_T$ (with p_T in GeV/c) is achieved. The three-dimensional impact parameter[2] resolution can be parametrized as $(34+70/p) \times (1+1.6\cos^4\theta)$ μm, with p in in GeV/c [65].

For the analysis a charged track is generally used if it satisfies the following criteria:

- $|\cos\theta| < 0.95$;
- $N_{\text{TPC}} \geq 4$, being N_{TPC} the number of TPC hits;
- $|d_0| < 2.0$ cm and $|z_0| < 10.0$ cm.

Such a track is known as *good charged track*.

3.3.2 Lepton identification

The ALEPH detector can provide an efficient and reliable lepton identification by means of standard estimators using the TPC and the calorimeter information. In this section, the identification algorithms are briefly discussed.

Electron identification

Particles that do shower in the ECAL can be identified as electrons or hadrons through the use of the longitudinal and transverse shower shapes together with the dE/dx information

[2]The three-dimensional impact parameter r_0 is defined as the distance between a particle track and the estimated particle production point, i.e. the interaction point.

from the TPC. To use the shower shapes, two estimators - the transverse estimator and the longitudinal estimator - are constructed in order to quantify how much a given shower resembles a typical electron shower. The transverse estimator R_T is constructed using E_4/p, the fraction of a track energy deposited in the four towers closest to the extrapolated track position. This quantity is expected to be large for electrons, since the shower resulting from the passage of an electron through the ECAL tends to be contained in the four towers nearest the track, since the ECAL tower dimension was designed just for this purpose. On the contrary hadron showers in the ECAL tend to be much broader. The value of E_4/p is therefore smaller than it is in the electron case. The transverse estimator is then defined to be the number of standard deviations between the measured value of E_4/p and the mean value of E_4/p for an electron. The longitudinal estimator R_L is constructed using X_L, the mean depth of the energy deposition in the ECAL. Electrons will generally have small values of X_L, since electrons tend to shower in the front of the ECAL. Hadrons behave differently: in case they shower at all in the ECAL the charge deposition accumulates at the back. The value of X_L tends to be large in this case. The longitudinal estimator is defined in a manner analogous to the transverse estimator; it is the number of standard deviations between the measured value of X_L and the mean value of X_L for an electron.

For many of the ALEPH analyses, a standard set of electron identification cuts is $-1.8 < R_L < 3.0$, $-1.6 < R_T$, and $-2.5 < R_I$, where R_I is the estimator for the electron hypothesis based on the dE/dx measurement defined by the relation (3.5). Using these cuts, the efficiency for identifying electrons in a hadronic environment is $\sim 65\%$, while the probability of misidentifying a hadron as an electron is about 0.1%.

Muon identification

Muons are identified by requiring, in association to a reconstructed charged particle, a hit pattern in HCAL and in the muon chambers compatible with those expected for a minimum ionizing particle.

Every track with a measured momentum greater than 1.5 GeV/c is extrapolated through ECAL, the magnet coil and HCAL, taking into account the magnetic field and the estimated energy loss by ionization. Digital clusters in HCAL are associated to a track when:

1. there are less than four strips in the cluster;

2. the cluster is in the same module and plane of a point of the extrapolated trajectory of the track;

3. the distance in the plane orthogonal to the HCAL tubes between the centre of the cluster and the extrapolation point is less than $3\sqrt{\langle r^2 \rangle} + 3$ cm, where $\langle r^2 \rangle$ is the estimated transverse displacement due to the Coulomb multiple scattering.

The following quantities, relative to the track extrapolation in HCAL, are used by the muon identification algorithm:

- N_{exp}: the number of planes crossed by the track extrapolation in an active zone of HCAL;

- N_{fir}: the number of planes with at least one associated cluster ("fired" planes);

- N_{10}: the number of fired planes in the last ten expected planes;
- X_{mult}: the number of clusters in the last 11 planes inside a two-dimensional cone around the extrapolated track, of width equal to 20 cm at the innermost HCAL plane and increasing by 1 cm at each plane, divided by the number of planes containing at least one of these clusters (if the number of these planes is less than 4, $X_{\text{mult}} \equiv 0$).

The association of muon chamber hits to tracks is performed in a similar way: tracks with an initial momentum larger than 2.2 GeV/c are extrapolated through HCAL and the distance Δ between each hit in a muon chamber and the estimated crossing point of the muon is compared to the estimated mean displacement $\Delta_{m.s.}$ from the extrapolated trajectory due to multiple scattering. If the distance Δ from a hit is less than $\Delta_{cut} = 4 \times \langle \Delta_{m.s.} \rangle$ (or 5 cm) the hit is associated to the track. If hits are associated in both the muon chamber layers and the difference Θ between the direction of the line connecting them and the estimated muon direction is greater than $\Theta_{cut} = 10 \times \Theta_{m.s.}$ (or 5°), where $\Theta_{m.s.}$ is the estimated mean deviation due to multiple scattering, the hits are rejected.

A "loose" muon identification is provided by the request that

- $N_{\text{fir}}/N_{\text{exp}} \geq 0.4$, $N_{10} \geq 5$ and $X_{\text{mult}} < 2.05$, or
- there are at least 2 hits in the muon chambers.

A "tight" muon identification is obtained with more stringent cuts on the relevant estimators. It must be

- $N_{\text{fir}}/N_{\text{exp}} \geq 0.4$, $N_{10} \geq 5$, $N_{\text{exp}} \geq 10$, $X_{\text{mult}} < 1.5$ and at least one hit in a muon chamber, or
- $\Delta/\Delta_{cut} < 0.5$ for each hit, $\Theta/\Theta_{cut} < 0.15$, $X_{\text{mult}} < 1.5$ and at least one hit in each layer of muon chambers.

Requiring the tight muon identification an efficiency of identifying a muon in a hadronic environment of $\sim 80\%$ and a probability of misidentifying a hadron as a muon of less than 0.5%.

3.3.3 The Energy Flow Algorithm

The tracking information and the energy deposits in the calorimeters are combined by a package of algorithms, known as "Energy Flow", that generates a list of physical objects, known as *reconstructed particles*, each one identified as charged particle, neutral particle or photon by appropriate estimators.

In particular, these algorithms properly deal with the multiple energy and momentum signatures of single tracks to avoid double-counting. The excellent momentum resolution of the TPC is combined with calorimetry and particle identification techniques. Energy deposited in the luminosity subdetectors is also used, extending the solid angle calorimetry coverage down to 34 mrad in polar angle.

An initial event cleaning procedure is performed on charged tracks and calorimeter clusters. Charged particle tracks must meet one of the following sets of criteria:

1. the charged track must be good;

2. the charged particle tracks rejected by the criteria above are recovered if they are found to belong to a reconstructed V0, that is a decay vertex of a neutral particle (i.e. K^0_S or Λ_0) or a γ conversion vertex. In this case, the neutral particle or the γ direction must be compatible with originating from the nominal interaction point within a cylinder of length 30 cm and radius of 5 cm coaxial with the beam.

The cleaning procedure also identifies noisy ECAL and HCAL channels and does not use them for calorimeter cluster finding. Fake energy deposits due to occasional calorimeter noise are found and removed when the corresponding signal is incompatible with the signal measured independently on the ECAL wire planes or HCAL streamer tubes.

Charged particle tracks are extrapolated from the tracking chambers to the calorimeters. Topologically connected tracks and calorimeter clusters are used to compose calorimeter objects. The calorimeter objects are processed via a series of particle identification algorithms which classify electrons, muons, photons, neutral pions or neutral hadrons. Hence, for each event a set of classified energy flow objects is built and can be used in the offline analysis of events.

This energy flow algorithm allows jets to be reconstructed with a typical angular resolution of 20 mrad both for the polar and azimuthal angles, and a relatively uniform energy resolution over the whole detector acceptance parametrized as $\sigma_E = (0.60\sqrt{E/\,\mathrm{GeV}} + 0.6) \times (1 + \cos^2\theta)$ where E is the jet energy and θ is the jet polar angle [65].

3.4 ALEPH Monte Carlo Simulation

The ALEPH detector simulation program is called `GALEPH`. It uses the known position of material and responses of subdetector components in conjunction with the `GEANT3` [66] and `GHEISHA` [67] packages to simulate the passage and possible interactions of charged and neutral particles through the ALEPH detector. The output of `GALEPH` is in a format identical to the raw data from the detector with additional information relating the detector signals to event generator-level particles (referred to as *Monte Carlo truth* information).

4 Monte Carlo Simulation

The Monte Carlo simulation is very important for a search analysis. The efficiency of a selection can be evaluated from the samples of simulated signal events. The background simulation is necessary to estimate the expected amount of background events we may observe with a given luminosity. The discovery power of the selection depends both on the signal efficiency and on the expected background. Thus the simulations are crucial for the optimization of the selection itself.

The full simulation relies upon an event generator using Monte Carlo techniques to provide four-vectors of final state hadrons, leptons and photons. These four-vectors are processed through the detector simulation (see 3.4) and then through JULIA [64], the same event reconstruction program used for data analysis.

4.1 Squark signal simulation

From the point of view of the simulation, the squark signal in e^+e^- collisions can be divided into three steps: the production of the bare squarks, the build up of the physical final state deriving from the decay and the hadronization (not necessarily in this order) and the interaction of the final state within the detector. The most significant issues to be addressed are the treatment of the squark perturbative gluon radiation, hadronization and decay.

The production simulation is made by SQUOR [68], a dedicated generators based on the standard packages PYTHIA [69], that simulates the partons production, and JETSET [69] devoted to the hadronization, fragmentation and gluon emission of the coloured particles. The interaction within the detector needs non standard tools only in the case of long living heavy stop hadron production.

The squarks couples are produced according the differential cross section (2.5). The initial state radiation is taken into account with the REMT package [21].

The phenomenology that follows the bare squarks production yielding to the observable final state, consists of two different cases to be considered: the decay of stop hadrons (in case that the squark has a lifetime large enough to hadronize) and the decay of free squarks that occurs before the hadronization process between the coloured particles.

4.1.1 Squark hadronization

From the width values given in section 2.3.2 one realizes that the stop visible at LEP2 has a lifetime much more greater than the typical hadronization time[1]. The same consideration could be valid for the sbottom and the other squarks, in case that the combinations of Δm and the MSSM parameters yields to a lifetime greater than the typical hadronization time. To correctly simulate the hadronization several aspects need careful attention.

Gluon emission

Since the squark is a scalar particle, the spectrum of gluon emission differs from that of a quark. The simulation of gluon radiation would require a dedicated study. Nevertheless some considerations can be used to state that the existing algorithms can be safely used [23][70]. The gluon emission probability P of a coloured particle Q is given by the Altarelli-Parisi

[1] $\Gamma_{\tilde{t}} \sim 10^{-8} \div 10^{-2}\,\mathrm{MeV} \Rightarrow \tau_{\tilde{t}} \sim 10^{2} \div 10^{8}\,\mathrm{MeV}^{-1} \gg 10^{-2}\,\mathrm{MeV}^{-1} \sim \mathcal{O}(10^{-23}\mathrm{s}) \sim t_{\mathrm{hadr}}$.

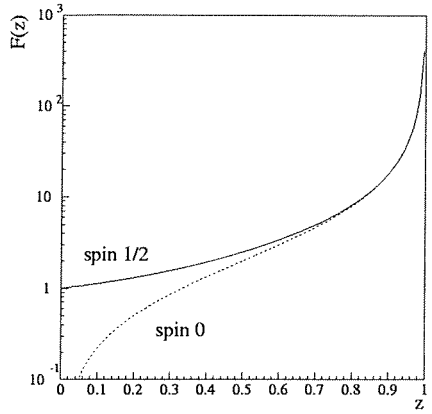

Figure 4.1: F function in case of spin 1/2 (solid line) and spin 0 (dashed line).

"splitting" function:

$$P(z) = \frac{\alpha_s N_C}{2\pi} F(z, spin), \tag{4.1}$$

where z is the momentum fraction of the final state Q, α_s the strong interaction constant and N_C the colour factor. The F function is

$$F(z, spin = \frac{1}{2}) = \frac{1+z^2}{1-z}, \tag{4.2}$$

for spin-1/2 particle and becomes

$$F(z, spin = 0) = \frac{1+z^2}{1-z} - (1-z), \tag{4.3}$$

for a scalar particle. As plotted in fig. 4.1, in the infrared limit $z \to 1$, where the emission probability is maximal, the difference between the two functions vanishes. Moreover, since an heavy squark is always produced at low β the hard gluon probability emission ($z \to 0$) is very small. It turns out that the difference in the energy loss due to gluon radiation between the spin-0 and spin-1/2 case is less than 0.1%, completely negligible at Monte Carlo level. Thus the squark gluon emission is simulated by the standard algorithms used for quarks. This algorithms produces an off-shell (virtual) quark, with the invariant mass depending on the radiation probability (4.1). The extra energy respect to the on-shell energy is then used to radiate the gluons. At the end of the emission chain the quark results on-shell.

After the gluon emission, colour neutral supersymmetric hadrons $\widetilde{Q}$ of the type $\tilde{t}q$, $\tilde{t}qq'$ or $\tilde{b}q$, $\tilde{b}qq'$ are formed following the scheme sketched in fig. 4.2. This scheme is implemented into the generator making the squark hadronizing as ordinary quarks using the "Lund" string fragmentation algorithm implemented in `JETSET 7.4` [69]. As the fig. 4.2 shows, the string connects all the particles of the colour singlet, in this case the squark couple plus the radiated gluons.

Fragmentation

The fraction z of the original squark energy transferred to the stop hadron is parametrized using the Peterson fragmentation function [71]:

$$f(z) = \frac{1}{z\left(1 - \frac{1}{z} - \frac{\epsilon_{\tilde{q}}}{1-z}\right)^2}. \tag{4.4}$$

The phenomenological parameter $\epsilon_{\tilde{q}}$ can be extrapolated from the measured ϵ_b of the bottom quark, since it scales inversely with the square of the mass,

$$\frac{\epsilon_{\tilde{t}}}{\epsilon_b} = \frac{m_b^2}{m_{\tilde{t}}^2}, \quad \frac{\epsilon_{\tilde{b}}}{\epsilon_b} = \frac{m_b^2}{m_{\tilde{b}}^2}. \tag{4.5}$$

The values $m_b = 5\,\text{GeV}$ and $\epsilon_b = 0.0035$ [72] are used while the uncertainties on ϵ_b are taken into account studying the systematic effects (see section 6.1).

Squark hadron decay

The decay of a squark hadron is simulated using the "spectator model" [73]. Within this model the kinematic of the hadron decay is fixed mostly by the kinematic of the decaying parton (the stop). According to the spectator model the decay of the stop hadron $\widetilde{Q}$, caused by the process $\tilde{q} \to q'$ LSP X, is

$$\widetilde{Q} = \begin{bmatrix} \tilde{t} \\ q'' \\ (q''') \end{bmatrix} \to \begin{matrix} q' \text{ LSP } X \\ q'' \\ (q''') \end{matrix}. \tag{4.6}$$

The several decay processes are described in detail below.

The corrections coming from QCD and the bound state structure of the hadron are taken into account in the spectator model by the parameter m_{eff}, known as *effective spectator quark mass.*

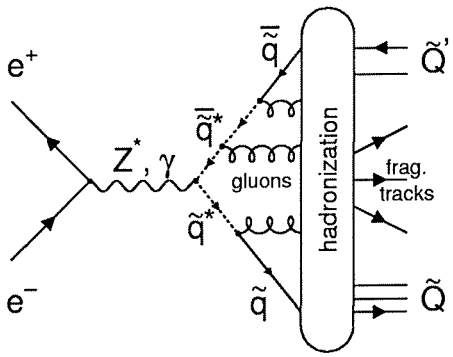

Figure 4.2: Squark hadronization scheme.

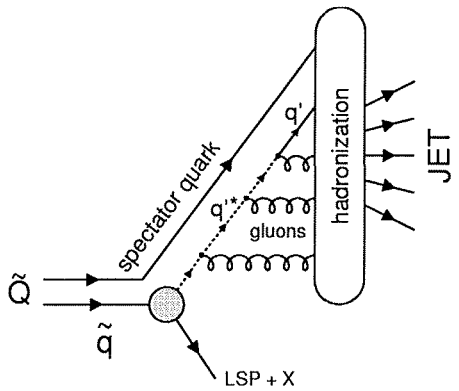

Figure 4.3: Squark hadron decay scheme.

To take into account either the binding energy and the soft component of the gluon emission that increases the final jet invariant mass, the effective spectator quark mass is chosen to be

$$m_{\text{eff}} = 500\,\text{MeV} + m_{q''}\ (+m_{q'''}). \tag{4.7}$$

Thus the stop hadron mass results to be:

$$m_{\tilde{Q}} = m_{\tilde{q}} + 500\,\text{MeV} + m_{q''}\ (+m_{q'''}). \tag{4.8}$$

The speed of the q′ quark, coming from the stop decay, depends on the mass difference between the $\tilde{t}$ and the LSP. Thus for higher values of Δm, where the q′ speed is higher, also the hard component of gluon emission has to be taken into account. According to the spectator model, this is done allowing only the quark q′ from the decay to emit gluons. After the gluon emission the "Lund" hadronization scheme is applied connecting all the coloured particles of the colour singlet. These are the quark q′ from the decay, the spectator quark(s) and the radiated gluons. The entire process of the decay of a squark meson is sketched in fig. 4.3. Typically the final state of the squark hadron decay will contain only one jet, since the squark decay involves only a quark with a dominant energy respect to the others.

Decays within the squark hadron

It is worth to discuss the various squark decays within the squark hadron, since the gluon emission treatment is peculiar respect to the free squark decay discussed later.

- $\tilde{t} \to c\chi$, $\tilde{b} \to b\chi$
  The kinematic of a two-body decay is completely fixed: the q and the χ are emitted back-to-back in the center of mass frame. Since the $\tilde{q}$ is scalar the emission axis is isotropically distributed in the center of mass frame and thus it is extracted uniformly at the Monte Carlo level. It turns out that in the laboratory frame the q and χ directions are fixed by the Lorentz transformation and there is not any other correlation with the $\tilde{q}$ flight axis.

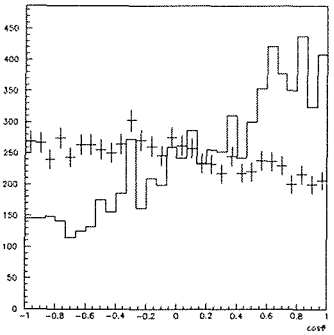

Figure 4.4: Predicted distributions of $\cos\theta$ for the phase space model (+) and the matrix element (−), θ being the angle between the b and the ℓ^+ in the decay in the $\tilde{t}$ frame ($m_{\tilde{t}} = 70\,\text{GeV}$, $m_{\tilde{\nu}} = 30\,\text{GeV}$ and $\sqrt{s} = 161\,\text{GeV}$.

To correctly take into account the gluon emission from the final q, the energy to make the q virtual must be subtracted from the χ [74]. The hadronization is then performed via the "Lund" scheme connecting all the coloured particles coming also the decay.

- $\tilde{t} \to b\ell^+\tilde{\nu}$
  The three-body decay $\tilde{t} \to b\ell^+\tilde{\nu}$ occurs via the exchange of a virtual chargino. It results convenient to split the process into two subprocesses in cascade, $\tilde{t} \to b\chi^{+*} \to b\ell^+\tilde{\nu}$. In the first one a virtual chargino is produced. At Monte Carlo level the mass is extracted according to the probability distribution given by the squared chargino propagator:

$$\frac{1}{\left[(p_{\tilde{t}} - p_b)^2 - m^2_{\chi^+}\right]^2}, \tag{4.9}$$

  where the m_{χ^+} is set at high values. In fact the gaugino sector must be heavy to have the $\tilde{\nu}$ as LSP. The momenta are determined by the phase space model [69].

  The structure of the matrix element [24] is also considered in comparison with the phase space model since the matrix element depends on the MSSM parameters μ and $m_{1/2}$ (assuming the GUT relations (1.80) that bind the gaugino sector masses to the common mass $m_{1/2}$). If the lightest chargino is a pure wino the matrix element structure is purely vector-axial that is proportional to $\gamma^\mu(1-\gamma_5)$, but it includes also scalar and pseudoscalar contributions if the chargino has a higgsino component also. A full treatment of the matrix element would therefore require that the values of μ and $m_{1/2}$ to be specified to generate the signal sample. Nevertheless an approximate matrix element allows to ignore the MSSM parameter dependence and to make a reliable comparison between the matrix element computation and the simpler phase space model. Fig. 4.4 shows the $\cos\theta$ distribution for the two models, where θ is the angle between the b and the lepton in the $\tilde{t}$ frame. The matrix element distribution shows a peak when the b and the lepton are collinear as one expects from considerations

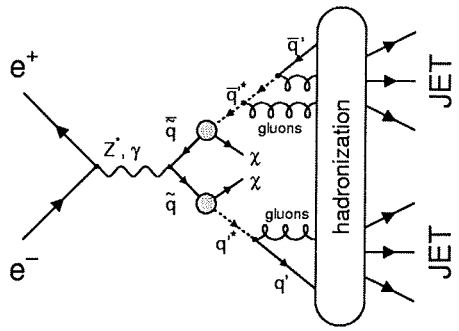

Figure 4.5: Free squarks decay scheme.

on the helicity of the two fermions[2]. Since an evident discrepancy is visible, two sets of $\tilde{t} \to b\ell^+\tilde{\nu}$ samples are generated, one with the matrix element computation, one with the phase space model, in order to evaluate how the efficiencies of the selections described in chapter 5 depend on the procedure applied (see chapter 6).

Also for this decay the gluon radiation is considered. Since JETSET allows to take into account the gluon radiation only in two-body decays, the gluons are radiated by the b quark after the first two-body decay $\tilde{t} \to b\chi^+$, similarly to the $\tilde{q} \to q'\chi$ decay, but in this case the energy needed to make the b virtual is given by the chargino. The hadronization then proceeds as in the $\tilde{q} \to q'\chi$ decay case.

4.1.2 Free squarks decay

For the squarks $\tilde{u}$, $\tilde{d}$, $\tilde{c}$, $\tilde{s}$ and $\tilde{b}$, the width coming from the decay $\tilde{q} \to q'\chi$ yields to lifetimes that could be shorter than the hadronization time. To treat this case at the simulation level, the free squark is made decaying before applying the algorithms that simulate the colour particles hadronization.

For the bare decay processes the same considerations made in the previous section are valid, also about the treatment of the gluon emission. The only difference is about the hadronization mechanism performed, as usual, with the "Lund" algorithm. The string must connect the coloured particle forming the colour singlet. In this case the colour singlet is the $q'\overline{q}'$ system plus the emitted gluons. In fact the couple $\tilde{q}\overline{\tilde{q}}$ produced in the e^+e^- interaction is a colour singlet and the colour is conserved in a decay $\tilde{q} \to q'\chi$. The scheme of the overall process is sketched in fig. 4.5.

4.1.3 Signal simulation in case of very small Δm

As already discussed, if the Δm is very small, the final state consists of stable or metastable stop hadrons. The simulation of this signal is not feasible with squark standard Monte Carlo tools. Thus, either the process generator and the detector simulation programs have been

[2]The initial spin is zero, and thus also the final spin must be zero. In the limit of vanishing masses, also the final helicity must be zero. Since the b and ℓ^+ are produced with an opposite helicity they have to be collinear. In the limit of non zero masses this distribution is smeared as in fig. 4.4, but still peaked at $\theta = 0$.

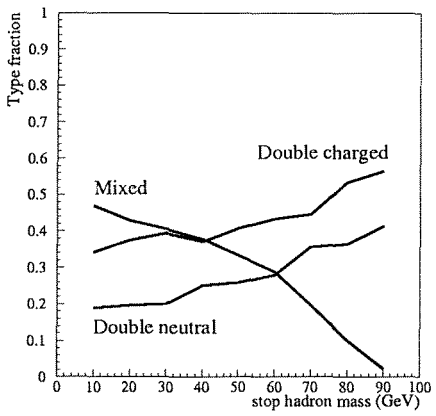

Figure 4.6: The fraction of the three possible $\widetilde{T}\widetilde{T}$ charge combinations at 189 GeV.

modified on purpose. The usual generator for stop simulation is used with few changes. Stop-hadrons $\widetilde{T}$ are formed as explained before but since the stop hadron has now a huge lifetime, three issues become crucial respect to the previous cases:

- the relative composition of the produced stop hadrons;
- the treatment of stop hadron decay inside the apparatus;
- the treatment of the stop hadron interaction within the matter.

Stop hadrons relative composition

The JETSET top hadron list, based on the quark model of hadrons [69], is used with the top quark replaced by the stop to take into account all the hadrons that could be produced by the stop hadronization.

Since at this level it is impossible to have a reasonable prediction of the mass spectra of these hadrons and of their excited states as well, some assumption have to be done. All the stop hadrons are equal in mass and the excited states and the double charged states are ignored. The generic stop hadron will be indicated simply with $\widetilde{T}$. The stop hadron can be produced neutral or ± 1 in charge. Thus the final state could be double neutral ($\widetilde{T}^0\widetilde{T}^0$), mixed ($\widetilde{T}^{\pm}\widetilde{T}^0$) or double charged ($\widetilde{T}^+\widetilde{T}^+$, $\widetilde{T}^+\widetilde{T}^-$, $\widetilde{T}^-\widetilde{T}^-$). Since the initial state is neutral, in case that a $\widetilde{T}\widetilde{T}$ system with a non zero total electric charge is produced the charge conservation is ensured by the fragmentation tracks. Fig. 4.6 shows the simulated relative composition of neutral, mixed and charged $\widetilde{T}\widetilde{T}$ state as a function of the $\widetilde{T}$ mass for a centre-of-mass energy of 189 GeV. Since the energy available to produce fragmentation tracks is smaller at higher masses, also the fraction of mixed $\widetilde{T}\widetilde{T}$ decreases in that mass region. To be notice that the double charged state mainly consists of $\widetilde{T}^+\widetilde{T}^-$ couples for the same reason.

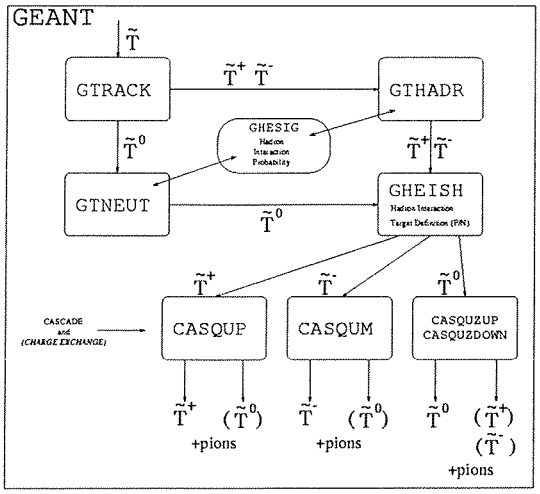

Figure 4.7: The flow chart of the GALEPH routines for the $\widetilde{\mathrm{T}}$ interaction simulation.

Stop hadron decay

Since the stop hadron decay could occur in the ALEPH sensitive volume and thus at the detector simulation level, the $\widetilde{\mathrm{T}}$ decay must be simulated at this level as well. GALEPH allows to define a simplified decay table for a given particle. If kinematically allowed ($\Delta m < m_{\mathrm{D}}$), the stop decay elementary process is $\tilde{\mathrm{t}} \to \mathrm{c}\chi$ and the c quark hadronizes in D type mesons. Hence the $\widetilde{\mathrm{T}}$ decay has been implemented filling the $\widetilde{\mathrm{T}}$ decay tables with the LSP plus the most important decay products of the D type mesons.

Stop hadron interaction within the matter

The main issue is the simulation of the interaction of these stop hadrons in the detector, that has been implemented from scratch in GALEPH at the GEANT level.

The electromagnetic interaction of the stop hadrons are simulated trough the standard GEANT routines: they are treated like massive pions.

About the strong interactions few considerations have been done. In the scattering of a stop-hadron $\widetilde{\mathrm{T}}$ of energy $E_{\widetilde{\mathrm{T}}}$ with a nucleon N at rest, the centre-of-mass energy E_{cm} is

$$E_{cm}^2 = M_{\widetilde{\mathrm{T}}}^2 + M_{\mathrm{N}}^2 + 2M_{\mathrm{N}}E_{\widetilde{\mathrm{T}}}. \tag{4.10}$$

The generic reaction is $\widetilde{\mathrm{T}} + \mathrm{N} \to \widetilde{\mathrm{T}} + \mathrm{N} + X$, since the R-parity and the barion number are both conserved. The Q-value, that is the energy available for the X system, is

$$\mathrm{Q} = E_{cm} - M_{\widetilde{\mathrm{T}}} - M_{\mathrm{N}}. \tag{4.11}$$

The center-of-mass energy E_{cm} is typically close to $M_{\widetilde{\mathrm{T}}}$ thus the Q-value sits around few hundreds of MeV. For example, if $M_{\widetilde{\mathrm{T}}} \sim 50\,\mathrm{GeV}$ and $E_{\widetilde{\mathrm{T}}} \sim 90\,\mathrm{GeV}$ the resulting Q-value is $\sim 800\,\mathrm{MeV}$. So only few pions may be extra produced in the inelastic reaction. The stop-hadron behaves like a pion with the same kinetic energy in passing through matter.

Therefore, the standard GEANT routines for the treatment of pions strong interaction can be used with appropriate modifications:

- all the energy based quantities are rescaled to the $\widetilde{\mathrm{T}}$ kinetic energy;
- the low energy pion-nucleon resonance are removed from the cross section.

Fig. 4.7 shows the flow chart for the code part for which modifications or new routines were necessary. The routines used to treat the inelastic processes are CASQUP, CASQUM, CASQUZUP and CASQUZDOWN. They are all derived from the GEANT similar routines for pions cascade.

4.2 Signal samples production

Signal events are generated at $\sqrt{s} = 189\,\mathrm{GeV}$ and $\sqrt{s} = 200\,\mathrm{GeV}$. In order to design the selection criteria, many signal Monte Carlo samples of 1000 events each were processed through the full ALEPH detector simulation, for various $(m_{\tilde{\mathrm{q}}}, m_{\chi})$ and considering all decay channels we are looking for.

For the small Δm case, several samples have been produced for various stop hadron masses and lifetimes in order to have the decay vertices uniformly distributed within the ALEPH sensitive volume. The Δm value was set at $3\,\mathrm{GeV}/c^2$. Moreover a series of samples with the stable stop hadron has been produced for various stop masses. In the small Δm simulations the mixing angle $\theta_{\tilde{\mathrm{q}}}$ was set to 56°. Fig. 4.8 shows a Monte Carlo event where a couple of charged stable $\widetilde{\mathrm{T}}$ have been produced, while in the event shown in fig. 4.9 a couple of neutral stable $\widetilde{\mathrm{T}}$ have been produced. Fig. 4.10 shows two decaying $\widetilde{\mathrm{T}}$ and the kinks coming from the decays are clearly visible.

4.3 Background processes simulation

The Standard Model processes that are most likely to produce signal-like events (see section 2.6) are all considered at the simulation level. Unfortunately there are no reliable generators for cosmic ray events and for the machine background events.

Monte Carlo samples corresponding to integrated luminosities at least 100 times as large as that of the data have been fully simulated for all major standard background reactions at $\sqrt{s} = 189\,\mathrm{GeV}$, $\sqrt{s} = 200\,\mathrm{GeV}$. These include the annihilation processes $\mathrm{e^+e^-} \to \mathrm{f\bar{f}}$ and the various processes leading to four-fermion final states ($\mathrm{e^+e^-} \to \mathrm{W^+W^-}$, $\mathrm{e^+e^-} \to \mathrm{We}\nu$, $\mathrm{e^+e^-} \to \mathrm{Ze^+e^-}$ and $\mathrm{e^+e^-} \to \mathrm{ZZ^*}$). Two-photon processes ($\gamma\gamma \to \ell^+\ell^-$ and $\gamma\gamma \to \mathrm{q\bar{q}}$) were also simulated with an integrated luminosity about five times greater than the expected one.

The generators used are PYTHIA [69] for all two fermions and four fermions processes and KORALZ [75] and GRC4F [76] have been used for $\mathrm{e^+e^-} \to \tau^+\tau^-$ and $\mathrm{e^+e^-} \to \mathrm{We}\nu_{\mathrm{e}}$ processes respectively.

The process $\gamma\gamma \to \tau^+\tau^-$ was generated with PHOTO2 [77]. Finally, two generators have been used for the two photon process $\gamma\gamma \to \mathrm{q\bar{q}}$: PHOTO2 has been used to generate the sample in which one of the final state electrons is deflected into the detector (the "tagged" sample) while PHOJETS [78] has been used to generate the sample in which neither electron is deflected into the detector (the "untagged" sample). This background is very difficult to

simulate, since the four momentum transferred to the hadronic system is usually very low and the quarks undergo to low energy hadronic interactions. These cannot be simulated with the tools in use for quark hadronization and fragmentation since the low energy hadron interaction is heavily not perturbative and requires the low energy resonances and bound states to be taken into account. For this reason, these events are sometimes generically referred as $\gamma\gamma \rightarrow$ hadrons events.

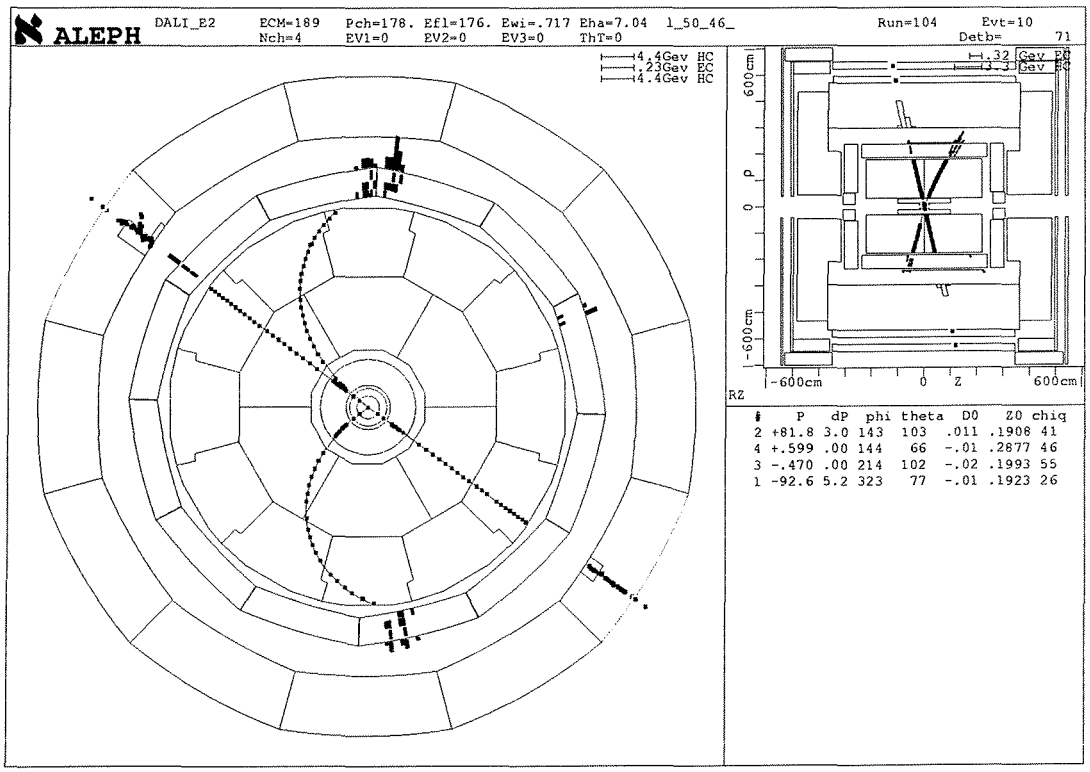

Figure 4.8: A double charged Monte Carlo $\widetilde{\mathrm{T}}\widetilde{\mathrm{T}}$ event.

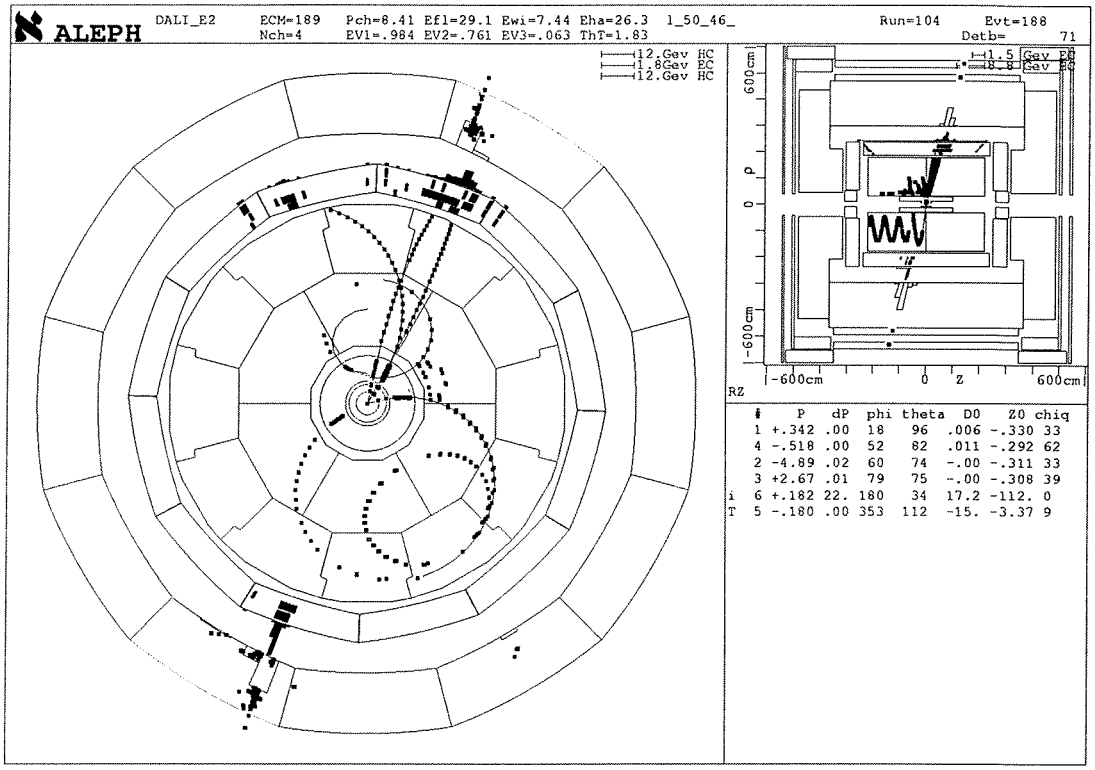

Figure 4.9: A double neutral Monte Carlo $\widetilde{\mathrm{T}}\widetilde{\mathrm{T}}$ event.

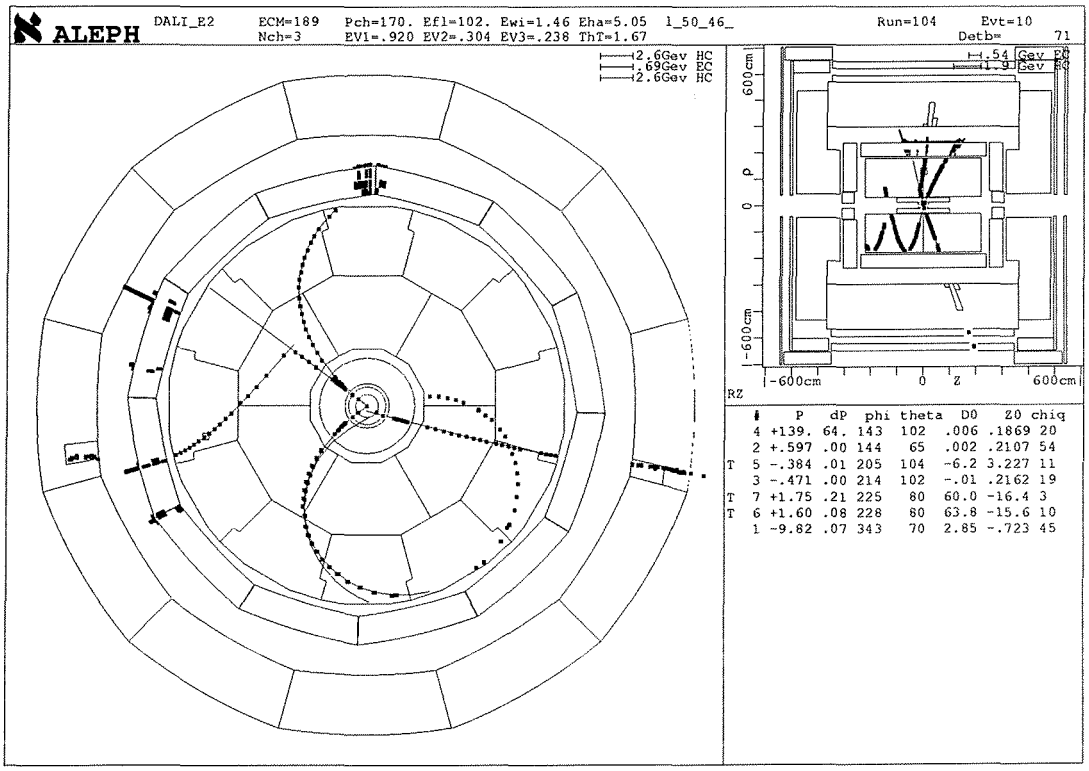

Figure 4.10: A Monte Carlo $\widetilde{\mathrm{T}}\widetilde{\mathrm{T}}$ event with both stop hadrons decaying inside the apparatus.

5 Selections

In this chapter the selections used to search for a squark signal are described and some details are also given on the criteria used to design and optimize these selections. Moreover the performances of the selections on the squark signal are discussed.

5.1 The search experiment

In the hypothesis that the squarks are accessible at LEP, the squark production events would be present in the data collected by the detector. The sample of these events, object of the search analysis, is usually known as *signal*. The signal will be mixed with all other events coming from the Standard Model processes. They would be much more in number since their cross section is several order of magnitude bigger than the one expected for the signal. The events coming from known processes are usually referred as *background*.

The search experiment consists in a selecting procedure (*selection*) applied to the data sample recorded by the detector. The procedure, acting on the variables that describe the event, is designed to tag the possible signal events, rejecting the background events. A data event surviving the selection is known as *candidate*.

Since the main target of this kind of experiments is the discovery of the new signal, the selections are designed to maximize the discovery power or, in other words, to exclude as much as possible the presence of the signal in the collected data events.

5.1.1 Search experiment parameters

A given search experiment, that is a selection applied on the data, is characterized by two parameters:

- the *signal efficiency* ε describes both the detector capability to record the signal event (detector efficiency, ε_d) and the selecting power of the selection (selection efficiency, ε_s) when applied on sample of signal events recorded by the experiment. It is defined as

$$\varepsilon = \varepsilon_d \varepsilon_s = \frac{N_{\text{sel}} \;=\; \text{no. of selected events}}{N \;=\; \text{no. of events produced}}. \tag{5.1}$$

  The error on the efficiency can be estimated from the properties of the binomial distribution[1]:

$$\sigma_\varepsilon = \sqrt{\frac{\varepsilon(1-\varepsilon)}{N}}. \tag{5.2}$$

  The number of signal events expected to remain after the selection over a signal sample corresponding to the integrated luminosity $\mathcal{L}$ is:

$$\nu_s = \varepsilon \sigma_s \mathcal{L}, \tag{5.3}$$

  σ_s being the signal cross-section.

[1] This formula is only an approximation, since the error on the estimated mean of a binomial distribution is not symmetric; thus the formula fails when the estimated efficiency is near to zero or one.

- the *expected number of background events* ν_b, that is the expected number of candidates indicated by the selection when it is applied to a sample of background events corresponding to the integrated luminosity $\mathcal{L}$.

Therefore, if the data sample corresponding to the integrated luminosity $\mathcal{L}$ contains also the signal, the total number of expected candidates surviving the selection is $\nu_c = \nu_s + \nu_b$.

The efficiency and the background expectation can be estimated only applying the selection over appropriate Monte Carlo samples of which the content is exactly known.

5.1.2 Search experiment results

The output of the selection performed over the real data sample is a number of candidates n_c. The number of candidates is a Poisson variable, being ν_c the mean value, with the probability distribution

$$p(n_c, \nu_c = \nu_s + \nu_b) = \frac{e^{-\nu_c}}{n_c!} (\nu_c)^{n_c}. \tag{5.4}$$

If there is no signal evidence, i.e. if n_c is consistently similar to ν_b, the search experiment yields to an upper limit on the signal production cross-section σ_s. Two methods are generally applied depending on the amount of expected background and on the reliability of the background simulation. The method *without background subtraction* is used when ν_b is small. Since all the candidate events are assumed to come from signal while deriving the limit, this more direct method is preferred if the background is small or if the background simulation and thus the ν_b estimation are not reliable. In this case, in fact, the limit does not depend at all on the background expectation and no systematic uncertainties come from this source. On the contrary, the method *with background subtraction* must be used when the background level is significant. Since the limit is found comparing n_c with ν_b, the method needs a reliable estimation of ν_b.

In the squark searches the expected background is small enough that the first method can be always safely used. Thus only the method without the background subtraction is described.

Limit without the background subtraction

The method relies on the assumption that the expected number of background events is small and the number of the candidates surviving the selection applied to the data sample is compatible with this expectation. In this case it is reasonable to assume that none candidate is a "true" signal event but a background event. Thus an upper limit on the mean number of signal events or on the signal cross section can be set.

Being n_{oc} the observed number of candidates and $\nu_c = \nu_s + \nu_b$ the unknown mean number of candidates, it is possible to define the quantity ν_{oc} as the ν_c value such that the probability of finding in the search experiment $n_c \leq n_{oc}$ candidates is α:

$$P(n_c \leq n_{oc}; \nu_{oc}) = \sum_{i=0}^{n_{oc}} \frac{e^{-\nu_{oc}}}{i!} \nu_{oc}^i = \alpha. \tag{5.5}$$

Observed Candidates n_{oc}	Upper Limit 95% C.L. ν_{oc}
0	3.0
1	4.7
2	6.3
3	7.7

Table 5.1: 95% C.L. upper limits ν_{oc} for some values of the number of observed candidates n_{oc}.

The parameter ν_{oc} can be extracted numerically and it is found to be a monotonically increasing function of ν_{oc}. It turns out that

$$\alpha = P(n_c \leq n_{oc}; \nu_{oc}) = P'(\nu_c \geq \nu_{oc}; n_{oc}) = 1 - P'(\nu_c < \nu_{oc}; n_{oc}), \tag{5.6}$$

where $P'(\nu_c \geq \nu_{oc}; n_{oc})$ is the probability to have ν_c greater than or equal to ν_{oc} when the observed candidates are n_{oc} in number. More precisely, ν_{oc}, which is a random variable depending on n_{oc}, would be less than or equal to the "true" value ν_c in a fraction α of a large number of repeated experiments. Writing

$$P'(\nu_c \geq \nu_{oc}; n_{oc}) \geq 1 - \alpha, \tag{5.7}$$

one realizes that the probability of the mean number of candidates, i.e. the unknown "true" value ν_c to be less than or equal to ν_{oc} is not less than $1 - \alpha$. The quantity $1 - \alpha$ is referred as *confidence level* and ν_{oc} is known as the upper limit for ν_c within that confidence level. It is evident that a small value of α is chosen to set the limits. Usually α is 0.05 and the limits are set at 95% of confidence level (95% C.L.). Table 5.1 shows ν_{oc} (95% C.L.) for some values of n_{oc}.

The upper limit on the mean number of candidates ν_{oc} can be translated in an upper limit on the signal cross section using the relation (5.3). To be conservative one assumes that in ν_{oc} the background component is negligible.

5.1.3 Selection optimization

From the above discussion it turns out that the obtainable limit within an available data sample depends both on the signal efficiency and on the expected background. The selection can be optimized in order to get the signal efficiency and the background expectation corresponding to the best obtainable limit. The so called $\overline{\sigma}_{95}$ or $\overline{n}_{95}$ *criterion* can be used on purpose [79]. Let's define $\overline{\sigma}_{95}$ as the average of the expected upper limit at 95%C.L. on the signal cross-section in the assumption that no signal is observed, i.e. all candidates are background. $\overline{\sigma}_{95}$ depends on the signal efficiency ε and on the expected amount of background ν_b. Since n_{oc} follows a Poisson distribution with mean ν_b, it turns out that

$$\overline{\sigma}_{95} = \frac{1}{\varepsilon\mathcal{L}} \sum_{i=0}^{\infty} \nu_{oc}(i, 0.05) \frac{e^{-\nu_b}}{i!} \nu_b^i = \frac{e^{-\nu_b}}{\varepsilon\mathcal{L}} \left(3.00 + 4.74\nu_b + 6.30\frac{\nu_b^2}{2} + 7.75\frac{\nu_b^3}{6} + ...\right) \tag{5.8}$$

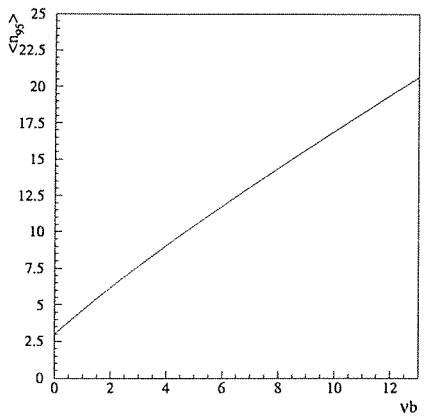

Figure 5.1: $\overline{n}_{95}$ as a function of ν_b assuming $\varepsilon = 1$.

where $\nu_{oc}(i, \alpha)$ is the upper limit in case of i candidates observed within $1 - \alpha$ confidence level. The average limit can be expressed also in terms of number of produced signal events defining the quantity $\overline{n}_{95} = \overline{\sigma}_{95}\mathcal{L}$. The optimization criterion asks the selection to minimize $\overline{\sigma}_{95}$ or $\overline{n}_{95}$.

To get completely unbiased selection the optimization is performed only at the Monte Carlo simulation level using the estimated signal efficiency and the background expectation. Since the number of kinematic variables used in the squark searches is consistent a dedicated program based on the `MINUIT` package [80] is used to minimize the $\overline{n}_{95}$ quantity, a function of the cuts parameters.

Fig. 5.1 shows $\overline{n}_{95}$ as a function of ν_b assuming $\varepsilon = 1$. Since $\overline{n}_{95}$ results only inversely proportional on the efficiency it is evident that $\overline{n}_{95}$ increases much faster while ν_b is increasing than while ε is decreasing. If the luminosity of the sample for which the selection has to be optimized increases, the general consequence of the $\overline{n}_{95}$ criterion is a greater rejection of the background (harder cuts) rather than an improvement of the signal efficiency (looser cuts).

In the squark searches case the $\overline{n}_{95}$ procedure has not been strictly applied only for the cuts used to reject the $\gamma\gamma \rightarrow q\overline{q}$ background in case it is dominant. The reason is that the simulations for that processes are thought to be not satisfactory as discussed in section 4.3. Moreover the statistics of the $\gamma\gamma \rightarrow q\overline{q}$ is relatively small with respect to the other Monte Carlo samples (only five times the data luminosity) as a consequence of their huge cross section. The cuts against $\gamma\gamma$ background are thus tighter with respect to the values that the $\overline{n}_{95}$ procedure would suggest.

5.2 The event variables

In this section the quantities used in the selections are defined and briefly discussed with respect to their background rejection power. In the following *particle* or *reconstructed particle* means the object coming as output from the energy flow algorithm (see section 3.3.3). Each particle is identified as charged particle, neutral hadron or photon. A charged particle

can be identified as e or μ by the criteria described in section 3.3.2.

The event variables used within this work are:

- the number of good charged tracks $N_{\rm ch}$, also know as *event multiplicity*. It is small for purely leptonic events and much bigger for hadronic events where the fragmentation tracks are present. The impact parameters d_{0i} and z_{0i} (see section 3.3.1), the momentum $\vec{p}_i$ and the charge hypothesis Q_i are available for the i-th charged track, $i = 1, ..., N_{\rm ch}$ the tracks being ordered in decreasing momentum.

- The energy E_{ℓ_j}, where j runs over all the particles identified as μ or e ordered in decreasing energy.

- The visible mass $M_{\rm vis}$, defined as the invariant mass of the reconstructed particles. The hadronic component of the visible mass can be estimated computing the visible mass excluding the most energetic particle identified as lepton ($M_{\rm vis}^{{\rm ex}\,\ell_1}$) or excluding the two most energetic particles identified as leptons ($M_{\rm vis}^{{\rm ex}\,\ell_1\ell_2}$).

- The total visible energy $E_{\rm vis}$, defined as the total energy of all reconstructed particles; $E_{\rm vis}^{\rm NH}$ is the visible energy coming from particles reconstructed as neutral hadrons; $E_{\rm vis}^{\rm ch}$ the visible energy coming from charged particles; $E_{\rm vis}^{\gamma}$ the visible energy coming from particles reconstructed as photons (thus including also neutral pions contribution from $\pi^0 \rightarrow \gamma\gamma$).

- The transverse $p_{\rm t}$ and longitudinal p_z components, with respect to the beam axis, of the total momentum $\vec{p}_{\rm vis}$. The total momentum $\vec{p}_{\rm vis}$ is computed over all reconstructed particles. The contribution to $p_{\rm t}$ coming from the charged tracks is indicated with $p_{\rm t}^{\rm ch}$, while $p_{\rm t}$ computed excluding the particles reconstructed as neutral hadrons is indicated with $p_{\rm t}^{{\rm ex}\,{\rm NH}}$.

- The missing momentum $\vec{p}_{\rm miss} = \vec{p}_{\rm initial\,state} - \vec{p}_{\rm vis}$, where $\vec{p}_{\rm initial\,state} = \vec{p}_{e^+} + \vec{p}_{e^-} \sim 0$ is the initial state momentum.

- The missing energy $E_{\rm miss} = \sqrt{s} - E_{\rm vis}$, since $\sqrt{s}$ is the initial state energy.

- The missing mass $M_{\rm miss} = \sqrt{E_{\rm miss}^2 + |\vec{p}_{\rm miss}|^2}$.

- The energy $E(\phi_{\vec{p}_{\rm miss}} \pm 15°)$ detected in a wedge of 30° of azimuthal angle with respect to the $\vec{p}_{\rm miss}$ direction.

- The energies $E_z^{\bowtie 12°}$ and $E_z^{\bowtie 30°}$ measured in a cone around the beam axis in both directions of 12° and 30° respectively.

- The *thrust* $T_{\rm thrust}$ defined as:

$$T_{\rm thrust} = \max_{\hat{n}} \frac{\sum_i |\vec{p}_i \cdot \hat{n}|}{\sum_i |\vec{p}_i|} = \frac{\sum_i |\vec{p}_i \cdot \hat{\rm a}_{\rm thrust}|}{\sum_i |\vec{p}_i|} \tag{5.9}$$

  where i runs over all reconstructed particles. The direction $\hat{\rm a}_{\rm thrust}$ is known as *thrust axis* or *event axis*. The thrust $T_{\rm thrust}$ ranges between 0.5, for open events, and 1, for events with two well collimated jets. By using the thrust axis the event can be divided into two hemispheres 1 and 2, with respect to the plane normal to the thrust axis passing trough the origin.

- The *acollinearity angle* $\Phi_{\rm acol}$ is the angle between $\vec{p}^{\rm h1}$ and $\vec{p}^{\rm h2}$, $\vec{p}^{\rm h1}$ and $\vec{p}^{\rm h2}$ being the total momenta of the tracks whose momenta point in the hemispheres 1 and 2 respectively. If all of the produced particles in an event are detected, the total visible momentum must be zero. In this case the momentum directions of the two event hemispheres are about back-to-back and $\Phi_{\rm acol}$ distribution results peaked at 180°.

- In the case of events where an ISR photon or an undeflected electron goes undetected inside the beam pipe (i.e. $q\bar{q}\gamma$ or $\gamma\gamma$ events), the acollinearity results far from 180° value as a consequence of z imbalance of the momentum components. In this case, it is more effective to consider the *acoplanarity angle* $\Phi_{\rm acop}$ defined as the angle between the momenta $\vec{p}_{\rm t}^{\rm h1}$ and $\vec{p}_{\rm t}^{\rm h2}$, that are the hemisphere momenta projected in the transverse plane. The acoplanarity is peaked at 180° for events that are essentially balanced in the transverse plane.

- If the event is strongly unbalanced along the z direction, as it occurs for $\gamma\gamma$ with large p_z, also the event axis may come out to be close in direction to the z axis with the net result that all or a great part of the tracks are contained in only one hemisphere. The other hemisphere may contain few soft tracks with a total momentum small and probably poorly measured. The acoplanarity would result largely inaccurate. It is more effective in this case to project the event into the plane transverse to the beamline, to calculate the two-dimensional thrust axis, and then divide the event into two hemispheres by a plane perpendicular to this axis. The *transverse acoplanarity angle* $\Phi_{\rm acop_T}$ is the angle between the two-dimensional hemisphere axes. The behaviour of the transverse acoplanarity is similar to the one of the $\Phi_{\rm acop}$, but more robust against very peculiar $\gamma\gamma$ events.

- $\theta_{\rm scat}$ and $\theta_{\rm point}$ are two angles computed assuming the event to be a $\gamma\gamma$ with one of the two electrons undeflected and the other not detected, i.e. as a consequence of some inefficiency. $\theta_{\rm scat}$ is the angle of the undetected scattered electron with respect to the beam line. It is reconstructed from the visible momentum and energy assuming the other electron to escape parallel to the z axis[2]. $\theta_{\rm point}$ is the polar angle of nearest calorimetric deposits with respect to the reconstructed scattered electron directions. The $\gamma\gamma \rightarrow q\bar{q}$ events having an over estimated $p_{\rm t}$ due to bad detection of a scattered electron have a large $\theta_{\rm scat}$ and a small $\theta_{\rm point}$ since the reconstructed electron direction points toward the deposit. For $\gamma\gamma$ events where the electron is not scattered in a sensitive region of the detector, $\theta_{\rm scat}$ is peaked at 0° and $\theta_{\rm point}$ will be randomly distributed being uncorrelated with $\theta_{\rm scat}$.

- The energies $E_{\ell_i}^{<30^\circ}$ detected in a cone of 30° with to the direction of the i-th particle reconstructed as lepton.

- The energies $E_{\rm NH_i}$ of the i-th particle reconstructed as a neutral hadron. The ordering is decreasing in energy.

- The energy $E_{\rm jet_i}$, momentum $p_{\rm jet_i}$, number of charged tracks $N_{\rm ch}{}^{\rm jet_i}$ of the i-th jet, where i runs over the reconstructed jets[3] ordered in decreasing energy.

[2]There are two possible solutions for $\theta_{\rm scat}$. Both have to satisfy the cut on $\theta_{\rm scat}$ below described.

[3]The particles produced in the decay of a quark or a τ lepton are globally referred as *jet* since they are

- The event probability $P_{\rm uds}$ quantifies the compatibility of the event with respect to the presence of light quarks u, d, s that have no lifetime. Requiring a small $P_{\rm uds}$ means requiring the event to be characterized by the production of heavy quarks with consistent lifetime, like b quarks. For that the $P_{\rm uds}$ event variable is referred as b-*tag variable.*

  The b-tag variable is constructed by using the `QIPBTAG` algorithm [82]. First two jets are formed using the `JADE` clustering algorithm[4]. Then the algorithm detects the presence of B hadrons using S_{r_0}, the three-dimensional impact parameter significance of a track; this quantity is defined to be the distance of closest approach of the track r_0 to the reconstructed primary vertex (see section 3.3.1), divided by the estimated error on that distance. It is given a positive/negative sign, according to whether the track passes closest to the estimated B hadron flight path down/up-stream of the primary vertex. The flight path is the momentum vector of the nearest jet forced through the primary vertex.

  Ignoring detector resolution, decay tracks from B hadrons have a positive S_{r_0}, while decay tracks from particles with no lifetime have a null S_{r_0}. The finite detector resolution smears these distributions; the decay tracks in b events still tend to have positive significance, but the significance distribution will have a small negative part. The decay tracks with no lifetime information form a significance distribution that is evenly distributed on the positive and negative sides. The positive part of the overall significance distribution contains the lifetime information while the negative part can be used to measure $\rho(S_{r_0})$, the intrinsic S_{r_0} resolution.

  For each track i, `QIPBTAG` defines a quantity $\alpha_i = \int_{S_{r_0}{}_i}^{\infty} \rho(x)dx$. This quantity is related to the probability that a track comes from the primary vertex, and it is used to give the event probability $P_{\rm uds} = \Pi \sum_{j=0}^{N_{\rm ch}-1} \frac{(-\ln \Pi)^j}{j!}$ (where $\Pi = \prod_{i=1}^{N_{\rm ch}} \alpha_i$) for the charged

close to the decaying particle direction and thus well collimated. Appropriate algorithms exist to cluster together a set of reconstructed particles into "jets". The `DURHAM` algorithm [81] used here proceeds as follows:

1. all possible pairs between the particles to be clustered are formed, and the quantity
$$M_{ij}^2 = 2[\min(E_i, E_j)]^2(1 - \cos\theta_{ij}) \tag{5.10}$$
is evaluated, where
$$\cos\theta_{ij} = \frac{\vec{p}_i \cdot \vec{p}_j}{|\vec{p}_i||\vec{p}_j|}, \tag{5.11}$$
E_i, $\vec{p}_i$ (E_j, $\vec{p}_j$) being respectively the energy and the momentum of the i-th (j-th) particle.
2. the pair with the minimum value of M_{ij}^2 is replaced with a pseudo-particle with energy $E_i + E_j$ and momentum $\vec{p}_i + \vec{p}_j$,
3. the first two step are iterated over the set of pseudo-particles and survived particles until the quantity $y_{ij} \equiv M_{ij}^2/E_{\rm tot}^2$ ($E_{\rm tot} = \sum_i E_i$) exceeds a given value $y_{\rm cut}$ or the number of clusters is equal to a given value $n_{\rm cut}$. The clusters so obtained represent reconstructed jets.

[4]The `JADE` clustering algorithm [83] is equal to the `DURHAM` algorithm once the quantity M_{ij} is defined as follows:
$$M_{ij}^2 = 2E_iE_j(1 - \cos\theta_{ij}). \tag{5.12}$$

particles of the event to have come from the main interaction point. By construction, this quantity has a uniform distribution between 0 and 1 for events in which all the tracks come from the primary vertex. This is generally the case when the jets in the event are formed from the decay and hadronization of u, d, or s quarks. In the case of c or b quarks production instead, long-lived hadrons are formed and then subsequently decay; some of the tracks in the event will therefore come from a secondary vertex. The distribution of P_{uds} in this case will be shifted toward 0. This shift is more pronounced when b quarks are produced, since B hadrons are longer lived than D hadrons. A very small value of P_{uds} therefore tags the event as containing b quarks.

- The electromagnetic calorimeter ECAL measures the particle signal during a fixed gate window, which is synchronous with the bunch crossing. The measurement occurs by sampling the gate window in 8 time intervals, separated by 512 ns. From these 8 samples a linear interpolation is used to find the half-height, giving a measurement of the arrival time of the signal with a resolution of $\sim$ 20 ns. By using this time measurement a signal can be associated or not to a given bunch crossing. With t_{min} and t_{max} we respectively mean the minimum and the maximum ECAL signal time with respect to the beam crossing time for a given event.

- For a charged track, the specific ionization loss in a given particle hypothesis can be defined by the relation (3.5); in the following the specific ionization loss in the muon hypothesis R_{μ}^{I} will be used.

5.3 The selections for squark searches

The squark searches described in this work rely on three different sets of selections in order to cope with the several topologies discussed in chapter 2. They are:

- the *acoplanar jets selection* (AJ) designed for the processes $e^+e^- \rightarrow \tilde{t}\bar{\tilde{t}} \rightarrow c\bar{c}\chi\chi$ and $e^+e^- \rightarrow \tilde{b}\bar{\tilde{b}} \rightarrow b\bar{b}\chi\chi$; the AJ selection is used also for degenerate squarks couple production process $e^+e^- \rightarrow \tilde{q}\bar{\tilde{q}} \rightarrow q\bar{q}\chi\chi$; for the sbottom production channel the AJ selection is improved by using b-tagging techniques;

- the *acoplanar jets plus leptons selection* (AJL) designed for the process $e^+e^- \rightarrow \tilde{t}\bar{\tilde{t}} \rightarrow b\bar{b}\ell\ell'\tilde{\nu}\tilde{\nu}'$;

- the long living hadron selection (LLH) designed for the long living stop hadrons.

Fig. 5.2 shows the total energy distribution for data events in comparison with the simulated total background and some simulated $\tilde{t} \rightarrow c\chi$ distributions corresponding to a signal production cross section of 0.1 pb. The events above the LEP energy are due to the smearing from the detector resolution. The main background sources are also separately shown. We can notice that the $\gamma\gamma \rightarrow q\bar{q}$ events dominate the background where the small Δm signal is expected, even if the plot has been produced with some preliminary cut ($p_t > 3\%\sqrt{s}$, $M_{\mathrm{vis}} > 4\,\mathrm{GeV}/c^2$, $N_{\mathrm{ch}} > 4$, $|\cos\theta_{\vec{p}_{\mathrm{miss}}}| < 0.9$ and $E_z^{\bowtie 12^\circ} < 0.1\sqrt{s}$) to partially reject the $\gamma\gamma \rightarrow q\bar{q}$ events. On the contrary at higher Δm values the $q\bar{q}$ and four-fermion events dominates the background. For that reason both AJ and AJL selections consist of two sub-selections ("low Δm" and "high Δm") to cope with the dependence of the topologies on

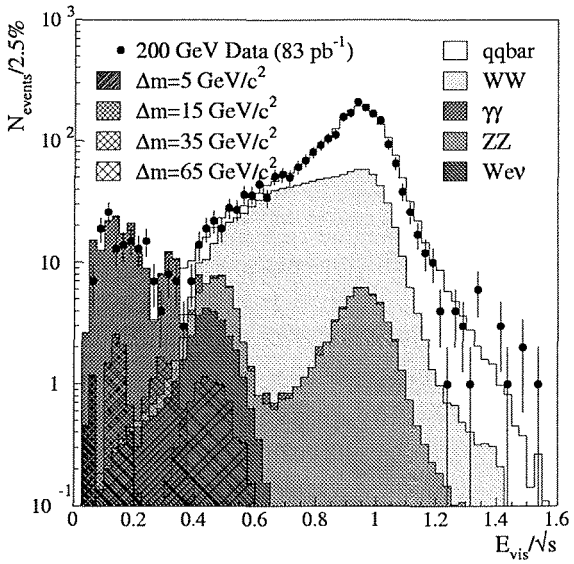

Figure 5.2: Total energy distribution for 200 GeV data and Monte Carlo backgrounds. The signal of a 95 GeV/c^2 stop for various Δm values is also shown, the signal cross section set at 0.1 pb.

Δm, the difference in mass between the squark and the LSP. The "low Δm" subselection essentially features more stringent cuts against $\gamma\gamma$ background.

If the signal we are looking for is very dependent on some unknown parameter ξ of the model (i.e. in the squark case the visible mass is very dependent on Δm) a so called *sliding cut* can be effectively applied. In the sliding cut the condition $C(\xi)$ on the event variable v to declare the event acceptable depends on the parameter ξ:

$$v < C(\xi). \tag{5.13}$$

As a consequence of the sliding cut the event for which the variable v assumes the value v_0 can be a candidate only in the parameter regions where $C(\xi) > C(\xi_0) = v_0$.

Also the LLH selection consists of two sub-selections: the *intermediate lifetime* LLH selection is designed to tag heavy hadrons decaying in the detector volumes, the *long lifetime* LLH selection to tag heavy hadrons that remain stable inside the detector.

5.3.1 Data samples and optimization

The data samples usable by the analysis working groups to produce physics results consist of events found to meet the requirements that ensure the full detector functionality and that allow to discard events suffering hardware or data acquisition problems. Moreover the events can be discarded within a given analysis if parts of event informations that are essential for that analysis are found to be unreliable. This preliminary selection is made on the basis of a classification of data performed by a team of experts using the database of hardware problems compiled during the data taking and also the output of appropriate

$\sqrt{s}$ (GeV)	$\mathcal{L}$ (pb^{-1})
189	174.20 ± 0.20
192	29.042 ± 0.084
196	80.109 ± 0.142
200	82.901 ± 0.147
202	34.533 ± 0.096

Table 5.2: Data samples and luminosities used in this work from 1998 and 1999 data taking.

monitoring programs (*run quality*), which checks for inconsistencies or defects directly on the data, after the acquisition.

The criteria that have to be satisfied from the event to be accepted are the following:

1. the run which the event belongs to must not have been flagged as "bad", i.e. none of the subdetectors seriously malfunctioning;
2. the VDET is fully operational to prevent poor tracking performances;
3. the energy flow measurement is reliable, i.e. HCAL, ECAL and the tracking system fully operational;
4. the LCAL is reliable as luminosity detector as well as low-angle electromagnetic calorimeter.

The available data samples from 1998 and 1999 data taking that result from the application of the above criteria are summarized in table 5.2. This data sample does not contain the full 1999 statistics but the official selection for the LEPC (LEP Committee) of November 8th, 1999. In particular $\sim 1.2\,\mathrm{pb}^{-1}$ are missed at 200 GeV and $\sim 7\,\mathrm{pb}^{-1}$ at 202 GeV.

Ideally speaking each data sample at each center-of-mass energy would require a dedicated optimized selection. This is clearly unpractical since it would imply huge Monte Carlo productions of background samples and signal samples. Moreover it is evident that no big changes are expected for few GeV of energy increment either in the signal and background event shapes.

The LLH selections are completely new and still preliminary and have been applied to 189 GeV and 192 GeV data samples. They have been designed using signal and background Monte Carlo samples produced at 189 GeV and optimized for the luminosity available at that energy. Since the difference in energy is small and the luminosity at 192 GeV is not large enough to justify a new dedicated optimization, the same selections have been used unchanged for the 192 GeV data sample.

The AJ and AJL selections presented here are designed for the data taken by ALEPH in 1999 at a centre-of-mass energies between 196 GeV and 202 GeV. They are mainly the 189 GeV AJ and AJL selections [84] apart small changes suggested by the $\overline{n}_{95}$ procedure in order to optimize the performances for the data samples at 196, 200 and 202 GeV. The 189 GeV selections have been used unchanged for the sample at $\sqrt{s} = 192$ GeV. The optimization has been done for the total luminosity available at the energies between 196 GeV and 202 GeV using signal and background Monte Carlo samples produced at 200 GeV. In order to take into account that the data sample for which the selections have to be used

consists of three different energies, the definition of $\overline{n}_{95}$ has been modified according to the formula (7.5). That formula allows to combine several samples in a limit setting procedure considering the signal cross section dependency on the center-of-mass energy.

As far as the background expectation it concerns, all Standard Model background processes are far from any thresholds or resonances. Therefore, since the difference in the center-of-mass energy is limited to few GeV, the background expectations at 196 and 202 GeV of AJ and AJL selections are obtained just rescaling to the luminosity the 200 GeV expectations given by the Monte Carlo simulations. The same procedure has been used to evaluate the 192 GeV background of the LLH selections starting from the simulation performed at 189 GeV.

The efficiencies can be assumed unchanged in case of a small variation of the center-of-mass energy. Therefore the AJ AJL and LLH selections efficiencies estimated on 189 GeV signal Monte Carlo samples have been used for the 192 GeV analysis, while the AJ and AJL selections efficiencies estimated on 200 GeV signal Monte Carlo samples have been used for the 196 GeV and 202 GeV analyses.

5.3.2 The acoplanar jets selection AJ

The acoplanar jet selection consists of two sub-selections for "low Δm" case and "high Δm" case. They have in common a preselection against the $\gamma\gamma \rightarrow q\overline{q}$ background:

- $N_{ch} > 3$,
- $M_{vis} > 4\,\mathrm{GeV}/c^2$,
- $p_t > 2\%\sqrt{s}$.

The low angle calorimeter LCAL is crucial to detect the electrons at small angle from the $\gamma\gamma$ events. As a consequence of its mechanical structure (see section 3.2.8), it has a vertical crack where the detection efficiency is smaller. The p_t would be over estimated in a $\gamma\gamma$ where a low angle electron would escape undetected. Thus the following cut is also applied:

- $p_t > 4\%\sqrt{s}$, if the $\vec{p}_{miss}$ azimuthal angle falls within 15° from the LCAL cracks.

The $\gamma\gamma \rightarrow q\overline{q}$ events can be also characterized by $\vec{p}_{miss}$ close to the beam. In fact the scattered electron can be partially or completely undetected since it escapes at very small angle in the peripheral regions of the luminosity monitors or even along the beam pipe. To reject these events the following cuts are useful:

- $|\cos\theta_{\vec{p}_{miss}}| < 0.95$,
- $E_z^{\bowtie 12^\circ} < 5\%\sqrt{s}$,
- $\Phi_{acop} < 175^\circ$,
- $\Phi_{acop_T} < 175^\circ$.

The cuts in acoplanarity are also useful against $q\overline{q}$ events.

Fig. 5.3(a), fig. 5.3(b) and fig. 5.4(a) show some distributions of variables relevant for the preselection (N_{ch}, $p_t/\sqrt{s}$ and $|\cos\theta_{\vec{p}_{miss}}|$ respectively) for data and Monte Carlo. The AJ

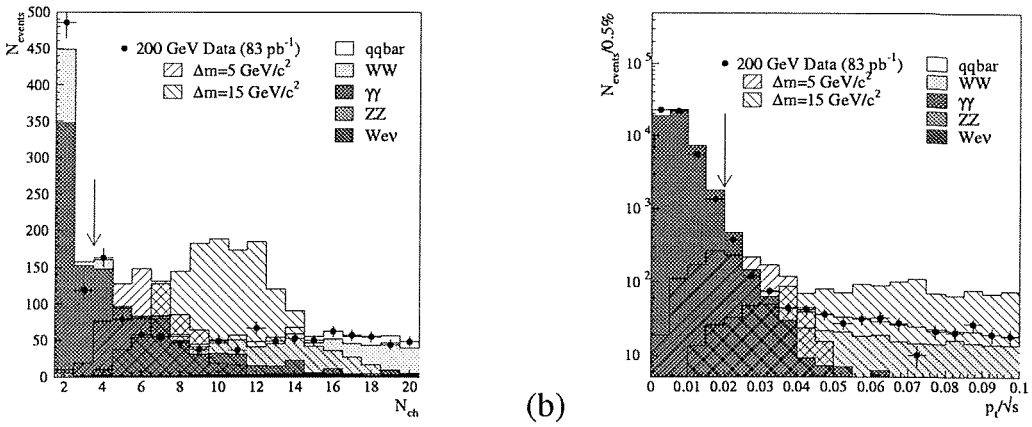

Figure 5.3: $N_{\rm ch}$ distribution (a) and $p_{\rm t}/\sqrt{s}$ distribution (b) for data and Monte Carlo. The arrows indicate the cut positions. The expected 20 pb signal distributions for $m_{\tilde{\rm t}} = 95\,{\rm GeV}/c^2$ and two Δm values are also shown.

preselection cuts (except the cut on the plotted variable) have been used to produce the plots that also show the expected signal distributions for $m_{\tilde{\rm t}} = 95\,{\rm GeV}/c^2$ and $\Delta m = 5, 15\,{\rm GeV}/c^2$, normalized to a 20 pb cross section[5]. In all cases it is evident the huge $\gamma\gamma$ contribution to background in the small Δm region.

5.3.3 The "low Δm" AJ selection

Since the $\gamma\gamma \to {\rm q\bar{q}}$ background is dominant, in this region the $\gamma\gamma \to {\rm q\bar{q}}$ rejection is so crucial to require extra cuts with respect to the already good preselection in order to cope with the detection problem that ALEPH shows in some particular kind of events. Moreover some other Standard Model process needs dedicated cuts to be rejected.

The cut on the visible mass is harder than the preselection one, but only in the highest Δm region:

- $M_{\rm vis} > 7.5\,{\rm GeV}/c^2$ if $\Delta m > 7\,{\rm GeV}/c^2$.

The $\gamma\gamma \to {\rm q\bar{q}}$ events are characterized by low momentum tracks. Sometimes the energy flow (see section 3.3.3) fails to associate low momentum tracks to their calorimetric deposits yielding to spurious calorimetric objects that are badly identified as neutral. Thus the momentum of those tracks is double counted and the $p_{\rm t}$ is over estimated. The $p_{\rm t}$ cut is tightened by using the "charged" components $p_{\rm t}^{\rm ex\,NH}$ and $p_{\rm t}^{\rm ch}$ of $p_{\rm t}$ and asking for not too much energetic neutral hadrons:

- $p_{\rm t}^{\rm ex\,NH} > 2\%\sqrt{s}$,
- $p_{\rm t}^{\rm ch} > 1\%\sqrt{s}$,
- $E_{\rm NH_1} < 30\% M_{\rm vis}$.

[5]The same normalization will be used in all plots shown in this chapter if not differently stated.

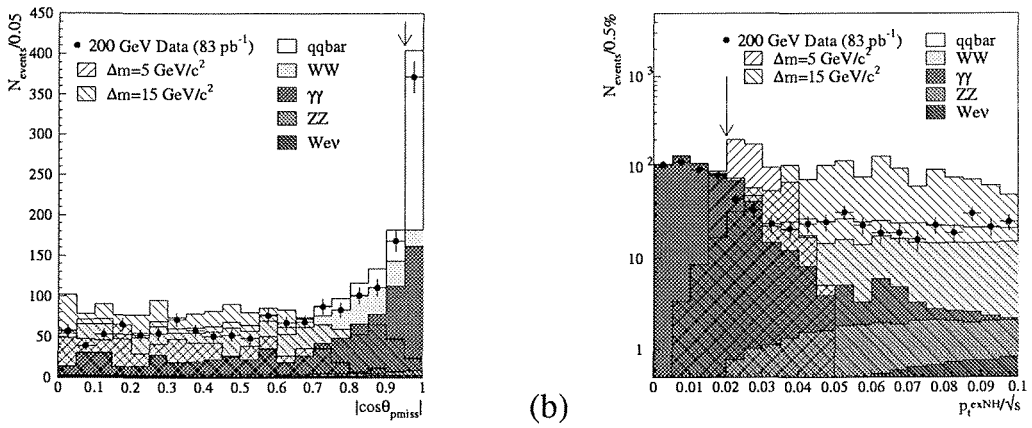

Figure 5.4: $|\cos\theta_{\vec{p}_{\rm miss}}|$ distribution (a) and $p_{\rm t}/\sqrt{s}$ distribution (b) for data and Monte Carlo. The arrows indicate the cut positions. The expected 20 pb signal distributions for $m_{\tilde{\rm t}} = 95\,{\rm GeV}/c^2$ and two Δm values are also shown.

The data and Monte Carlo $p_{\rm t}^{\rm ex\,NH}/\sqrt{s}$ distribution is shown in fig. 5.4(b) after the preselection cuts.

A dangerous background for the "low Δm" AJ selection comes from the $\gamma\gamma \to {\rm q\bar{q}}$ events with low visible mass. These events are likely to have the scattered electron at such a small angle that often is poorly detected. Against these events the following cuts are useful:

- $M_{\rm miss} < 25 M_{\rm vis}$,
- $E_z^{\bowtie 12^\circ} = 0$,
- $|\cos\theta_{\vec{p}_{\rm miss}}| < 0.8$,
- $|\cos\theta_{\hat{\rm a}_{\rm thrust}}| < 0.75$,
- $\theta_{\rm point} > 5^\circ$. The cut is reinforced for large $\theta_{\rm scat}$ by using the bidimensional cut $\theta_{\rm point} > 60^\circ - 10 \cdot \theta_{\rm scat}$ that rejects also events with small $\theta_{\rm scat}$.

The bidimensional cut can be seen in fig. 5.5 together with the $\Delta m = 15, 20, 25, 30\,{\rm GeV}/c^2$ signal and the $\gamma\gamma$ background distributions (no cut applied).

A special set of cuts is also needed to reject the $\gamma\gamma \to \tau^+\tau^-$ events. Since in preselection $N_{\rm ch}$ is required to be at least 4, the surviving $\gamma\gamma \to \tau^+\tau^-$ have a τ decaying in three charged tracks (*three-prong*) and the other decaying in one charged track (*one-prong*). To prevent these events to be selected the following cuts are applied:

- $M_{\rm vis} > 8\,{\rm GeV}/c^2$ (if $N_{\rm ch} = 4$),
- $\Phi_{{\rm acop}_{\rm T}} < 150^\circ$ or $M_{\rm vis} > 20\,{\rm GeV}/c^2$ (if $N_{\rm ch} = 4$),
- forcing only two jets to be reconstructed in the event, ${N_{\rm ch}}^{\rm jet_1} > 1$ and ${N_{\rm ch}}^{\rm jet_2} > 1$ (if $N_{\rm ch} = 4$).

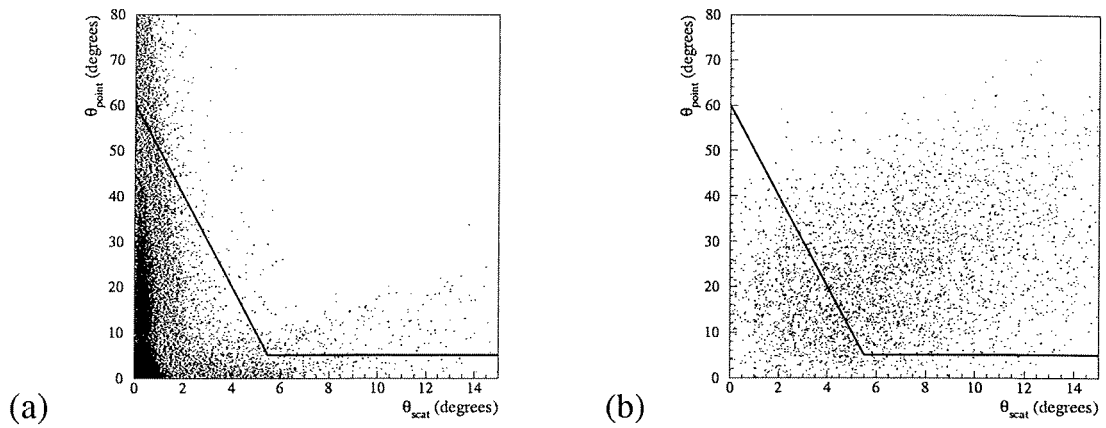

Figure 5.5: Bidimensional distribution θ_{point} vs. θ_{scat} for $\gamma\gamma \rightarrow q\bar{q}$ Monte Carlo events (a) and $\Delta m = 15, 20, 25, 30\,\text{GeV}/c^2$ signal (b). The solid line represents the applied cut.

The background still surviving the selections consists of four fermion processes with low visible mass. A cut on T_{thrust} is effective against the $Z\gamma^*$ events with the Z decaying into neutrinos. The WW and $We\nu_e$ are reduced by cutting on the visible energy. A cut on the hadronic visible mass is effective for the processes of the type WW $\rightarrow \ell\nu_\ell\tau\nu_\tau$, the τ subsequently undergoing a three-prong decay. Some $q\bar{q}\gamma$ events with energetic neutrinos from semileptonic heavy quark decay could have a consistent $\vec{p}_{\text{miss}}$. They are easily rejected asking the $\vec{p}_{\text{miss}}$ to be well isolated, that is a typical signature of supersymmetric processes. In particular:

- $T_{\text{thrust}} < 0.915$,
- $E_{\text{vis}} < 20\%\sqrt{s}$,
- $M_{\text{vis}}^{\text{ex}\,\ell_1} > 3\,\text{GeV}/c^2$,
- $E(\phi_{\vec{p}_{\text{miss}}} \pm 15°) < 25\%\sqrt{s}$.

5.3.4 The "high Δm" AJ selection

The four fermion processes are the most dangerous for the "high Δm" AJ selection. In fact the $\gamma\gamma$ events are safely rejected applying the following cuts, similar to the anti-$\gamma\gamma$ ones in the preselection and in the "low Δm" case:

- $N_{\text{ch}} > 6$,
- $p_{\text{t}} > 5\%\sqrt{s}$ and $p_{\text{t}} > 7.5\%\sqrt{s}$ if the $\vec{p}_{\text{miss}}$ azimuthal angle falls within 15° from the LCAL cracks,
- $p_{\text{t}} > 20\%E_{\text{vis}}$,
- $\theta_{\text{point}} > 5°$ or $\theta_{\text{scat}} > 15°$.

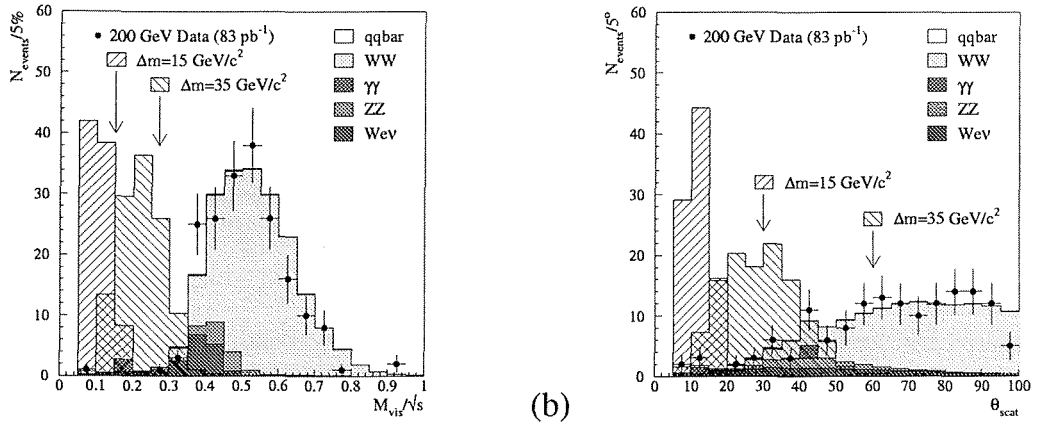

Figure 5.6: $M_{\rm vis}/\sqrt{s}$ distribution (a) and $\theta_{\rm scat}$ distribution (b) for data and Monte Carlo. The arrows indicate the cuts positions depending on Δm. The expected 2 pb signal distributions for $m_{\tilde{\rm t}} = 95\,{\rm GeV}/c^2$ and three Δm values are also shown.

With respect to the "low Δm" case these cuts are tighter since the "high Δm" signal is enough different from $\gamma\gamma$ events that harder cuts do not compromise the efficiency.

As in the "low Δm" selection it is necessary to guard against $\gamma\gamma$ events that have a large $p_{\rm t}$ due to a missed association between soft tracks and calorimetric deposits. This is done by using the following cuts:

- $E_{\rm vis}^{\rm NH} < 30\% E_{\rm vis}$ or only $E_{\rm vis}^{\rm NH} < 45\% E_{\rm vis}$ if $p_{\rm t}^{\rm ex\,NH} > 3\%\sqrt{s}$,
- $E_z^{\bowtie 30^\circ} < 30\% E_{\rm vis}$,
- $E(\phi_{\vec{p}_{\rm miss}} \pm 15^\circ) < 7.5\%\sqrt{s}$.

At this level only the four fermion processes like ZZ, WW, We$\nu_{\rm e}$ and Zγ^* survive to the selection. If a lepton is present in the final state normally its energy is large. The following cut on the leading lepton energy is useful in case that the lepton is charged:

- $E_{\ell_1} < 20\%\sqrt{s}$.

If the lepton is a neutrino the missing energy is consistent but also the visible mass due to the other particles is high, especially if they come from the decay of a massive boson like W or Z. For these events an upper cut on the visible mass is effective providing the cut to be looser when Δm increases:

-

$$M_{\rm vis} < \begin{cases} 0.15\sqrt{s} & \Delta m < 15\,{\rm GeV}/c^2 \\ (0.06 + 0.006 \cdot \frac{\Delta m}{{\rm GeV}/c^2})\sqrt{s} & 15\,{\rm GeV}/c^2 < \Delta m < 40\,{\rm GeV}/c^2 \\ 0.3\sqrt{s} & 40\,{\rm GeV}/c^2 < \Delta m \end{cases} . \quad (5.14)$$

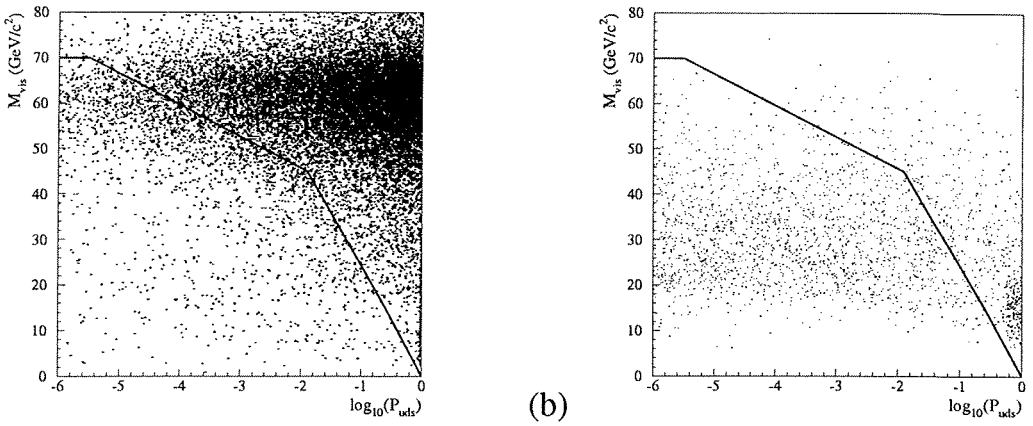

Figure 5.7: Bidimensional distribution $M_{\rm vis}$ vs. $\log_{10} P_{\rm uds}$ for Monte Carlo four fermion and $q\bar{q}\gamma$ events (a) and $\Delta m = 15 \div 45\,\mathrm{GeV}/c^2$ sbottom signal (b). The solid line represents the applied cut.

The $M_{\rm vis}/\sqrt{s}$ distribution is shown in fig. 5.6(a) for data and Monte Carlo after all "high Δm" AJ cuts except $M_{\rm vis}$ cut and $\theta_{\rm scat}$ cut. It is clear how the visible mass upper cut is very effective to discriminate signal from WW background.

The last cut for the "high Δm" AJ selection is needed to further reject the We$\nu_{\rm e}$ events for which the electron is not scattered enough and goes down in the beam pipe. An upper cut on $\theta_{\rm scat}$ is useful since in this case $\theta_{\rm scat}$ will give the scattering angle of the neutrino which tends to be large. Since this happens also for the signal, as far as the Δm increases the upper cut on $\theta_{\rm scat}$ is made dependent on Δm similarly to the cut on $M_{\rm vis}$:

•

$$\theta_{\rm scat} < \begin{cases} 30^\circ & \Delta m < 20\,\mathrm{GeV}/c^2 \\ -10^\circ + 2^\circ \cdot \frac{\Delta m}{\mathrm{GeV}/c^2} & 20\,\mathrm{GeV}/c^2 < \Delta m < 95\,\mathrm{GeV}/c^2 \\ \text{no cut} & 95\,\mathrm{GeV}/c^2 < \Delta m \end{cases} . \qquad (5.15)$$

Fig. 5.6(b) shows the $\theta_{\rm scat}$ distribution for data and Monte Carlo after all "high Δm" AJ cuts except $M_{\rm vis}$ cut and $\theta_{\rm scat}$ cut. Also the signal is reported now with a lower cross section (2 pb). Both the sliding cuts on $M_{\rm vis}$ and $\theta_{\rm scat}$ have been studied as a function of Δm following the $\overline{\rm n}_{95}$ prescription.

5.3.5 The AJ selection for the $\tilde{\rm b} \to {\rm b}\chi$ channel

The $e^+e^- \to \tilde{b}\bar{\tilde{b}} \to b\bar{b}\chi\chi$ topology is very similar to the $e^+e^- \to \tilde{t}\bar{\tilde{t}} \to c\bar{c}\chi\chi$ one. The selections are therefore quite similar and the only difference comes from the presence of b quarks in the final state. The b quarks are the heaviest quarks accessible at LEP and are characterized by a not negligible lifetime.

From the experimental point of view in the "low Δm" case it is possible to profit of the generally larger visible mass due to the presence of B hadrons. Thus the only difference

with respect to the "low Δm" AJ selection for $\tilde{t} \to c\chi$ is on the visible mass cut, here not dropped for lower Δm values:

- $M_{\rm vis} > 7.5\,{\rm GeV}/c^2$ for each Δm.

For the "high Δm" selection, the only difference is the use of the probability $P_{\rm uds}$. The sliding cuts on $M_{\rm vis}$ and $\theta_{\rm scat}$ are replaced by a cut on $T_{\rm thrust}$ plus a bidimensional cut in the plane $M_{\rm vis} - \log_{10} P_{\rm uds}$:

- $T_{\rm thrust} < 0.925$,
- the bidimensional cut is defined by interpolating the following three optimal cuts starting from the origin

$$M_{\rm vis} < \begin{cases} 15\,{\rm GeV}/c^2 & \log_{10} P_{\rm uds} = -0.6 \\ 45\,{\rm GeV}/c^2 & \log_{10} P_{\rm uds} = -1.9 \\ 70\,{\rm GeV}/c^2 & \log_{10} P_{\rm uds} < -5.5 \end{cases} . \qquad (5.16)$$

These cuts are effective against We$\nu_{\rm e}$, WW and and Zγ^*. Since these backgrounds are mostly present at large values of $M_{\rm vis}$, the cut on $P_{\rm uds}$ gets tighter as $M_{\rm vis}$ increases as shown in fig. 5.7 where the cut profile is visible over the signal and background distributions (no cut applied).

The b-tagging efficiency based on $P_{\rm uds}$ is essentially independent on the b quark boost since the impact parameter is almost a Lorentz invariant. Nevertheless if the b quark momentum gets very small, as it happens in $\tilde{b} \to b\chi$ for very small Δm, the b decay length gets small as well and the secondary vertex becomes really not visible. This is the reason why the $P_{\rm uds}$ cut would be not useful at all in the "low Δm" case.

5.3.6 The AJ selections efficiencies and backgrounds

The AJ selections applied to the $\tilde{t} \to c\chi$ yield to the efficiencies shown in fig. 5.8(a) as a function of Δm. The efficiency is shown for a stop mass value of $95\,{\rm GeV}/c^2$. Taking into account also the background expectations, shown in fig. 7.1, it turns out from the $\overline{n}_{95}$ behaviour shown in fig. 5.8(b) that the optimal switching point between "low Δm" and "high Δm" region is $\Delta m = 13\,{\rm GeV}/c^2$. The $200\,{\rm pb}^{-1}$ background in the "low Δm" region (~ 2.6 events for the loosest configuration of the cuts) is due almost completely to $\gamma\gamma \to q\overline{q}$ events (~ 1.2 events) and We$\nu_{\rm e}$ events (~ 1.2 events). In the "high Δm" region the main components come from We$\nu_{\rm e}$ processes (~ 5.5 events of ~ 9.1 events when the loosest cuts are applied) and ZZ processes (~ 1.6 events).

As far as the AJ plus b-tag are concerned, the resulting efficiencies are shown in fig. 5.9(a). The effectiveness of the b-tag cut is evident from the background expectation in the "high Δm" region ($\sim$ 1.1 events for $200\,{\rm pb}^{-1}$) with respect to the AJ selection without the b-tag. Fig. 5.9(b) shows that the optimal switching point in this case is $\Delta m = 20\,{\rm GeV}/c^2$. The AJ plus b-tag selection dominant backgrounds consist of We$\nu_{\rm e}$ (~ 0.5 events) and ZZ processes (~ 0.4 events) the remaining being $q\overline{q}$ processes. The AJ "low Δm" selection for the sbottom channels features slightly harder cut on the visible mass that reduces the background expectation from ~ 2.6 events to ~ 2.5 events.

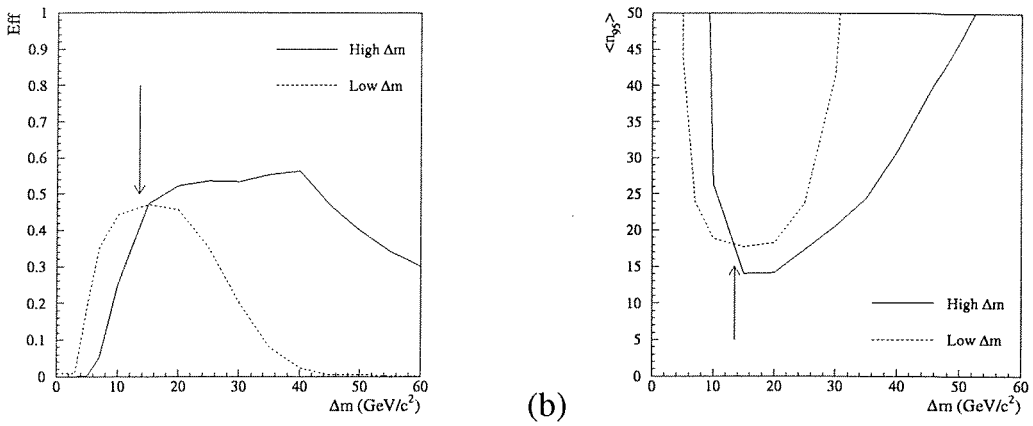

Figure 5.8: Efficiency (a) and $200\,\mathrm{pb}^{-1}$ $\bar{n}_{95}$ (b) for the AJ selection applied to 200 GeV $\tilde{t} \to c\chi$ signal. The arrows indicate the switching point.

5.4 The AJL selection

The experimental signature of the process $e^+e^- \to \tilde{t}\bar{\tilde{t}} \to b\bar{b}\ell\bar{\ell}\tilde{\nu}\bar{\tilde{\nu}}$ consists of two leptons and two acoplanar jets with missing energy and momentum. The presence of leptons makes easier the signal tagging with respect to the $\tilde{q} \to \tilde{q}\chi$ channels. Even if at low Δm values the lepton are softer and thus poorly identified, the event is however characterized by an useful higher multiplicity. Moreover the b quarks and leptons in the final state yield to large E_{vis} and M_{vis}. Unfortunately the b quark is generally too soft to apply successfully the b-tagging techniques. As usual a preselection is applied against $\gamma\gamma$ events:

- $N_{\mathrm{ch}} > 6$,
- $M_{\mathrm{vis}} > 6\%\sqrt{s}$,
- $E_{\mathrm{vis}} > 8\%\sqrt{s}$,
- $p_{\mathrm{t}} > 1.25\%\sqrt{s}$,
- $E_z^{\bowtie 12^\circ} < 2\,\mathrm{GeV}/c^2$,
- $\theta_{\mathrm{point}} > 50^\circ - 20 \cdot \theta_{\mathrm{scat}}$,
- $|p_z| < 18.6\%\sqrt{s}$.

The p_z cut is useful to reject the Z radiative returns in $q\bar{q}\gamma$ events as shown in fig. 5.10(a), where the $p_z/\sqrt{s}$ distribution for data and Monte Carlo is reported after the preselection cuts (except the p_z cut).

5.4.1 The "low Δm" AJL selection

A first set of the "low Δm" AJL selection is made up of a bulk of anti-$\gamma\gamma$ cuts. Since the multiplicity is generally higher for the signal with respect to the $\gamma\gamma \to q\bar{q}$ events, it turns

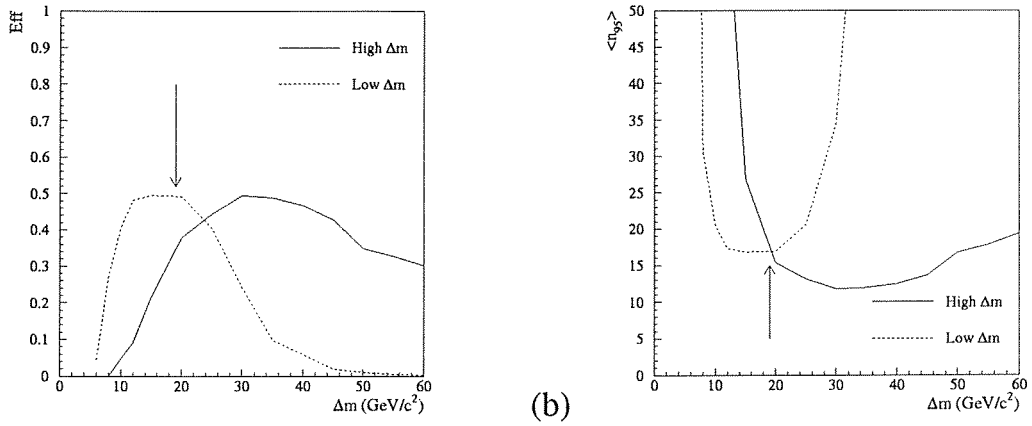

Figure 5.9: Efficiency (a) and $200\,\mathrm{pb}^{-1}$ $\overline{\mathrm{n}}_{95}$ (b) for the AJ selection applied to 200 GeV $\tilde{\mathrm{b}} \rightarrow \mathrm{b}\chi$ signal. The arrows indicate the switching point.

out useful to cut on the quantity

$$\overline{E_{\mathrm{ch}}^{\mathrm{ex}\,\ell_1}} = \frac{(\sum_{i=1}^{N_{\mathrm{ch}}} E_i) - E_{\ell_1}}{N_{\mathrm{ch}} - 1}. \tag{5.17}$$

that, if at least one lepton is identified, represents the mean energy of charged tracks excluding the leading lepton energy track. The $\overline{E_{\mathrm{ch}}^{\mathrm{ex}\,\ell_1}}/\sqrt{s}$ distribution is shown in fig. 5.10(b). $\overline{E_{\mathrm{ch}}^{\mathrm{ex}\,\ell_1}}$ is used together with more usual cuts:

- $\overline{E_{\mathrm{ch}}^{\mathrm{ex}\,\ell_1}} < 1\%\sqrt{s}$,
- $E_z^{\bowtie 12^\circ} = 0$,
- $E_z^{\bowtie 30^\circ} < 20\% E_{\mathrm{vis}}$,
- $|\cos\theta_{\vec{p}_{\mathrm{miss}}}| < 0.8$,
- $|\cos\theta_{\hat{\mathrm{a}}_{\mathrm{thrust}}}| < 0.8$,
- $p_{\mathrm{t}}^{\mathrm{ch}} > 0.75\%\sqrt{s}$ and $p_{\mathrm{t}}^{\mathrm{ex\,NH}} > 0.75\%\sqrt{s}$,
- $|p_z| < 30\% E_{\mathrm{vis}}$,
- $E_{\mathrm{vis}}^{\mathrm{NH}} < 35\% E_{\mathrm{vis}}$.

The leptons in the "low Δm" signal are soft and poorly identified. The events are then accepted even if no identified leptons are present. However, if there are no identified leptons above $1\%\sqrt{s}$ in energy, the p_{t} and θ_{point} cuts are reinforced:

- $p_{\mathrm{t}} > 2\%\sqrt{s}$ and $\theta_{\mathrm{point}} > 115^\circ - 20 \cdot \theta_{\mathrm{scat}}$ if $E_{\ell_1} < 1\%\sqrt{s}$.

Finally other three cuts are applied, the first two being effective against $\mathrm{q\bar{q}}\gamma$ events, the last being effective against the WW events:

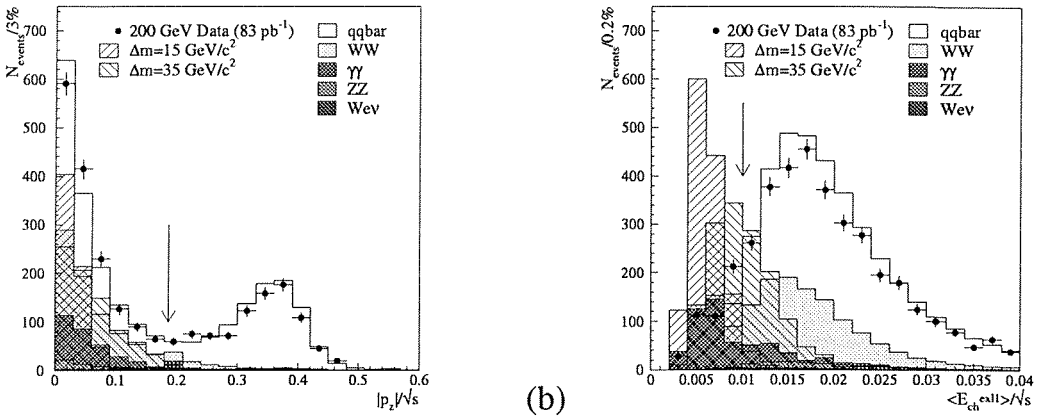

Figure 5.10: $p_z/\sqrt{s}$ distribution (a) and $\overline{E_{\mathrm{ch}}^{\mathrm{ex}\,\ell_1}}/\sqrt{s}$ distribution (b) for data and Monte Carlo. The arrows indicate the cut positions. The expected 20 pb signal distributions for $m_{\tilde{\mathrm{t}}} = 95\,\mathrm{GeV}/c^2$ and two Δm values are also shown.

- $100° < \Phi_{\mathrm{acop}} < 179°$,
- $T_{\mathrm{thrust}} < 0.9$,
- $M_{\mathrm{miss}} > 82.5\%\sqrt{s}$.

5.4.2 The "high Δm" AJL selection

In the "high Δm" signal the energy available for the leptons and quarks in the final state is higher, even if some missing mass is still to be expected since the sneutrinos escape. Energetic and isolated leptons are a typical signature:

- $M_{\mathrm{miss}} > 25\%\sqrt{s}$,
- $2\,\mathrm{GeV} < E_{\ell_1} < 86\,\mathrm{GeV}$,
- $E_{\ell_1}^{\sphericalangle 30°} < 2.7 \cdot E_{\ell_1}$.

The potential backgrounds consist as usual of $\gamma\gamma$ and four-fermion processes (WW, Zγ* and Weν_{e}) survived to the preselection. A first rejection of $\gamma\gamma$ events relies on the following cuts:

- $|\cos\theta_{\vec{p}_{\mathrm{miss}}}| < 0.95$,
- $\Phi_{\mathrm{acol}} < 174°$, $\Phi_{\mathrm{acop}} < 176°$ and $\Phi_{\mathrm{acop_T}} < 176°$.

As far as the four fermion processes are concerned, the N_{ch} cut within the preselection ensures that no purely leptonic events had survived. If leptons come from those processes they are both decay product of the same vector boson. Thus the visible mass computed without the identified leptons sits around the boson mass and also the visible mass is generally high. Thus cutting on the "hadronic masses" $M_{\mathrm{vis}}^{\mathrm{ex}\,\ell_1}$ and M_{vis} is effective. In this way the four-fermion background is rejected by using the following cuts:

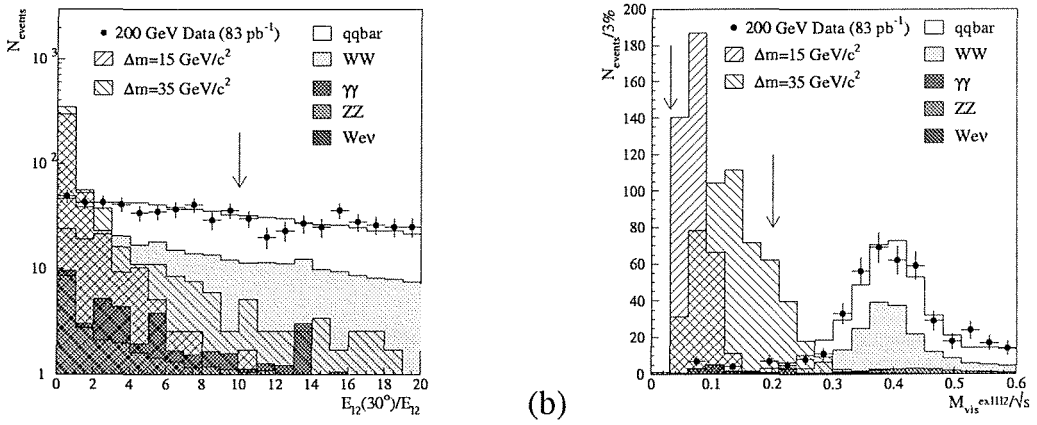

Figure 5.11: $E_{\ell_2}^{\sphericalangle 30^\circ}/E_{\ell_2}$ distribution (a) and $M_{\rm vis}^{{\rm ex}\,\ell_1\ell_2}/\sqrt{s}$ distribution (b) for data and Monte Carlo. The arrows indicate the cut positions. The expected 10 pb signal distributions for $m_{\tilde{\rm t}} = 95\,{\rm GeV}/c^2$ and two Δm values are also shown.

- $M_{\rm vis} > 74\%\sqrt{s}$,
- $6.2\%\sqrt{s} < M_{\rm vis}^{{\rm ex}\,\ell_1} < 25\%\sqrt{s}$,

Moreover, from the four-fermion processes kinematical characteristics, it is useful to ask the quadratic mean of the two inverse hemispheres boosts to be greater 0.2, that is:

- $\frac{1}{2}\sqrt{\left(\frac{m_{\rm h1}}{E_{\rm h1}}\right)^2 + \left(\frac{m_{\rm h2}}{E_{\rm h2}}\right)^2} > 0.2.$

The requirements of the $\vec{p}_{\rm miss}$ isolation and a cut on the $T_{\rm thrust}$ are useful against $\rm q\bar{q}\gamma$ events:

- $T_{\rm thrust} < 0.925$.
- $E(\phi_{\vec{p}_{\rm miss}} \pm 15^\circ) < 18.5\%\sqrt{s}$.

From now on the selection is slightly different depending on the number of identified leptons.

If only one lepton is identified: the identified lepton is e or μ. In this case at least a τ lepton is required in the event:

- The JADE algorithm is applied with $y_{\rm cut} = 0.001$, that corresponds to the τ lepton mass. Among the jets resulting from the application of the JADE algorithm a τ jet candidate[6] must be present.

[6] For our needs it is enough to consider τ leptons decaying one-prong with no extra neutral hadrons ($\sim 50\%$ of the τ decays). Therefore a jet must satisfy the following criteria to be a τ jet candidate:
- $E_{{\rm jet}_\tau} < 30\,{\rm GeV}$,
- $E_{{\rm jet}_\tau}^{\rm NH} < 2\,{\rm GeV}$,
- the angle between the τ jet axis and the nearest jet must be at least 20°.

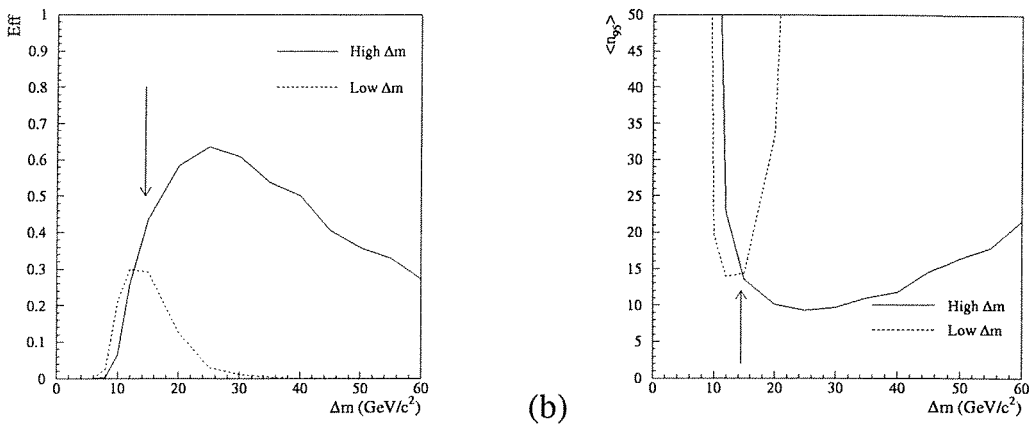

Figure 5.12: Efficiency (a) and 200 pb^{-1} $\overline{\mathrm{n}}_{95}$ (b) for the AJL selection applied to 200 GeV $\tilde{\mathrm{t}} \to \mathrm{b}\ell\chi$ signal. The arrows indicate the switching point.

Since much of the background in case of only one lepton identified comes from $\gamma\gamma \to \mathrm{q\bar{q}}$, the cuts on p_t and $\cos\theta_{\vec{p}_\mathrm{miss}}$ are tightened and a cut on the energy carried by neutral hadrons is introduced:

- $p_\mathrm{t} > 3\%\sqrt{s}$,
- $\cos\theta_{\vec{p}_\mathrm{miss}} < 0.9$,
- $E_\mathrm{vis}^\mathrm{NH} < 30\% E_\mathrm{vis}$.

If more than one lepton is identified: the cut on $M_\mathrm{vis}^{\mathrm{ex}\,\ell_1}$ is correctly reinforced by a cut on $M_\mathrm{vis}^{\mathrm{ex}\,\ell_1\ell_2}$ and conditions on the second lepton also apply:

- $3\%\sqrt{s} < M_\mathrm{vis}^{\mathrm{ex}\,\ell_1\ell_2} < 20\%\sqrt{s}$,
- $2\,\mathrm{GeV} < E_{\ell_2} < 35\,\mathrm{GeV}$,
- $E_{\ell_2}^{\sphericalangle 30^\circ} < 10 \cdot E_{\ell_2}$.

The effectiveness of the cuts on $E_{\ell_2}^{\sphericalangle 30^\circ}/E_{\ell_2}$ and $M_\mathrm{vis}^{\mathrm{ex}\,\ell_1\ell_2}/\sqrt{s}$ results evident from the fig. 5.11(a) and (b) where their distribution for data, background and signal simulation are shown after the preselection cuts and requiring at least two leptons identified. The $\tilde{\mathrm{t}} \to \mathrm{b}\ell\tilde{\nu}$ signal distributions corresponding to a 10 pb cross section are also shown.

5.4.3 The AJL selection efficiencies and backgrounds

The AJL selection applied at the $\tilde{\mathrm{t}} \to \mathrm{b}\ell\tilde{\nu}$ gives the efficiencies shown in fig. 5.12(a). The background for the "low Δm" region amounts at $\sim$ 1.4 events for 200 pb^{-1} and consists almost completely of $\gamma\gamma \to \mathrm{q\bar{q}}$ events. In the "high Δm" region the background is $\sim$ 1.2 events of which $\sim$ 0.8 events come from $\mathrm{q\bar{q}}$ and $\sim$ 0.3 from ZZ and WW processes. As a consequence of this very low level, has been studied the possibility that the application of the logical OR of the "low Δm" and "high Δm" selection might be convenient in the

"low Δm" region improving the efficiency without any substantial background increment. Nevertheless, applying the $\bar{n}_{95}$ procedure it turns out that the standard way to combine "low Δm" and "high Δm" regions is slightly more convenient[7]. Fig. 5.12(b) shows that the optimal switching point is at $\Delta m = 14\,\mathrm{GeV}/c^2$.

5.5 The LLH selection

The LLH selection for the stop hadron with lifetime has been recently developed for 189 GeV and 192 GeV data and it is still preliminary. The selection must take into account the peculiar characteristics of the signal with respect to the simulation. The simulation of the stop hadron interaction with the matter has been developed within this work. It is very difficult to evaluate the reliability of this modelization. For that reason the selection does not make use of the calorimetric event variables as a crucial information to tag the signal.

5.5.1 The LLH selection for Intermediate lifetimes

The LLH selection for intermediate lifetime is specifically designed to look for stop hadrons decaying inside the detector. The selection is based essentially on the tracks with high impact parameter from the stop hadron decay products. This search strategy allows us to look for both neutral and charged stop hadron and it is also almost independent on the stop hadron decay length. The selection described here has been optimized for $\Delta m = 3\,\mathrm{GeV}/c^2$.

The Δm is very small and the stop hadron is produced with a relatively low momentum, especially at high masses. Thus the heavy LSP carries out the main part of the energy available in the decay vertex and the visible decay product system is characterized by few soft tracks: the visible stop hadron decay products generally consists of the decay products of the D meson formed by the c quark hadronization with few or no c quark fragmentation tracks from the decay vertex. Moreover, since the stop hadron speed is low, the directions of the decay products are almost uncorrelated with the stop hadron direction.

There are two main background contributions. The first one comes from the $\gamma\gamma$ processes characterized by a huge cross section and by a visible energy that could be very small. The high impact parameter tracks could be present as a consequence of a photon conversion, a charged track multiple scattering or some nuclear interaction. The second contribution is to be expected from the events where some cosmic ray track has been accidentally recorded together with the particles coming from a standard e^+e^- process. These tracks do not come from the primary vertex and generally have a huge impact parameter. The cosmic ray crosses the TPC volume typically off-time with respect to the bunch crossing time. As a consequence of that the track z coordinates measurements, based on the drift time measurement, is shifted toward the endcaps if the cosmic ray interacts after the bunch crossing or in the opposite directions if the cosmic ray interacts before the bunch crossing. It is clear that the track splits into two branches if the cosmic ray true trajectory passes trough the $z = 0$ plane where the membrane divides the two TPC drift volumes.

For this selection all charged tracks exceeding 1 GeV/c in momentum are considered (the usual "good charged track" restriction is not used for the peculiarity of the topology). They are divided into two categories:

[7]This result is different with respect to 189 – 192 GeV optimization for which the logical OR results better.

- the tracks coming from the primary vertex (PV), if $|\vec{p}| > 1\,\mathrm{GeV}/c$, $|\cos\theta_{\vec{p}}| < 0.95$, $|d_0| \leq 0.5$ cm, $|z_0| \leq 3$ cm and $N_{\mathrm{TPC}} \geq 4$;
- the tracks not coming from the primary vertex (tracks with IP - impact parameter), if $|d_0| > 0.5$ cm or $|z_0| > 3$ cm and $|\vec{p}| > 1\,\mathrm{GeV}/c$.

The total number of PV tracks is expected low because the stop hadrons could be neutral, and there are no too much fragmentation tracks from the primary vertex especially at high masses. On the other hand at least a track with IP must be present. Therefore, the first cuts are:

- ${N_{\mathrm{ch}}}^{\mathrm{PV}} < 9$;
- ${N_{\mathrm{ch}}}^{\mathrm{wIP}} > 1$.

The quantities related to the two leading tracks from the PV (with IP) are referred with the suffix PV_i (wIP_i) $i = 1, 2$. In both cases the $i = 1$ indicates the highest momentum track.

The next requirement is based on the lack of visible energy due to the escaping LSPs. However if one or both the stop hadrons are charged and have a decay length such that their tracks are correctly detected and reconstructed, the energy flow would record their energy. Therefore the visible energy is actually small only if one or both the stop hadron are neutral. Thus the visible energy is properly computed excluding the stop hadron track candidates. The leading or next to leading charged track is considered a stop hadron track candidate if it comes from the PV, ends up in a decay vertex[8] and its momentum exceeds 20 GeV. This visible energy is expected small. Moreover, since the stop hadron energy is close $\sqrt{s}/2$, the leading charged track and the next-to-leading charged track from the PV, if present, are expected to have a large momentum even in case of large stop hadron mass. The following requirements can be done:

- the visible energy E_{vis} minus the stop hadron track candidate(s) energy must be less than $20\%\sqrt{s}$.
- $p_{\mathrm{PV}_1} > 20\%\sqrt{s}$ if ${N_{\mathrm{ch}}}^{\mathrm{PV}} = 1$,

[8] A dedicated algorithm has been developed to look for the stop hadron decay vertices. The peculiar characteristics of the signal do not allow to use standard vertex finding algorithms in use for the heavy flavour physics.

The algorithm looks for charged tracks that are topologically close in the space and it is based on the YTOP routine [85]. The YTOP routine tries to fit in a common vertex the set of tracks in input. It returns a failure code or the vertex coordinates with errors plus the vertex probability P_{VX}. Both coordinates errors and vertex probability are based on the accuracy of the input tracks parameters. The vertex probability can be used to estimate the consistency of the returned vertex hypothesis and the vertex is generally accepted as good if $P_{\mathrm{VX}} > 1\%$. The algorithm performs the following procedure:

1. All possible pairs between charged tracks are formed; a pair is discarded if does not contain at least a track with IP; by using YTOP the two tracks in each pair are tried to be fitted into a common vertex and all the good two tracks vertices are saved.
2. All possible pairs between saved vertices found at the previous step are formed; by using YTOP the tracks forming the initial two vertices are tried to be fitted into a new common vertex. If the returned vertex is good the two initial vertices are replaced by the new one.
3. The step n. 2 is repeated until no more vertices are joined together.

- $p_{\mathrm{PV}_2} > 20\%\sqrt{s}$ if ${N_{\mathrm{ch}}}^{\mathrm{PV}} > 1$.

A set of standard and reliable cuts is used to effectively discard the cosmic ray events and make their contribution negligible. Since there is not a Monte Carlo simulation for the cosmic background, the anti cosmic criteria have been fixed "a posteriori" using their typical characteristics. In fact, cosmic ray events can be easily collected by running the ALEPH detector without beams in LEP, the acquisition being started by a random trigger. The cosmic ray track is completely uncorrelated with the beam crossing; the ECAL signal time can be used effectively to tag off-time signals in the event. Moreover since the JULIA reconstruction algorithm is forced to consider all tracks as coming from a e^+e^- process, an in-time cosmic ray passing only in one half-cylinder of the TPC is reconstructed as two different tracks with respect to the closest point to the primary vertex. These two tracks result almost back-to-back and this feature can be used to tag in-time cosmic ray events.

Therefore, the anti cosmics cuts are:

- $|t_{\mathrm{min}}| < 100$ ns and $|t_{\mathrm{max}}| < 100$ ns;
- $|\cos\theta_{\mathrm{wIP}_1} + \cos\theta_{\mathrm{wIP}_2}| > 0.02$ and $|\cos\phi_{\mathrm{wIP}_1} + \cos\phi_{\mathrm{wIP}_2}| > 0.04$.

The latter cut is also effective against the in-time cosmic ray events even if both TPC half cylinder are interested. In fact the two branches in which the cosmic ray helix is split for the wrong z coordinate reconstruction, are anyhow almost parallel.

The $\gamma\gamma$ events are rejected by using a standard set of anti $\gamma\gamma$ cuts:

- $|\cos\theta_{\vec{p}_{\mathrm{miss}}}| < 0.6$,
- $M_{\mathrm{vis}} > 2\%\sqrt{s}$,
- $E_z^{\bowtie 12^\circ} = 0$,
- $|\cos\theta_{\mathrm{PV}_1}| < 0.6$, if at least one track from the PV is present,
- $|\cos\theta_{\mathrm{wIP}_1}| < 0.6$.

The rejection of the cosmic background and of the Standard Model background is completed by cutting on the momentum and on the impact parameter of the leading track with impact parameter:

- $1\%\sqrt{s} < p_{\mathrm{wIP}_1} < 8\%\sqrt{s}$,
- $1\ \mathrm{cm} < |\mathrm{d}_{0\mathrm{wIP}_1}| < 100\ \mathrm{cm}$ and $|z_{0\mathrm{wIP}_1}| < 100$ cm.

Fig. 5.13 shows the scatter plots $|d_{0\mathrm{wIP}_{1,2}}|$ vs. p_{wIP_1} for data, Standard Model Monte Carlo and signal samples. The plots are produced after that the anti-$\gamma\gamma$ and anti-cosmic cuts are applied. Nevertheless a large contribution of cosmic events is still present (large $|d_{0\mathrm{wIP}_{1,2}}|$, large p_{wIP_1} region). These events have only one half of the cosmic ray track correctly reconstructed and the anti-cosmic cuts do not work; they are rejected by the combined cut on the track momentum and impact parameter represented in the plots by the solid line.

The final requirement consists in a lower cut on the momentum of the two leading tracks with IP to tag the D meson decay:

- $|p_{\mathrm{wIP}_1}| > 4\,\mathrm{GeV}/c$ if ${N_{\mathrm{ch}}}^{\mathrm{wIP}} = 1$,
- $|p_{\mathrm{wIP}_1}| + |p_{\mathrm{wIP}_2}| > 4\,\mathrm{GeV}/c$ if ${N_{\mathrm{ch}}}^{\mathrm{wIP}} > 1$.

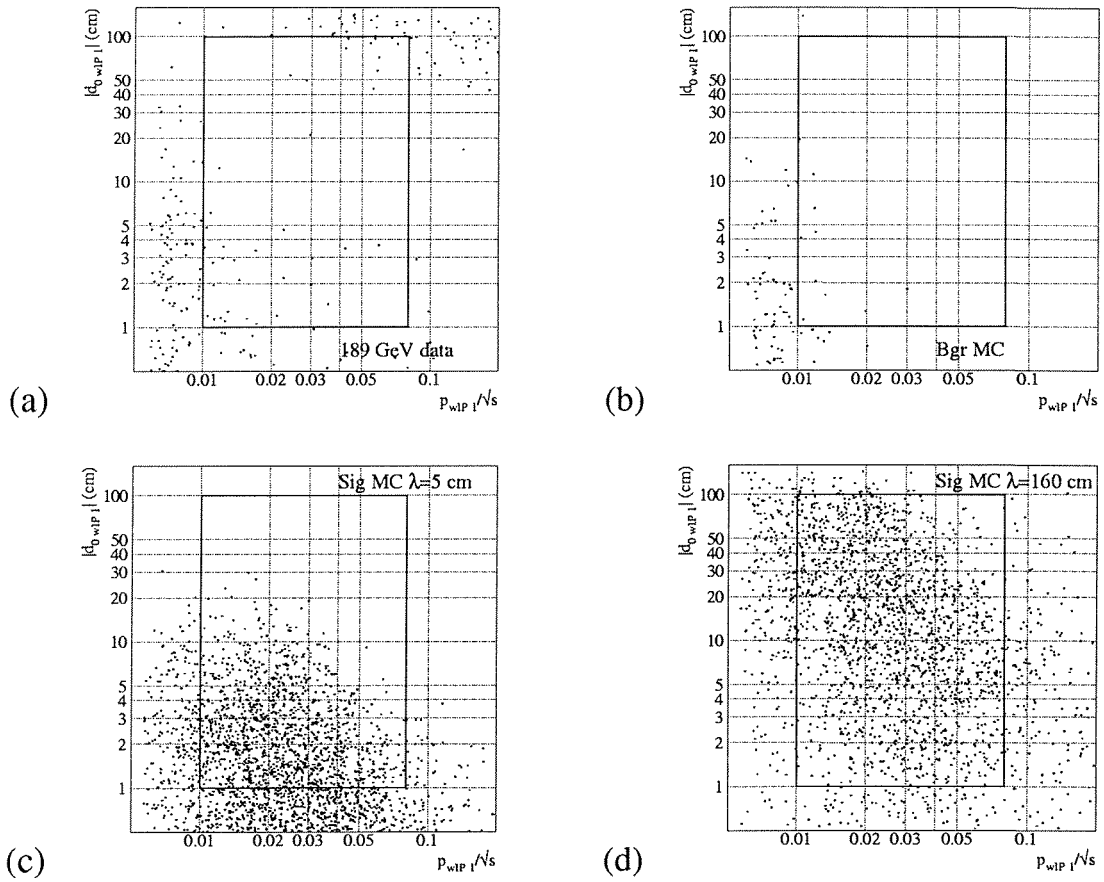

Figure 5.13: Distribution of $|d_{0\mathrm{wIP}_{1,2}}|$ vs. p_{wIP_1} for data (a), Standard Model Monte Carlo (b) and stop hadron signal with decay length of 5 cm (c) and 160 cm (d). The selection cut is also reported.

5.5.2 The LLH selection for long lifetimes

When both stop hadrons do not decay into the detector, the selection must ignore the full neutral topology since in this case only the calorimetric informations could be used. Moreover it results convenient to look for the more shrinking full charged topology since, as fig. 4.6 shows, the loss in efficiency is small especially in the high $\widetilde{\mathrm{T}}$ mass region. From the selection point of view the $\widetilde{\mathrm{T}}$ behaves as an heavy charged hadron. The $\widetilde{\mathrm{T}}$ can be identified by using the characteristic kinematics of their pair-production and the high specific ionization that it is expected to release in the TPC. The selection is very similar to the one used to search for heavy charged particles [86].

The following preselection cuts are first applied:

- $N_{\mathrm{ch}} > 1$,
- $E^{\gamma}_{\mathrm{vis}} < 5\,\mathrm{GeV}$.

The further requirements are based on the two leading tracks characteristics:

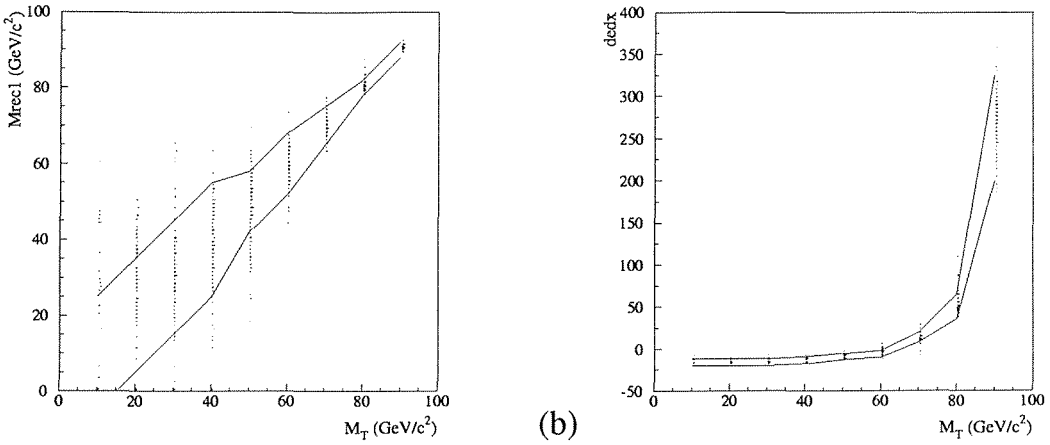

Figure 5.14: Sliding cuts on the reconstructed mass (a) and on the specific ionization loss (b) as a function of the true stop hadron mass. The expected distributions for signal Monte Carlo are shown.

- both the leading two tracks must not be identified as electrons;
- $Q_1 + Q_2 = 0$, i.e. vanishing total charge for the two leading tracks;
- $p_{t1} > 10\%\sqrt{s}$ and $p_{t2} > 10\%\sqrt{s}$ (from now on the index 1 and 2 refers to the leading and next-to-leading charged track respectively);
- the total energy of the HCAL deposits associate to the two leading charged tracks must not exceed 50 GeV,
- the total energy of the ECAL deposits associate to the two leading charged tracks must not exceed 20 GeV,
- $\Phi_{\rm acol} > 160°$, the $\Phi_{\rm acol}$ being now defined as the angle between the two leading tracks momenta $\vec{p}_1$ and $\vec{p}_2$;
- $|\vec{p}_1| - |\vec{p}_2| < 3\sqrt{\sigma^2_{|\vec{p}_1|} + \sigma^2_{|\vec{p}_2|}}$, i.e. the two leading tracks momenta should be equal within 3 standard deviations;
- $E^{\rm ch}_{\rm vis} - |\vec{p}_1| - |\vec{p}_2| < 5$ GeV, i.e. small contribution to total charged energy from charged tracks other than the two leading ones.

Finally a standard set of simple anti-cosmics cuts is used (it is clear that the same set cannot be used in the intermediate lifetime topology):

- $|d_{01}| + |d_{02}| < 0.3$ cm, $|z_{01} + z_{02}| < 5$ cm and $|z_{01} - z_{02}| < 1$ cm.

The selection is finalized by using two sliding cuts. The $\widetilde{\rm T}$ mass can be reconstructed starting from the track momentum $\vec{p}_i$ and by assuming a $\widetilde{\rm T}$ energy equal to $\sqrt{s}/2$:

$$M_i^{\rm rec} = \sqrt{\frac{s}{4} - |\vec{p}_i|^2}. \tag{5.18}$$

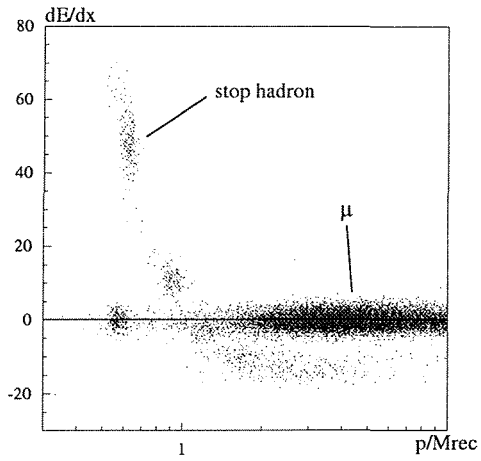

Figure 5.15: Specific ionization loss for signal events (curved distribution) and dimuon events (horizontal distribution) as a function of the reconstructed $\beta\gamma$.

Both $M_1^{\rm rec}$ and $M_2^{\rm rec}$ are required to be compatible with a given mass hypothesis as a function of the $\widetilde{\rm T}$ mass $m_{\widetilde{\rm T}}$:

- $|M_1^{\rm rec} - m_{\widetilde{\rm T}}| < M^{\rm cut}(m_{\widetilde{\rm T}})$ and $|M_2^{\rm rec} - m_{\widetilde{\rm T}}| < M^{\rm cut}(m_{\widetilde{\rm T}})$.

The sliding cut on the reconstructed mass is shown in fig. 5.14(a).

The dimuon background is further reduced by using the specific ionization in the muon hypothesis of the two leading tracks, $R_I^\mu|_1$ and $R_I^\mu|_2$ respectively. Also this cut, depends on the stop mass hypothesis:

- $R_I^{\rm min}(m_{\widetilde{\rm T}}) < R_I^\mu|_1 + R_I^\mu|_2 < R_I^{\rm max}(m_{\widetilde{\rm T}})$.

The optimal cut value for various $\widetilde{\rm T}$ mass hypothesis are given in table 5.3. For the intermediate $m_{\widetilde{\rm T}}$ values a linear interpolation is used. The sliding cut on the specific ionization loss is shown in fig. 5.14(b).

For stop mass between 45 and 65 GeV/c^2 the specific ionization is similar to the muon one. This corresponds to the overlap between hadron signal distribution and muon distribution shown in fig. 5.15, where the specific ionization loss is plotted as a function of the reconstructed $\beta\gamma = p/m$ of the particle. In this region the cut on the specific ionization is replaced by a tighter kinematic cut:

- $\Phi_{\rm acol} > 178°$ and $|M_1^{\rm rec} - M_2^{\rm rec}| < 8\,{\rm GeV}/c^2$.

$m_{\widetilde{\rm T}}$ [GeV/c^2]	10	20	30	40	50	60	70	80	90
$M^{\rm cut}$ [GeV/c^2]	15.	15.	15.	15.	8.	8.	5.	2.	2.
$R_I^{\rm max}$	-12.	-12.	-12.	-10.	-6.	-2.	20.	65.	325.
$R_I^{\rm min}$	-20.	-20.	-20.	-18.	-13.	-10.	8.	35.	200.

Table 5.3: Optimal values for cuts on $M^{\rm rec}$ and total R_I^μ.

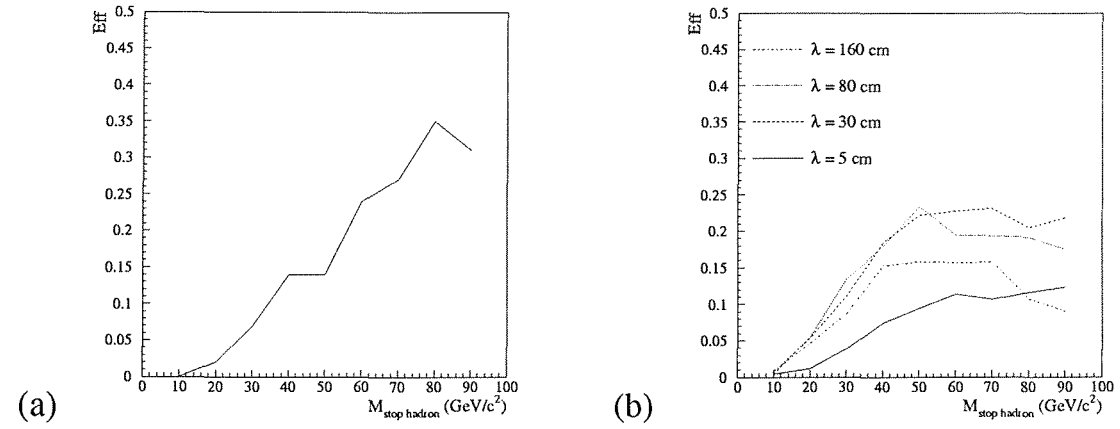

Figure 5.16: (a) Efficiency for LLH long lifetime selection applied to 189 GeV stable stop hadron signal. (b) Efficiency for the LLH intermediate lifetime selection applied to 200 GeV stop hadron signal with different decay lengths λ: 5 cm, 30 cm, 80 cm and 160 cm.

5.5.3 The LLH selection efficiencies and backgrounds

The LLH selections consist of the long lifetime selection, applied to samples of stable $\widetilde{\mathrm{T}}$ hadrons and of the intermediate lifetime selection applied to samples of $\widetilde{\mathrm{T}}$ hadrons decaying inside the ALEPH tracking volume.

In the first case the resulting efficiency, shown in fig. 5.16(a), ranges between 10% and 35% in the relevant high mass region. It is worth to recall that this low efficiency is also a consequence of the choice to consider only the full charged topology (not more than $\sim 50\%$ of the produced events). The expected background for $200\,\mathrm{pb}^{-1}$ at 189 GeV depends on the stop hadron mass since there are the sliding cuts. It is anyhow very small and peaked (0.23 events) in the region where the specific ionization loss cut is not applied, the main component being $\mu^+\mu^-$ as expected from the consideration on the specific ionization loss.

The LLH intermediate lifetime selection gives the efficiencies shown in fig. 5.16(b) when applied to $\widetilde{\mathrm{T}}$ hadron event samples with $\Delta m = 3\,\mathrm{GeV}/c^2$ and decay lengths ranging from 5 cm to 160 cm, to test the selection capability over the entire tracking volume of the ALEPH detector. As one could expect the highest efficiencies values ($\sim 20\%$) result for the intermediate decay lengths considered. These low values of efficiencies are due to the peculiarity of the topology and to the soft spectrum of the $\widetilde{\mathrm{T}}$ hadron decay products, often suffering reconstruction problems. The background expectation for $200\,\mathrm{pb}^{-1}$ at 189 GeV is very low (~ 0.44 events) mainly consisting of $\tau^+\tau^-$ and $\gamma\gamma$ events.

6 Systematic uncertainties

The results of the squark searches performed by using the selections described in the previous chapter will be given in chapter 7 translating the upper limit on the mean number of candidates ν_{oc} in a limit on the signal cross section:

$$\sigma_s < \frac{\nu_{oc}}{\varepsilon \cdot \mathcal{L}}. \tag{6.1}$$

Therefore, the systematic uncertainties on the upper limit of σ_s depend on the systematic uncertainties on the integrated luminosity $\mathcal{L}$ and on the signal efficiency ε. However, since the error on the integrated luminosity is below 1% and thus totally negligible, the systematic studies concentrate on the evaluation the uncertainties of the efficiency due the following contributions:

- the *theoretical uncertainties*, mainly due to the limited knowledge of squark hadronization and decay. The systematic effects associated with these processes are studied by varying the parameters of the physics model used in the squark generator (see chapter 4) and checking the resultant effects on the efficiency.
- The uncertainties due to the limited statistic of the signal Monte Carlo samples and also due to the accuracy of the efficiency parametrization used to derive the limits.
- The *detector uncertainties*, the uncertainties related to detector effects. For the AJL and LLH selections the uncertainty due to the lepton identification, lepton momentum and energy measurements is taken into account, and the uncertainty due to the b-tagging is considered with respect to the efficiencies on $\tilde{b} \rightarrow b\chi$. Some data versus Monte Carlo comparison on impact parameter distributions, dE/dx have been considered to evaluate reliability of LLH selections.

The background estimation error is not considered since all selections are characterized by a background expectation extremely low and to derive limits the method without background subtraction can be used. As already discussed, this method does not suffer from background uncertainties. Also the accuracy of the beam energy measurement (see section 3.1) is such that the effect on the signal efficiency is totally negligible.

The table 6.1 summarizes the contribution of all effects that are discussed in detail in the following sections.

6.1 Theoretical uncertainties

Jets mass

The most relevant model dependency of the selection efficiency is on the squark jet mass that in the used modelization is fixed by m_{eff}. A variation δm_{eff} in the effective spectator quark mass m_{eff} yields to a large change in the efficiency since the hadronic system invariant mass distribution shifts of δm_{eff} as well thus affecting the multiplicity and the event shape especially if the mass available for the visible system is intrinsically small. In fact table 6.1 shows that the uncertainty associated with the squark hadronization parameter is greater for the low Δm region. To quantify these effects, m_{eff} is varied from $0.3\,\text{GeV}/c^2$ to $1.0\,\text{GeV}/c^2$. This variation leads to a relative uncertainty on the selection efficiency of 10-15%, depending on the channel. When Δm is large, on the other hand, the selection efficiencies are insensitive to the value of this parameter, changing by only $\sim 2\%$ relative even for $m_{\text{eff}} = 2\,\text{GeV}/c^2$.

	$\tilde{t} \to c\chi$		$\tilde{b} \to c\chi$		$\tilde{t} \to b\ell\tilde{\nu}$		$\widetilde{T}$	
	high Δm	low Δm	high Δm	low Δm	high Δm	low Δm	intermediate lifetime	long lifetime
m_{eff}	3	10	4	11	3	15	hadronization	-
$\epsilon_{\tilde{t}}, \epsilon_b$	2	2	-	-	2	2	and decay	2
$\epsilon_{\tilde{b}}, \epsilon_b$	-	-	1	2	-	-	modelization	-
ϵ_c	3	7	-	-	-	-	12	-
$\theta_{\tilde{t}}$	1	3	-	-	2	1	3	3
$\theta_{\tilde{b}}$	-	-	3	2	-	-	-	-
MC stat.	3	3	3	3	3	3	3	3
Leptons	negl.	negl.	negl.	negl.	3	3	negl.	3
b-tag	-	-	4	-	-	-	-	-
Total	6	13	7	12	6	16	13	6

Table 6.1: Summary of relative systematic uncertainties on the squark selection efficiencies.

Fragmentation parameters

The selection efficiency depends on the fragmentation process that affects many event variable distributions, the number of charged tracks distribution in particular. The fragmentation parameters are varied over a range suggested by LEP1 measurements [72]. In the case of $\epsilon_{\tilde{t}}$ the error is propagated from ϵ_b according to the formula (4.5), and for the $\tilde{t} \to b\ell\tilde{\nu}$ channel ϵ_b is varied simultaneously with $\epsilon_{\tilde{t}}$. Similarly, for the $\tilde{b} \to b\chi$ channel $\epsilon_{\tilde{b}}$ is varied simultaneously with ϵ_b, and in the generic squark case $\tilde{q} \to q\chi$, $\epsilon_{\tilde{q}}$ is varied simultaneously with ϵ_q. For the "low Δm" case the fragmentation parameters are varied more drastically, but even drastic variations have little effect on the efficiency; for instance, when $\epsilon_{\tilde{t}} = \epsilon_b$, the relative change in "low Δm" stop efficiencies is only $\sim 2\%$.

Sbottom and degenerate squarks hadronization

As already discussed in the chapter 4, the squarks decay into the standard partner quark occurs, if accessible, before or after the hadronization depending on the MSSM parameters. The selection efficiency might depend on the time order of hadronization and decay. The signal generators implements both possibilities and a systematic study has been performed. It turns out that the efficiency is always lower in case that the hadronization occurs before the squark decay. In fact in this case the fragmentation particles are often below 1 GeV/c in momentum thus suffering a lower detection efficiency. For a conservative estimation of the efficiencies all $\tilde{b}$ and $\tilde{q}$ samples are produced with the "hadronization before decay" scheme.

The $\tilde{t} \to b\ell\tilde{\nu}$ matrix element

For the $\tilde{t} \to b\ell\tilde{\nu}$ simulation the phase space model is used: the events are distributed according to the phase space probability for a given kinematic configuration neglecting the matrix element dependencies on the outcoming particles four-vectors. The matrix element described in section 4.1.1 introduces a correlation among the outcoming b and ℓ that could affect the efficiency. The vectorial coupling, dominant in the main part of the MSSM param-

eter space, is the most dangerous since it makes the b and ℓ directions strictly correlated. As a consequence of that the ℓ results in average less isolated than the phase space simulation case. Nevertheless the efficiency evaluated over samples produced with the matrix element decay model results compatible with the phase space sample efficiency within the statistical error. Therefore the uncertainty from this source is neglected.

Long living stop hadron decay

The contribution of m_{eff}, $\epsilon_{\tilde{t}}$ and the other decay parameters uncertainties of the "low Δm" AJ selection have been propagated also for the case of LLH intermediate lifetime selection, since the decay is introduced very simplified at the GEANT level and there is no the possibility to accurately study the uncertainties coming from the modelization of the hadronization and decay.

Mixing angle

The effect of changing the mixing angles has also been investigated. Changing these angles the spectrum of initial state radiation changes; this affects the angle between the two hemispheres in an event and hence the acoplanarity and the transverse acoplanarity. The systematic effect of varying the mixing angles is quantified by evaluating the efficiencies on a set of $\tilde{t}$ samples generated with $\theta_{\tilde{t}} = 56°$ and on a set of $\tilde{b}$ samples generated with $\theta_{\tilde{b}} = 68°$. For these values of mixing, the stops and sbottoms decouple from the Z and the change in efficiencies due to the differing spectra of initial state radiation is maximal. For all selections, the relative change in the efficiency is $\sim 1 \div 3\%$.

6.2 Monte Carlo statistics

The standard size of the signal samples amounts at 1000 events and leads to a relative uncertainty of less than 2%, while the parametrization of the signal efficiencies leads to an additional relative uncertainty of about 2%. The total statistical relative uncertainty associated with the Monte Carlo signal simulation is therefore $\sim 3\%$.

6.3 The detector uncertainties

The precision and accuracy with which a given quantity can be measured is dictated by the detector capabilities. These capabilities are modeled in the ALEPH detector simulation that is applied to the signal and background samples. Any inaccuracy in the detector simulation constitutes a possible source of systematic uncertainty. In order to study this possible uncertainty due to "detector effects", comparisons between data and Monte Carlo have been performed for the variables used in the analyses and for the other quantities on which the final signal efficiency may depend. In all cases a good agreement is seen between the data and the Monte Carlo prediction. However in the following sections some detail is given about the checks done.

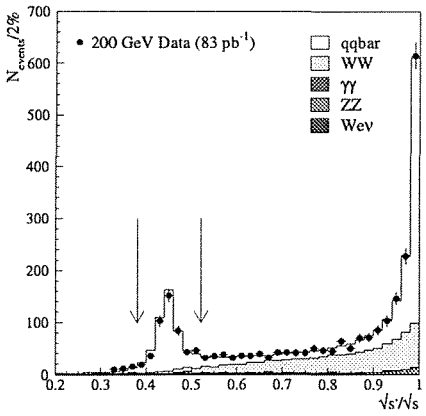

Figure 6.1: $\sqrt{s'/s}$ distribution for 200 GeV data and Monte Carlo. The arrows indicate the cuts applied.

6.3.1 General checks on selection variables

The detector response has been checked comparing the data distribution of many of the used variables with respect to the Monte Carlo simulation. As shown by the plots in the previous chapter, used to describe the selection cuts, all distributions are in good agreement with the Monte Carlo simulation. Nevertheless some crucial variable or discriminant cut has been object of particular cross checks.

An independent check can be performed by selecting the Z resonance events occurred after an hard ISR emission (Zγ events) or the WW events. These samples are characterized by a consistent statistic and resemble the signal event shape.

Checks on Zγ events

The Zγ events are selected by using the quantity $\sqrt{s'/s}$, s' being the squared energy of the produced Z boson [87]. After the event has been forced into two jets, $\sqrt{s'/s}$ can be estimated by the following relation that assumes the hard ISR photon to escape down into the beam pipe:

$$\frac{s'}{s} = \frac{\sin\theta_{\mathrm{jet}_1} + \sin\theta_{\mathrm{jet}_2} - |\sin(\theta_{\mathrm{jet}_1} + \theta_{\mathrm{jet}_2})|}{\sin\theta_{\mathrm{jet}_1} + \sin\theta_{\mathrm{jet}_2} + |\sin(\theta_{\mathrm{jet}_1} + \theta_{\mathrm{jet}_2})|}, \tag{6.2}$$

where θ_{jet_1} and θ_{jet_2} are the jets polar angles. The Zγ sample for our checks is first selected requiring:

- $p_{\mathrm{t}} > 5\%\sqrt{s}$, $N_{\mathrm{ch}} > 4$ and $M_{\mathrm{vis}} > 20\%\sqrt{s}$ to reduce $\gamma\gamma$.

Fig. 6.1 shows the $\sqrt{s'/s}$ distribution for 200 GeV data and Monte Carlo after the above cuts. The Z resonance is clearly visible and can be isolated requiring:

- $0.38 < \sqrt{s'/s} < 0.52$.

The selected sample is used to produce the distribution of M_{vis}, $M_{\mathrm{vis}}^{\mathrm{ex}\,\ell_1}$, T_{thrust} and $\cos\theta_{\hat{\mathrm{a}}_{\mathrm{thrust}}}$ shown in fig. 6.2. The agreement is generally good.

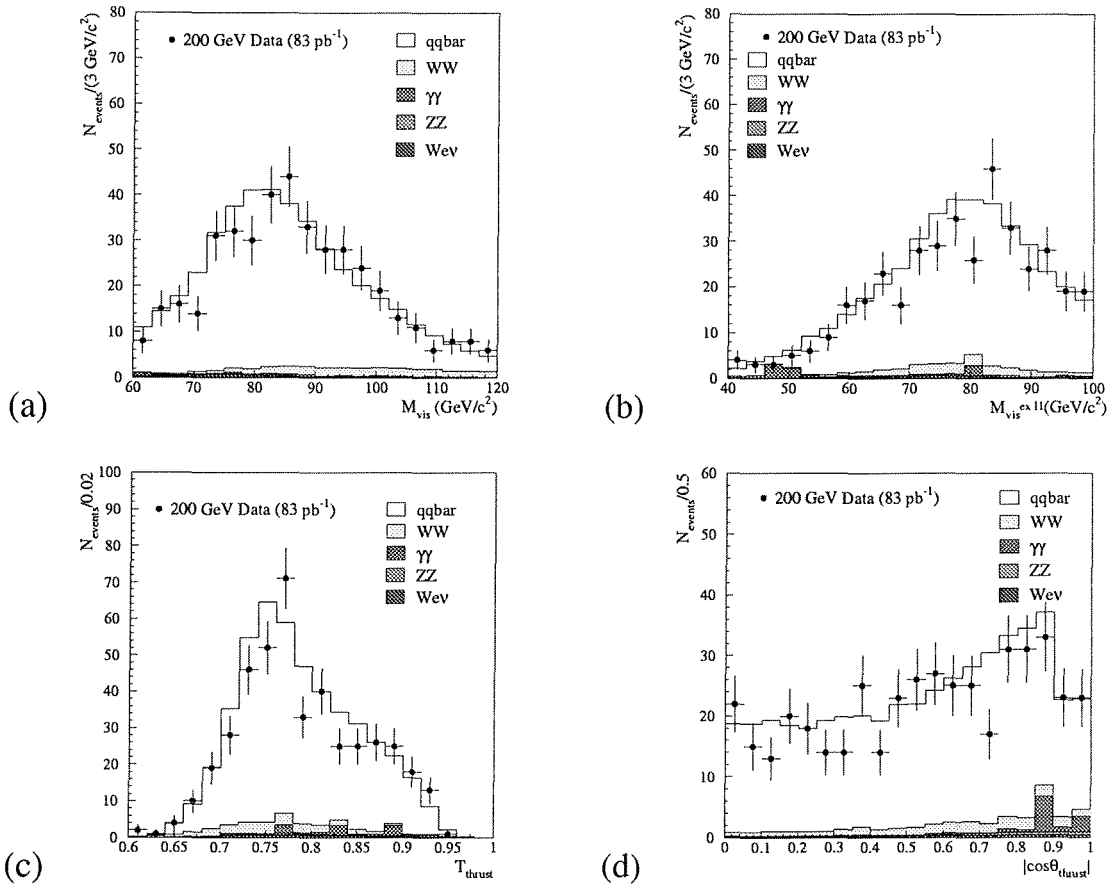

Figure 6.2: Variables distribution for the 200 GeV radiative Z returns sample and Monte Carlo: $M_{\rm vis}$ (a), $M_{\rm vis}^{{\rm ex}\,\ell_1}$ (b), $T_{\rm thrust}$ (c) and $\cos\theta_{\hat{\rm a}_{\rm thrust}}$ (d).

Checks on WW events

Some WW events can be selected by using the AJ selection without the $\theta_{\rm point}$ vs. $\theta_{\rm scat}$ and in particular without all the upper cuts on $M_{\rm vis}$ added just to reject WW events. As the $M_{\rm vis}$ distribution in fig. 5.6(a) shows, the selected events are mainly WW.

With these events the distribution of $E_{\rm vis}^{\rm NH}$, $E(\phi_{\vec{p}_{\rm miss}}\pm 15°)$, $N_{\rm ch}$ and $\theta_{\rm scat}$ shown in fig. 6.3 have been produced. Also in this case the agreement is generally good.

$E_z^{\bowtie 12°}$

A small $E_z^{\bowtie 12°}$ is a very effective criterion against $\gamma\gamma$ events and in fact this requirement is made in the "low Δm" AJ and AJL selections. This cut has been found to introduce an extra 2% of inefficiency as a consequence of detector and beam related noise. In other words a 2% fraction of events have a spurious $E_z^{\bowtie 12°}$ contribution not coming from the e^+e^- physics process but from detector noise or LEP background (i.e. bremsstrahlung photons, beam gas interactions). This estimation has been done looking to random trigger events

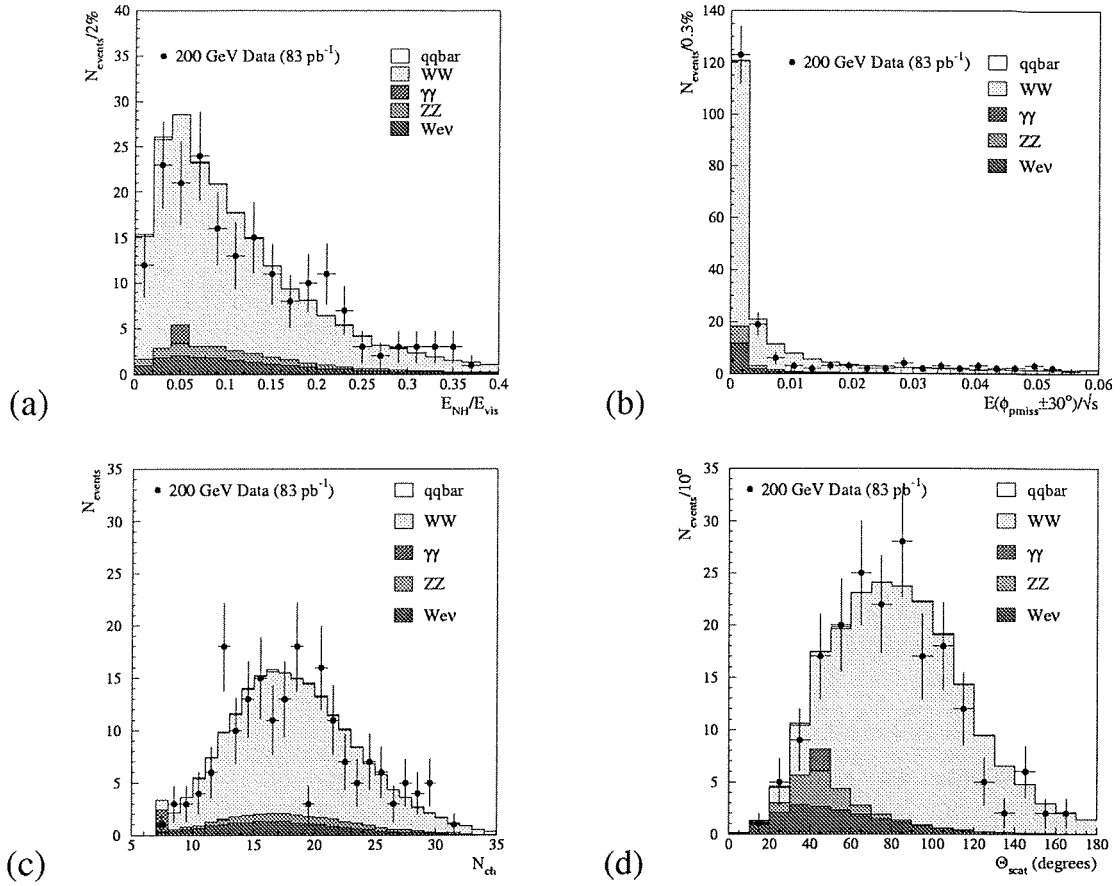

Figure 6.3: Variables distribution for a 200 GeV WW event sample and Monte Carlo: $E_{\rm vis}^{\rm NH}$ (a), $E(\phi_{\vec{p}_{\rm miss}} \pm 15°)$ (b), $N_{\rm ch}$ (c) and $\theta_{\rm scat}$ (d).

in the data. Since these effects are not taken into account in the simulations, the selection efficiencies estimated by using the Monte Carlo samples have to be reduced of a 2%.

Lepton identification

The lepton identification is described in section 3.3.2. The uncertainty on the identification efficiency has been measured directly on the data. A sample of two tracks events with $M_{\rm vis} > 80\,{\rm GeV}/c^2$ and an angle between the two tracks in the transverse plane[1] greater than 175° has been selected. This sample consists mainly of $e^+e^- \to \mu^+\mu^-$ and $e^+e^- \to e^-e^+$ with less than 1% of $e^+e^- \to \tau^+\tau^-$ and can be used to evaluate the e and μ identification efficiency by using a double tagging method. The comparison with Monte Carlo expectation shows a good agreement for muon identification while the e identification efficiency results overestimated by a 3% factor in the simulation. This has been traced back to be due to a small shift in the R_L estimator. These uncertainty is taken into account in deriving results.

[1]This is the definition of $\Phi_{{\rm acop}_{\rm T}}$ for leptonic events.

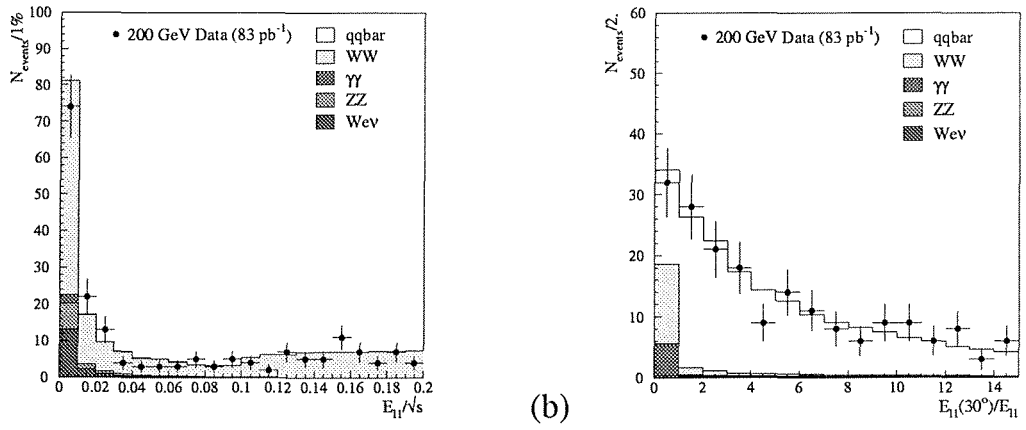

Figure 6.4: (a) Leading lepton energy distribution for 200 GeV WW events and Monte Carlo. (b) Lepton isolation $E_{\ell_1}^{\sphericalangle 30^\circ}$ distribution for 200 GeV $Z\gamma$ hadronic events and Monte Carlo.

Lepton energies and isolation

The lepton energies distributions have been studied with the WW sample. The data vs. Monte Carlo comparison shown in fig. 6.4(a) is in a good agreement. Fig. 6.4(b) shows the leading lepton isolation $E_{\ell_1}^{\sphericalangle 30^\circ}$ distribution for the $Z\gamma$ hadronic events. Also in this case a good agreement is found.

Momentum and dE/dx measurements

The LLH intermediate lifetimes selection makes use of the momentum compatibility between the two charged tracks and of the specific ionization loss measurements. The reliability of the simulation with respect to these two quantities has been checked comparing data and Monte Carlo on a sample of dimuon events.

Bad measurements of momentum compatibility may come from momentum unbalance between positive and negative charged particles. Fig. 6.5(a) shows separately the momentum distributions for positive and negative muons in the 192 GeV and 196 GeV dimuon events. The shift is negligible from the point of view of the LLH long lifetime selection. The dE/dx distribution for dimuon events is shown in fig. 6.5(b) for 192 – 196 GeV data and Monte Carlo. Since the agreement is good in both cases no systematic uncertainties are considered from these sources.

Impact parameter and b-tagging

The impact parameter measurements are important for LLH intermediate lifetime selection and also for the AJ selection plus b-tagging used for the $\tilde{b} \to b\chi$ channel.

The impact parameter distribution has been checked on the hadronic events collected during 1999 runs at the Z resonance. Fig. 6.6(a) shows the negative part of the d_0 distribution for 1999 Z $q\bar{q}$ data and corresponding Monte Carlo. The negative part is not affected

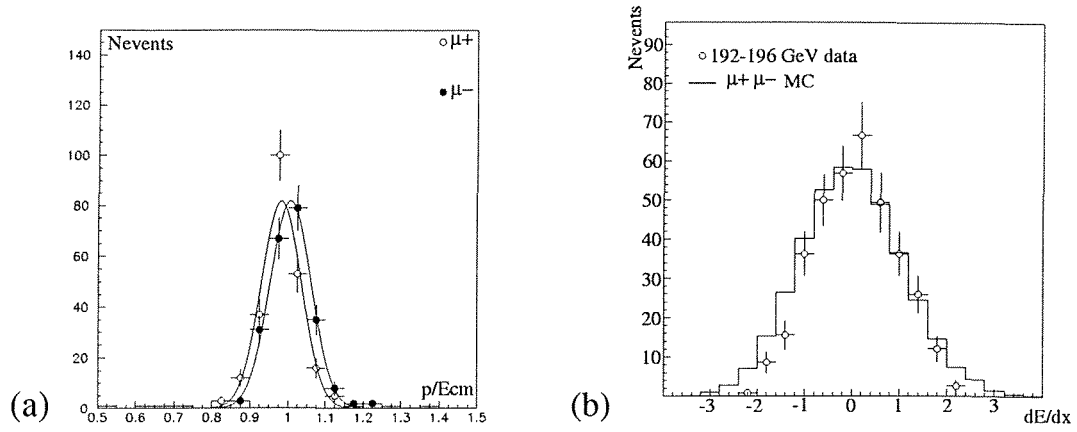

Figure 6.5: (a) Momentum distribution for 192 – 196 GeV positive (o) and negative (•) muons; (b) data and Monte Carlo comparison for dimuon events specific ionization loss.

by the quarks lifetime and therefore is used to evaluate the impact parameter resolution. Monte Carlo simulation and data are in good agreement.

Further checks have been done directly on the b-tagging by measuring its efficiency on the 1999 Z resonance data. The $Z \to b\bar{b}$ over $Z \to q\bar{q}$ decay fraction (R_b) can be measured by using the `QIPBTAG` algorithm [88], i.e. with the same b-tagging technique used to tag $\tilde{b} \to b\chi$ events within the AJ selection. The disagreement between this R_b measure and the R_b world average $R_{bWA} = 0.217 \pm 0.0004$ [89] is a straightforward evaluation of the uncertainty on the b-tagging efficiency, that is the dominant systematic source.

The R_b values as a function of the efficiency are shown in fig. 6.7 together with the world average. The three plots corresponds to the different Z data samples available in 1999. The degradation of the agreement is due to a problem occurred to the TPC as a consequence of a beam loss inside the TPC sensitive volume resulting in a electric field distortion. The maximum disagreement ($\sim 4\%$) is assumed as a systematic on the efficiency. It is worth to recall that the difference in center-of-mass energy is not critical since the b-tagging efficiency is independent on the b quark boost, being the impact parameter almost a Lorentz invariant. Fig. 6.6(b) shows the perfect agreement between the b-tagging efficiency and the $\tilde{b}$-tagging efficiency ($\Delta m = 35\,\mathrm{GeV}/c^2$) when plotted as a function of the cut on $\log_{10} P_{\mathrm{uds}}$.

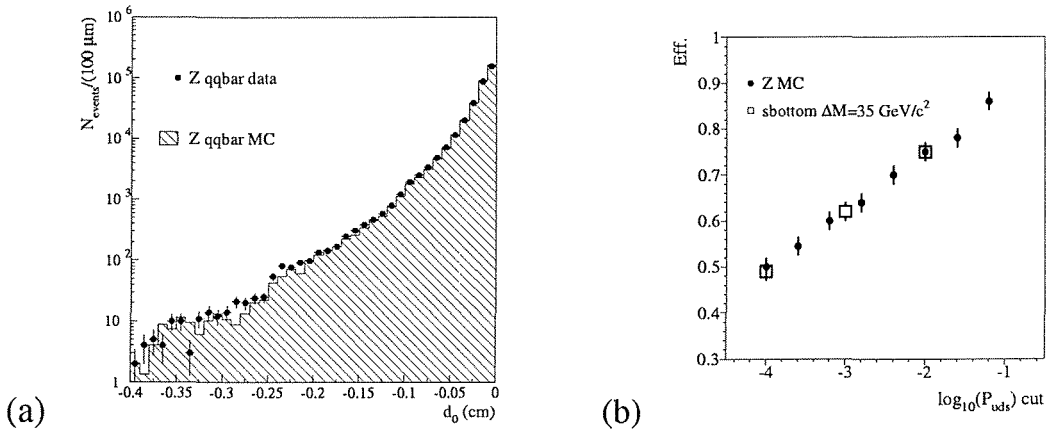

Figure 6.6: (a) Negative part of the d_0 distribution for the 1999 hadronic Z events and corresponding simulation. (b) The b-tagging efficiency (•) and the $\tilde{b}$-tagging efficiency at $\Delta m = 35\,\mathrm{GeV}/c^2$ (□) as functions of $\log_{10} P_{\mathrm{uds}}$ cut.

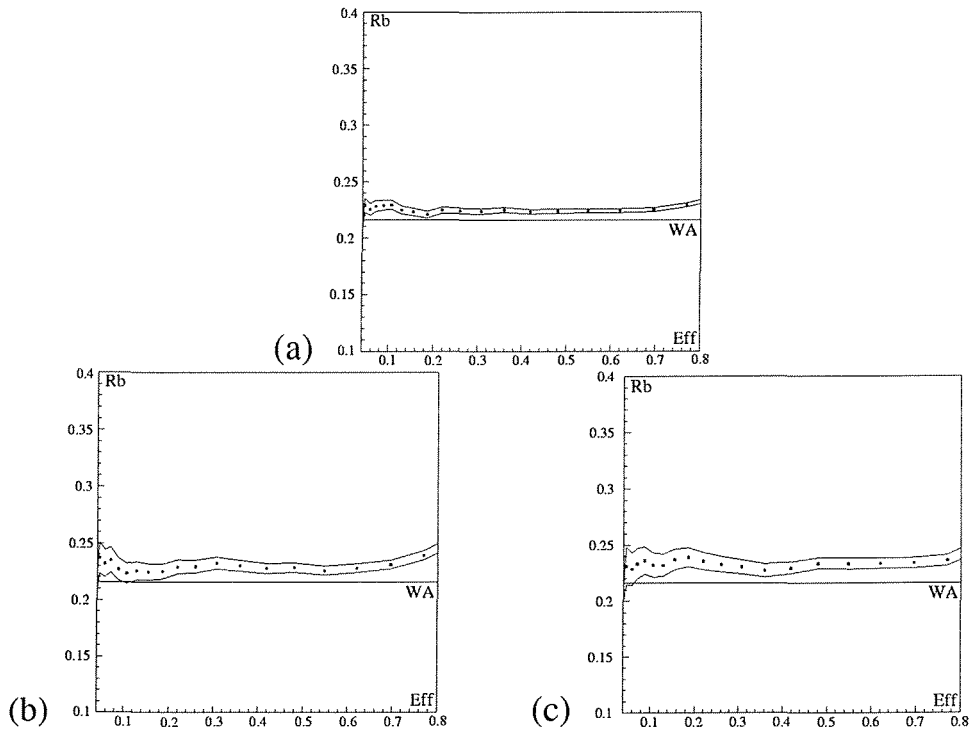

Figure 6.7: The R_b values as a function of the efficiency for the three different Z data samples available in 1999: start of run (a), middle of run (b) and end of run (c).

7 Results and interpretations

$\sqrt{s}$			$M_{\rm vis}$	AJ		Δm	AJ +b-tag		AJL	
[GeV]	#run	#evt	[GeV/c^2]	low	high	[GeV/c^2]	low	high	low	high
196	49961	11754	41.9		✓	>26				
196	50129	2125	44.3		✓	>28				
196	50487	18012	24.7						✓	
196	50488	19660	6.7	✓		<7				
196	50740	14989	27.2		✓	any				
200	50757	9193	11.4	✓	✓	any	✓			
200	51468	9950	22.0						✓	
200	51543	12447	16.5						✓	
202	51834	5767	41.2		✓	>25				
202	51858	12447	17.2						✓	
202	51947	16018	31.5		✓	>32				
202	52046	2720	29.7		✓	any		✓		
202	52242	900	47.1		✓	>29		✓		

Table 7.1: Squark candidates between $\sqrt{s} = 192\,\text{GeV}$ and $\sqrt{s} = 202\,\text{GeV}$ for AJ and AJL selections.

In this chapter the results of applying the AJ, AJL and LLH selections to the data are presented. Since no evidence for a signal has been found, these results will take the form of limits on the masses of stops and sbottoms. Limits on generic squarks will also be presented. Moreover a completely new and still preliminary result in the very small Δm region is reported.

The used data samples have been already described in detail in the section 5.3.1. Nevertheless it is worth to recall that the AJ and AJL selections presented in the chapter 5 are applied to the 196, 200 and 202 GeV data sample for a total integrated luminosity of about $\sim 196\,\text{pb}^{-1}$. The "old" selections (described in [84] and optimized for the data sample at 189 GeV) have been used for the 189 and 192 GeV data sample ($\sim 203\,\text{pb}^{-1}$). In this chapter only the results deriving from the application of these selections to the 1999 data (i.e. from 192 GeV to 196 GeV) are presented in detail. They update the previously published results at lower energies [90][91][84].

The new LLH selections, optimized at 189 GeV, have been used for the 189 GeV and 192 GeV data sample and the results are presented here in detail.

7.1 AJ and AJL selections candidates

In this section the number of candidates resulted from the application of the AJ and AJL selections to 1999 ALEPH data samples is reported. The table 7.1 summarizes some relevant numbers of all the found candidates that, together with the candidates from lower energies, contribute to the combined exclusion plots given later. For each candidate is given the Δm region of compatibility according to the sliding cuts used in the selections.

Four candidates are shown in fig. 7.2, fig. 7.3, fig. 7.4 and fig. 7.5. It is not easy to provide a shrinking interpretation of the candidate events in terms of Standard Model pro-

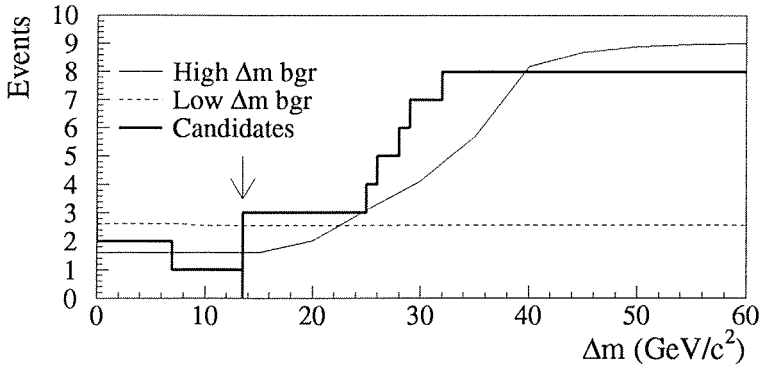

Figure 7.1: Background expectation and number of candidates for AJ selection at 196 GeV, 200 GeV and 202 GeV. The arrow indicates the switching point between "low Δm" and "high Δm" selections.

cesses, since the low visible energies they show is quite unusual both for two-fermion and four-fermion processes. Moreover, if the activity at small angles is poor and the missing momentum (indicated by the straight line in the plots) is far from the beam axis also the event interpretation in terms of a $\gamma\gamma$ process cannot be safely supported. Among the events displayed, maybe only the event `#evt`=12447 `#run`=51543, shown in fig. 7.3, could be a $\gamma\gamma$ process since the missing momentum has a small polar angle. In the other cases, the most probable Standard Model interpretation thus consists in processes like ZZ, Zγ^*, WW or Weν_e where one boson is produced largely above the resonance mass value (off-shell). Then the low visible mass can be given by this off-shell boson decaying in partially visible final state (as a W decaying leptonically) or completely invisible final state (as a Z decaying in neutrinos). This is also confirmed from the generally high missing mass values (well above 100 GeV/c^2) present in these events. It is worth to notice that the event `#evt`=9193 `#run`=50757 (see fig. 7.2), where all the visible particles recoil the missing momentum, is selected by both "low Δm" and "high Δm" selections. Similar topology is featured also by the event `#evt`=16018 `#run`=51947 in fig. 7.4. Fig. 7.5 shows the event `#evt`=2720 `#run`=52046 that is indicated by the AJ plus b-tag selection. The enlarged views of VDET region and of the primary vertex region show the tracks displaced with respect to the interaction point that make the event compatible with the production of long living particles.

The AJ selection indicates a total of 9 candidates. No candidates are found at 192 GeV for which the old AJ selection (i.e. the AJ selection optimized for 200 pb^{-1} at 189 GeV [84]) gives a maximal expected background of $\sim$ 0.2 events at "low Δm" and $\sim$ 0.6 events at "high Δm". These expectations both reduce to $\sim$ 0.1 considering the AJ version for the $\tilde{b} \to b\chi$ channel. At higher energies the AJ "low Δm" selection indicates 2 candidates (with $\sim$ 2.6 expected), of which only one (with $\sim$ 2.5 expected) is compatible with the hardest cut on $M_{\rm vis}$ used for the $\tilde{b} \to b\chi$ channel. A total of 8 candidates results from the "high Δm" AJ selection, in agreement with the expected $\sim$ 9.1 events for the loosest cut configuration as also shown in fig. 7.1 where the distribution of background and candidates is plotted as a function of Δm. By mean of the b-tag cut only 2 of these 8 candidates turn out to be compatible with the $\tilde{b} \to b\chi$ search requirements. The expected background in this case is

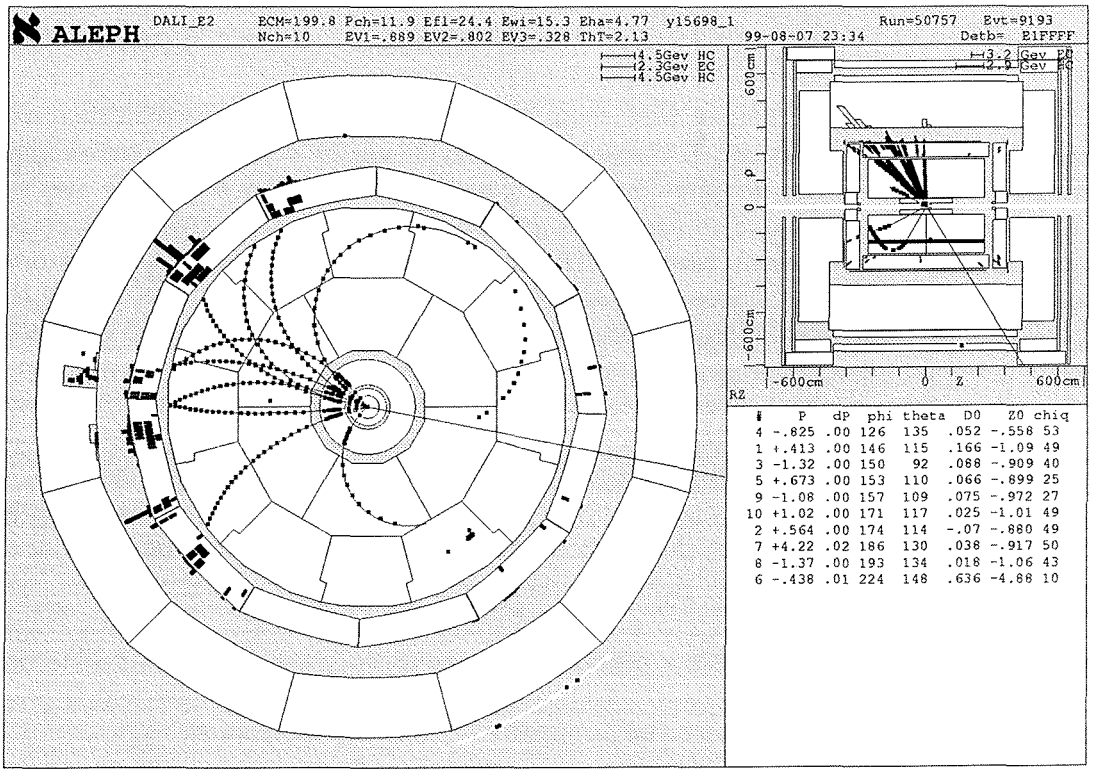

Made on 19-Nov-1999 14:22:46 by sguanzon with DALI_E2.
Filename DG050757_009193_991119_1422.PS

Figure 7.2: Candidate #evt=9193 #run=50757 selected by AJ selections in both "low Δm" and "high Δm" regions.

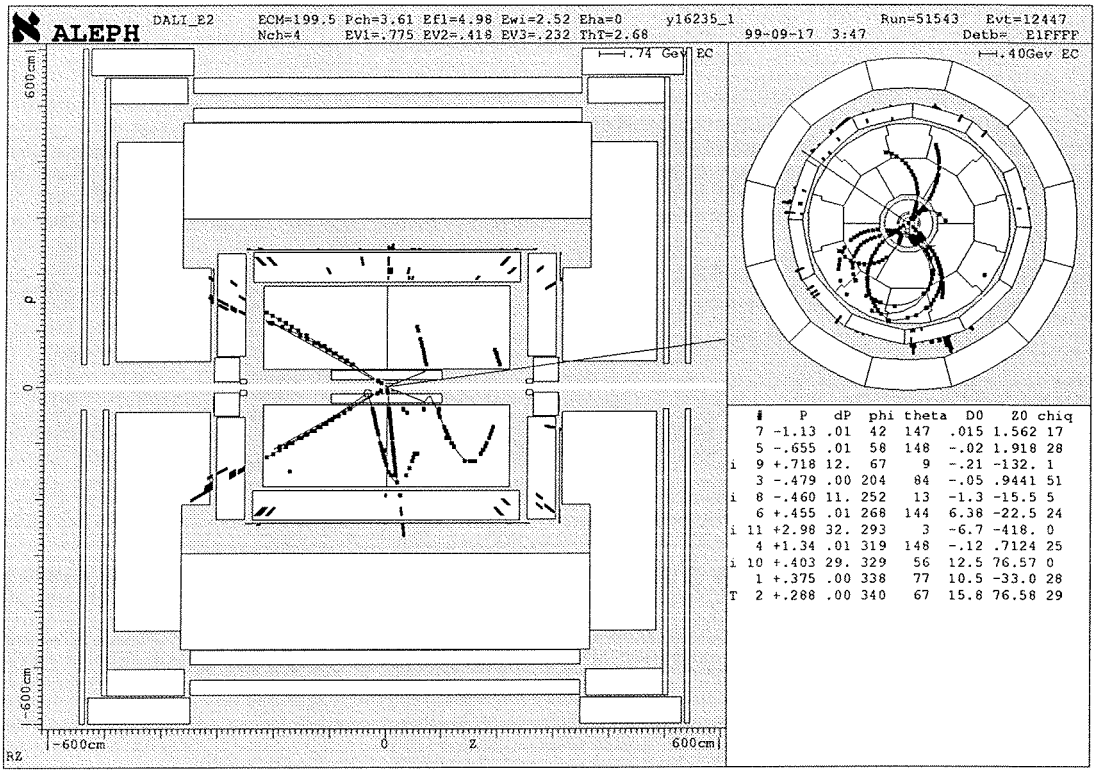

Figure 7.3: Candidate `#evt`=12447 `#run`=51543 selected by AJL "low Δm" selection.

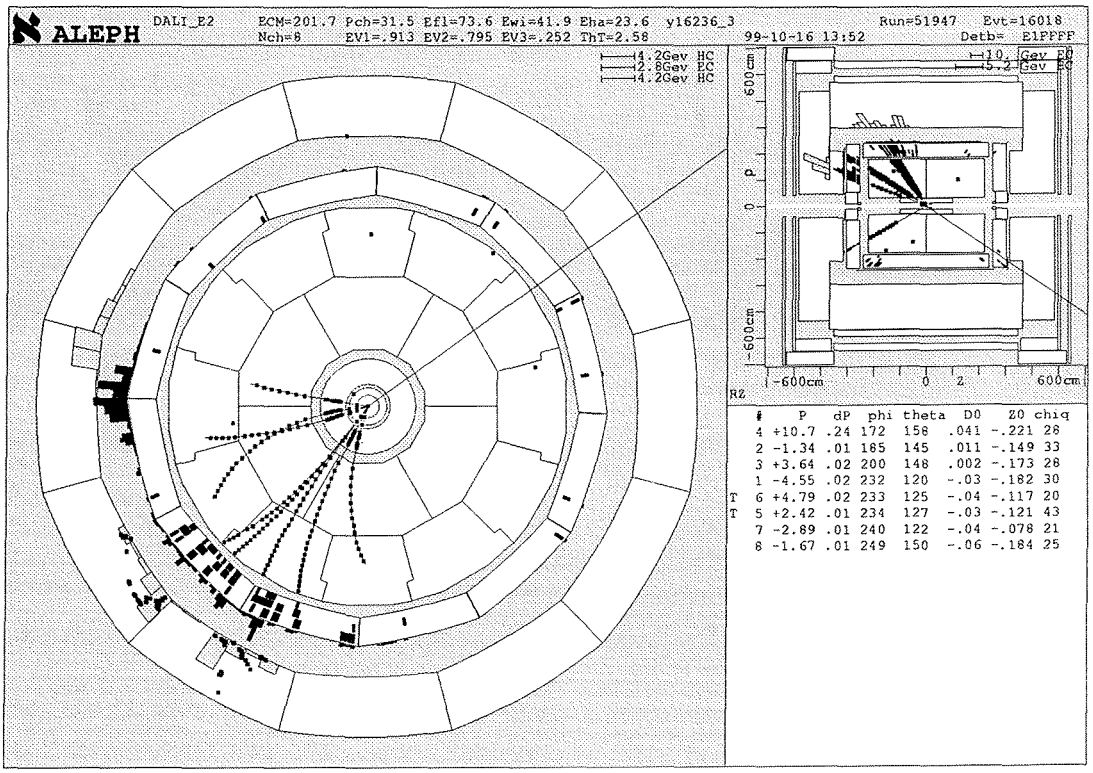

Figure 7.4: Candidate `#evt`=16018 `#run`=51947 selected by AJ "high Δm" selection.

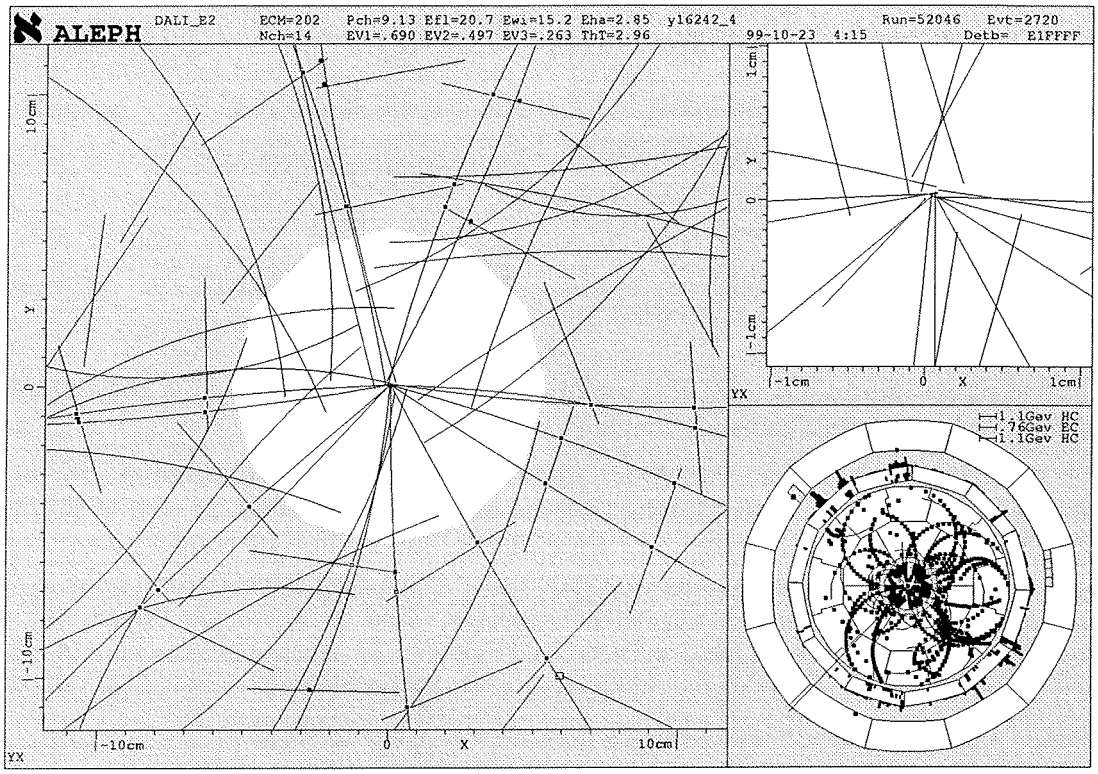

Made on 29-Nov-1999 11:25:28 by sguazzon with DALI_E2.
Filename: DG052046_002730_991129_1125.PS

Figure 7.5: Candidate #evt=2720 #run=52046 selected by AJ plus b-tag "high Δm" selection. The VDET region and the primary vertex region are shown enlarged.

1.1 events.

As far the AJL selection it concerns, 4 events survive. No candidates are found at 192 GeV by the old AJL selection designed for 189 GeV of center-of-mass energy [84], according to an expected background of ~ 0.3 events from the "low Δm" selection and ~ 0.2 events from the "high Δm" selection. No candidates are found at higher energies in the "high Δm" region (where ~ 1.2 were expected), thus all the four candidates come from the AJL "low Δm" selection: one at 196 GeV, two at 200 GeV and one at 202 GeV. The "low Δm" expected backgrounds amounts at ~ 1.4 events. Therefore the observed events are slightly but not significantly in excess. Nevertheless it is worth to recall that the expected background could be over estimated since the main background component consists here of $\gamma\gamma \rightarrow q\bar{q}$ events, well known to be poorly simulated (see section 4.3).

7.2 LLH candidates

The LLH selection indicates a total of 2 candidates (see table 7.2), both from the 189 GeV data sample, while no candidates are found at 192 GeV.

The first candidate (`#evt`= 962 `#run`=46415) results from the intermediate lifetime selection for which the expected Standard Model background amounts at ~ 0.44 events. Nevertheless it is clear that in this event, shown in fig. 7.6, an in-time cosmic muon track has been recorded. The reconstruction program fails to join into a track part of the TPC hits visible in the bottom half of the detector section. The reconstructed branch of the cosmic muon trajectory, for which a $\sim 9.9\,\mathrm{GeV}/c$ momentum is measured, simulates the decay track of a neutral stop hadron. The second candidate (`#evt`= 11920 `#run`=46846) is selected from the long lifetime selection. It results compatible with the stop hadron mass region that needs harder kinematic cuts in place of dE/dx cut to reject the dimuon background which expected value amounts at ~ 0.23 events. A dimuon event is in fact the most probable interpretation of this candidate, shown in fig. 7.7. The two tracks have hits in the muon chambers and also the HCAL hits pattern is compatible with this hypothesis. A momentum of about 71 GeV is measured for both tracks yielding to a reconstructed stop hadron mass of about $60\,\mathrm{GeV}/c^2$. Such a low momentum, quite far from $\sqrt{s}/2$, is probably due to a photon emission that lowers the effective center-of-mass energy of the process. In particular an almost symmetrical double photon emission occurred since the two tracks are perfectly back-to-back, otherwise the acollinearity cut would have worked.

$\sqrt{s}$ [GeV]	`#run`	`#evt`	LLH intermediate lifetime	LLH long lifetime	$m_{\tilde{T}}$ [GeV/c^2]
189	46415	962	✓		
189	46846	11920		✓	45-65

Table 7.2: Squark candidates between $\sqrt{s} = 189\,\mathrm{GeV}$ and $\sqrt{s} = 192\,\mathrm{GeV}$ for LLH selections.

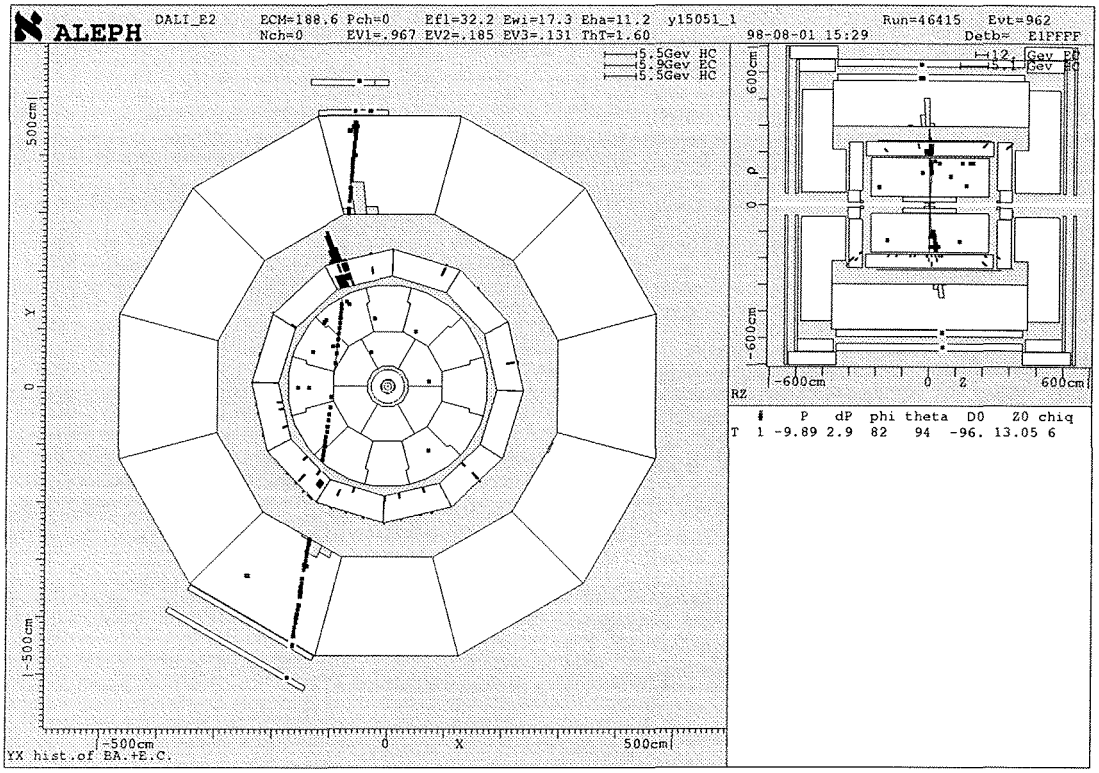

Figure 7.6: Candidate event of the LLH intermediate lifetime selection.

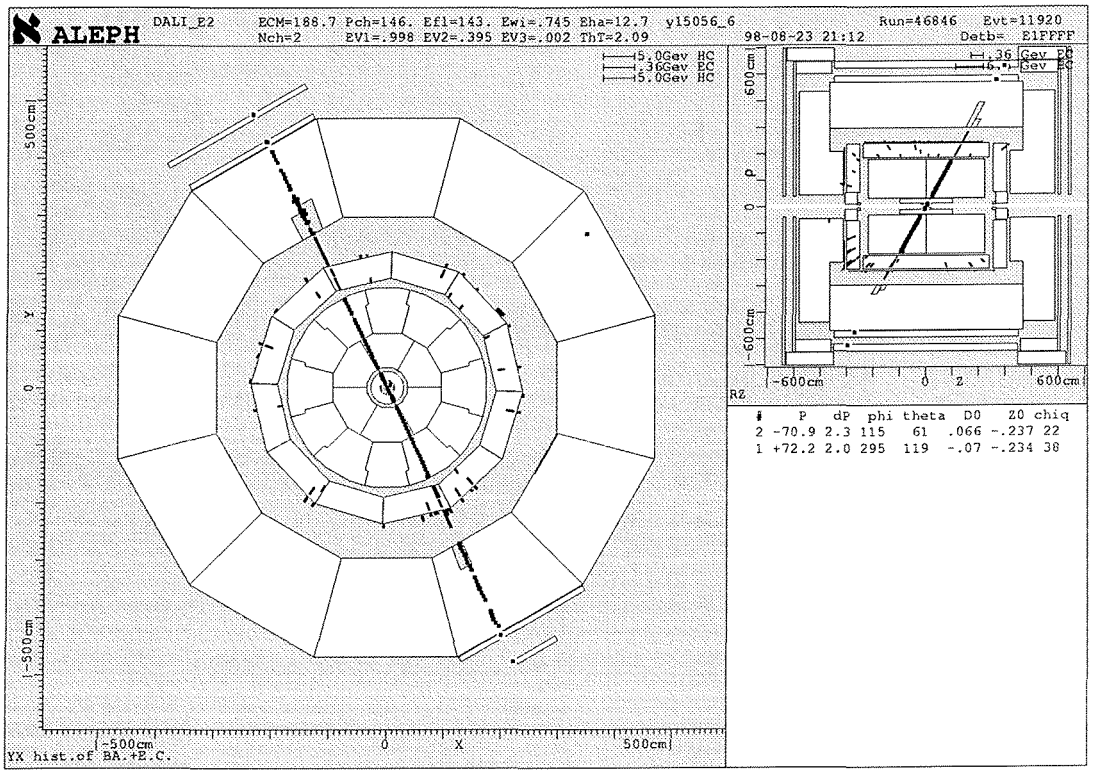

Made on 19-Nov-1999 17:28:29 by sguazzon with DALI_E2.
Filename: DC046846_011920_991119_1728.PS

Figure 7.7: Candidate event of the LLH long lifetime selection.

7.3 Combining samples at different energies

The number and the distributions of the observed candidates is compatible with the expected background in all selections. The absence of signal can be used to set limits on the squark mass. These limits depend on the MSSM parameters in the squark sector since the production cross section depend on $m_{\tilde{q}}$ and $\theta_{\tilde{q}}$ and the signal efficiency depends on $m_{\tilde{q}}$, Δm and, in general, on other parameters (as the decay length, for example). The number of expected signal events can be generally written

$$\nu_s = \varepsilon(\Delta m, m_{\tilde{q}}, ...)\sigma(m_{\tilde{q}}, \theta_{\tilde{q}})\mathcal{L}. \tag{7.1}$$

The general method to derive limits from a search experiment has been already discussed. The low background level confirms the choice to not apply the background subtraction to derive limits. Nevertheless the general good agreement between the surviving candidates number with Standard Model expectations could in principle allow us to use the background subtraction method that implies a good background simulation. The improvement in limits would be anyhow marginal with respect to the more conservative method without the background subtraction applied here.

As a consequence of our sliding cuts, the upper limit in the mean number of candidates ν_{oc} depends on the parameter Δm for the AJ and AJL selections and on $m_{\tilde{T}}$ for the LLH long lifetime selection. Let's use the first case to do an example. From the eq. (7.1) follows:

$$\nu_{oc}(\Delta m) > \varepsilon(\Delta m, m_{\tilde{q}})\sigma(m_{\tilde{q}}, \theta_{\tilde{q}})\mathcal{L} \;\Rightarrow\; \sigma(m_{\tilde{q}}, \theta_{\tilde{q}}) < \nu_{oc}(\Delta m)/\left[\varepsilon(\Delta m, m_{\tilde{q}})\mathcal{L}\right]. \tag{7.2}$$

Since $\Delta m = m_{\tilde{q}} - m_{\mathrm{LSP}}$, the relation above allows to exclude the regions in the three dimensional space $(m_{\tilde{q}}, \theta_{\tilde{q}}, m_{\mathrm{LSP}})$, that is where the SUSY predicted cross section is greater than $\nu_{oc}(\Delta m)/[\varepsilon(\Delta m, m_{\tilde{q}})\mathcal{L}]$. For graphical reasons the excluded region are often given in the plane m_{LSP} vs. $m_{\tilde{q}}$ for $\theta_{\tilde{q}}$ fixed at some relevant values (i.e. minimum and maximal production cross section values).

The above method can be generalized for the case that more samples at different energies are available. In particular, it turns out that

$$\sum_{\sqrt{s_i}>2m_{\tilde{q}}} \nu^i_{oc} > \sum_{\sqrt{s_i}>2m_{\tilde{q}}} \nu^i_s = \sum_i \varepsilon_i \sigma(\sqrt{s_i}, m_{\tilde{q}})\mathcal{L}_i, \tag{7.3}$$

where the index i runs over all the available samples, ν^i_{oc} is the upper limit on the number of candidates and ε_i and $\mathcal{L}_i$ are the efficiencies and the luminosities of the i-th data sample. We have introduced the explicit dependence of the cross section on the center-of-mass energy. Since the relation above can be rewritten

$$\sum_{\sqrt{s_i}>2m_{\tilde{q}}} \nu^i_{oc} > \sigma(\sqrt{s_1}, m_{\tilde{q}}) \sum_{\sqrt{s_i}>2m_{\tilde{q}}} \varepsilon_i \frac{\sigma(\sqrt{s_i}, m_{\tilde{q}})}{\sigma(\sqrt{s_1}, m_{\tilde{q}})}\mathcal{L}_i, \tag{7.4}$$

the eq. (7.2) can be generalized as follows:

$$\sigma(\sqrt{s_1}, m_{\tilde{q}}) < \frac{\sum_{\sqrt{s_i}>2m_{\tilde{q}}} \nu^i_{oc}}{\sum_{\sqrt{s_i}>2m_{\tilde{q}}} \varepsilon_i \frac{\sigma(\sqrt{s_i}, m_{\tilde{q}})}{\sigma(\sqrt{s_1}, m_{\tilde{q}})}\mathcal{L}_i}. \tag{7.5}$$

This relation takes into account that a candidate found at the energy $\sqrt{s_i}$ is a good candidate only for the region $m_{\tilde{q}} < \sqrt{s_i}/2$. In the case of squark production, the ratios $\sigma(\sqrt{s_i}, m_{\tilde{q}})/\sigma(\sqrt{s_1}, m_{\tilde{q}})$ are equal to $(\beta_i^3/\beta_1^3)(s_1/s_i)$ since the cross section for a scalar is proportional to β^3/s, where β is the speed of the produced particle (see section 2.3.1). Although not optimal, this method to combine different energy samples is easy and conservative and it is used within this work.

In deriving the results the efficiencies have suitably rescaled to take into account systematic uncertainties, quantified in a relative error $\Delta\varepsilon/\varepsilon$ on the efficiencies for each selection. The most straightforward and most conservative approach to incorporate this uncertainty would be to simply subtract it from the selection efficiency. Following this approach, the efficiency ε_i used in (7.5) would be replaced by the quantity $\varepsilon_i(1 - \Delta\varepsilon_i/\varepsilon_i)$. An alternative approach, described in [92], is used instead. In this approach, the 95% C.L. limits ν_{oc}^i given in table 5.1 and used in (7.5), are modified by an amount which depends on the systematic uncertainty. In particular:

$$\nu_{oc}^i \rightarrow \nu_{oc}^i \left[1 + \frac{\nu_{oc}^i - n_{oc}}{2} \left(\frac{\Delta\varepsilon_i}{\varepsilon_i} \right)^2 \right]. \tag{7.6}$$

7.4 Limits on stop and sbottom production

The number of observed candidates is used to derive the upper limit on the cross section at 95 % C.L. This limit is usually referred as σ_{95} that is different from $\overline{\sigma}_{95}$ since the first is computed on the real number of candidates, the latter on the mean of expected candidates. Since a candidate is valid only for a certain range of the squark masses and Δm, σ_{95} results not constant in the plane $m_{\tilde{t}}$ vs. m_χ. The excluded region in this plane comes from the comparison of σ_{95} with the theoretical cross sections given in section 2.3.1. All the exclusion plots shown in this chapter are obtained combining the most recent results based on $192 \div 202$ GeV data with the results at lower energies, if available (as for the AJ and AJL selections), according to the combination method described in the previous section. Therefore σ_{95} is given by the right side of the relation (7.5) once the upper limits on the mean number of candidates is computed at 95 % C.L., i.e. $\alpha = 0.05$ in the relation (5.7), and the systematic uncertainties are included by using the relation (7.6).

$\tilde{t} \rightarrow c\chi$

The σ_{95} obtained on the $\tilde{t} \rightarrow c\chi$ channel applying the AJ selections to all available data samples is shown in fig. 7.8(a). The sudden change from lighter to darker colour corresponds to a discontinuity in the σ_{95} value; the exclusion in the darker region is weaker than the exclusion in the lighter region as a consequence of an higher number of candidates not balanced by a consistent luminosity. In the exclusion plot these sudden steps appear as kinks and irregularities in the boundaries of the excluded regions.

The excluded regions are defined as the regions where σ_{95} is lower than the theoretical cross section. It is computed for two different values of the mixing angles: $\theta_{\tilde{t}} = 56°$ for which the cross section is minimal and for $\theta_{\tilde{t}} = 0°$ for which the cross section is maximal. The excluded region in the plane $m_{\tilde{t}}$ vs. m_χ are shown in fig. 7.8(b). The plot reports also the excluded regions from the TEVATRON experiments, and the region kinematically

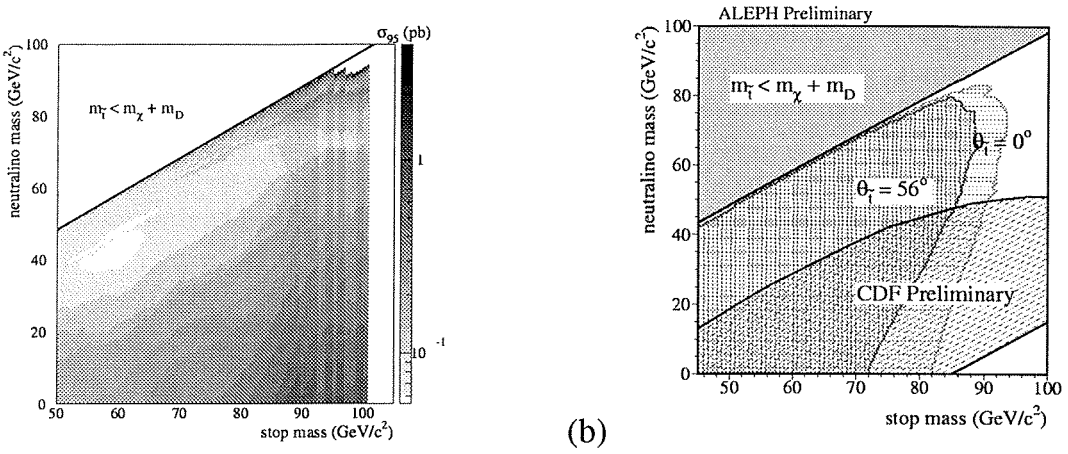

Figure 7.8: Limits for the $\tilde{t} \to c\chi$ channel in the m_χ vs $m_{\tilde{t}}$ plane: excluded cross section σ_{95} (a) and excluded regions for theoretical cross section computed for two different mixing angles (b). In the latter the TEVATRON results are also shown.

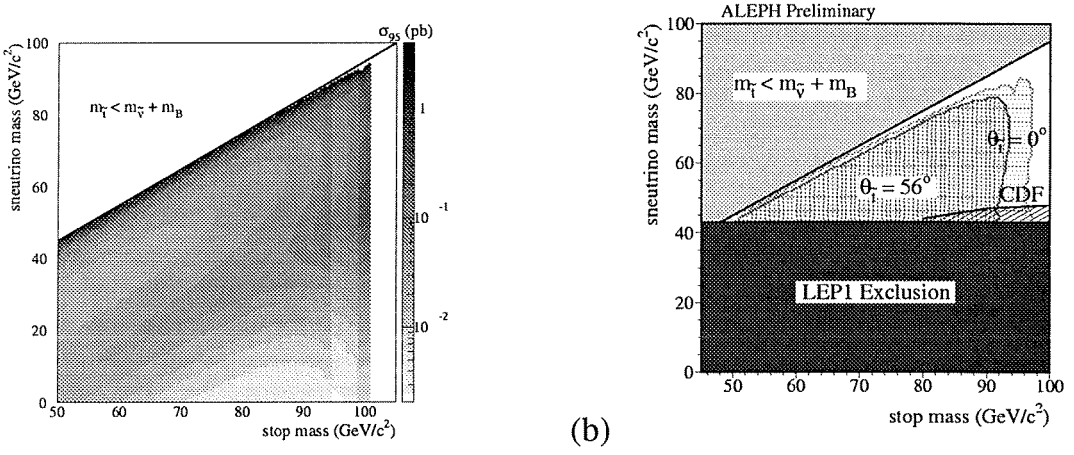

Figure 7.9: Limits for the $\tilde{t} \to b\ell\tilde{\nu}$ channel in the $m_{\tilde{\nu}}$ vs $m_{\tilde{t}}$ plane: excluded cross section σ_{95} (a) and excluded regions for theoretical cross section computed for two different mixing angles (b). The LEP1 sneutrino limit is visible in (b).

forbidden to the $\tilde{t} \rightarrow c\chi$ decay ($m_{\tilde{t}} < m_{\chi}+m_{D}$). In the region in the right bottom angle of the plot, the decay $\tilde{t} \rightarrow bW\chi$ is kinematically allowed but not excluded from the TEVATRON experiments. The ALEPH results are then complementary to the TEVATRON ones since they allow to exclude the lower Δm region.

The scalar β^3 behaviour makes the cross section vanishing close to the kinematic limit. As a consequence of that, also the excluded regions in the mass plane do not reach the kinematic limits.

The 95 % C.L. limit on the stop mass in case of $\tilde{t} \rightarrow c\chi$ decay channel can be quantified in $72\,\mathrm{GeV}/c^2$ for $\Delta m > 8\,\mathrm{GeV}/c^2$ when the cross section is minimal and in $82\,\mathrm{GeV}/c^2$ for $\Delta m > 8\,\mathrm{GeV}/c^2$ when the cross section is maximal. With respect to the 1998 results (up to 189 GeV in the center-of-mass energy), the mass limit has improved of about $2\,\mathrm{GeV}/c^2$, depending on the Δm region.

$\tilde{t} \rightarrow b\ell\tilde{\nu}$

Fig. 7.9(a) shows the σ_{95} obtained for the $\tilde{t} \rightarrow b\ell\tilde{\nu}$ applying the AJL selections to all ALEPH data. The excluded region in the $m_{\tilde{\nu}}$ vs. $m_{\tilde{t}}$ plane are shown in fig. 7.9(b) for the two relevant values of the mixing angle. It has been assumed that the branching ratios in the three lepton families are equal. The LEP1 limit on the sneutrino mass given by the invisible width measurements from the Z lineshape is also shown.

The 95 % C.L. limit on the stop mass in case of $\tilde{t} \rightarrow b\ell\tilde{\nu}$ decay channel can be quantified in $91\,\mathrm{GeV}/c^2$ ($\Delta m > 8\,\mathrm{GeV}/c^2$) for the minimal value of the production cross section and $95\,\mathrm{GeV}/c^2$ ($\Delta m > 8\,\mathrm{GeV}/c^2$) in case of maximal cross section. The stop mass limit improvement in this channel can be evaluated in about $6\,\mathrm{GeV}/c^2$ with respect to the 1998 results.

$\tilde{b} \rightarrow b\chi$

The AJ selection plus the b-tag allows to set an upper limit on the production cross section of sbottom squarks in case of $\tilde{b} \rightarrow b\chi$ decay channel. Fig. 7.10(a) shows the σ_{95} from which the excluded regions in the m_{χ} vs. $m_{\tilde{b}}$ plane shown in fig. 7.10(b) are obtained. The two relevant mixing angle are shown as usual: $\theta_{\tilde{b}} = 68°$ and $\theta_{\tilde{b}} = 0°$ for which the cross section is minimal and maximal respectively. The 95 % C.L. limit on the sbottom mass independent from the mixing angle is $78\,\mathrm{GeV}/c^2$ assuming $\Delta m > 8\,\mathrm{GeV}/c^2$. In case of maximal cross section ($\theta_{\tilde{b}} = 0°$) the limit is $90\,\mathrm{GeV}/c^2$ for $\Delta m > 8\,\mathrm{GeV}/c^2$. With respect to the 1998 results, the mass limit has improved of about $4\,\mathrm{GeV}/c^2$.

7.5 Limits on degenerate squarks

The degenerate squark production process accessible at LEP is $e^+e^- \rightarrow \tilde{q}\bar{\tilde{q}} \rightarrow q\bar{q}\chi\chi$ since the squark decay is $\tilde{q} \rightarrow q\chi$. The topology is similar to $\tilde{t} \rightarrow c\chi$ and the AJ selections are used. By using simulated samples of degenerate squark signal the selection efficiencies have been verified to be similar to the $\tilde{t} \rightarrow c\chi$ case. The hypothesis of five flavour families ($\tilde{u}$, $\tilde{d}$, $\tilde{c}$, $\tilde{s}$ and $\tilde{b}$) degenerate in mass is assumed as TEVATRON experiments do in deriving their results.

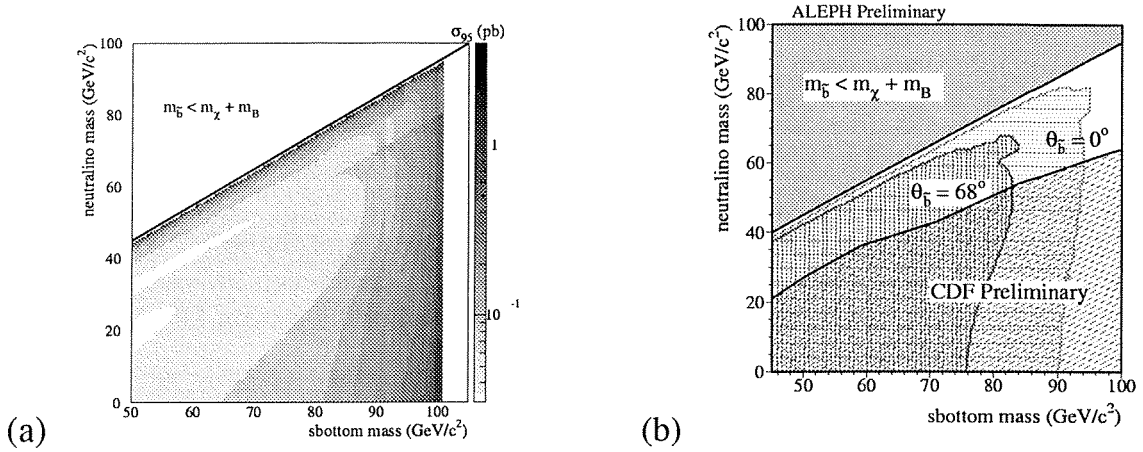

Figure 7.10: Limits for the $\tilde{b} \rightarrow b\chi$ channel in the m_χ vs $m_{\tilde{t}}$ plane: excluded cross section σ_{95} (a) and excluded regions for theoretical cross section computed for two different mixing angles (b). The LEP1 sneutrino limit is visible in (b).

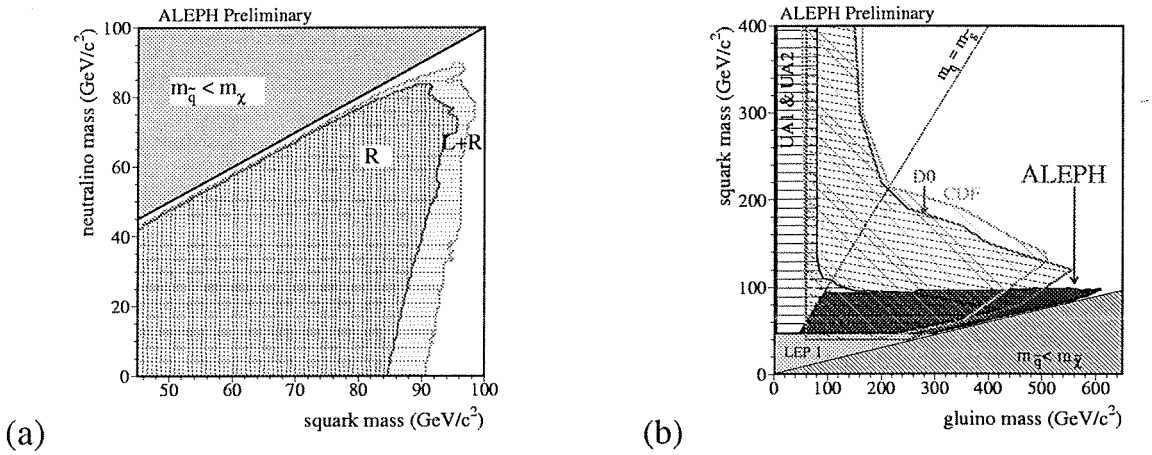

Figure 7.11: Degenerate squarks mass limits versus the neutralino mass (a) and degenerate squarks mass limits with respect to the gluino mass (b).

The resulting excluded regions in the m_χ vs. $m_{\tilde{q}}$ plane are shown in fig. 7.11(a) for two different hypothesis: only the $\tilde{q}_R$ is accessible at LEP2 (the right squark is expected lightest) and both $\tilde{q}_R$ and $\tilde{q}_L$ are accessible at LEP2. The 95 % C.L. mass limits in these cases are $84\,\mathrm{GeV}/c^2$ (only $\tilde{q}_R$) and $90\,\mathrm{GeV}/c^2$ (both $\tilde{q}_R$ and $\tilde{q}_L$). The limits are valid for $\Delta m > 8\,\mathrm{GeV}/c^2$ and improve of about $6\,\mathrm{GeV}/c^2$, depending on Δm, the similar result based on data up to 189 GeV in center-of-mass energy.

The degenerate squarks are one of the most important topics of the SUSY searches at TEVATRON (see section 2.4). ALEPH degenerate squark results can be interpreted to give competitive limits with respect to the hadronic collider ones in certain MSSM regions where the squarks are lighter than gluinos.

Assuming the GUT relations (1.76) the gluino and gaugino common masses M_3 and M_1 both depend on the gaugino common mass $m_{1/2}$. In particular at the LEP2 scale $M_3 = 6.8 M_1$. While the gluino mass is just M_3, the lightest neutralino mass depends on the mixing matrix parameters M_1, μ and $\tan\beta$ (see relation (1.100)) since it is a superposition of binos and neutral higgsinos. If $|\mu| \gg m_{1/2}$ it turns out that $m_{\tilde{g}} \sim 6.8 m_\chi$ since the lightest neutralino is mainly bino there. For lower values of $|\mu|$ the relation is valid almost unchanged and only for very low $|\mu|$ values the $m_{\tilde{g}}/m_\chi$ ratio rapidly increases. This behaviour is similar for all $\tan\beta$ value. Anyhow it results always true that the gluino mass is limited from below by the neutralino mass.

As a consequence of that the ALEPH degenerate squark excluded regions in the m_χ vs. $m_{\tilde{q}}$ plane can be directly translated in excluded regions in the $m_{\tilde{g}}$ vs. $m_{\tilde{q}}$ plane as shown in fig. 7.11(b). The CDF and D0 results are also reported to allow a direct comparison. ALEPH is competitive in the high gluino masses and small squark masses region where the collider topologies are characterized by a small missing energy and thus less discriminable from the minimum bias background. Moreover the cross section there is very small. The ALEPH degenerate squark mass limit at 95 % C.L. is valid for gluino masses up to $\sim 600\,\mathrm{GeV}/c^2$.

7.6 Limits on very small Δm region from stop hadrons

It is clear from the results given until now that an absolute limit on the squark mass can be given only assuming an arbitrary lower limit on Δm. By using the LLH selections the stop mass exclusions in the very low Δm regions can be improved.

The very low Δm exclusion that we can obtain by the AJ selection can be evaluated considering the selection efficiencies for small Δm values. Fig. 7.12(a) shows the efficiency as a function of the stop mass for $\Delta m = 3\,\mathrm{GeV}/c^2$ and $\Delta m = 5\,\mathrm{GeV}/c^2$ from which it turns out that the efficiency drops very rapidly and then vanishes when Δm does not allows the production of the D meson. In fact at least a D meson has to be formed by the hadronization of the c quark in the $\tilde{t} \to c\chi$ decay. Fig. 7.12(b) shows the excluded regions that follow. It is worth to notice that, from the point of view of the energy available to the $\tilde{t}$ decay, the effective Δm_{eff} value is $m_{\tilde{t}} + m_{\mathrm{eff}} - m_\chi$ rather than simply $m_{\tilde{t}} - m_\chi$. In fact also the spectator quark effective mass m_{eff} (see section 4.1.1) contributes to the energy available to the final state. Therefore it turns out the limit on the "true" $\Delta m = m_{\tilde{t}} - m_\chi$ depends on the effective mass value used to simulate the signal. We obviously ignore which is the m_{eff} that best reproduces the squark phenomenology and no clear hints come from the theory

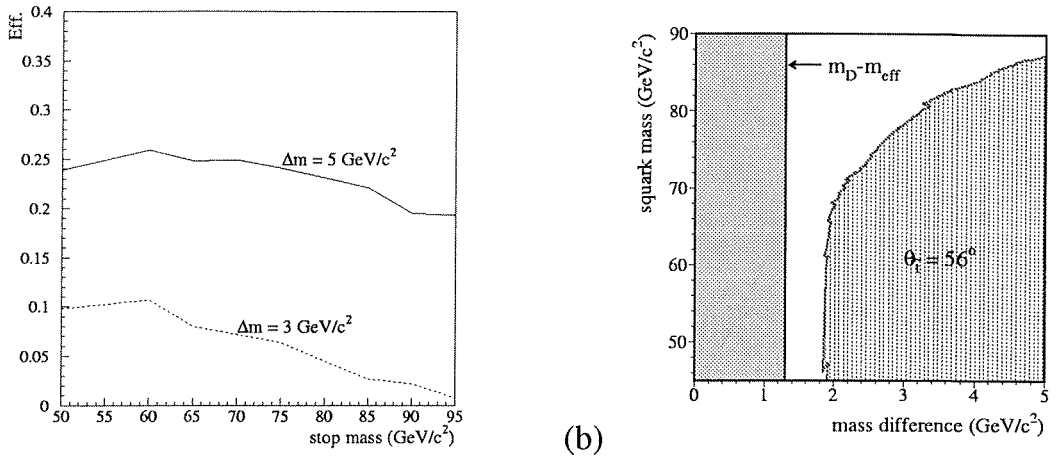

Figure 7.12: AJ selection efficiency (a) and excluded regions (b) for very low Δm values.

about this.

Moreover from the decay length studies reported in section 2.3.2, we know that the $\tilde{t}$ decay length in the very small Δm region is absolutely not negligible as fig. 2.6 shows. As a consequence of that the efficiencies of fig. 7.12(a) may be completely over estimated and totally unreliable. For example, the AJ selection requires the charged tracks to be "good" (see section 3.3.1), that means a condition on the impact parameter that cannot be satisfied if the decay length is consistent[1].

To cope with these difficulties the LLH selection have been designed. The limits on the stop hadron mass we can obtain are shown in fig. 7.13(a) for the four considered values of the decay length and for the long lifetime case. The limit is given by the stop hadron mass value for which the σ_{95} is equal to the theoretical cross section also reported in the plot.

These model independent results can be translated into excluded regions in the Δm vs. $m_{\tilde{t}}$ plane by using the relation between Δm and the decay length discussed in section 2.3.2. To do this the selection efficiencies have to be parametrized also as a function of the stop decay length, that is:

- the long lifetime selection efficiency is exponentially scaled in order to have zero efficiencies for small decay length, that is

$$\varepsilon_{\text{LLH long}} \propto 1 - e^{-\frac{\lambda}{\lambda_0}}, \tag{7.7}$$

  where, from the simulations, λ_0 results of ~ 90 cm;

- the intermediate lifetime selection efficiency is scaled according to the following relation

$$\varepsilon_{\text{LLH inter.}} \propto e^{-\frac{\lambda}{\lambda_0}}(1 - e^{-\frac{\lambda}{\lambda_1}}), \tag{7.8}$$

  and the simulations give $\lambda_0 \sim 380$ cm and $\lambda_1 \sim 8$ cm;

[1]It is worth to recall how this condition has been dropped in the LLH intermediate lifetime selection

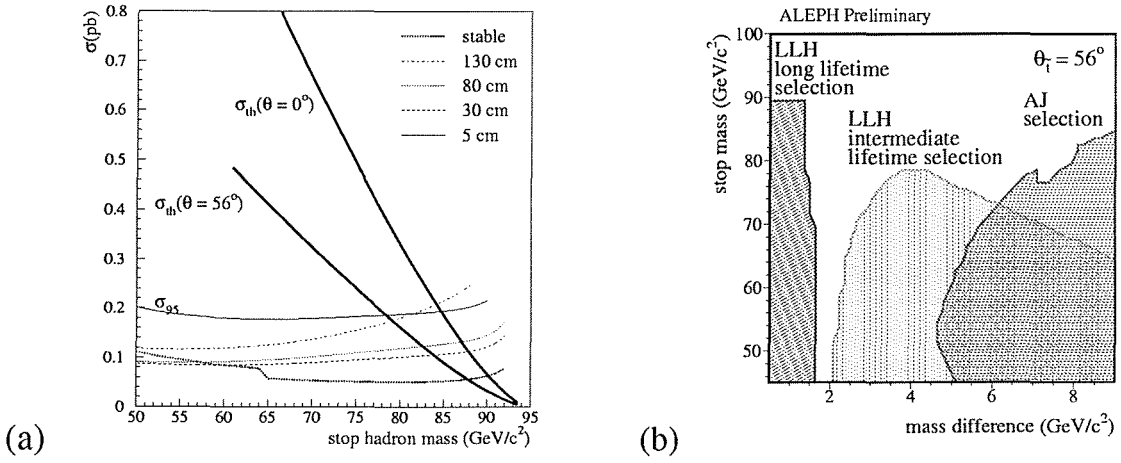

Figure 7.13: Stop hadron mass limits from the LLH selections with respect to the decay length (a). Limits for very small Δm values from LLH long lifetime selection, LLH intermediate lifetime and standard AJ selection (b).

- the standard AJ selection efficiency is exponentially scaled in order to have zero efficiencies for large decay length, i.e.

$$\varepsilon_{\mathrm{AJ}} \propto e^{-\frac{\lambda}{\lambda_1}} \tag{7.9}$$

where λ_1 has been set to 1 cm to be conservatively consistent with the good charged track criteria.

The resulting excluded regions are shown in fig. 7.13(b). The standard AJ selection exclusions are now consistently weaker in comparison with the exclusions shown in fig. 7.12(b), where the stop lifetime is neglected. Even if the reported study on the "low Δm" phenomenology is still preliminary, it is rather clear that the AJ selection performances in this difficult region are worse than usually thought.

Unfortunately as a consequence of the missing overlap between the long lifetime and the intermediate lifetime selections, there is a corridor in Δm where a mass limit cannot be set. The lower limits can be quantified in 73 GeV at 95 % C.L. for $\Delta m > 3\,\mathrm{GeV}/c^2$ and 89 GeV at 95 % C.L. for $\Delta m < 1.5\,\mathrm{GeV}/c^2$.

Nevertheless, the LLH selections are still very preliminary and probably consistent improvements can be expected. In particular, since the intermediate lifetime is based on the stop hadron decay products thus suffering the same problems of the standard analysis as far as Δm approaches to the lower kinematic limit, it would result impossible to significantly improve this selection toward smaller Δm values. On the contrary, the LLH long lifetime selection criteria can be probably extended to cope with smaller stop decay lengths.

Conclusions

In this thesis is described the extensive search of new physics performed on samples of e^+e^- interactions recorded by the ALEPH experiment, one of the four experiments on the LEP collider, during operations of 1998 and 1999. In those years ALEPH collected $\sim 174\,pb^{-1}$ at $\sqrt{s} = 189\,GeV$, $\sim 29\,pb^{-1}$ at $\sqrt{s} = 192\,GeV$, $\sim 80\,pb^{-1}$ at $\sqrt{s} = 196\,GeV$, $\sim 83\,pb^{-1}$ at $\sqrt{s} = 200\,GeV$ and $\sim 35\,pb^{-1}$ at $\sqrt{s} = 202\,GeV$.

The search consists of selections designed to look for the following hadronic topologies that are not typically compatible with Standard Model processes:

1. acoplanar jets and missing mass and energy;
2. acoplanar jets plus leptons and missing mass and energy;
3. acoplanar b-like jets and missing mass and energy;
4. heavy stable hadrons;
5. heavy stable hadrons decaying inside the apparatus.

The selections 1 to 3 have been optimized for and applied to the data sample at center-of-mass energies between 196 GeV and 202 GeV. They improve the results of similar selections applied to the data samples at lower energies. The selections 4 and 5 have been optimized for and applied to the data sample at center-of-mass energies between 189 GeV and 192 GeV. The number of observed events (candidates) is in agreement with the expected background from Standard Model processes. In particular, in each case:

1. 10 candidates and 11.7 expected;
2. 4 candidates and 2.6 expected;
3. 3 candidates and 3.6 expected;
4. 1 candidate and 0.2 expected;
5. 1 candidate and 0.4 expected.

Since the searched topologies are predicted by theories beyond the Standard Model as SuperSymmetry (SUSY), the negative results of the searches can be translated in lower limits on the masses of some of these new particles.

In most cases the minimal supersymmetric extension of Standard Model (the Minimal Supersymmetric Model - MSSM) is assumed. It predicts the existence of partners of the standard particles having the same quantum numbers of the standard particle except the spin, that differs of 1/2. These new particles undergo to the Standard Model gauge interactions and the conservation of the R-parity is assumed. This means that each elementary vertex of standard model can be translated into a vertex involving supersymmetric particles replacing an odd number of the particles with their supersymmetric partners. The following relevant consequences follows:

- the LSP (the lightest supersymmetric particle) is stable; it must be neutral and weakly interacting to have escaped detection up to now;
- the supersymmetric particles can be produced only in couples at LEP;
- an odd number of LSPs must be present at the end of the decay chain of any supersymmetric particle.

Among the others new particles, the MSSM predicts the existence of the scalar partners of the standard quarks, know as squarks. For certain configurations of the unknown parameters of the model, the scalar partners of the top (stop, $\tilde{t}$) and bottom (sbottom, $\tilde{b}$) could be the lightest charged supersymmetric particles and well accessible at LEP. They can be produced in couples and their expected decays could be $\tilde{t} \rightarrow c\chi$ or $\tilde{t} \rightarrow b\ell\tilde{\nu}$, and $\tilde{b} \rightarrow b\chi$ where the χ (superposition of the partners of neutral gauge fields and of the partners of the Higgs boson fields) and $\tilde{\nu}$ (partner of the neutrino) are the LSP candidates. It is clear that the stop signal yields to the topologies 1 or 2 while the sbottom yields to the topology 3.

If the mass difference Δm between the squark and the LSP become very small (less than few GeV) the squarks acquire a consistent lifetime resulting in topologies for which the selections 4 and 5 can be used.

Comparing the observed events with the theoretical cross section predicted by the MSSM, the following 95 % C.L. limits on the squark mass can be set:

- stop mass greater than $72\,\mathrm{GeV}/c^2$ at 95 % C.L. in case $\Delta m > 8\,\mathrm{GeV}/c^2$, if the stop decay is $\tilde{t} \rightarrow c\chi$;
- stop mass greater than $91\,\mathrm{GeV}/c^2$ at 95 % C.L. in case $\Delta m > 8\,\mathrm{GeV}/c^2$, if the stop decay is $\tilde{t} \rightarrow b\ell\tilde{\nu}$;
- sbottom mass greater than $78\,\mathrm{GeV}/c^2$ at 95 % C.L. in case $\Delta m > 8\,\mathrm{GeV}/c^2$, if the sbottom decay is $\tilde{b} \rightarrow b\chi$.

In the hypothesis that all the squarks except the stop are degenerate, the selection for topology 1 can be used and the following limits results:

- degenerate squark mass greater than $92\,\mathrm{GeV}/c^2$ at 95 % C.L. for $\Delta m > 7\,\mathrm{GeV}/c^2$.

In the very low Δm region the negative results of the selections for topologies 4 and 5 allow to set the following limits:

- stop mass greater than 73 GeV at 95 % C.L. for $\Delta m > 3\,\mathrm{GeV}/c^2$;
- stop mass greater than 89 GeV at 95 % C.L. for $\Delta m < 1.5\,\mathrm{GeV}/c^2$.

It has been shown how the consistent stop lifetime significantly alters the performances of the selection for topology 1 that up to now was generally used for the "low Δm" region neglecting the lifetime. Nevertheless the selection for topologies 4 and 5 allow to recover this problem and improve the results in the "low Δm" region.

Acknowledgements

In the first place I wish to thank Prof. E. Focardi for giving me the possibility of spending these three years of PhD fellowship under his fruitful supervision.

Then I must express my deepest gratitude to two colleagues and friends without whom this thesis would certainly have been worse: Mario Antonelli for his patience and help as ALEPH squark expert and Gerardo Ganis for his incredibly accurate proofreading of the manuscript and for the huge number of suggestions as a great SUSY expert.

I also wish to thank all the ALEPH SUSY Task Force and all my closest friends in Pisa and CERN: M. Aleppo, P. Azzurri, T. Boccali, Prof. E. Borzacchini, C. Bozzi, V. Ciulli, F. Ligabue, F. Palla, A. Sciabà, P. Spagnolo and A. Venturi.

Bibliography

[1] S. Weinberg, Phys. Rev. Lett. **19** (1967) 1264;
S. Glashow, Nuc. Phys. **22** (1961) 579;
A. Salam, Proc. 8th Nobel Symposium, Stockholm 1968, Ed. N. Svartholm (Almqvist and Wiksells, Stockholm 1968) 3678.

[2] G. 't Hooft, Nucl. Phys. **B 33** (1971) 173.

[3] LEP Higgs Working group, ALEPH-CONF/99-052 (1999).

[4] LEP Electroweak Working group, CERN-EP/99-15 (1999).

[5] S.P. Martin, in Perspectives on Supersymmetry ed. G. Kane, World Scientific, Singapore (1997), hep-ph/9709356.

[6] M. Drees, hep-ph/9611409 (1996).

[7] H.P. Nilles, Phys. Rep. **C 110** (1984) 1;
H.E. Haber and G.L. Kane, Phys. Rep. **C 117** (1985) 75; R. Barbieri, Riv. Nuovo Cimento 11 (1988) 1.

[8] Ed. M. Jacob, *Supersymmetry and Supergravity*, North-Holland and World Scientific, (1986).

[9] S. Dawson, hep-ph/9709356 (1997).

[10] H. Dreiner, hep-ph/9707435.

[11] L. Girardello e M.T. Grisaru, Nucl. Phys. **B 194** (1982) 65.

[12] H. Georgi, Phys. Lett. **B 169** (1986) 231.

[13] Y. Nir, N. Seiberg, Phys. Lett. **B 309**, 337 (1993).

[14] K.R. Dienes and C. Kolda, in Perspectives on Supersymmetry ed. G. Kane, World Scientific, Singapore (1997), CERN-TH/97-292, hep-ph/9712322.

[15] R. Arnowitt and P. Nath, in Perspectives on Supersymmetry ed. G. Kane, World Scientific, Singapore (1997), hep-ph/9708254.

[16] R.Barbieri, M. Frigeni, Phys. Lett.**B 258** (1991) 395.

[17] ALEPH Collaboration, ALEPH-CONF/99-041 (1999).

[18] M. Drees, K. Hikasa, Phys. Lett. **B 252** (1990) 127.

[19] H. Eberl, A. Bartl and W. Majerotto, `hep-ph/9603206`.Phys. Lett. **B 349** (1995) 463.

[20] J. Schwinger, *Particles sources and Field* Vol II. (Addison-Wesley) cap. 5.4.

[21] F.A. Berends and R. Kleiss, Nucl. Phys. 178 (1981)141. α^2_{QED} modifications as in P. Janot, *The HZHA generator* in *Physics at LEP2*, Eds. G.Altarelli, T.Sjöstrand and F.Zwirner, CERN 96-01(1996), Vol.2, p.309.

[22] C.F. Weizsäcker, Z. Phys. **88** (1934) 612;
E.J. Williams, Phys. Rev. **45** (1934) 729.

[23] Various authors, *Physics at LEP2*, CERN 96-01 (1996), ed. G. Altarelli, T. Sjöstrand e Z. Zwirner.

[24] K. Hikasa, M. Kobayashi, Phys. Rev. **D 36** (1987) 724.

[25] Fortran package for MSSM computation based on [18], [19] and [24] for the squark sector. Tha package can be obtained from G. Ganis (`g.ganis@cern.ch`).

[26] ALEPH Collaboration, CERN EP/99-093 (1999).

[27] D0 Collaboration, Phys. Rev. Lett. **76** 2222 (1996).

[28] Result presented at ICHEP98: Abstract 652, Vancouver, BC, June 1998.

[29] D0 Collaboration, Phys. Rev. Lett. **75** (1995) 618.

[30] CDF Collaboration, Phys. Rev. **D 56** (1997) 1357.

[31] M. Chertok, The CDF Collaboration, FERMILAB-CONF-98/156-E, Proceedings 33rd Rencontres de Moriond: QCD and High Energy Hadronic Interactions, Les Arcs, France, March 21-18, 1998.

[32] Amber Boehnlein (D0 Collaboration), Fermilab Wine and Cheese Seminar, 19 September 1997.

[33] ALEPH collaboration, European Physical Journal **C 7** (1999) 383.

[34] *LEP design report* v.1 and v.2, CERN LEP 84-01 (1984).

[35] *LEP design report* v.3, CERN AC 96-01 (LEP2) (1996).

[36] S. Myers, *The LEP Collider, from design to approval and commissioning*, CERN 91-08 (1991).

[37] DELPHI Collaboration, P. Aarnio et al., Nucl. Instrum. Methods **A 303** (1991) 233.

[38] L3 Collaboration, B. Adeva et al., Nucl. Instrum. Methods **A 289** (1990) 35.

[39] OPAL Collaboration, K. Ahrnet et al., Nucl. Instrum. Methods **A 305** (1991) 275.

[40] W. Herr et al., in *Workshop on LEP Performance* ed. by J. Poole, CERN SL/94-06(DI) (1994).

[41] B. Goddard et al., Part. Accel. **57** (1997) 237.

[42] L. Arnaudon, et al., Z. Phys. **C 66** (1995) 45.

[43] A.A. Sokolov and I.M. Ternov, Sov. Phys. Dokl. **8** (1964) 1203.

[44] J. Wenninger, in *Workshop on LEP Performance* ed. by J. Poole, CERN SL/94-06(DI) (1994).

[45] LEP Energy Working Group, A. Blondel et al., CERN EP/98-191 (1998).

[46] M. Böge et al., CERN SL/98-034 (1998).

[47] M. Placidi, *Perspectives for energy calibration and extrapolation* in Proceedings of VII Chamonix workshop (1998).

[48] J. Wenninger, *Physics and energy calibration* in Proceedings of VIII Chamonix workshop (1999).

[49] L. Arnaudon et al., Nucl. Instrum. Methods Phys. Res. **A 357** (1995) 249.

[50] J. Wenninger, CERN SL/99-025(OP) (1995).

[51] LEP Energy Group, E. Bravin et al., Nucl. Instrum. Methods Phys. Res. **A 417** (1998) 9.

[52] ALEPH Collaboration, D. Decamp et al., Nucl. Instrum. Methods **A 294** (1990) 121.

[53] *The ALEPH handbook 1995*, ed. by C. Bowdery.

[54] ALEPH Collaboration, Nucl. Instrum. Methods **A 360** (1995) 481.

[55] B. Mours et al., Nucl. Instrum. Methods **A 379** (1996) 101.

[56] E. Focardi, Nucl. Instrum. Methods **A 386** (1997) 18.

[57] A. Bonissent, D. Rousseau, M. Thulasidas and K. Trabelsi, ALEPH/97-116 (1997).

[58] G. Sguazzoni et al., Nucl. Phys. **B** (Proc. Suppl.) **78** (1999) 301.

[59] S. Montéil and F. Palla, ALEPH-NOTE/99-100.

[60] R. Baldini et al., Nucl. Instr. Meth. A **247** (1986) 438.

[61] D. Decamp et al., Zeit. Phys. C **53** (1992) 375.

[62] D. Bédérède et al.,

[63] D. Buskulic et al., Zeit. Phys. C **62** (1994) 539.

[64] J. Knobloch and E. Lancon, ALEPH 94-151 SOFTWR 94-013.

[65] R. Barate et al., Phys. Lett. **B 412** (1997) 155.

[66] `http://wwwcn.cern.ch/asdoc/geant/GEANTMAIN.html`

[67] H.C. Fesefeld, PITHA/85-02 (1985).

[68] M. Antonelli, ALEPH/97-77, MCARLO/97-03 (1997).

[69] T. Sjöstrand, Comput. Phys. Commun. **82** (1994) 74.

[70] W. Beenaker, R. Hopker, M. Spira and P.M. Zerwas, Phys. Lett **B 349** (1995) 463.

[71] C. Peterson, D. Schlatter, I. Schmitt and P.M. Zerwas, Phys. Rev. **D 27** (1983) 105.

[72] ALEPH Collaboration, Phys. Lett **B 384** (1996) 427.

[73] G. Altarelli, N. Cabibbo, G. Corbo, L. Maiani and G. Martinelli, Nucl. Phys. **B 208** (1982) 365.

[74] V. Khoze, T. Sjöstrand, Phys. Lett. **B 328** (1994) 466.

[75] S. Jadach and Z. Was, Comput. Phys. Commun. **36** (1985) 191.

[76] Minami-Tateya collaboration, "GRACE Manual ver 1.0", KEK Report **92-19** (1993), Minami-Tateya collaboration, "Brief Manual of GRACE system ver 2.0β ", (1995).

[77] J.A.M. Vermarasen in *Proceedings of the IVth Interantional Workshop on Gamma Gamma Interactions*, Eds. G. Cochard and P. Kessker, Springer & Verlag, 1980.

[78] R. Engel, Z. Phys. **C 66**, (1995) 203;
R. Engel and J. Ranft, Phys. Rev. **D 54** (1996) 4244.

[79] ALEPH Collaboration, Phys. Lett. **B 384** (1996) 427;
J.F. Grivaz, F. Le Diberder, LAL **92-37** (1992).

[80] CERN Program Library Long Writeup D506, MINUIT.

[81] W. J. Stirling, J. Phys. **G 17** (1991) 1567.

[82] D. Brown and M. Frank, ALEPH 92-135 PHYSIC 92-124, (1992).

[83] JADE Collaboration, Phys. Lett. **B 213** (1988) 235.

[84] ALEPH collaboration, CERN EP/99-140, (Submitted to Phys. Lett. B) (1999).

[85] ALEPH 91-132 SOFTWR 91-005, submitted on 91-09-27

[86] ALEPH 96-127 PHYSIC (PHYSICs) 96-116, (1996).

[87] ALEPH 98-042 PHYSIC (PHYSICs) 98-021 (1998).

[88] ALEPH Collab., Phys. Lett. **B 313** (1993) 535.

[89] Review of Particle Physics, Phys. Rev. **D 54** (1996).

[90] ALEPH Collaboration, Phys. Lett. **B 413** (1997) 431.

[91] ALEPH Collaboration, Phys. Lett. **B 434** (1998) 189.

[92] R.D. Cousins, V.L. Highland, Nucl. Instrum. and Methods **A 320** (1992) 331.